



THE HONG KONG
POLYTECHNIC UNIVERSITY

香港理工大學

Pao Yue-kong Library

包玉剛圖書館

Copyright Undertaking

This thesis is protected by copyright, with all rights reserved.

By reading and using the thesis, the reader understands and agrees to the following terms:

1. The reader will abide by the rules and legal ordinances governing copyright regarding the use of the thesis.
2. The reader will use the thesis for the purpose of research or private study only and not for distribution or further reproduction or any other purpose.
3. The reader agrees to indemnify and hold the University harmless from and against any loss, damage, cost, liability or expenses arising from copyright infringement or unauthorized usage.

If you have reasons to believe that any materials in this thesis are deemed not suitable to be distributed in this form, or a copyright owner having difficulty with the material being included in our database, please contact lbsys@polyu.edu.hk providing details. The Library will look into your claim and consider taking remedial action upon receipt of the written requests.

The Hong Kong Polytechnic University
Department of Mechanical Engineering

**Nanopatterning by Atomic
Force Microscopy**

By

Tang Qian

**A dissertation submitted in partial fulfillment of
the requirements for the degree of Doctor of
Philosophy**

January, 2006

Certificate of Originality

I hereby declare that this thesis is my own work and that, to the best of my knowledge and belief, it reproduces no materials previously published or written nor material which has been accepted for the award of any other degree or diploma, except where due acknowledgment has been made in the text.

_____ **(Signed)**

Tang Qian

_____ **(Name of Student)**

Abstract

For the first time, we fabricated nanostructures of a ferroelectric polymer, poly(vinylidene fluoride-trifluoroethylene) [P(VDF-TrFE)] on gold substrate via dip-pen nanolithography ink. Lines as thin as 32 nm and dot radius as small as 20 nm have been fabricated. The P(VDF-TrFE) molecules were well oriented on the gold substrate. The hydrophobic P(VDF-TrFE) produced a black contrast in the lateral force microscopy (LFM) images. The DPN-generated P(VDF-TrFE) patterns hold ferroelectric properties. The interaction between the P(VDF-TrFE) and the gold substrate was Van der Waals' interaction. The growth of dot radii/line-width was proportional to $t^{1/2}$.

We studied the influence of experimental conditions on dip-pen nanolithography. The results show: The transport rate of ink increased as the temperature increased for all of the inks. For P(VDF-TrFE), a deviation from Arrhenius plot at about 55°C was observed. It may be caused by a ferroelectric phase transition. Surface roughness influenced both the contrast in LFM images and the transport rate of ink. Surfaces with less roughness resulted in good contrast in LFM images, while rough surfaces resulted in poor contrast. The transport rate of ink increased as the roughness decreased; however, the extent of the influence was strongly ink-dependent. The influence of relative humidity depended on the solubility of the ink in water. The transport rate of hydrophilic inks increased as the relative humidity increased, while the transport rate of hydrophobic inks experienced small change as the relative humidity increased. At the same

condition, a tip with a larger curvature radius could generate a larger pattern than a tip with a smaller curvature radius due to a bigger contact point or the formation of a meniscus with a larger size. The chemical affinity was also one of the key controlling parameters for DPN. It is necessary to consider the ink affinity to both the substrate and the tip when designing a new DPN system.

We fabricated nanostructures via anodic nanooxidation and force nanolithography. In addition, we characterized the protein patterns with AFM by adsorption of a protein surfaces with different adsorption properties, and discussed the mechanism of the protein adsorption on these surfaces.

Publications Arising from the Thesis

(1) Journal Papers

1. **Qian Tang**, San-qiang Shi and Li-min Zhou. Nanofabrication with Atomic Force Microscopy. *Journal of Nanoscience and Nanotechnology*, 2004, 4, 948-963.
2. **Qian Tang**, Chun-Hua Xu, San-Qiang Shi, Li-Min Zhou. Formation and Characterization of Protein Patterns on the Surfaces with Different Properties. *Synthetic Metals*, 2004, 147, 247-252.
3. **Qian Tang**, San-Qiang Shi, Hai-Tao Huang, Li-Min Zhou. Fabrication of Highly Oriented Microstructures and Nanostructures of Ferroelectric P(VDF-TrFE) Copolymer via Dip-pen Nanolithography. *Superlattice and Microstructures*, 2004, 36, 21-29.
4. **Qian Tang**, San-Qiang Shi, Li-Min Zhou. Effect of Surface Roughness on Dip-pen Nanolithography. *Journal of Nanoscience and Nanotechnology*, 2005, 5, 2167-2171.
5. **Qian Tang**, San-Qiang Shi, Li-Min Zhou. The Effect of Temperature and Relative Humidity on the Patterning of a Ferroelectric Polymer P(VDF-TrFE) via Dip-pen Nanolithography. *International Journal of Nanoscience*, 2006 (accepted).

(2) Book Chapter

Qian Tang, San-Qiang Shi, Li-Min Zhou, an invited book chapter entitled “Nanostructures of Polymer Constructed via Atomic Force Microscopy and Their Applications” to be published in “Polymeric Nanostructures and Their Application” by American Scientific Publisher, 2005.

(3) Conference Papers

1. **Qian Tang**, San-Qiang Shi, Li-Min Zhou, Chun-Hua Xu. Comparative Study of Fabrication Patterns of a Ferroelectric Polymer P(VDF-TrFE) on Gold Thin Film and Gold Ball via Dip-pen Nanolithography, pp.711-714, vol. 2, Technical Proceedings of the 2005 NSTI Nanotechnology Conference and Trade Show (Anaheim, May 8-12, 2005). ISBN: 0-9767985-4-9.
2. Chun-Hua Xu, San-Qiang Shi, **Qian Tang**. Synthesis of Antimony Oxide Nanoparticles by Thermal-Oxidation, pp.54-57, vol. 2, Technical Proceedings of the 2005 NSTI Nanotechnology Conference and Trade Show (Anaheim, May 8-12, 2005). ISBN: 0-9767985-4-9.

Acknowledgments

I would like to express my sincere gratitude to my supervisor, Professor Shi San-qiang, and co-supervisor, Professor Zhou Li-min, for their guidance, encouragement and many thoughtful discussions regarding this research. Special thanks go to Professor Shi San-qiang for the considerable time he spent on my work.

I would like to thank Dr. Xu Chun-hua, Dr. Huang Hai-tao and Mr. Hardy Liu for the helpful discussion, Dr. Tan Weiqi and Miss Yang Yan for providing some materials, Dr. Wang Yu for preparing substrates, and technician Zhang Ya-peng for preparing experimental conditions.

I'm grateful to the financial support from the Hong Kong Polytechnic University under grant no. RG 6L.

Finally, Thanks go to my husband, Mr. Gong Chengbin, and my son for their support and encouragements.

Table of Contents

List of Tables	xiii
List of Figures	xiv
Chapter 1 Introduction	1
1.1 Motivation and Objectives	1
1.2 Thesis Structure	6
Chapter 2 Literature review	8
2.1 Basics of Atomic Force Microscopy	8
2.2 Nanofabrication by AFM	12
2.2.1 Nanoforce Sensing	12
2.2.2 Nanofabrication by Physically or Mechanically Modifying Surfaces	15
2.2.2.1 AFM Tip Manipulation of Nanoclusters, Nanoparticles and Biomolecules	16
2.2.2.2 Force Nanolithography or Direct Mechanical Modification	18
2.2.2.3 AFM Assisted Electrostatic Nanolithography (AFMEN)	22
2.2.2.4 Polarizing Ferroelectric Materials	23
2.2.3 Nanofabrication by Chemically Modifying Surfaces	26
2.2.3.1 Nanografting	26
2.2.3.2 AFM Tip Controlled Surface Reaction	32
2.2.3.3 Electric Field Enhanced AFM Tip-directed Nanooxidation	33

2.2.3.4 Dip-pen Nanolithography	36
2.3 Theoretical Analysis in DPN	56
Chapter 3 Fabrication of Ferroelectric Micro- to Nanostructures via Dip- pen Nanolithography	71
3.1 Introduction	71
3.2 Experimental	73
3.3 Results and Discussion	74
3.3.1 Examination of Coated Tip with Field Emission Scanning Electron Microscope	74
3.3.2 Fabrication of Micro- to Nano-patterns on Gold Substrate with P(VDF-TrFE) Coated AFM Tip	76
3.3.3 XPS Analysis of DPN-generated P(VDF-TrFE) Patterns	80
3.3.4 Mechanism of the Deposition of P(VDF-TrFE) to Gold	82
3.3.5 Detection of Ferroelectric Properties in the DPN- Generated P(VDF-TrFE) Patterns	83
3.3.6 Kinetics of Diffusion of P(VDF-TrFE) on Gold	86
3.4 Summary	93
Chapter 4 Effects of Experimental Conditions on Dip-pen Nanolithography	94
4.1 Introduction	94
4.2 Effect of Temperature	96
4.2.1 Experimental	96
4.2.2 Results and Discussion	96

4.3 Effect of Surface Roughness	114
4.3.1 Experimental	115
4.3.2 Results and Discussion	116
4.3.2.1 Characterization of Gold Ball and Gold Thin Film with AFM	116
4.3.2.2 Comparison of the DPN Patterning of P(VDF-TrFE) on the Gold Ball and Gold Thin Film	118
4.3.2.3 Effect of Surface Roughness on DPN	120
4.4 Effect of Relative Humidity	127
4.4.1 Experimental	127
4.4.2 Results and Discussion	128
4.5 Effect of Tip Size	137
4.6 Effect of Chemical Affinity	142
4.6.1 Experimental	143
4.6.2 Results and Discussion	144
4.7 Summary	155

Chapter 5 Anodic Nanooxidation, Force Nanolithography and

Characterization of Protein Patterns with AFM	158
5.1 Anodic Nanooxidation with AFM	158
5.1.1 Anodic Nanooxidation of Silicon	158
5.1.1.1 Experimental	158
5.1.1.2 Results and Discussion	159
5.1.2 Nanomodification of Au	163
5.2 Force Nanolithography with AFM	167

5.2.1 Experimental	168
5.2.2 Force Nanolithography on PMMA	168
5.2.3 Force Nanolithography on PZT Film	176
5.3 Characterization of Protein Patterns with AFM	179
5.3.1 Introduction	179
5.3.2 Experimental	181
5.3.3 Results and Discussion	182
5.3.3.1 Gold Film and SAMs	182
5.3.3.2 Protein Patterns and Mechanism for Protein Adsorption	183
5.3.4 Summary	191
Chapter 6 Conclusion and Recommendation for Future Work	192
6.1 Major Conclusions	192
6.1.1 Fabrication of Ferroelectric Miro- to Nanostructures via Dip- pen Nanolithography	192
6.1.2 Effects of Experimental Conditions on Dip-pen Nanolithography	193
6.1.3 Anodic Nanooxidation, Force Nanolithography and Characterization of Protein Patterns with AFM	195
6.2 The Limitations of AFM Nanopatterning	197
6.3 Recommendation for Future Work	199
6.3.1 Dip-pen Nanolithography	199
6.3.2 Anodic Nanooxidation	200
6.3.3 Force Nanolithography	200

References	201
-------------------	-------	-----

List of Tables

Table 2-1 Typical conducting polymers and their monomers	40
Table 2-2 Transfer rate of dendrimers versus molecular weight and functional Groups	44
Table 4-1 The surface properties of five gold thin films	121
Table 4-2 The capillary force sensed by an AFM tip coated with inks which have different solubilities	135
Table 4-3 The capillary force sensed by an AFM tip coated with inks which have different solubilities	136
Table 4-4 Comparison of the contact radius with/without meniscus at 25°C and 50% relative humidity for the three types of tips	142
Table 4-5 DPN results on gold substrate with ODT and P(VDF-TrFE) as inks using Si, Si ₃ N ₄ , Au tips	145

List of Figures

Fig.2-1 The schematic plot of the relationship between Van der Waals force and tip-sample separation	9
Fig.2-2 Schematic diagram of a scanned sample AFM	10
Fig.2-3 Schematic diagram for the determination of the interaction between biomolecules. (a) Attach at the surface (b) Retract from the surface (c) Force vs. distance curves.  and  are a pair of biomolecules [12]	13
Fig.2-4 (a) The preparation of an active cantilever biosensor array and an illustration of the basic principle of nanomechanical label-free biodetection (inset). The incubation of individual gold-coated cantilevers (dimensions: $500 \times 100 \times 1 \mu\text{m}$) in microcapillaries, each containing a different solution of thiolated probe DNA. (b) Absolute deflection signals from an eight-cantilever array were monitored in real time. (c) Detection of 250 nM BioB1C in the presence of 20 μM BioB7C [49]	15
Fig.2-5 (a) AFM image ($300 \times 300 \text{ nm}$) of a DNA strand cut by an AFM tip. (b) AFM image ($500 \times 500 \text{ nm}$) of a letter "N" from DNA molecules by pushing with the AFM tip [65]	17
Fig.2-6 (a) Schematic illustration of force nanolithography. (b) A storage field with IBM logo (writing with the 32×32 cantilevers array) represented by bit indentation/separation equivalent to a storage density of 100-200 Gbit/in. ² [98]	19

Fig.2-7 The simplified experimental setup for performing thermomechanical writing with an AFM tip [89]	21
Fig.2-8 Experimental setup for the polarizing and measurement of piezoelectric properties using AFM and Piezoelectricity image of P(VDF-TrFE) [116]	24
Fig.2-9 (a) Close-up of 6 Gbit cm ⁻² array written with 3 ms, 10 V pulses. (b) Three domains were sequentially erased by the application of -10 V pulses. (c) Subsequently, the bottom left domain was rewritten with the original 3 ms, 10 V pulse. The center domain was then rewritten, and the bottom left domain was re-erased [125]	26
Fig.2-10 Schematic illustration of AFM tip-based nanografting [12]	27
Fig.2-11 (a) Schematic diagram of meniscus force nanografting. (b) Slim DNA lines fabricated via meniscus force nanografting [132]	29
Fig.2-12 Hybridization of DNA nanostructures fabricated via nanografting, exhibiting high specificity and selectivity. (a), (b), and (c) show AFM topographs containing nanostructures of T35(40 ×250 nm ²) and T25 (80 ×220 nm ²) with incubation in polyA for 0, 4, and 14 h, respectively. (e), (f), and (g) show AFM topographs containing nanostructures of T25 with incubation in polyG for 0, 4, and 14 h, respectively. Scale bars represent 100 nm [139]	31
Fig.2-13 Schematic plot of AFM tip-directed oxidation [12]	34
Fig.2-14 (a) Schematic diagram of dip-pen nanolithography. (b) Lateral force image of 1-octadecanethiol (ODT) point array on gold substrate. The hydrophobic thiol produces black contrast. The contact time for the three dots from left to right is 2, 4, 16 min, respectively at	

relative humidity of 45%. (c) Lateral force image of 16-mercaptohexadecanoic acid (MHA) point array on gold substrate. The hydrophilic thiol produces white contrast. The contact time for the three dots from left to right is 10, 20, 40 s, respectively at relative humidity of 35% [194] 37

Fig.2-15 Nanoscale patterns written with the peptide MH2 on a gold surface using Tapping Mode DPN. (a) Height image of “AF” written using an aspect ratio of 1:64 and various scan angles. The corresponding phase image (c) shows a darkened patterned region. (c) Height and (d) phase image of “+” written with aspect ratio of 1:32. Lines with widths of 70 nm can be draw [196] 38

Fig.2-16 A light sensor fabricated via DPN and its light detection properties. (a) Optical micrograph of a light sensor composed of conducting polymer between a 2 mm electrode gap fabricated via DPN. (b) *I-V* curve of the sensor in dark and illuminated states. (c) Repeated photo-responses of the sensor. (d) The dependence of resistance to the relative light intensity [204] 42

Fig.2-17 (a) Schematic illustration of the synthesis of polymer via site-specific ring-opening metathesis polymerization on DPN-patterned template. (b) Polymer lines with average full-width at half-maximum of 480 nm. (c) Polymer dot array. The average diameter of the dot is 78(±4) nm and the average height 5(±1) nm. (d) The height of polymer plotted as a function of polymerization reaction time [208] 46

Fig.2-18 Schematic diagram of the immobilization of a 15-residue TAT peptide to chemically modified SiO_x by Michael addition 48

Fig.2-19 Thiolated biomolecules can be deposited to gold through the formation of Au-S covalent bond.

(a) Phase image of thiolated collagen nanolines on gold substrate fabricated via DPN. (b) Topography of nanopatterns of thiolated DNA on gold [211,213] 49

Fig.2-20 (a) Schematic illustration of the facilitated deposition of biomolecules by UV irradiation using photocleavable cross-linker with two terminals. One terminal allows a biomolecule to be conjugated, and the other terminal allows chemical binding to the tip. UV irradiation cleaves the biomolecule-bond, thus releasing biomolecules and forming nanostructures. Topographies before (b) and after (c) UV irradiation. Scale: $5 \times 5 \mu\text{m}$ [220] 50

Fig.2-21 (a) Schematic of the procedure to fabricate a biosensor. (b) Photography of the biosensor prepared by immobilizing Anit-p24 IgG to the DPN-generated MHA nanopattern through electrostatic interaction, and passivating the unmodified MHA pattern with BSA for reducing unwanted binding in the following analysis. (b) Detection of p24 antigen using this biosensor. The detection limit is 0.025 pg per ml. (d) Amplified antigen-nanofeatures by binding of gold nanoparticles functionalized with polyclonal antibody [226] ... 53

Fig.2-22 Dependence of radius squared on dwell time as a function of relative humidity [245] 60

Fig.2-23 Schematic plot of the 2D random walk theory [249] 63

Fig.2-24 Line widths as a function of AFM tip speed with ODT [247] 67

Fig.2-25 DPN process in this model [247] 68

Fig.2-26 LFM image of DDA on mica [251]	69
Fig.2-27 DPN process with weak surface binding [251]	70
Fig.3-1 Schematic diagram of the methods for the preparation of thin film of P(VDF-TrFE)	73
Fig.3-2 FE-SEM micrographs of the AFM before (a) and after (b) coated with P(VDF-TrFE)	75
Fig.3-3 Topographic (a) and lateral force microscopy (b) images of the polycrystalline gold	76
Fig.3-4 Micro and nanopatterns of P(VDF-TrFE) on gold substrate fabricated via DPN at 22°C. (a) Topography of point array written at different contact time at relative humidity of 7%. The contact times for these dots are 1, 2, 3, 4, 5, 6, 8, 10, 12, 15, 20 and 30min, respectively. (b) Lateral force image of the point array obtained simultaneously with (a). (c) Lateral force image of a word "POLYME" written with an AFM tip coated with P(VDF-TrFE) at relative humidity of 64%, writing rate :156 Å/s	78
Fig.3-5 (a) Schematic diagram of the sample composed of DPN-generated P(VDF-TrFE) patterns within a mark analyzed with XPS. Results of the XPS for the F 1s (b) and Au 4f (c) spectra of the gold surface patterned with P(VDF-TrFE)	81
Fig.3-6 The topography image obtained after applying a linearly varied DC voltage from -10V to +10V (between a conductive AFM tip and the sample) to draw a circle from point A counter-clockwise in (a). There was no apparent change in the sample when a positive voltage was	

applied, while a negative voltage produced a protruded pattern on the surface. The greater the voltage applied, the higher the protrusion obtained. The protruded pattern slowly returned to its original state after a certain time; (b) is the image of the same area after one hour 84

Fig.3-7 (a) Schematic diagram of the orientation of P(VDF-TrFE) on gold.

The positive part of the P(VDF-TrFE) contact with gold, while the negative part is positioned far from the gold. Therefore, a net dipole moment pointing from the upper part to the gold is formed. (b)

Polarization hysteresis loop of the P(VDF-TrFE 70:30) 2 monolayers at 25°C measured by Bune et al's [259] 86

Fig.3-8 Lateral force images of P(VDF-TrFE) points array at 25°C and relative humidity of 64% for 60 s (a), 120 s (b), 180 s (c), 240 s (d) and 300 s (e) respectively. (f) is the curve of dot radius as a function of contact time, and panel (g) is the curve of dot area as a function of contact time, averaged from five independent measurements. The error bars are standard deviations 88

Fig.3-9 Lateral force images of three lines (a) and six lines (b) written with an AFM tip coated with P(VDF-TrFE) at 25°C, relative humidity of 64%. Panel (c) is line width (W) versus inverse rate (ν^{-1}), and (d) is the curve of $W^2 \sim \nu^{-1}$. The error bars are standard deviations 89

Fig.3-10 The schematic plot of the DPN process with P(VDF-TrFE) ink. O is

the contact point between the tip and the gold substrate, and C_0 is the concentration of P(VDF-TrFE) at point O. C_r is the concentration of P(VDF-TrFE) at a distance of r from O. The concentration is symmetrical with respect to $r = 0$, tends to zero when $r \rightarrow \infty$ for $t > 0$. The concentration gradient is the driving force for the P(VDF-TrFE) molecules diffusion 91

Fig.4-1 Lateral force microscopy images of P(VDF-TrFE) points array at 30°C and relative humidity of 64% for 60 s (a), 120 s (b), 180 s (c), 240 s (d), and 300s (e), respectively, and panel (f) is the curve of dot radius averaged from five independent measurements as a function of contact time. The error bars are standard deviations 97

Fig.4-2 Lateral force microscopy images of P(VDF-TrFE) points array at 35°C and relative humidity of 64% for 60 s (a), 120 s (b), 180 s (c), 240 s (d), and 300s (e), respectively, and panel (f) is the curve of dot radius averaged from five independent measurements as a function of contact time. The error bars are standard deviations 98

Fig.4-3 Lateral force microscopy images of P(VDF-TrFE) points array at 40°C and relative humidity of 64% for 60 s (a), 120 s (b), 180 s (c), 240 s (d), and 300s (e), respectively, and panel (f) is the curve of dot radius averaged from five independent measurements as a function of contact time. The error bars are standard deviations 99

Fig.4-4 Lateral force microscopy images of P(VDF-TrFE) points array at 45°C and relative humidity of 64% for 60 s (a), 120 s (b), 180 s (c), 240 s (d), and 300s (e), respectively, and panel (f) is the curve of dot radius averaged from five independent measurements as a function of

contact time. The error bars are standard deviations 100

Fig.4-5 Lateral force microscopy images of P(VDF-TrFE) points array at 50°C and relative humidity of 64% for 60 s (a), 120 s (b), 180 s (c), 240 s (d), and 300s (e), respectively, and panel (f) is the curve of dot radius averaged from five independent measurements as a function of contact time. The error bars are standard deviations 101

Fig.4-6 Lateral force microscopy images of P(VDF-TrFE) points array at 55°C and relative humidity of 64% for 60 s (a), 120 s (b), 180 s (c), 240 s (d), and 300s (e), respectively, and panel (f) is the curve of dot radius averaged from five independent measurements as a function of contact time. The error bars are standard deviations 102

Fig.4-7 Lateral force microscopy images of P(VDF-TrFE) points array at 60°C and relative humidity of 64% for 60 s (a), 120 s (b), 180 s (c), 240 s (d), and 300s (e), respectively, and panel (f) is the curve of dot radius averaged from five independent measurements as a function of contact time. The error bars are standard deviations 103

Fig.4-8 Lateral force microscopy images of P(VDF-TrFE) points array at 65°C and relative humidity of 64% for 60 s (a), 120 s (b), 180 s (c), 240 s (d), and 300s (e), respectively, and panel (f) is the curve of dot radius averaged from five independent measurements as a function of contact time. The error bars are standard deviations 104

Fig.4-9 Lateral force microscopy images of P(VDF-TrFE) points array at 70°C and relative humidity of 64% for 60 s (a), 120 s (b), 180 s (c), 240 s (d), and 300s (e), respectively, and panel (f) is the curve of dot radius averaged from five independent measurements as a function of

contact time. The error bars are standard deviations	105
Fig.4-10 The relationship between the a and temperature (a) and the b and temperature (b)	106
Fig.4-11 (a) Plot of $\ln v$ versus the inverse temperature $\frac{1}{T}$ (Arrhenius plot) for P(VDF-TrFE). (b) Arrhenius plot of ODT measured by Schwartz [247]. (c) Comparison of transport rate of ODT and P(VDF-TrFE) to gold at the same experimental conditions (25°C and relative humidity of 50%)	108
Fig.4-12 Heating DSC thermograms of the P(VDF-TrFE 80:20)	109
Fig.4-13 Dielectric properties of the ferroelectric Langmuir-Blodgett-deposited P(VDF-TrFE 70:30) films with different thickness measured by Bune [261]. The arrows show the direction of temperature change	110
Fig.4-14 Force –distance curves measured as a function of the substrate temperature between (a) a bare tip and gold substrate (b) a bare tip and a thin film of P(VDF-TrFE) coated on gold substrate, and (c) a tip coated with a thin film of P(VDF-TrFE) and gold substrate. (d) is the plot of the relative pull-off amplitude as a function of temperature from a (curve 1), b (curve 2), and c (curve 3)	112
Fig.4-15 Characterization of the facets on a gold ball and on a polycrystalline gold thin film with AFM: (a) Topographic image of the facets on a gold ball in the tapping mode. (b) Profile of the line scan in (a), demonstrating that the surface steps are 0.25~0.3 nm. Topography (c) and lateral force image (d) of the facets on a gold ball in the	

contact mode. The lateral force image shows no information about the surface steps. Topography (e) and lateral force image (f) of the gold thin film in the contact mode. A crystalline boundary exists both in the topography and the LFM image 117

Fig.4-16 Patterns of P(VDF-TrFE) on the gold ball fabricated via DPN:

Topography (a) and LFM image (c) of two points of P(VDF-TrFE) on a gold ball (relative humidity of 64%, 22°C, contact time: 30s for the left dot and 60s for the right dot in air). (b) and (d) are profiles of the line scans in (a) and (c) 119

Fig.4-17 The dependency of the dot area (A) versus the contact time (t) curves for P(VDF-TrFE) patterns on a gold ball and a gold thin film via DPN at 22°C and a relative humidity of 80% 120

Fig.4-18 Effect of roughness on DPN with ODT ink at 22°C and a relative humidity of 50%: The LFM images of an ODT point array on 1[#] (a); 2[#] (b); 3[#] (c); 4[#] (d); and 5[#] (e). The contact times for the dots are 3, 6, 9, 12, 15, 18, 21, 24, and 27s, respectively. (f) is the dependency of the dot area (A) versus the contact time (t) measured as a function of roughness 122

Fig.4-19 Effect of roughness on DPN with P(VDF-TrFE) ink at 22°C and a relative humidity of 50%: LFM images of a P(VDF-TrFE) point array on 1[#] (a); 2[#] (b); 3[#] (c); 4[#] (d); and 5[#] (e). The contact times for the dots are 1, 2, 3, 4, 5, 6, 7, 8, and 9min, respectively. (f) is the dependency of the dot area (A) versus the contact time (t)

measured as a function of roughness	124
Fig.4-20 The dependency of the transport rate on the surface roughness: (a) ODT. Inset plot is diffusion constant versus substrate RMS [266]. (b) P(VDF-TrFE)	125
Fig.4-21 Schematic illustration of the AFM experimental system for DPN. AFM was placed in a chamber. Purge dry N ₂ in to the system to obtain low relative humidity, while let N ₂ pass through a water bottle to obtain high relative humidity	128
Fig.4-22 Lateral force images of P(VDF-TrFE) points array at 30°C and relative humidity of 7% for 60 s (a), 120 s (b), 180 s (c), 240 s (d), and 300s (e), respectively, and panel (f) is the curve of dot radius averaged from five independent measurements as a function of contact time. The error bars are standard deviations	129
Fig.4-23 Lateral force images of P(VDF-TrFE) points array at 30°C and relative humidity of 17% for 60 s (a), 120 s (b), 180 s (c), 240 s (d), and 300s (e), respectively, and panel (f) is the curve of dot radius averaged from five independent measurements as a function of contact time. The error bars are standard deviations	130
Fig.4-24 (a) $A-t$ curves measured as a function of relative humidity for P(VDF-TrFE). A is averaged from three independent measurements, and the error bars are standard deviations. The humidity dependencies of the growth rate of ODT (b) [246,248] and MHA (c) [245,248]	131
Fig.4-25 Schematic diagram of the ODT distribution when there is no	

meniscus (a), water meniscus exists (b), and ethanol meniscus exists (c). ODT dissolved in the ethanol meniscus and then deposited on gold [247]	133
Fig.4-26 Schematic diagram for the deposition of hydrophobic (a) and hydrophilic (b) inks	135
Fig.4-27 Schematic diagram of the calculation of contact radius for tips which have different curvature radius when no meniscus is formed between the tip and the substrate	138
Fig.4-28 Schematic diagram of the calculation of contact radius for tips with different curvature radius when meniscus is formed between the tip and the substrate	141
Fig.4-29 SEM micrographs of (a) clean Si tip, (b) Si tip coated with ODT, (c) clean, (d) Si ₃ N ₄ tip coated with ODT, (e) clean Au tip and (f) Au tip coated with ODT	146
Fig.4-30 (a) LFM image of an ODT point array fabricated with a Si tip coated with ODT at 25°C and a relative humidity of 50%. Contact time: 180s. (b) LFM image of an ODT point array fabricated with a Si ₃ N ₄ tip coated with ODT at 25°C and a relative humidity of 50%. Contact time: 20s. (c) Comparison of the transport rate of ODT to gold using a Si tip and a Si ₃ N ₄ tip at the same experimental conditions (25°C and a relative humidity of 50%)	147
Fig.4-31 SEM micrographs of tips coated with P(VDF-TrFE): (a) Si tip, (b) Si ₃ N ₄ tip, and (c) Au tip	149
Fig.4-32 (a) LFM image of a P(VDF-TrFE) point array fabricated with a Si tip coated with P(VDF-TrFE) at 25°C and a relative humidity of 50%.	

Contact time: 240s. (b) LFM image of an P(VDF-TrFE) point array fabricated with a Si₃N₄ tip coated with P(VDF-TrFE) at 25°C and a relative humidity of 50%. Contact time: 20s. (c) Comparison of the transport rate of P(VDF-TrFE) to gold using a Si tip and a Si₃N₄ tip at the same experimental conditions (25°C and a relative humidity of 50%) 150

Fig.4-33 Lateral force microscopy images of points array on silver substrate (25°C, RH 50%). (a) and (b) is a point array of P(VDF-TrFE) fabricated with Si₃N₄ tip and Si tip for 180 s per dot, respectively. (c) and (d) is a point array of ODT fabricated with Si₃N₄ tip and Si tip for 20 s per dot 152

Fig.4-34 The influence of chemical affinity on dip-pen nanolithography .. 151

Fig.5-1 The effect of applied voltage on the oxidation of Si. (a) AFM topographic image of silicon after nanooxidation (From left to right: -4 V, -5 V, -6 V, -7 V, and -8 V applied to the tip for 2 milliseconds at a relative humidity of 28% and 20°C. (b) The dependence of oxide height versus voltage 159

Fig.5-2 The effect of duration on the oxidation of Si. (a) AFM topographic image of silicon after nanooxidation by the application of -8 V at 20°C and at a relative humidity of 28% for 5, 10, 20, 40 and 80 milliseconds (from left to right), respectively. (b) The dependence of oxide height versus $t^{\frac{1}{2}}$ 160

Fig.5-3 The effect of relative humidity on the oxidation of Si. (a) AFM topographic image of silicon after nanooxidation by the application of -10 V for 1 millisecond at 20°C and at a relative humidity of 54%,

44%, 34% and 29% (from left to right), respectively. (b) Lateral contour of the lines	161
Fig.5-4 The Hong Kong Polytechnic University Logo (300 nm x 300 nm) fabricated using raster lithography at 20°C and a relative humidity of 28% by the application of voltage from -4 V to -8 V to the tip for 2 milliseconds to 5 milliseconds	162
Fig.5-5 Nanopatterns on Gold film and gold ball by the application of certain voltage on a conductive AFM tip. (a) A line constructed on gold film with -6 V applied to the tip for 1 millisecond per point. (b) Two lines constructed on gold ball with -4 V applied to the tip for 0.15 and 0.2 milliseconds per point. (c) A 3 x 3 point array on gold ball constructed with -5 V applied to the tip for 0.1 milliseconds per point	164
Fig.5-6 The dependence of pattern height versus voltage	166
Fig.5-7 EDX spectra outside (a) and inside (b) the patterned area	166
Fig.5-8 AFM topographic image of a point fabricated with 1.0 µN applied to the tip for 20 ms (a) and the section profile along the AA' direction (b)	169
Fig.5-9 AFM topographic image of a point fabricated with 0.6 µN applied to the tip for 20 ms (a) and the section profile along the AA' direction (b)	170
Fig.5-10 AFM topographic image of a point fabricated with 0.25 µN applied to the tip for 20 ms(a) and the section profile along the AA' direction (b)	171
Fig.5-11 AFM topographic image of a point fabricated with 0.15 µN applied to the tip for 20 ms (a) and the section profile along the AA'	

direction (b)	172
Fig.5-12 Relationship between the loading force and the pit depth, showing a roughly scaling behavior. The data are averaged from 5 independent measurements, and the error bars are standard deviations	173
Fig.5-13 (a) topographic image of a 4×4 point array created on a PMMA film with a thickness of 16 nm with 0.15 μ N applied to the tip for 20 ms, lateral contour of line 1 (b), line 2 (c), line 3 (d), line 4 (e) and line 5 (f)	174
Fig.5-14 (a) A topographic image of four lines fabricated on a PMMA film with a thickness of 20 nm with 0.20 μ N applied to the tip for 20 ms. (b) Lateral contour of line in (a). (c) A topographic image of a circle fabricated on a PMMA film with a thickness of 20 nm with 0.20 μ N applied to the tip for 15 ms. (d) Lateral contour of line in (c). (e) A topographic image of a rectangular fabricated on a PMMA film with a thickness of 16 nm with 0.15 μ N applied to the tip for 20 ms, and (f) lateral contour of line in (e)	175
Fig.5-15 (a) The topographic image of a hole fabricated on PZT thin film with a thickness of 400 nm by the application of 0.5 μ N for 10 ms, and (b) lateral contour of the line in (a). (c) The topographic image of a line fabricated on PZT thin film with a thickness of 400 nm by the application of 0.5 μ N for 10 ms, and (d) lateral contour of the line in (c)	177
Fig.5-16 Topographies of gold film (a), ODT SAMs (b), and the mixture 1:1 SAMs (c)	182

Fig.5-17 Protein immobilization on gold film. (a) Topography of gold after absorb BSA. (b) Cross section of the line in (a). (c) Schematic illustration for the protein immobilization on gold film 184

Fig.5-18 Protein adsorption on MHA SAMs. (a) Topography of protein pattern on MHA SAMs. (b) Cross section of the line in (a). (c) Schematic illustration for the adsorption of protein on MHA SAMs 185

Fig.5-19 Protein adsorption on ODT SAMs. (a) Topography of protein pattern on ODT SAMs. (b) Cross section of the line in (a). (c) Schematic illustration for the adsorption of protein on MHA SAMs 187

Fig.5-20 Protein adsorption on the Mixture 1:1 SAMs. (a) Topography of protein pattern on the Mixture 1:1 SAMs. (b) Cross section of the line in (a). (c) Schematic illustration for the protein adsorption on the Mixture 1:1 SAMs 188

Fig.5-21 Protein adsorption on the Mixture 1:10. (a) Topography of protein pattern on the Mixture 1:10. (b) Cross section of the line in (a). (c) Schematic illustration for the protein adsorption on the Mixture 1:10 SAMs 189

Chapter 1 Introduction

1.1 Motivation and Objectives

Nanotechnology is defined as the technology of constructing and controlling matter on the scale of ~ 100 nm or below, which contains preparation of nanosize objects, positioning of nanosize objects, creation of nanosize patterns (2D) and objects (3D) on surfaces, and development of nanotools. Nanotechnology is likely to have a profound impact on our economy and society in the early twenty-first century, comparable to that of semiconductor technology, information technology, or cellular and molecular biology. Science and technology research in nanotechnology promises breakthroughs in such areas as materials and manufacturing, nanoelectronics, medicine and healthcare, energy, biotechnology, information technology, and national security. It is widely felt that nanotechnology will be the next industrial revolution. Therefore, nanotechnology has attracted significant research interest in recent years. Nanofabrication is defined as the fabrication of nanostructures on the scale of individual atoms or molecules (100 nm or smaller), which usually employs advanced lithography and precision planar processing. Nanostructures provide an interesting tool in studying electrical, magnetic, optical, thermal, and mechanical properties of matter at the nanometer scale. Nanofabrication is commonly divided into top-down and bottom-up categories.

Introduction

Many methods have been developed to fabricate micro- to nanostructures. Photolithography [1] is typically utilized in semiconductor manufacturing applications as well as patterning polymers due to their high throughput; however, photolithography is limited in resolution (about 110 nm) by the wavelength of light. Direct-write electron and ion beam lithographies [2-3] have demonstrated the best resolution of the conventional patterning strategies, achieving well spaced 8-10-nm-wide lines; however, this methodology is fiscally expensive, and it is mainly applicable to pattern metallic materials and semiconductor. The achievable resolution is greatly affected by the proximity of the features to one another and by the substrate material. Microcontact printing (μ CP) [4] is a simple method to construct parallel patterns, but it can only provide submicrometer-feature resolution, nanoscale fabrication methods are still under development. Nanoimprint lithography (NIL) [5] can fabricate nanometer-scale features. However, both μ CP and NIL have little control over the amount of material deposited, and the stamp fabrication (which decides the resolution) is challenging. Scanning probe microscopy (SPM), such as scanning tunneling microscopy (STM) [6] and atomic force microscopy (AFM) [7-8] can visualize surfaces with atomic resolution [9-10]. Taking advantage of the sharpness of the tips, STM and AFM can also be used for nanofabrication, offering the advantages of nanometer resolution and flexibility in pattern generation [11-13]. However, only conductive or semi-conductive materials are applicable to STM, because STM utilizes tunneling current between a conductive tip and a sample to determine surface properties. While various materials, such as insulators, semiconductors and conductors can be visualized and

Introduction

nanopatterned with AFM, because AFM utilizes the Van der Waals interaction between an AFM tip and a sample to determine the surface properties. Therefore AFM has wider applications than STM.

Since its invention, many AFM-based nanotechnologies, such as nanomanipulation, force nanolithography, anodic nanooxidation, nanoforce sensing, and dip-pen nanolithography have been developed. These methods have demonstrated wide versatility, high precision, and high resolution in the fabrication of nanostructures compared to other technologies. In addition, the fabricated nanostructures have potential applications in the development of sensors, catalysis, and electric and optical devices at a nanometer scale. However, most of these methods are still at experimental stage. For them to become promising and competitive nanopatterning in future, much more effort will be needed in the development of hardware, software, analytical tools, and methodologies.

Dip-pen nanolithography developed recently is an AFM-based lithography. Compared to other lithographies (photolithography, E-beam lithography, and so forth), dip-pen nanolithography is a simple and cheap method that is commonly conducted at ambient conditions. Various materials, such as some inorganic materials, organic materials, conducting polymers, and biomaterials have been used as DPN inks. However, ferroelectric polymer, which is an important class of functional materials with potential applications in electrical, optical, biomedical, robotic, and sensing devices, has not been

Introduction

used in dip-pen nanolithography. Among the known ferroelectric polymers, poly(vinylidene fluoride-trifluoroethylene) shows the highest ferroelectric polarization and electromechanical response; therefore, it is widely used as acoustic sensors and transducers with a thickness of several to tens microns. Thin films of P(VDF-TrFE) is helpful in investigating the ferroelectric phenomena in low-dimension system. Furthermore, thin films of ferroelectric polymer have potential applications in optical, electronic and sensing technologies.

Dip-pen nanolithography is commonly conducted under ambient conditions. The experimental conditions, such as temperature, relative humidity, substrate surface properties, chemical affinity in the designed system, as well as tip properties would all influence the deposition of ink from the tip to the substrate. However, only the influence of temperature and relative humidity on DPN for thiol (ink)-gold (substrate) system has been studied. To understand the influence of experimental conditions is helpful in controlling the transport rate of the ink and pattern quality.

Anodic nanooxidation can be used to chemically modify semiconductors (Si, Si_3N_4 , Ge, Ga) and transition metals (Al, Ti), which have potential applications in electric and optic nanodevices. To fabricate complicate 3-D nanostructures in a single scan is very important for some delicate nanodevices. Au nanopatterns are very useful in many research fields such as biotechnology, catalysis, etc. Would anodic nanooxidation chemically modify Au surface?

Introduction

Force nanolithography is another powerful method to fabricate nanopatterns. The fabrication of desired nanopatterns on soft polymer and PZT would have potential applications in data storage devices and piezoelectric, pyroelectric, non-volatile random access memory devices, imaging systems sensors and actuators in smart structures.

Protein adsorption on solid surface is a very important and active area of research due to its potential applications from fundamental studies in cell biology to the development of various “biochip” platforms. Immobilizing protein in micro- or nanoscales using self-assembled monolayers (SAMs) method is an alternate method. AFM is an ideal tool to visualize the formed protein patterns.

The proposed research project consists of three main tasks:

- 1) To study the patterning of a ferroelectric polymer, poly(vinylidene fluoride-trifluorethylene) P(VDF-TrFE) via dip-pen nanolithography.
- 2) To study the influence of experimental conditions, such as temperature, surface roughness of the substrate, relative humidity, tip size and tip material as well as chemical affinity on dip-pen nanolithography.
- 3) To fabricate nanostructures on Si, Au via anodic nanooxidation and to construct nanostructures on polymer and PZT sol film via force nanolithography. In addition, AFM is used to characterize micro- to nanometer protein patterns.

1.2 Thesis Structure

The main body of this thesis contains four chapters, each covering one aspect of the topics.

Chapter 2 is the literature review. In this chapter, an introduction about AFM is firstly given. Then studies on AFM-based nanotechnologies both in theory and experiment are reviewed.

In Chapter 3, for the first time, a ferroelectric polymer, poly(vinylidene fluoride-trifluoroethylene) P(VDF-TrFE) is used as DPN ink. The micro- and nanostructures of P(VDF-TrFE) are constructed via DPN onto the gold substrate, and is proven by XPS. The topographic and lateral force microscopy images of the DPN-generated P(VDF-TrFE) are characterized via AFM using the same tip. The molecule orientation and ferroelectric properties in this pattern are studied, and mechanism for the deposition of P(VDF-TrFE) to gold substrate is discussed and a simplified diffusion model adopting Fick's first law is proposed to interpret the growth rate of dot radii/linewidth.

In Chapter 4, the effect of temperature, surface roughness of the substrate, relative humidity, tip size and tip material as well as chemical affinity on the DPN are studied. The effect of one controlling parameter on DPN is studied by keeping the other controlling parameters as a constant and changing the testing parameter while measuring the effect of this parameter on the transport rate of ink.

Introduction

Chapter 5 summarizes results of another two AFM-based nanotechnologies (anodic oxidation and force nanolithography) and the characterization of protein adsorption on solid surface with AFM. (1) AFM is used to characterize the various micron to nanometer protein patterns on six different surfaces. The mechanism for the protein adsorption on each surface is discussed. (2) Anodic nanooxidation is used to produce silicon oxide nanopatterns. The effect of voltage, duration, relative humidity on the oxidation has been studied. More complicate nanostructure is fabricated using raster lithography. Anodic nanooxidation is also used to study the chemical modification of a noble metal, gold. EDX is used to analyze the chemical composition. (3) Fabrication of desired nanopatterns on a soft polymer PMMA and an unsintered PZT sol film is studied. Pit depth versus applied load and the effect of probe shape on the formed pattern are discussed.

In the last chapter, Chapter 6, the main results and conclusions are summarized. The limitations of the present research project are discussed. Some recommendations for future work are given.

Chapter 2 Literature Review

2.1 Basics of Atomic Force Microscopy

An atomic force microscope contains the following main parts: (1) a sharp tip, (2) a flexible cantilever, (3) high-resolution scanner, and (4) a sensitive deflection sensor. At present, the commercial tips, which are fabricated using integrated circuit methods, are mainly composed of silicon or silicon nitride with a thin reflective layer on their backsides. The curvature radius of tip is made as small as 10 nm. It can be further reduced to several nanometers by using carbon nanotube as the AFM tip, which is attached to the end of a commercial AFM tip. This very sharp tip can provide higher imaging resolution [14-15]. The conductivity of the tip can be increased by doping the silicon or coating a thin conductive layer on the silicon or silicon nitride tip. This coated tip has a greater curvature radius than an uncoated tip, generally 30 to 60 nm. The tip is mounted at the end of a small cantilever. The cantilever may be in a triangular shape or in a rectangular shape. The cantilevers are classified as contact cantilevers and non-contact cantilevers, according to their spring constants and resonance frequencies. Contact cantilevers have small spring constants and low resonance frequencies. On the other hand, non-contact cantilevers have large spring constants and high resonance frequencies. The scanner is a piezoelectric tube composed of PZT and dopants. The piezoelectric scanner can be connected with the tip or with the sample. The function of the piezoelectric scanner in the AFM is to move the tip or the sample in the X, Y and Z directions with sub-angstrom resolution. The piezoelectric scanner

Literature Review

connected with the tip is called scanned tip, while the piezoelectric scanner connected with the sample is called scanned sample. Most of the AFM systems utilize an optic deflection sensor to measure the vertical deflection of the cantilever. A laser beam shines on the reflective backside of the cantilever and is reflected to a position-sensitive photodetector consisting of two side-by-side photodiodes. A small deflection of the cantilever will tilt the reflected beam and change the position of beam on the photodetector. The difference between the signals of the two photodiodes indicates the position of the laser spot on the detector, and thus results in the angular deflection of the cantilever.

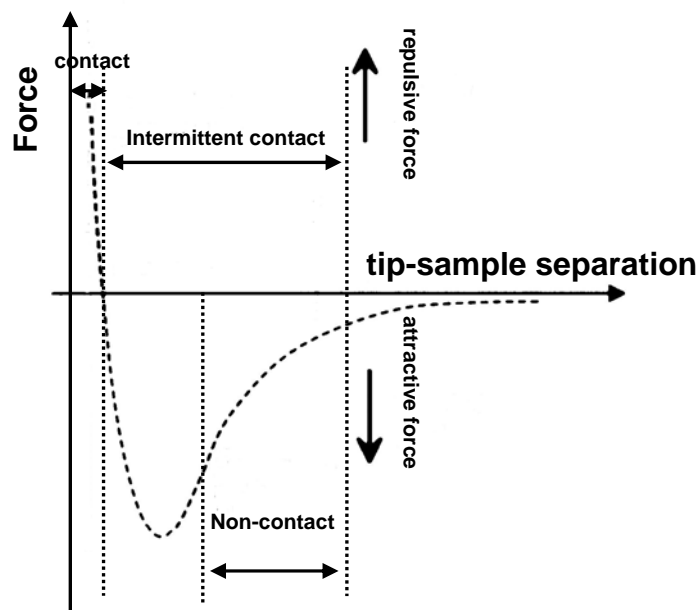


Fig.2-1 The schematic plot of the relationship between Van der Waals force and tip-sample separation.

In principle, a sharp tip scans over the sample surface in near-field. The Van der Waals interaction between the tip and the sample is utilized to determine the surface properties. As illustrated in Figure 2-1, when the separation is large (the right part), the attractive force is small and changes a little with the variation

Literature Review

of tip-sample separation therefore, the attractive force can be neglected. However, while the force changes with the variation of tip-sample separation, it cannot be neglected when the separation is less than hundreds of angstroms. AFM utilizes the relationship of force versus separation to provide surface properties. AFM is generally operated in two modes. The first mode is the constant force mode. In this mode, the electronic feedback is switched on, the piezoelectric scanner responds to any changes in force which are detected, and it alters the tip-sample separation to restore the force to a pre-determined value. Figure 2-2 is a schematic diagram of a scanned sample AFM in constant force mode. The cantilever, photodetector, electronics, scanner, and sample form a feedback loop. As the tip is scanned over the sample surface, the separation between the tip and the sample is kept constant by the feedback loop, therefore, the tip moves across the surface topography and provides information about surface properties. The second mode is the constant height mode with the electronic feedback switched off. It is particularly useful for imaging very flat samples at high resolution.

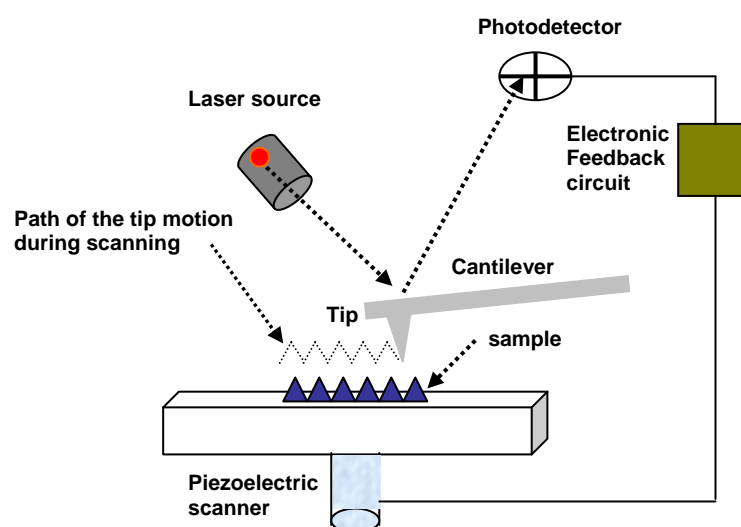


Fig.2-2 Schematic diagram of a scanned sample AFM.

Literature Review

There are three imaging methods in AFM. The first one is the contact mode, also called the DC mode or static mode. The force between the tip and the sample is a repulsive force (see Figure 2-1), and contact cantilevers (soft cantilevers) are used. The tip always comes into contact with the sample surface and the cantilever deflection is kept constant during scanning. Both the vertical deflection and the lateral static deflection of the cantilever are recorded. Hence, topography and lateral force microscopy (LFM) image can be obtained simultaneously. LFM image is helpful in the differentiation of the surface containing the different chemical materials which have different frictional properties [16]. The second and third methods are the non-contact mode and the intermittent mode (semi-contact mode), respectively. They are classified as the AC mode or the resonant mode, because the cantilever oscillates during scanning. In the non-contact mode, the probe is vibrated at a fixed frequency near the surface with a separation of tens to hundreds of angstroms during scanning, the variation of the attractive force between the tip and the sample causes a frequency shift in the resonance frequency of the cantilever that is used to operate the feedback. In the intermittent mode, the probe is also vibrated at a fixed frequency but comes into contact with the sample surface, and the variation of the repulsive force induces a damping of the cantilever oscillation amplitude that is used to operate the feedback. Local surface properties, such as adhesion [17], elasticity [18] can be measured by recording the phase lag of the cantilever oscillation relative to the driving signal in a second acquisition channel during imaging. Using a conductive tip or chemically modified tip, the electric [19-21], magnetic [22], chemical [23-24], ferroelectric [25-28], and mechanical properties [29-30] can also be characterized. In

addition, the contact mode and the intermittent contact mode can be operated in liquid; therefore, AFM can be used to characterize biomaterials in physiological condition [31-32]. The main feature and general application of AFM is to visualize surface properties of materials with high spatial resolution [33-34]. The imaging force can be as low as 10^{-7} N in air and 10^{-12} N or less in liquids, The scanning range can be as small as a few nanometers or as large as tens of microns at different temperatures and pressures [35-36].

2.2 Nanofabrication by AFM

Apart from visualizing the surface property, AFM is used for nanofabrication and nanoforce sensing.

2.2.1 Nanoforce Sensing

AFM has high sensitivity in measuring weak force as low as piconewton; therefore it is used as a force sensor to sense weak interactions between two biomolecules.

The first method is to measure weak biomolecular interactions under physiological conditions, such as molecular recognition between antibody and antigen; between receptor and ligand; and in complimentary strands of DNA, which are very important for life science, but are too weak to be detected by conventional force test techniques. One type of the two interacting molecules is immobilized to a soft tip with a known spring constant, and the other one to the substrate. The two types of molecules would interact with each other when the

Literature Review

tip approaches the substrate surface and stays for a certain time (Figure 2-3a). Then the tip is retracted from the surface (Figure 2-3b). The deflection of the cantilever versus the distance is recorded on approach and retraction, and is directly converted into force versus distance based on the spring constant using Hooke's law (Figure 2-3c). The interaction between the two types of biomolecules results in a deflection of the cantilever toward the substrate during retraction, exerting greater force than that during approach in the force-distance curve. Several types of interaction between biomolecules, such as the adhesive force between individual ligand and receptor pairs [37-38]; streptavidin and biotin pairs [39]; single complementary strands of DNA [40]; antigen and antibody of proteins; and two cell adhesion molecules [41-44], were

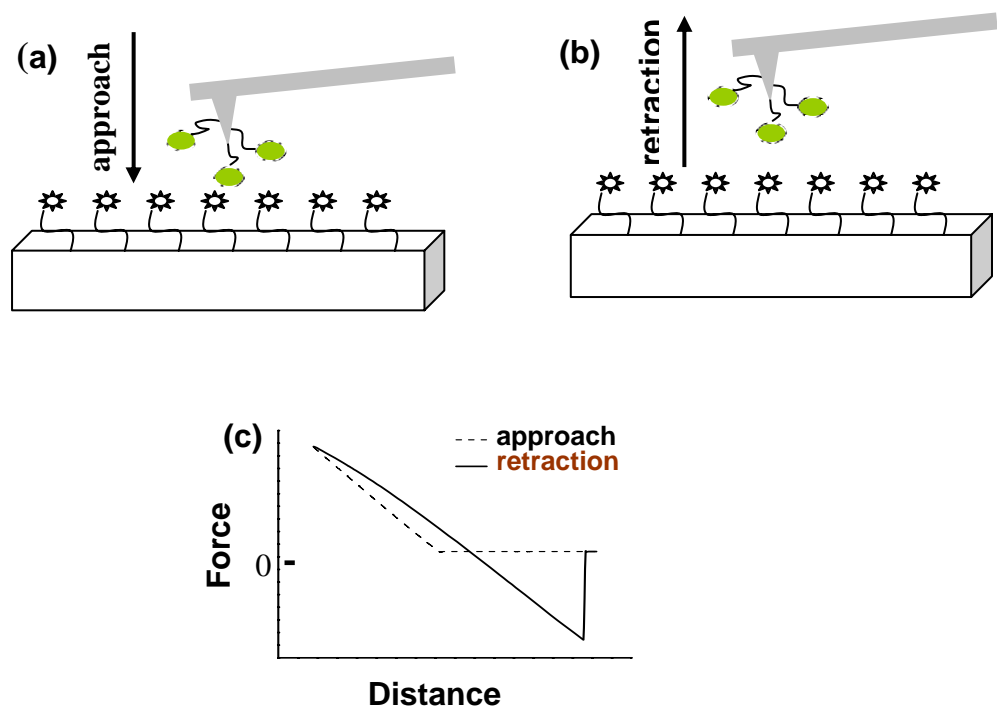


Fig.2-3 Schematic diagram for the determination of the interaction between biomolecules. (a) Attach at the surface (b) Retract from the surface (c) Force vs. distance curves. ● and ⚙ are a pair of biomolecules [12].

quantitatively measured at a nanonewton scale [12].

The second method is to use the nanomechanical AFM cantilever array for label-free biodetection. Intermolecular forces arising from adsorption of small molecules induce surface stress, which causes mechanical bending of a cantilever [45]. This can be utilized to realize molecular recognition. Similar to the first method, one type of molecules is immobilized on the cantilever, which is incubated in a solution containing the other type of molecules. The interaction between the two types of molecules causes the mechanical bending and is measured. In this method, labeling, optical excitation, or external probes, is not required. However, the result is not reliable from a single cantilever. A reference cantilever is generally adopted. Using the AFM cantilever array, multiple label-free biodetection can be realized by immobilizing different biomolecules on different cantilevers, thus different interactions are measured independently in the solution containing various molecules (Figure 2-4). DNA hybridization, receptor-ligand bind, and protein recognition were detected through nanomechanical cantilever array at high sensitivity (concentration less than tens of μM) and with high efficiency (within several minutes) [46-49].

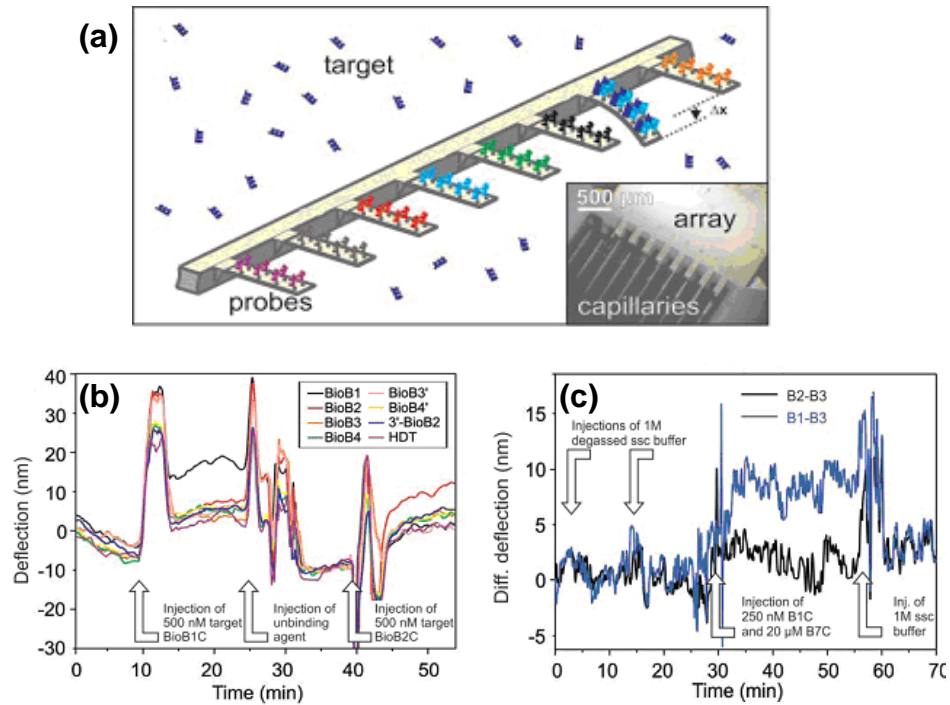


Fig.2-4 (a) The preparation of an active cantilever biosensor array and an illustration of the basic principle of nanomechanical label-free biodetection (inset). The incubation of individual gold-coated cantilevers (dimensions: $500 \times 100 \times 1 \mu\text{m}$) in microcapillaries, each containing a different solution of thiolated probe DNA. (b) Absolute deflection signals from an eight-cantilever array were monitored in real time. (c) Detection of 250 nM BioB1C in the presence of 20 μM BioB7C [49].

2.2.2 Nanofabrication by Physically or Mechanically Modifying Surfaces

The AFM tip is used to physically or mechanically modify the sample surface by applying certain load or bias, resulting in nanopatterns on the surface.

2.2.2.1 AFM Tip Manipulation of Nanoclusters, Nanoparticles and Biomolecules

The AFM tip is used to manipulate and position nanoclusters or nanoparticles (weakly adsorbed on the surface) to a desired place, thus forming 2D or 3D nanopatterns. The procedure can be conducted in a contact or a non-contact mode. In a contact mode, nanoparticles or nanoclusters are displaced by applying a higher load than that used for imaging. In a non-contact mode, two methods are adopted to manipulate and position these nanoparticles or nanoclusters. The first method is to switch off the feedback system when the tip approaches the desired nanoparticle or nanocluster while scanning. The resulting tip-particle contact can further push the particle to a new position. The second method is to change the setpoint when the tip is approaching the particle. The tip would contact the particle and further push it to a new position.

In the early days of visualizing surface with AFM in a contact mode, nanoparticles weakly bound on the surface were displaced to another position if the tip scans at a higher load [50-51]. It was viewed as an obstacle for imaging. Clever researchers realized that they can construct nanopatterns by manipulating these weakly bound nanoparticles or nanoclusters to a desired position. Nanoparticles or nanoclusters, such as C₆₀, Ag, Au, Pd, GaAs, and Cu were manipulated to form desired 2D and 3D nanopatterns [52-58]. Recently, multiwall carbon nanotubes and single-walled carbon nanotubes have also been manipulated by an AFM tip. The mechanical behavior between carbon nanotubes and the substrates and that of individual single-walled carbon nanotubes were studied. Furthermore, carbon nanotubes junction and electrical contact were created with AFM [59-62].

Literature Review

AFM can not only capture the image, but also manipulate the biomolecules from the level of the cell down to the scale of single molecules. Nanomanipulation can be conducted in a contact or a non-contact mode to dissect, push, arrange or extract bulky or single biomolecules.

In 1992, Hansma [63] and Henderson [64] reported for the first time the dissection of plasmid DNA using an AFM tip. Recently, dissection can be conducted within a single DNA molecule at nanometer precision (Figure 2-5a). The DNA fragments were pushed with an AFM tip in order to isolate a particular DNA fragment from a genome DNA molecule, or form artificial nanostructures on a solid surface (Figure 2-5b). The load on the tip during the pushing process should be greater than the imaging load and less than the cutting load [65-67]. Chromosome, protein and membrane can be also dissected with an AFM tip [68-73]. The forces applied on the tip ranged between 20 nN and 17 μ N, depending on the tips and the biomolecules. The dissection was conducted by first scanning the sample surface in a tapping mode, then during the second

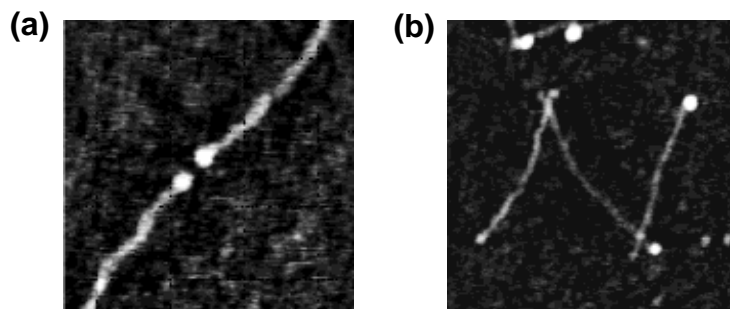


Fig.2-5 (a) AFM image (300×300 nm) of a DNA strand cut by an AFM tip. (b) AFM image (500×500 nm) of a letter "N" from DNA molecules by pushing with the AFM tip [65].

scanning, the tip is lowered down onto the surface of the intended site. This experiment was repeating until the biomolecules broken. After the dissection of chromosome, protein, and membrane, it became convenient to extract a single DNA molecule from the chromosome with an AFM tip [68-70] and to investigate the inner structures [72-75]. In addition, AFM can disrupt the antigen and antibody bonds at applied forces of >0.8 nN [76].

2.2.2.2 Force Nanolithography or Direct Mechanical Modification

A rigid AFM tip is used to mechanically modify a soft sample surface by applying certain loads in the range of 1000 to 1500 nN depending on the substrate. More rigid cantilevers and greater loads are needed for harder samples. It should be noted that the tip may become dull or may break if the sample is too hard. Force lithography can be conducted in a contact mode or a semi-contact mode. In a contact mode, the contact force not only causes difficulties in the tip moving direction but also creates undesired features on the sample surface, especially on soft materials. Hence, it is better to conduct force lithography in a semi-contact mode. A schematic illustration of force lithography is shown in Figure 2-6a, while Figure 2-6b shows a storage field with the IBM logo (writing with the 32×32 cantilevers array) represented by bit indentation/separation equivalent to a storage density of 100 to 200 Gbit/in.² created by force nanolithography. Applied load, lithography speed, and lithography cycles affect the pattern height and surface roughness.

The evolution of force nanolithography is based on previous experimental observations. Blackman and colleague [77] found that the upper layers of the

Literature Review

Langmuir-Blodgett films of cadmium arachidate were easily worn away by an AFM tip when they investigated the tribological properties of these films. Force nanolithography was then developed with increased load applied on the tip to create micro to nanoscale patterns on the sample surface [77-81].

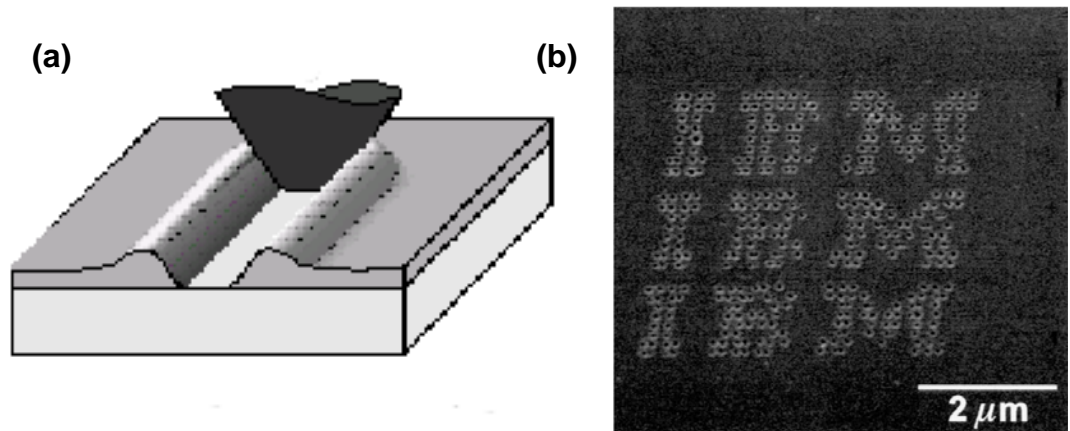


Fig.2-6 (a) Schematic illustration of force nanolithography. (b) A storage field with IBM logo (writing with the 32×32 cantilevers array) represented by bit indentation/separation equivalent to a storage density of $100\text{-}200 \text{ Gbit/in.}^2$ [98].

Patterns on soft materials were fabricated directly with force lithography. Micrometer sized patterns were fabricated with the tip having a larger curvature radius. Yun Kim et al., named the technique as micromachining in 1992 [50-51,81]. With the development of the AFM tip, the curvature radius of an AFM tip was reduced to smaller than 10 nm. Nanopatterns were fabricated on various materials, e.g., metal chalcogenide (SnSe_2 and NbSe_2) [82], Au or Pd nanocluster films [55], metal surfaces (Ni, Cu, Au), diamond-like carbon thin films, polymer, and single crystal silicon [83-88]. Nanostructures can be fabricated using force nanolithography with a heated tip. This work was

Literature Review

developed by the IBM research group. In 1992, this group heated the AFM tip with an infrared laser, which is illustrated in Figure 2-7. The focused laser beam propagates through transparent poly(methyl methacrylate) (PMMA) sample and shines on the tip. The tip surface is coated with a thin layer of gold for absorbing the light, which increased the tip temperature to more than 120°C. And a small pit and lines were constructed at the contact site on PMMA surface. The pattern size is determined by laser power, pulse width and static load [89-91]. The group then integrated piezoresistive sensors for data readback and resistive tip heaters in the cantilever, resulting in a simplified AFM thermomechanical recording and increased data rate and storage density with a data storage densities of up to 1 TBit/in.² [92-94]. The data rate of thermomechanical writing with a single tip is low and cannot be competitive for data storage or lithography. In 1999, the IBM research group micro-fabricated a 5 × 5 and a 32×32 2D cantilever arrays for parallel operation [95-96]. The arrays could provide ultrahigh density, and high-speed data storage. The group obtained initial areal densities of 100 to 200 Gbit/in.² with the 32×32 2D cantilever arrays (Figure 2-6b), which can be improved in the future. At the same time, the writing patterns can be erased by thermal reflow of a rectangular storage field as a whole [97-98].

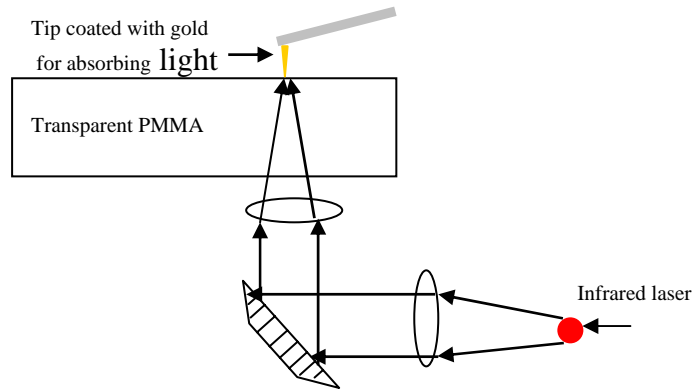


Fig.2-7 The simplified experimental setup for performing thermomechanical writing with an AFM tip [89].

Nanopatterns were fabricated on hard materials with the combination of a sacrificial layer and various selective etching techniques. For hard materials, such as semiconductor crystals or oxide layers, direct fabrication on them makes the silicon tip degrade rapidly. Furthermore, direct patterning often resulted in defects around the patterned structure, making it unsuitable for nanodevices, even though the fabrication has high precision. A better method to resolve this problem is to coat one or two thin soft sacrificial layers with a thickness of several nanometers, such as polymers, III-V semiconductors (10 nm deep) or soft metals (Al, Ti) on the surface. Patterns are first fabricated on the sacrificial layer. Desired nanometer scale patterns can be finally obtained through selective etching and after removing the sacrificial layer [99-106]. Other than using selective etching, nanopatterns were first fabricated on the sacrificial layer via force nanolithography, gold was then deposited on the exposed portions of the substrate (Ge) through an electroless deposition. The desired metallic features were last obtained through removing the resist layer. The gold

pattern may be discrete gold nanoparticles or continuous metallic structures, depending on the deposition time [107].

Force nanolithography is very useful in the fabrication of nanodevices, especially on a nonconducting substrate, that can not be oxidized with AFM tip-directed nanooxidation. Semiconductor quantum point contacts [108-109], weaklink Josephson junction [110], nanoscale transistor [111], and single electron transistor (SET) [112] were fabricated with the combination of force lithography and selective etching. The maximum critical current density j_c of a single Josephson junction with a typical width of 100 nm (fabricated with the combination of force lithography and selective etching) is 5.1×10^6 A/cm² [110].

2.2.2.3 AFM Assisted Electrostatic Nanolithography (AFMEN)

As described above, nanostructures of polymers can be fabricated via force nanolithography due to mechanical or thermomechanical modification. In addition, Lyuksyutov introduced an alternative AFM-nanolithography named electrostatic nanolithography. In this method, an electric field (5 to 50V) is applied between a conductive AFM tip and a thin film of polymer with a thickness of 20 to 100 nm spin coated on a bottom electrode in a contact mode or a amplitude-modulated mode. The applied electric field induces an electronic breakdown of the polymer resulting into charge transport through the polymer and a localized Joule heating of nano-amounts of polymer above its glass transition temperature. Applied with a current of 1-10 nA, electrostatic attraction of softened polymer film toward the AFM tips in the strong (10^8 to 10^9 V/m) non-uniform electric field produces protruded nanopatterns with 5 to 100 nm in width

and 0.1 to 100 nm in height, and the nanopatterns can be removed through heating the film above T_g without an applied potential, demonstrating that no removal or crosslinking of polymer occurs during pattern formation [113-115]. Electrostatic nanolithography produces nanopatterns on various polymer surfaces with high resolution and much higher processing speed (less than 1 μ s for fabricating a nanostructure). Making it has potential applications for data storage devices, sensors and nanoscale electron devices with polymers.

2.2.2.4 Polarizing Ferroelectric Materials

Apart from detecting ferroelectric domain, AFM can also polarize ferroelectric materials at a nanometer scale. In the conventional polarizing method, ferroelectric materials are sandwiched between a bottom and a top electrode. Then DC voltage is applied. The conventional polarizing method can only polarize a large area of a sample. AFM can be used to locally polarize ferroelectric material, producing ferroelectric domains in a nanometer scale. Furthermore, AFM can detect the ferroelectric domain after polarizing. For AFM polarizing and detecting, ferroelectric material is prepared on a bottom electrode. A conductive AFM tip is used for imaging as well as for polarizing (as the top electrode). The sample is polarized by applying a certain DC voltage between the tip and the bottom electrode in contact mode. Ferroelectric information is obtained by applying a small oscillating voltage (less than 20 V) and a frequency of 1 kHz between the tip and the substrate. The experimental setup is illustrated in Figure 2-8a. The applied AC field induces the converse piezoelectric effect, which modulates the tip position normal to the surface with the excitation frequency. The resulting information passes through a “lock-in

Literature Review

amplifier”, and output ferroelectric information of the surface. The piezoresponse force microscopy (PFM) signal is measured as the first harmonic component of bias-induced tip deflection $d = d_0 + A \cos(\omega t + \varphi)$. Phase φ provides information about the polarization direction. For example, if the polarization vector points downwards, a positive biased tip results in the expansion of the sample and bias-induced surface oscillations are in phase with

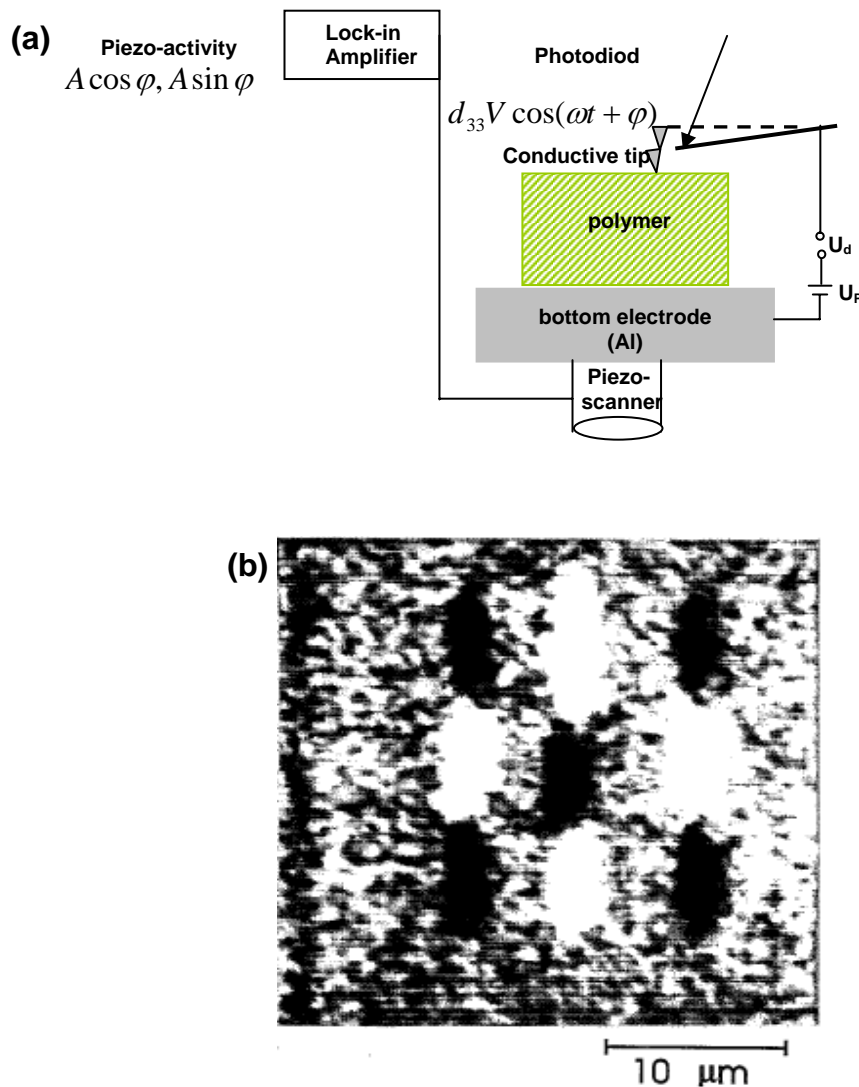


Fig.2-8 (a) Experimental setup for the polarizing and measurement of piezoelectric properties using AFM. (b) Piezoelectricity image of P(VDF-TrFE) [116].

Literature Review

tip voltage $\varphi=0^\circ$. On the other hand, if the polarization vector points upwards, then a positive biased tip results in the recession of the sample and bias-induced surface oscillations are out of phase with tip voltage $\varphi=180^\circ$ (Figure 2-8b). Amplitude A defines the local piezoresponse. At the same time, the “feedback system” provides the surface topography information. Therefore, PFM can provide information on polarization through local piezoresponse, i.e., the local ferroelectric polarity and domain structure.

Micro- to nano-sized ferroelectric domains were polarized and visualized non-destructively with AFM [116-126]. Figure 2-9a illustrates a close-up of 6 Gbit cm^{-2} array written with 3 ms, 10 V pulses. The domains can be erased and subsequently rewritten by the application of negative pulse and positive pulse, respectively. As shown in Figures 2-9b, 2-9c and 2-9d, three domains were sequentially erased by the application of -10 V pulses. Subsequently, the bottom left domain was rewritten with the original 3 ms, 10 V pulse. The center domain was then rewritten, and the bottom left domain was re-erased [125]. This provides a possible alternate method for preparing piezoelectric, pyroelectric, and non-volatile random access memory nanodevices.

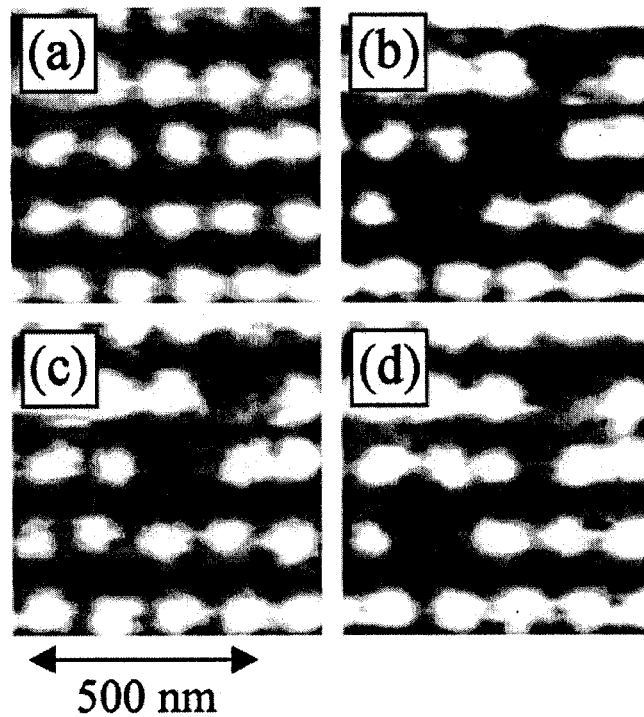


Fig.2-9 (a) Close-up of 6 Gbit cm⁻² array written with 3 ms, 10 V pulses. (b) Three domains were sequentially erased by the application of -10 V pulses. (c) Subsequently, the bottom left domain was rewritten with the original 3 ms, 10 V pulse. The center domain was then rewritten, and the bottom left domain was re-erased [125].

2.2.3 Nanofabrication by Chemically Modifying Surfaces

2.2.3.1 Nanografting

Nanografting, which evolved from force lithography, was developed by Liu and coworkers in 1997 [127]. In this method, an AFM tip is used to remove the material on a substrate and then to graft another material onto the exposed area, forming nanostructures composed of the newly grafted materials. There are mainly five methods to graft the second material. (1) Force lithography is

Literature Review

conducted in a solution containing the second material, which is grafted on the exposed area after the first material is removed. The sample is commonly a self-assembled monolayers (SAMs) assembled on a substrate of interest, usually thiol-gold system. An AFM tip is used as a nanoshaver to locally remove SAMs at high contact force (several tens of nanonewtons) and make the substrate exposed. The desired molecules in the solution would adsorb on the shaved area and form 2D or 3D nanostructures. The size of the patterns fabricated with nanografting can be drawn as small as several nanometers [127-129]. A schematic diagram of AFM tip-based nanografting is shown in Figure 2-10. (2) The second method is named as nanopen reader and writer (NPRW), which combines nanografting and DPN. Similar to DPN, the desired molecules are coated on the tip, not in a solution. An AFM tip coated with desired molecules is used to remove SAMs from desired location, and the molecules coated on the tip simultaneously adsorb on these areas and form nanostructures. NPRW is conducted in air. Therefore, an improved resolution

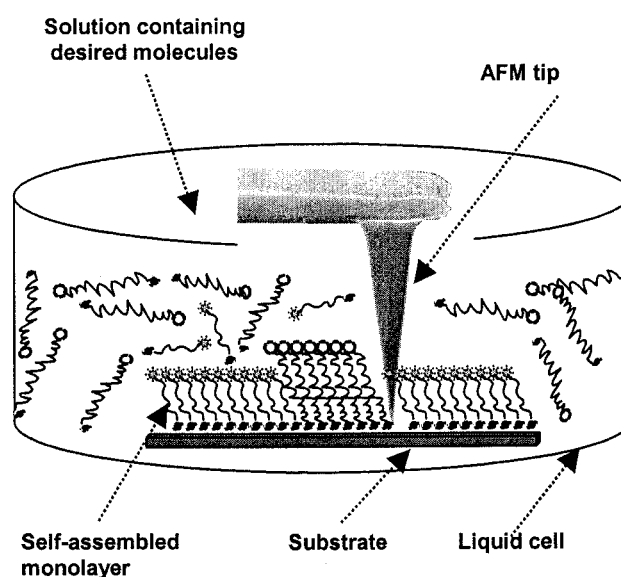


Fig.2-10 Schematic illustration of AFM tip-based nanografting [12].

than in solution can be obtained [130]. (3) In the third method, the first material is selectively removed with an AFM tip. The second material is deposited on the exposed area with other methods, for example, vesicle fusion for the deposition of a second lipid membrane on the exposed area [131]. (4) The fourth method is named as meniscus force nanografting (MFN). As shown in Figure 2-11a, the patterning material is applied as a small drop on a resist covered substrate, and is delivered to the substrate at high precision when the tip selectively penetrates the resist. The force (micronewton) supplied by the meniscus (surface tension of the drop) is sufficient to remove the resist layer and to flatten the substrate surface. Therefore, MFN can be conducted without an AFM feedback control at a fast patterning rate (about 3 orders of magnitude faster than the first three nanografting methods). Line width of DNA can be drawn as small as 15 nm (see Figure 2-11b) [132]. (5) The last method is named cathodic electrografting. In this method, a positive bias is applied to a conductive AFM tip, and the alkyne on the tip or in the solution is attached to the Si substrate and forms monolayer at a nanometer scale through the formation of Si-C covalent bond. This method is different from the other four methods because the first layer is not removed by the tip, but the electrochemical reaction between the Si and alkyne occurs, which is caused by the applied electric field. Lines alkyne monolayer can be drawn down to 40 nm lines [133].

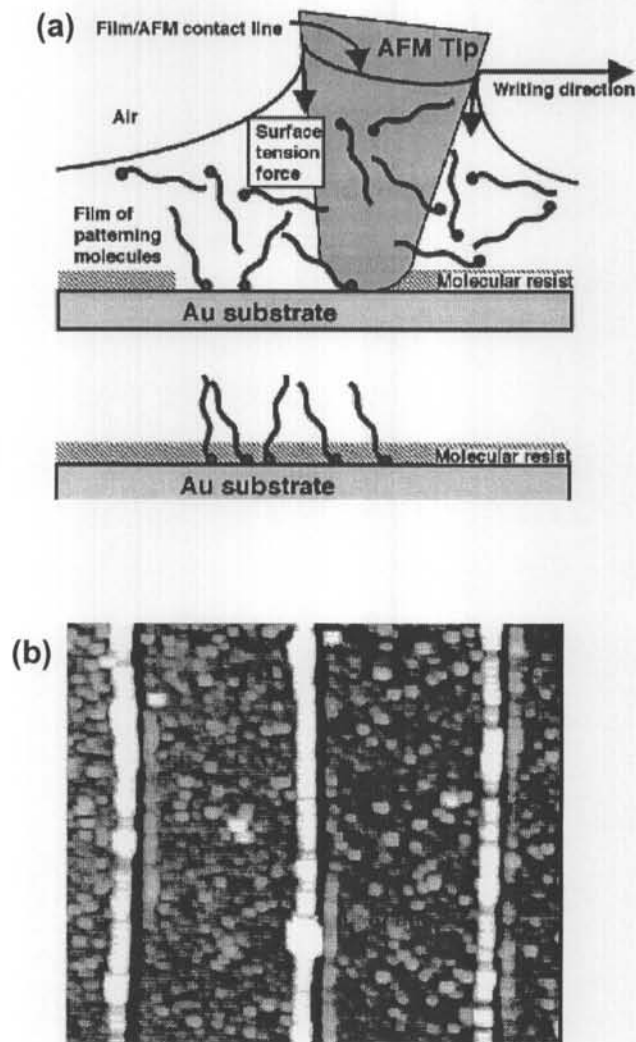


Fig.2-11 (a) Schematic diagram of meniscus force nanografting. (b) Slim DNA lines fabricated via meniscus force nanografting [132].

Nanografting can be used to fabricate complex nanostructures of thiols [128-129,134-137] and biomolecules, such as DNA [138-141], protein [142-146], virus [147], and active enzyme [148]. Biomolecules can be grafted to the exposed gold substrate directly through the formation of Au-S covalent bond or immobilized to a substrate with two or more components through electrostatic interaction or through the formation of effective chemical bond. In the latter case,

one of the component has a reactive terminal group, which can bind biomolecules while the other components are biologically inert, thus realizing selectivity. DNA nanostructures are important in gene mapping, disease diagnosis, DNA sequencing, drug discovery, and molecular device. DNA features as small as 10 nm can be drawn. Thiolated DNA adsorb chemically onto the exposed gold area within the alkyl thiol matrix [138-139] or another thiolated DNA matrix [140-141]. DNA molecules in these nanopatterns keep their bioactivities. The label-free hybridization of DNA nanostructures with complementary strands proved that they are highly selective and sensitive. Figure 2-12 is a hybridization experiment demonstrating high selectivity and specificity of DNA nanostructures fabricated via nanografting. Figure 2-12a show AFM topographs containing nanostructures of T35 [5'-HS-(CH₂)₆(T)₃₅] (40 ×250 nm²) and T25 [3'-HS-(CH₂)₆(T)₂₅] (80 ×220 nm²) produced sequentially using nanografting within a decanethiol SAM. Figures 2-12b and 2-12c show the same area after the incubation of the substrate in a solution containing polyA for 4 h and 14 h, respectively. T25 and T35 can hybridize with polyA through the interaction of adenine-thymine. polyA exclusively adsorb on the two patterns, and the mass of adsorbed polyA increase with increased incubation time. T25 cannot hybridize with polyG, polyG cannot adsorb to the T25 pattern (see Figures 2-12d, 2-12e and 2-12f). Label-free hybridization in the nanostructures also demonstrated that as few as 50 molecules can be detected [139].

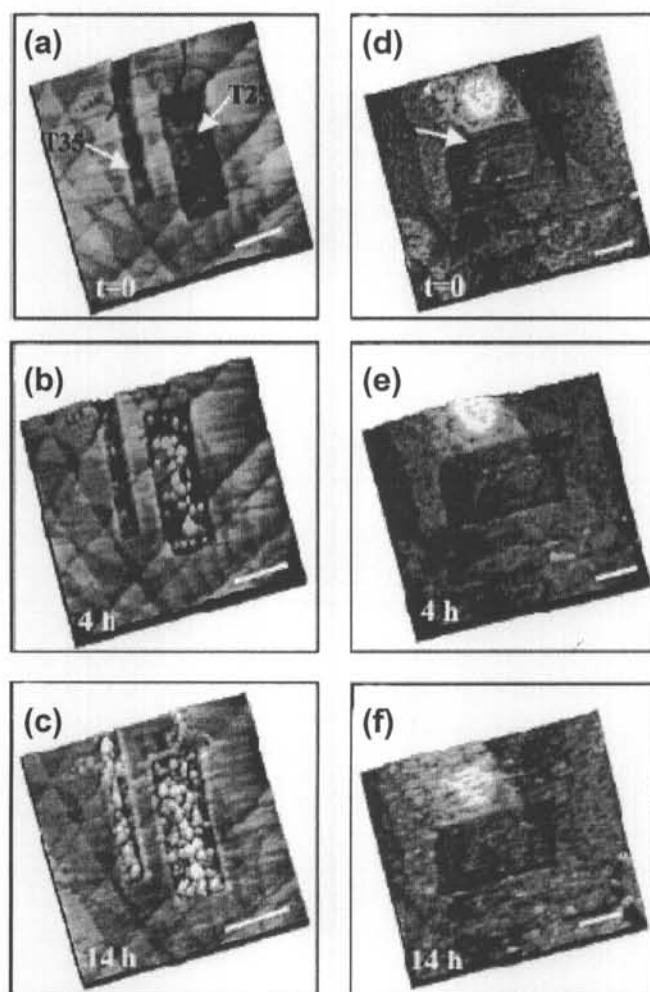


Fig.2-12 Hybridization of DNA nanostructures fabricated via nanografting, exhibiting high specificity and selectivity. (a), (b), and (c) show AFM topographs containing nanostructures of T35($40 \times 250 \text{ nm}^2$) and T25 ($80 \times 220 \text{ nm}^2$) with incubation in polyA for 0, 4, and 14 h, respectively. (e), (f), and (g) show AFM topographs containing nanostructures of T25 with incubation in polyG for 0, 4, and 14 h, respectively. Scale bars represent 100 nm [139].

Proteins have some charged parts and some reactive groups, hence, proteins can be immobilized to a substrate either through electrostatic interaction or through the formation of effective chemical bond (e. g., imine or amide) at

proper conditions [142-146]. A dot as small as $2 \times 4 \text{ nm}^2$ and a line width as thin as 10 nm can be obtained. Proteins in the nanostructures keep their bioactivities.

In addition, nanografting can be also used in the following fields: (1) by introducing reactive groups during nanografting process, multi-step chemical reactions or enzyme-catalyzed reactions can be induced and studied at a nanometer-scale (some special products can be trapped and condensed into the nanopatterns created via nanografting for further analysis) [136-137,148]; (2) measurement of film thickness [149]; (3) characterization of an AFM tip [150]; and (4) fabrication of nanostructures of conjugated materials for electronic nanodevices [133].

2.2.3.2 AFM Tip Controlled Surface Reaction

Using an AFM tip to control surface chemical reaction or biochemical reaction in nanometer scale has potential application for modifying surface properties, studying chemical reactions, or fabrication of nanostructures of biomolecules. Muller and coworkers made pioneering study in this field. They utilized an AFM tip coated with Pt, where Pt acted as a catalyst, to catalytically hydrogenate azide terminated self-assembled monolayer into amino terminated monolayer with high localization [151]. Following their study, Blasdel and coworkers selectively reduced a monolayer of imines to the corresponding secondary amine with an AFM tip coated with a reducing agent, $\text{Na}(\text{OAc})_3\text{BH}_4$ [152]. A tip coated with enzyme can be used to do enzymatic lithography on bio-surface in a buffered solution during the contact between the enzyme-coated tip and the

bio-surface, which can digest bio-molecules, build-up complex nanostructures of bio-molecules and modification of bio-molecules. A protease-coated AFM tip could digest the peptides locally [153]. This method has potential applications in the fabrication of DNA tip, BioMEMS, microTAS and microbiosensor, etc. Another type of tip-induced surface reaction is tip-induced electro-oxidation, also named as constructive nanolithography. Similar to AFM tip-induced nano-oxidation of semiconductors [12], an electric field is applied between a conductive AFM tip and the substrate, where the biased tip locally and non-destructively inscribe chemical information on the exposed outer surface of an organized organic monolayers, thus converting it into a chemoselective template for the construction of more complex nanostructures. The tip-induced modification is believed to be the local electrochemical oxidation/reduction of the top functions. For example, vinyl functions is oxidized to carboxylic acid functions, and Ag^+ is reduced to Ag [154 -156].

2.2.3.3 Electric Field Enhanced AFM Tip-directed Nanooxidation

A bias voltage applied between a conductive AFM tip and a substrate is capable of chemically modifying the sample surface. A negatively biased voltage applied between a conductive AFM tip and a semiconductor or metal sample would cause the sample to be locally oxidized. Either tip negatively biased or sample positively biased depends on the AFM system. The oxide formed becomes protruded, with higher features on the sample surface. It is also named as anodic oxidation. A schematic graph of AFM tip-directed nanooxidation is shown in Figure 2-13. The nanooxidation can be conducted in a contact mode,

a semi-contact mode and a non-contact mode. In a contact mode, the mechanical contact between the tip and

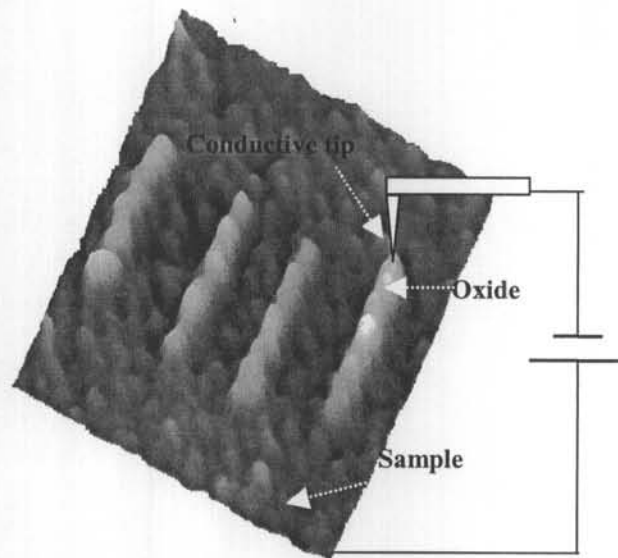


Fig.2-13 Schematic plot of AFM tip-directed oxidation [12].

the sample (especially hard sample) wears the conductive layer, resulting in short lifetime of the tip. A semi-contact mode and a non-contact mode cause less wear of the conductive layer on the tip. A semi-contact mode has higher resolution than a non-contact mode. A threshold voltage is required for oxidizing a sample in a non-contact mode due to a greater separation between the tip and the sample than that in a contact mode and a semi-contact mode. The bias voltage, substrate, separation between tip and sample surface, duration, and ambient humidity all have significant effect on the oxidation.

The detailed mechanism of the oxidation is complex in the presence of water and electric field. Several research groups studied the mechanism of the oxidation. Experimental results demonstrated that larger oxide patterns were

Literature Review

obtained at higher relative humidity [157-160]. Weak current (pico-ampere) during oxidation was measured [161-162]. These results illustrated that an electric field enhanced AFM tip-directed nanooxidation is an electrochemical process, where water from the environment acts as electrolyte, the sample and the tip act as anode and cathode, respectively, and the electric field between the tip and the sample surface ionizes the water and attracts oxygen [163]. The height of the oxide (z) is proportional to t^γ , where t is the time, and γ is a fitting parameter [163-166].

AFM tip-directed anodic nanooxidation has the applications in electric nanodevices of metals or semiconductors. Nanostructure of oxide as small as several nanometers to tens of nanometers were fabricated directly on poly(methylmethacrylate) (PMMA) [167], Si [163,166,168-172], octadecyltrichlorosilane (OTS), graphite, Ti and Si_3N_4 [169,171-183]. 2D or 3D nanostructures were constructed with the combination of anodic oxidation and selectively chemical etching [184-187]. 0.1 μm metal oxide semiconductor field-effect transistors and nanometer scale side-gate silicon field transistor [188-189], semiconductor quantum point contact on the surface of Ga[Al]As heterostructure [190], single-electron memory [191], and nano-electrical devices [92] were constructed by local anodic oxidation of semiconductors and metals.

Single-walled carbon nanotubes, 2 to 5 nm in diameter, were used as AFM tips for nanooxidation with high resolution. Bits as small as 6 nm in diameter were fabricated with 12 to 15 nm spacing, which allows data storage at densities upwards of 1.6 Tetrabit-per-square-inch to be fabricated [193].

2.2.3.4 Dip-pen Nanolithography

In 1999, Mirkin and co-workers developed a new AFM-based nanolithography called dip-pen nanolithography (DPN) [194]. In this method, an AFM tip is coated with a thin film of a chemical of interest by immersing the cantilever in a solution or by evaporation. The chemical is named as ink, which may be organic materials, biomolecules, or inorganic salts. Chemical molecules are deposited on the substrate surface during the contact between the coated tip and the substrate. Nanostructures composed of the chemical are locally formed by controlling the motion of the tip. Figure 2-14a is a schematic diagram of DPN. DPN is mainly conducted using a soft AFM tip with a spring constant less than 1 N/m in contact mode. Both topography and lateral force image obtained simultaneously provide information about the constructed nanopatterns. Lateral force image can give good contrast though the thickness of the nanopatterns is ultrathin. The first used ink is thiol, which contains a mercapto group(-SH) in their molecule [194]. Thiols easily form self-assembled monolayers on gold substrate due to the formation of Au-S covalent bond. This is assumed to be the chemical driving force for the deposition of thiols to gold substrate [195]. In lateral force images, hydrophobic ink (1-octadecanethiol (ODT)) produces dark contrast compared to gold substrate (Figure 2-14b), and hydrophilic ink (16-mercaptohexadecanoic acid (MHA)) produces white contrast (Figure 2-14c). DPN can also be conducted in a tapping mode, where phase image obtained simultaneously with topography is helpful to recognize the ink, as illustrated in Figure 2-15, the topographic images (see Figures 2-15a and 2-15b) and their corresponding phase images (Figures 2-15c and 2-15d) of peptide MH2

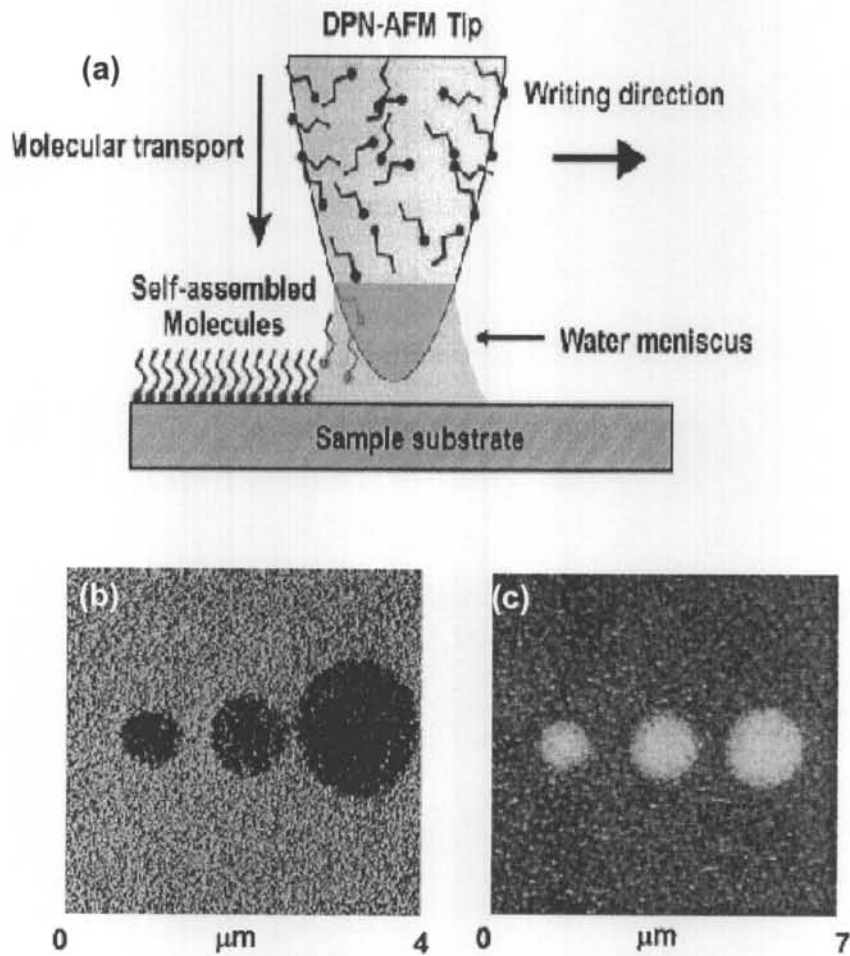


Fig.2-14 (a) Schematic diagram of dip-pen nanolithography. (b) Lateral force image of 1-octadecanethiol (ODT) point array on gold substrate. The hydrophobic thiol produces black contrast. The contact time for the three dots from left to right is 2, 4, 16 min, respectively at relative humidity of 45%. (c) Lateral force image of 16-mercaptohexadecanoic acid (MHA) point array on gold substrate. The hydrophilic thiol produces white contrast. The contact time for the three dots from left to right is 10, 20, 40 s, respectively at relative humidity of 35% [194].

nanopatterns on gold substrate are fabricated in a tapping mode. The drive amplitude is an important factor [196]. In both contact mode and tapping mode, the resolution of DPN is controlled by writing speed, tip size, writing mode, contact time and the ambient condition (relative humidity, temperature).

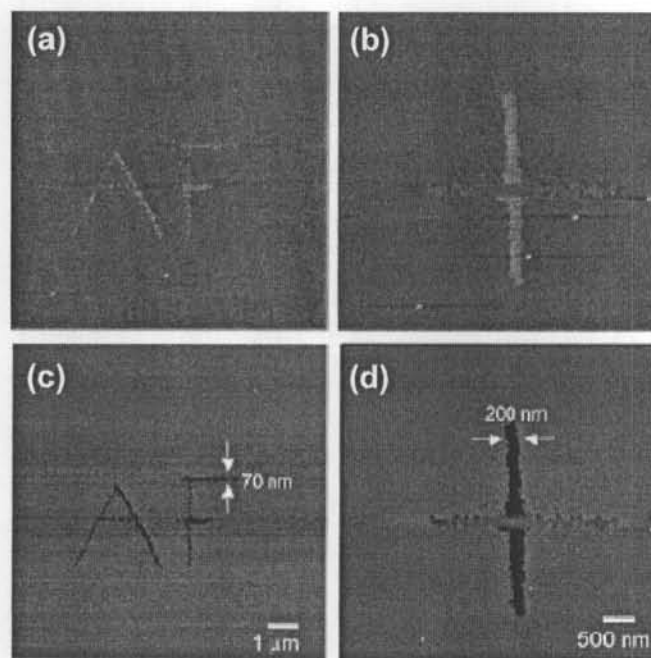


Fig.2-15 Nanoscale patterns written with the peptide MH2 on a gold surface using Tapping Mode DPN. (a) Height image of "AF" written using an aspect ratio of 1:64 and various scan angles. The corresponding phase image (c) shows a darkened patterned region. (b) Height and (d) phase image of "+" written with aspect ratio of 1:32. Lines with widths of 70 nm can be drawn [196].

Polymers, especially conducting polymers, have been used to fabricate nanostructures via DPN. Conducting polymers are intrinsically conducting organic materials, which are composed of C, H and simple hetero-atoms such

Literature Review

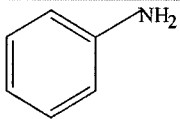
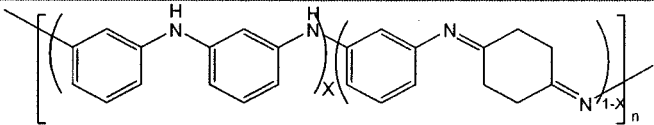
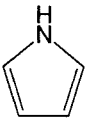
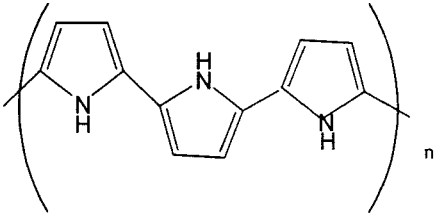
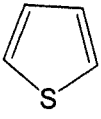
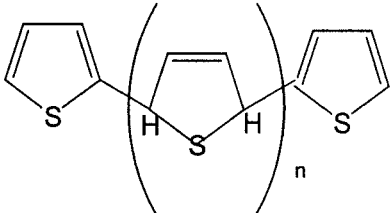
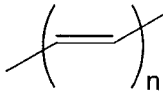
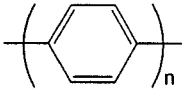
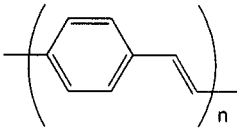
as N and S. Conducting polymers have the advantages of light weight, high strength, cost-effective, resistant to chemicals, as well as electric conducting. The typical representative conducting polymers and their monomers are listed in Table 2-1. The conductivity arises from π -conjugation in the polymer molecules. The conducting properties can be obtained through simple chemical or electrochemical oxidation or reduction to introduce charge centers by a number of simple anionic or cationic species. These anionic or cationic species are called "dopants." The common methods to synthesize conducting polymer are chemical or electrochemical polymerization. Conducting polymers have broad applications in batteries, light-emitting diodes (LEDs), sensors, electrocatalysis, biotechnology, electro-optic and optical devices, micro-wave and conductivity-based technologies, electrochromic devices, electrochemomechanical and chemomechanical devices and corrosion protection [197].

Fabrication of nanostructures composed of conducting polymer has great significance for creating nano-scale devices, such as nano-LED, molecular electronics, nanosensor, nanoelectro-optic and nano-optic devices, etc. DPN has the ability to construct nanostructures with a single-component or multi-component ink. Hence, nanostructures composed of conducting polymers can be fabricated by using polymer or polymer plus additives or monomer as DPN inks.

Nanostructures of conducting polymers were directly fabricated via DPN using polymer as the ink. A luminescent and conductive polymer poly[2-methoxy,5-2'-

ethyl-hexyloxy)-p-phenylene-vinylene] (MEH-PPV) was deposited directly onto a glass via DPN. A scanning optical confocal microscopy was used to visualize

Table 2-1 Typical conducting polymers and their monomers

Conducting polymer	monomer	Molecular formula
Poly(aniline)		
Poly(pyrrole)		
Poly(thiophenes)		
Poly(acetylene)	$HC\equiv CH$	
Poly(para-phenylene)		
Poly(para-phenylene-vinylene)		

the fabricated nanowires of this luminescent polymer; however, the width of these nanowires could not be obtained directly. Moreover, the electron transport properties and photoluminescent properties of these nanowires had not been measured [198]. Some polyelectrolytes, such as poly(diallyldimethylammonium) chloride (PDDA) and poly(styrenesulfonate) (PSS), were also directly deposited onto SiO_x and PDDA modified SiO_x through electrostatic interaction, respectively. Lines with average width of 120 nm and space of 500 nm have been obtained. The chemical compositions in the submicron features were analyzed with X-ray photoelectron spectroscopy [199-200]. Because doping conducting polymers have improved conductivity and solubility in water than non-doping conducting polymers, it is better to use doping conducting polymers as inks for the applications as electric nanodevices. Self-doped sulfonated polyaniline (SPAN) and doped polypyrrole (PPy) have been deposited successfully onto to the opposite charged substrate through the electrostatic interaction. The smallest dots with 130 nm in diameter have been constructed. The doping polymers deposited on the substrate were proved by using electrochemical method. The redox potentials of 300 mV for SPAN pattern and 335 mV for PPy pattern measured by differential pulse voltammetry are consistent with the solution measurements (303 mV for SPAN and 336 mV for PPy) and their theoretical $E_{1/2}$ (330 mV for SPAN and 340 mV for PPy) [201].

In terms of monomer as the DPN ink, in situ polymerization or direct surface patterning followed by polymerization were adopted depending on the ink. For example, monomer (3, 4-ethylenedioxythiophene) (EDOT) was electrochemically polymerized at the AFM tip/substrate interface to create poly-

EDOT nanowires on silicon by applying a negative bias on the conductive tip coated with EDOT during DPN process. Here the applied voltage electrochemically polymerized the EDOT. Lines as slim as 30 nm in width have been drawn [202], while 4-aminothiophenol in the nanopatterns (line-width of 170 nm) fabricated via DPN went through

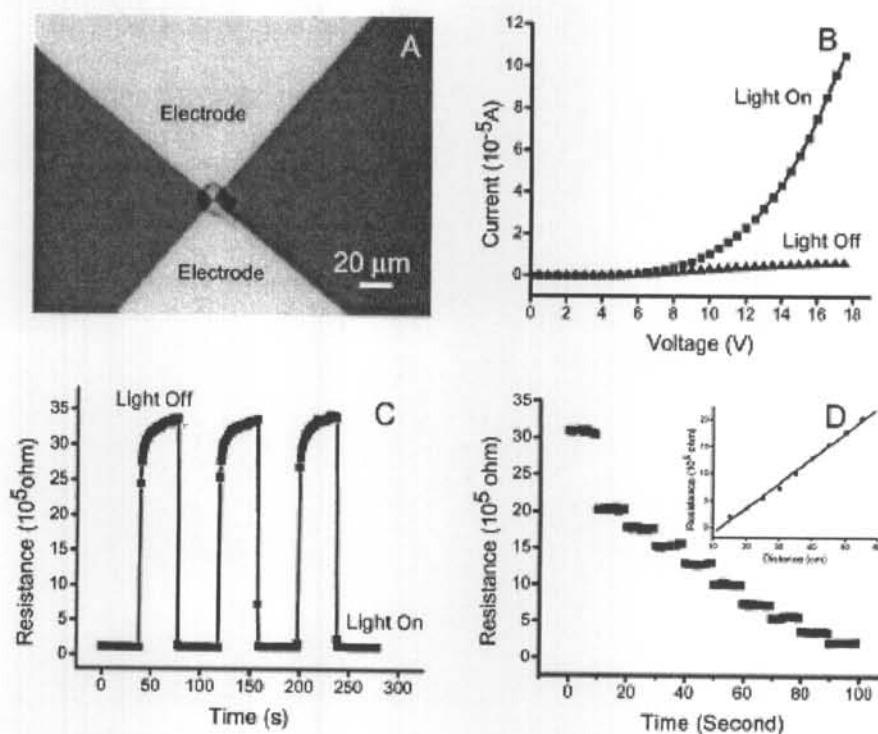


Fig.2-16 A light sensor fabricated via DPN and its light detection properties. (a) Optical micrograph of a light sensor composed of conducting polymer between a 2 mm electrode gap fabricated via DPN. (b) I - V curve of the sensor in dark and illuminated states. (c) Repeated photo-responses of the sensor. (d) The dependence of resistance to the relative light intensity.

enzyme-catalyzed polymerization in a following step. The formed (line-width 210 nm) was confirmed by XPS and Mass Spectroscopy. From an electrostatic force microscopy (EFM) measurement, the formed poly(4-aminothiophenol) has improved conductivity than its monomer [203]. Pyrrole mixed with perchloric acid was used as the ink. Polypyrrole was prepared through in situ acid-promoted polymerization of pyrrole during DPN process. Figure 2-16 shows a light sensor of polypyrrol fabricated via DPN using the mixture of pyrrole and perchloric acid as the ink and its light detection properties, demonstrating that polypyrrole prepared with this method has excellent response, recovery, and sensitivity [204].

Jang and coworkers [205] reported an alternate method other than DPN to construct nanostructures of conducting polymer. Similar to a biased tip-directed electrochemical nanooxidation [12], a conductive AFM tip serves as the working electrode and contacts the precursor polymer with a potential that is sufficient to initiate electrochemical oxidation. The precursor polymer is non-conducting and in the solid swollen state, which is oxidized into cross-linked conducting polymer at nanometer-scale by the applied electric field. This method is named as solid-state oxidative cross-linking (SOC). The resolution is controlled by writing speed, writing mode and applied potential. In SOC, a linewidth as slim as 45 nm has been obtained. Compared to DPN, no material is transferred from the tip to the substrate in a SOC method. It is a maskless and a one-step process with high efficiency. The method has potential application in the plastic nanoscale electronic devices; however, it is only applicable to some special non-conducting polymer.

Literature Review

Dendrimer is a type of polymer with flexible and branched structure, which has catalytic binding and optical properties. Their properties can be tailored by choosing appropriate functional groups at the end of the branching chains. Dendrimers in nanostructures have potential applications in the field of drug delivery, chemical sensors, and photosensitive materials. Some dendrimers can be patterned via DPN onto substrate through the electrostatic interaction, e.g., polyamidoamine (PAMAM) and polypropylene imine (DAB) to Si/SiO₂ with the smallest feature of 100 nm [206]. Some dendrimers were deposited onto the substrate through the formation of covalent bond, e.g., amine-terminated poly(amidoamine) dendrimers were deposited on self-assembled monolayers

Table 2-2 Transfer rate of dendrimers versus molecular weight and functional groups.

Dendrimer	Molecular weight	Functional groups	Transfer rate($\mu\text{m}^2/\text{s}$)
G1 PAMAM	1429	8 amino	6.2 \pm 1.2
G2 PAMAM	3256	16 amino	2.7 \pm 0.5
G3 PAMAM	6909	32 amino	2.5 \pm 0.5
G4 PAMAM	14215	64 amino	1.1 \pm 0.3
G4OH PAMAM	14279	64 hydroxyl	2.6 \pm 0.6
G5 DAB	7179	64 amino	2.2 \pm 0.3
polyethylene imine (PEI)	750000	polymer	<0.1

of 11, 11'-dithiobis(N-hydroxysuccinimidylundecanoate) through the formation of amide covalent bond with the smallest line-width of 30 nm [207]. As shown in Table 2-2, both the functional group and molecular weight affect the transfer rate of dendrimers, the transfer rate increases when the molecular weight decreases, while the effect of functional groups is more complex.

An alternate method to construct polymer nanostructures is to use DPN-patterned nanostructures composed of a precursor (not the monomer) as the template, then initiate further chemical reactions on the pre-designed nanopatterns to form polymer with special properties. In DPN method, the ink is coated onto the tip surface by either dipping the tip in a solution or by evaporating the ink. However, the solubility is low and the melting point is high for most of the polymers, and the transfer rate of ink decreases with the increase of molecular weight (Table 2-2). An ink with a light molecular weight is much easier to be controlled than a polymer ink. Therefore, an appropriate small molecule (precursor) is commonly used to form a template for further formation of polymer nanopatterns. For example, 10-(exo-5-norbornen-z-oxy)decane-1-thiol was patterned onto gold substrate via DPN, followed passivation of those areas where no ink was covered. Polymeric nanostructures were obtained on the template through a catalyst activation step and then through the ring-opening metathesis polymerization (ROMP), as illustrated in Figure 2-17a. Figures 2-17b and 2-17c show the formed polymer nanostructures. The size and shape of the patterns are controlled to nanometer scale by DPN [194], while the height of the polymer is controlled by polymerization reaction time (Figure 2-17d) [208].

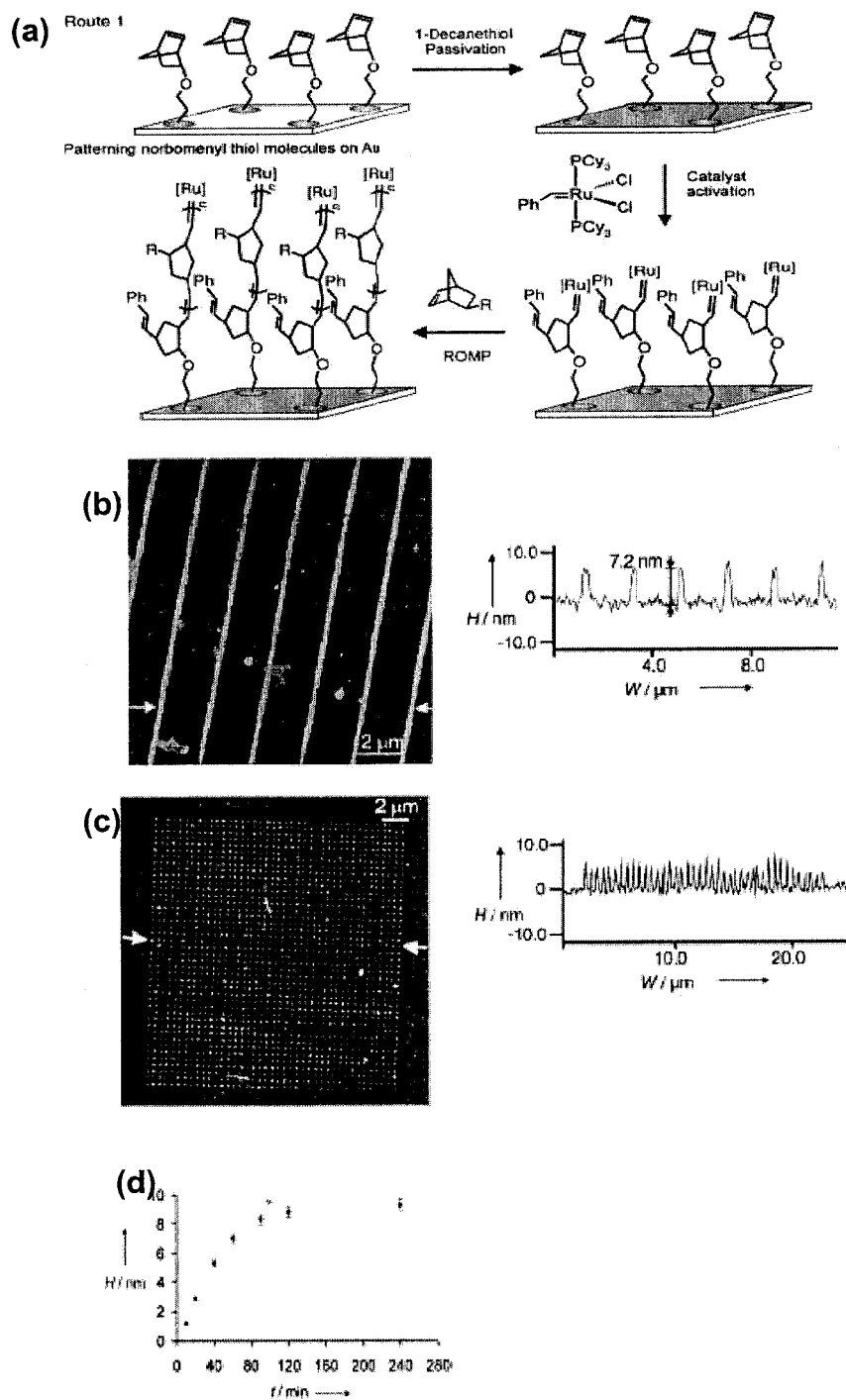


Fig.2-17 (a) Schematic illustration of the synthesis of polymer via site-specific ring-opening metathesis polymerization on DPN-patterned template. (b) Polymer lines with average full-width at half-maximum of 480 nm. (c) Polymer dot array. The average diameter of the dot is $78(\pm 4)$ nm and the average height $5(\pm 1)$ nm. (d) The height of polymer plotted as a function of polymerization reaction time [208].

Literature Review

Nanostructures containing biomolecules are extremely important for life science technologies such as cell research, pharmaceutical screening processes, panel immunoassays, gene mapping, drug discovery, DNA sequencing and disease diagnosis. Nanostructures that are composed of protein, peptide, or DNA can be fabricated directly or indirectly via DPN.

In direct methods, biomolecules are coated on the AFM tip and deposited to substrate of interest during the contact between the tip and the substrate. The biomolecules are immobilized to the substrate through either electrostatic interaction or the formation of covalent bond. An AFM tip, usually composed of Si or Si₃N₄, has weak affinity with biomolecules. Furthermore, biomolecules are macromolecules, therefore the transfer rate of biomolecules via DPN is slower than small molecules (e.g., ODT, MHA). The following methods are commonly adopted to increase the amount of biomolecules coated on the tip or accelerate the transfer rate: chemically modify the tip; apply electrostatic field during tip coating; and modify the substrate with special terminal groups (which have strong affinity with biomolecules) or electrical charge. In addition, chemically tailored biomolecules are commonly used in order to facilitate biomolecules adsorption to the substrate. For example, a 15-residue TAT peptide and DNA bearing 5'-terminal acrylamide groups can be deposited to chemically modified SiO_x surface through the formation of covalent bond by Michael addition, as shown in Figure 2-18 [209-211]. The formation of Au-S covalent bond in gold-thiol system [195] provides an easy method for patterning biomolecules containing sulfur onto gold substrate. Some proteins contain sulfur in their natural states, which can be directly used as inks. Some biomolecules (DNA,

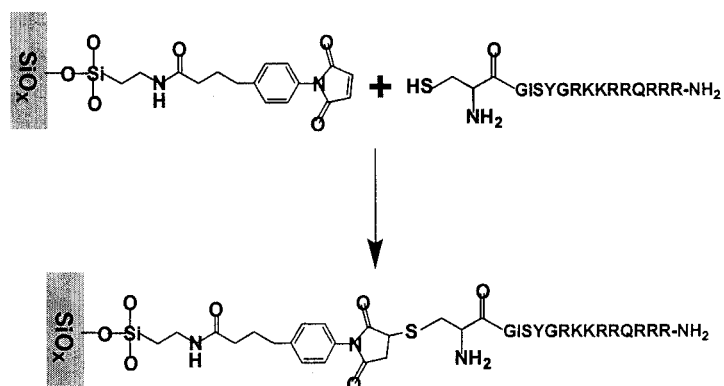


Fig.2-18 Schematic diagram of the immobilization of a 15-residue TAT peptide to chemically modified SiO_x by Michael addition.

protein) do not contain sulfur in their natural states. However, they can be artificially thiolated and deposited to gold substrate directly [196,211-214]. Figures 2-19a and 2-19b show DPN-generated nanostructures of a thiolated protein and a thiolated DNA on gold substrate, respectively. Resolution down to 30 nm in line-width has been obtained. Aldehyde terminated substrate-amine terminated biomolecules system is also adopted due to the formation of Schiff's base (-C=N-) [215]. Nickel oxide has a high affinity for polyhistidine residues; therefore, histidine-tagged biomolecules can be directly patterned onto a nickel oxide surface and form uniform biomolecules nanopatterns [216]. In addition to the formation of covalent bond, the electrostatic interaction between the biomolecules and oppositely charged surface can also induce the deposition of biomolecules [216]. In DPN process with some special inks, a negative or a positive bias is applied on the tip to induce electrochemical reaction, which is named as electrochemical dip-pen nanolithography (E-DPN) [217]. A negatively biased tip coated with histidine-tagged protein or peptide induces the ionization

Literature Review

of Ni (the substrate), resulting in the delivery of protein or peptide to the substrate through the nickel-histidine bond [218]. Some other methods, such as addition of biocompatible non-ionic surfactant or UV irradiation, can facilitate the deposition of biomolecules to the substrate of interest. Surfactant can increase the wettability of the substrate, hence it increases the transfer rate of ink. In the

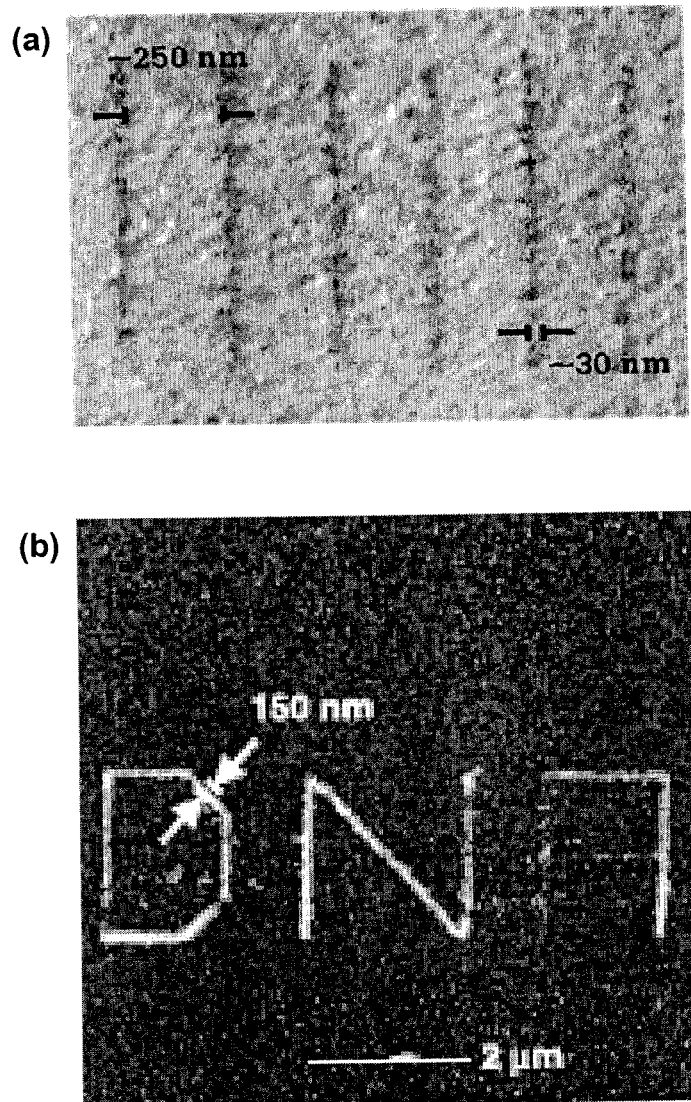


Fig.2-19 Thiolated biomolecules can be deposited to gold through the formation of Au-S covalent bond. (a) Phase image of thiolated collagen nanolines on gold substrate fabricated via DPN. (b) Topography of nanopatterns of thiolated DNA on gold [211, 213].

latter case, a bifunctional photocleavable cross-linker is used. One terminal allows a biomolecule to be conjugated, and the other terminal allows chemical binding to the tip. UV irradiation cleaves the biomolecule-bond, thus releasing biomolecules and forming nanostructures, as illustrated in Figure 2-20a. In this method, the formed nanopatterns cannot be well controlled (see Figure 2-20c) [219-220].

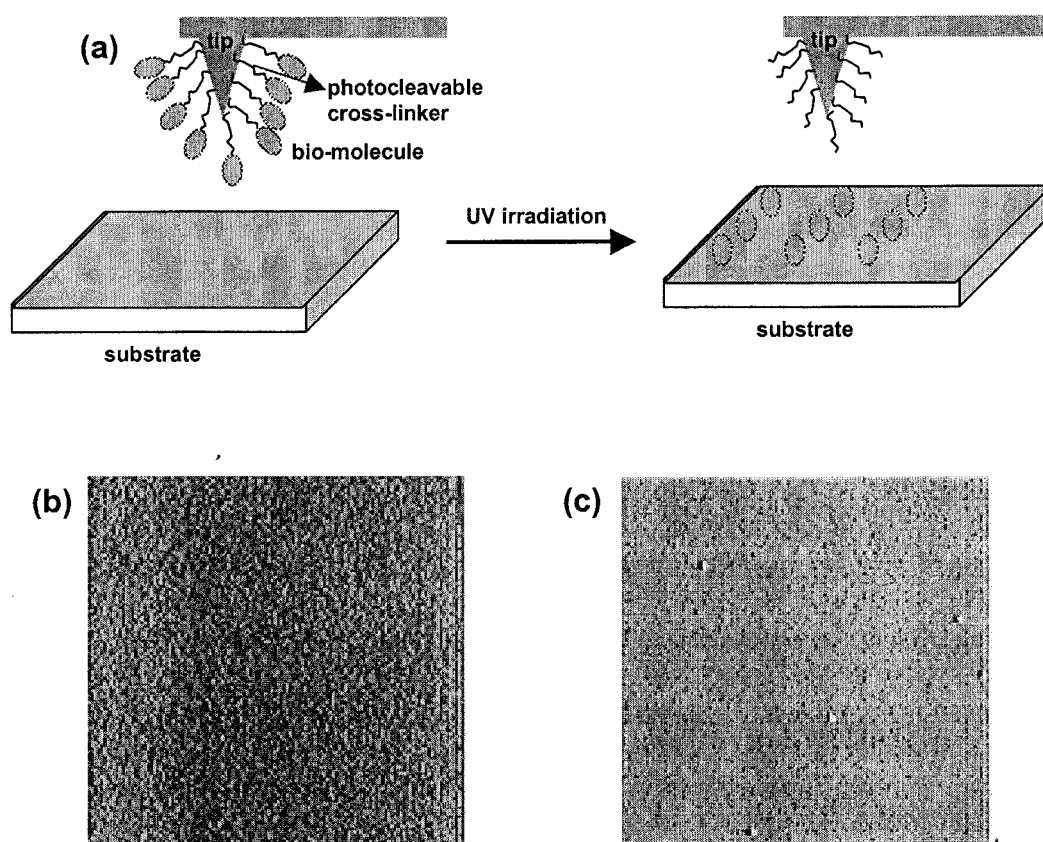


Fig.2-20 (a) Schematic illustration of the facilitated deposition of biomolecules by UV irradiation using photocleavable cross-linker with two terminals. One terminal allows a biomolecule to be conjugated, and the other terminal allows chemical binding to the tip. UV irradiation cleaves the biomolecule-bond, thus releasing biomolecules and forming nanostructures. Topographies before (b) and after (c) UV irradiation. Scale: $5 \times 5 \mu\text{m}$ [220].

Literature Review

In indirect, multi-step method, a chemoselective template containing nanopatterns is commonly created via DPN. Biomolecules are selectively adsorbed on the template in solution through electrostatic interaction or the formation of effective chemical bond, resulting in nanopatterns of biomolecules. Compared to direct method, cross contamination and non-specific adsorption sometimes occur during the formation of biomolecules nanostructures in indirect method. Therefore, the undesired area is always passivated with a resist layer in order to reduce the cross contamination and nonspecific adsorption. For example, Cys-virus is attached to a DPN-generated template containing maleimido functionality by Michael addition [153,221]. The DNA molecules can be aligned and stretched on poly(allylamine hydrochloride) template through electrostatic interaction by coupling molecular combing with DPN-generated templates. The formed DNA nanopatterns are further used as a template for Fe_3O_4 magnetic nanoparticles. The DNA molecules can be also pre-templated in a solution with Fe_3O_4 magnetic nanoparticles, and then aligned on a poly(sodium-4-styrenesulfonate) pattern generated via DPN [222-223]. Biomolecules are commonly attached to DPN generated MHA nanopatterns for the fabrication of bionanostructures or biosensor [224-229]. Several interesting methods are listed here. Hyun and coworkers fabricated an interesting and smart biomolecular nano-switch using stimuli-responsive elastin-like polypeptide (ELP) for the reversible, on-chip capture and release of a few hundred biomolecules [224]. ELP is a stimuli-responsive polypeptide, and undergoes a lower critical solution temperature (LCST) transition. Below its LCST, the ELP is soluble in water; above its LCST, a sharp phase transition results in the desolvation and aggregation of the polypeptide. Changes in the ambient

temperature, ionic strength or pH can trigger this completely reversible inverse transition [230]. The procedure is described as follows: 16-mercaptohexadecanoic acid (MHA) nanopatterns are generated via DPN, and the unpatterned area is passivated with 11-mercaptoundecyl-tri(ethylene glycol) (EG₃-SH). EG₃-SH is protein-resist and therefore can reduce nonspecific protein adsorption. The ELP would be covalently bond to the MHA nanopatterns. Then protein-ELP is immobilized to the ELP nanopatterns, followed by the specific binding of anti-protein to the protein-ELP pattern. The protein-ELP or anti-protein-protein-ELP complex can be captured and released in phosphate-buffered saline solution (PBS) by simply changing the temperature, ionic strength or pH of the solution. The average feature heights of ELP, after binding protein-ELP and anti-protein, and after release of the complex of protein-ELP and anti-protein in the nanopatterns are measured with AFM. The average feature height of ELP increases when protein-ELP and anti-protein bond to it step-by-step. And the average height of ELP after release of the complex of protein-ELP and anti-protein is nearly equal to its original height. Lee and co-workers fabricated a biosensor (antibody nanoarray), which was used to determine the presence of the human immunodeficiency virus type 1 (HIV-1) in blood samples. Figure 2-21a shows the procedure for fabrication of the biosensor and its analysis. In their method, nanostructures of MHA were first patterned via DPN. The areas surrounding MHA patterns were passivated with PEG-alkylthiol (11- mercaptoundecyl-tri(ethylene glycol)) in order to reduce the non-specific binding of protein. Then Anit-p24 IgG were immobilized to the MHA pattern through electrostatic interaction, and the unmodified MHA pattern was further passivated with BSA in order to reduce the unwanted binding in the

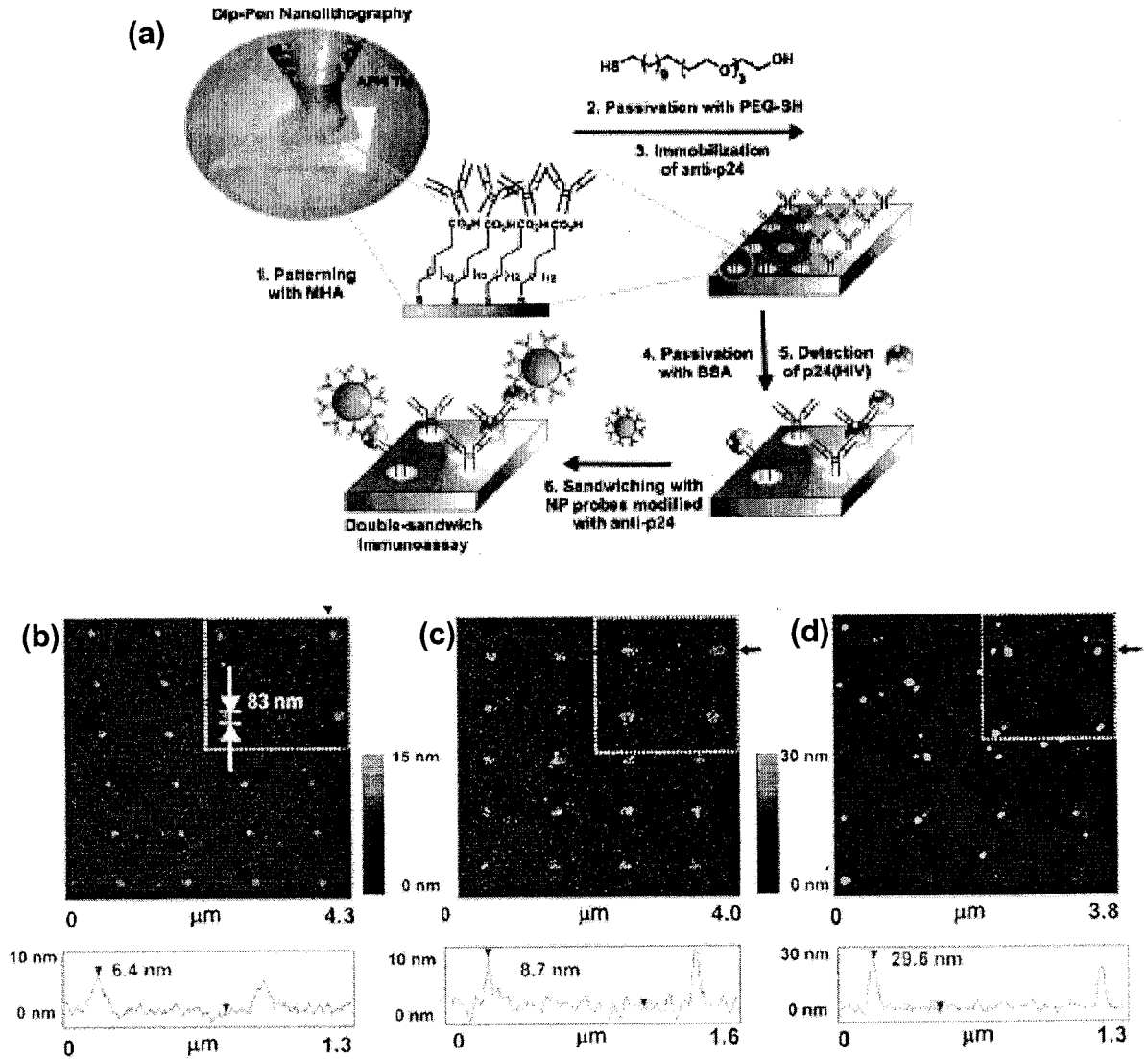


Fig.2-21 (a) Schematic of the procedure to fabricate a biosensor. (b) Photograph of the biosensor prepared by immobilizing Anti-p24 IgG to the DPN-generated MHA nanopattern through electrostatic interaction, and passivating the unmodified MHA pattern with BSA for reducing unwanted binding in the following analysis. (c) Detection of p24 antigen using this biosensor. The detection limit is 0.025 pg per ml. (d) Amplified antigen-nanofeatures by binding of gold nanoparticles functionalized with polyclonal antibody [226].

following analysis (Figure 2-21b). Thus prepared biosensor was used for the detection of p24 antigen (Figure 2-21c) with high resolution, the detection limit is 0.025 pg per ml, which exceeds the limit of detection of conventional enzyme-linked immunosorbent assay based immunoassays (5 pg per ml) by more than 1000-fold. Finally, the antigen nanofeatures were further amplified by the binding of gold nanoparticles functionalized with polyclonal antibody (Figure 2-21d) [226].

Micro- to nano-structures of biomolecules are also fabricated with the combination of DPN and microcontact printing. The first method is to deposit the biomolecules onto a patterned poly(dimethylsiloxane) (PDMS) stamp feature with a coated AFM tip, then to transfer the pattern onto the substrate by conformal contact with the substrate, thus form structures composed of biomolecules. In this method, inking can be controlled on individual feature for stamping, hence it is named as single feature inking and stamping (SFINKS) [231]. SFINKS inks individual features on the stamp, and can ink multiple components on a single stamp without cross-contamination. The resolution of SFINKS is defined by the size of stamp features. At present, the size is at micrometer scale; therefore the development of stamp features at nanometer scale is under development in order to obtain nanostructures of biomolecules of other materials. The second method is named as DPN stamp tip [232]. In this method, a conventional AFM tip coated with PDMS (stamp tip) is used for DPN patterning and imaging. PDMS absorbs chemicals much easily than Si_3N_4 or Si, which are common components of conventional tips. Sub-100 nm resolution

patterns were obtained with dendrimers and cystamine as inks using the PDMS tip.

The key issues for fabricating nanostructures of biomolecules are: 1) maintaining bioactivities; (2) high resolution; (3) high density of features; (4) address a specific feature on the surface; and (5) deposit different molecules to assemble complex structures. As described above, a DPN-generated bio-patterns (both directly and indirectly) suffice these requirements, i.e., by keeping bioactivity, the pattern feature as small as tens nanometer, features with high density, complex structures obtained through multi-step, address a specific feature on a pre-designed site. Therefore, DPN is a promising and alternate method for fabrication of nanostructures composed of biomolecules.

Nanostructures of magnetic materials have potential technological applications in molecular electronics, high-density recording and biosensors. Nanostructures of magnetic nanoparticles were first fabricated via indirect method, then positively charged Fe_3O_4 were selectively adsorbed on DPN-generated MHA (negatively charged) nanopatterns through electrostatic interaction. The pattern size is controlled in the range of 45-500 nm [233]. Magnetic materials can also be deposited to substrate of interest directly via DPN. [234-235].

Inorganic materials, such as metal nanoclusters [236], inorganic salt MCl_x [237], HAuCl_4 [238-239] and H_2PtCl_6 [217-218] were used as DPN ink to construct nanopatterns. For H_2PtCl_6 ink, a positive DC bias is applied to the tip. It was believed that H_2PtCl_6 is electrochemically reduced to Pt.

With the combination of DPN and wet chemical etching, complex nanostructures can be prepared. The area covered with thiol is more stable than gold or silicon oxide in some weak chemical etchants, thus forming a resistant layer. Combined with wet chemical etching, DPN had fabricated 3D multi-layered nanostructures, which implies potential applications of DPN in electronic nano-devices [240-241].

2.3 Theoretical Analysis in DPN

Some researchers conducted theoretical analysis on DPN. Two methods were utilized to do theoretical analysis. The first method was a pure theoretical research with numerical calculation or computer simulation. In this method, they investigated the parameters at a wide range without the limit of a definite condition. The second method was to design a model based on the experimental data. The DPN process was commonly divided into two processes: transport of ink molecules to the substrate and ink molecules diffusion on the substrate surface. The heat issues involved in these studies are the effects of meniscus on DPN and the mechanism and kinetics of the diffusion of ink molecules on the substrate surface.

Mirkin group thought the capillary force is probably the driving force for DPN when they developed DPN [202], which issued a hot discussion about the effect of relative humidity on the transfer rate of thiols. Thomas Stiffer calculated the capillary force utilizing Kelvin equation

Literature Review

$$RT \ln \frac{p}{p_0} = V\gamma \left(\frac{1}{r_1} + \frac{1}{r_2} \right) \quad (2-1)$$

and Young-Laplace equation

$$p = \gamma \left(\frac{1}{r_1} + \frac{1}{r_2} \right) \quad (2-2)$$

They deduced the following equation for the calculation of capillary force (F) by assuming the condensed liquid as sphere and the substrate as smooth plane,

$$F = p\pi x^2 = \gamma\pi x^2 \left(\frac{1}{r_1} + \frac{1}{r_2} \right) \quad (2-3)$$

They calculated the capillary force at varied humidity, surface tension, tip-substrate separation, tip geometry and contact angles, and obtained that higher humidity, higher surface tension, larger tip radius, and small contact angle exert a larger capillary force. They also calculated Lennard-Jones force between the tip and the sample and compared it with a capillary force. In a shorter separation (< 5 nm), Lennard-Jones force is comparable to a capillary force. In a longer separation (> 5 nm) Lennard-Jones is less than a capillary force [242].

Ratner and colleague modeled the fluid between the elliptic tip surface and substrate surface as a 2D lattice gas on a square lattice. They assumed that each lattice site is either empty or occupied by just one particle, and each occupied site interacts with its (occupied) nearest neighbor site with an attractive energy ϵ . Particles were confined vertically between the lower flat substrate surface located at $y = 0$ and the upper elliptic tip surface separated from each other by h lattice spacing. The lattice sites were divided into bulk, tip surface and substrate surface sites. A tip surface site felt an attractive binding energy b_T as well as the nearest neighbor attraction ϵ . A substrate surface site

felt an attractive binding energy b_s as well as the nearest neighbor attraction ϵ . A bulk site only feels the nearest neighbor attraction ϵ . By assuming the system was in the thermal and phase equilibrium, they performed a GCMC (grand canonical Monte Carlo) simulation. They investigated the liquid condensation by varying the humidity, tip-substrate separation, tip geometry as well as tip wettability. Tip wettability is related to ink molecule hydrophilicity. They obtained that high humidity, large tip geometry, low separation, completely wetting tip, as well as low temperature result in large meniscus [243-244]. Weeks and colleague studied the dissolution kinetics of MHA (a hydrophilic thiol) ink for DPN. In their experimental work, relative humidity exhibited significant influence in the range of 20% to 45% for MHA transport. No feature was obtained at relative humidity less than 15% and little change was observed on the pattern while above 45%. The dependence of the square of the dot radius on the dwell time was well fit by two linear regions separated by a sharp transition shown in Figure 2-22. They proposed a model to interpret the results. In their model, the tip moves at constant speed v - which is zero for fabrication of dots-through a water film of thickness δ on the surface. Because of a nonzero contact angle at the tip, the height (h) of the meniscus at the tip was different from δ . Thiol molecules dissolved from the tip into the meniscus, diffused through the meniscus, and attached to the surface, making continuous self-assembled monolayers (SAMs). After a time τ , the tip was removed from the water film. At this time, thiol molecules were both attached to the surface and dissolved in the meniscus. Through diffusion, the dissolved thiols would eventually reach the edge of the SAM and attached to the substrate, contributing to the final feature size. Regardless of the tip-meniscus geometry, the magnitude of the diffusion

Literature Review

constant, of the dissolution rate, the total number of molecule N transferred to the surface would be given by the integral of the transfer rate dN/dt over the total tip-surface contact time τ .

For the fabrication of a dot, molecules dissolve from the tip through the thermal activated detachment at a rate

$$\left(\frac{dN}{dt}\right)_+ = \frac{A}{\pi a^2} \beta_+ = \frac{A}{\pi a^2} \nu e^{-E_D/kT} \quad (2-4)$$

where A is the contact area between the tip and the meniscus, πa^2 is the average area per thiol ink molecule, E_D is the activation energy for ink detachment, k is Boltzmann's constant, T is the temperature, and ν is an attempt frequency. The molecules return to the tip simply due to the impingement and attachment at a rate given by

$$\left(\frac{dN}{dt}\right)_- = A\beta - C_0 \approx A\left(\frac{kT}{2\pi m}\right)^{1/2} e^{-E_a/kT} C_0 \quad (2-5)$$

where m is the mass of a thiol, E_a the activation energy for attachment, and C_0 is the concentration of thiols in solution adjacent to the tip. The dot radius R is related to N through $\pi R^2 = N\pi a^2$. Combining the three relationships and integrating give:

$$R^2 = A[\beta_+ \tau - \pi a^2 \beta - \int C_0(t) dt] \quad (2-6)$$

For patterning a line, the line width W is expressed as :

$$W = \left(\frac{A}{\nu}\right)[\beta_+ - \pi a^2 \beta - C_0(\nu)] \quad (2-7)$$

where ν is the tip scanning speed, and C_0 is expressed as a function of ν instead of t . C_0 is small at short contact times or high tip speeds. Therefore two

regimes emerge, as shown in Figure 2-22. At short contact times or high tip speeds $C_{0 \approx 0}$, hence $R^2 \propto A\tau$ and $W \propto A/v$, in this regime the surface kinetics dominates the transfer process. For long contact times or slow tip speed, C_0 reaches a limiting value $C_0 < C_e$, once again $R^2 \propto A\tau$ and $W \propto A/v$ but slopes of these linear relationships are reduced. In this regime the transfer process is controlled by diffusion. The humidity influences the meniscus height h on contact area A . The tip can be approximated as a cone terminated by a hemisphere of radius ρ . If $h \gg \rho$, A is approximately equal to that of a conical tip with half-cone angle ϕ , and height h , which is $\pi h^2 \sin \phi$. In contrast, for $h < \rho$, $A = e\rho^2 \cos^{-1}(1 - h/\rho)$. For $h \ll \rho$, this has an $h^{1/2}$ dependence, while for $h \approx \rho$ it is linear in h . Because A is a multiplicative factor, the transition from

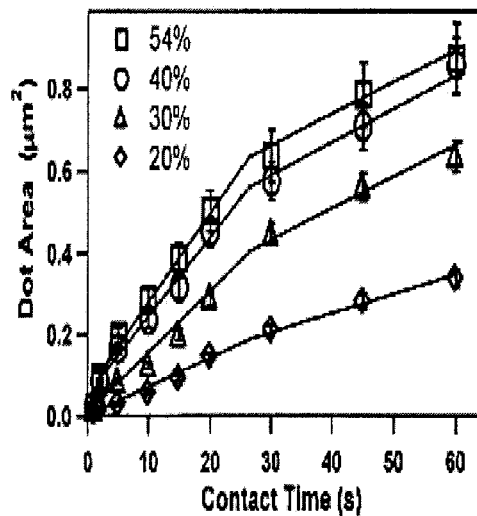


Fig.2-22 Dependence of radius squared on dwell time as a function of relative humidity [245].

Literature Review

dissolution-dominated to diffusion-dominated deposition should be independent of humidity and the functional form of the dependence of dot radius on humidity should be the same for all dwell times [245].

Sheehan and colleague studied the influence of humidity on DPN with ODT (a hydrophobic thiol) and gained some different results from Weeks and colleague's work. They found that ODT could be transported via DPN at any humidity condition. They concluded that the meniscus was not required for ODT transport, i.e., capillary force was not the driving force for DPN [246].

Schwartz and Mirkin [247-248] investigated the transport of both ODT and MHA. Both of them realized DPN with ODT and MHA and MHA ink at any humidity, but they provided different interpretation. Schwartz thought the realization of DPN with ODT and MHA ink due to molecule mobility, not due to capillary force from meniscus. Mirkin and colleague thought meniscus exists even at a relative humidity of 0%, so capillary force produces significant effect on the transport, relative humidity exerts different results on ODT and MHA due to the different solubility of the two molecules in water.

With respect to the diffusion of inks on the substrate surface, the generally used interpretation is diffusion theory, either with computer simulation or numerical model based on experimental data. Ratner and colleague [249] proposed a 2D self-assembly diffusion model. The substrate surface was assumed as a square lattice. Molecules became immediately trapped and were immobile once they reached one of the chemisorbing bare metallic lattices. The molecules arriving later have to travel above the molecule layer to find unoccupied lattice. The

driving force was the concentration gradient. The growth of patterns was thought of as the growth of a phase with a finite diffusivity in contact with a phase with zero diffusivity. The growth of circles reduced to problem of the phase growth in diffusion theory. Figure 2-23 is the schematic plot of the 2D random walk theory.

Molecules walk randomly between the sites on a square lattice with a grid length l and a time interval Δt , to conform to 2D diffusion picture, Δt and l should satisfy

$$4D\Delta t = l^2 \quad (2-8)$$

The random walk is isotropic. The tip was thought to generate a constant flux of ink molecules for fabricating a circle, or move between the discrete sites on the lattice. For the latter, a range of tip scan velocity v relative to the diffusion velocity, $v^* = v/(l/\Delta t)$, was studied. By assuming the density of ODT on the gold surface to be the monolayer density (about $1/25\text{\AA}^2$ from their experiment data), they assumed the number of ink molecules deposited per unit time is a constant n and calculated $n \approx 4.2 \times 10^5 \text{ s}^{-1}$ and used in the simulation. Various deposition rates relative to the diffusion time scale, $n^* = n\Delta t$, were studied.

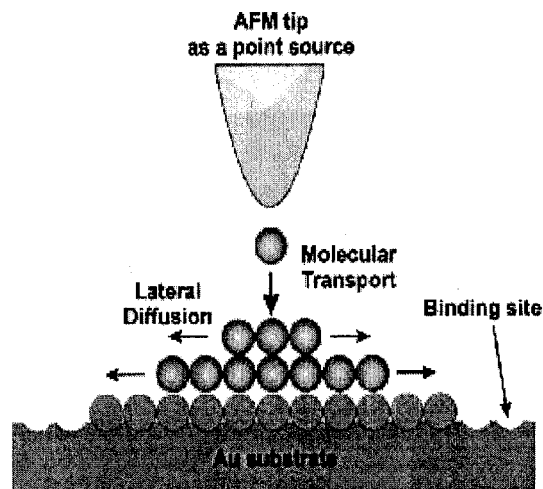


Fig.2-23 Schematic plot of the 2D random walk theory [249].

They also proposed an analytic theory (continuum theory) for the radial growth of circles by assuming cylindrical symmetry of diffusion and treating the position of ink molecule as continuous variable. Suppose at time t , the number density at distance r from the tip is given by $P(r,t)$, where $\int 2\pi r P(r,t) dr$ is the total number of molecules deposited until time t . For a given periphery, $R(t)$, they solved the diffusion equation for the number density within ($r < R$) and outside ($r > R$) the periphery with different diffusion constants D (finite) and $D' (\rightarrow 0)$ respectively. At the periphery, $r = R$, the number density is taken to be the monolayer density ρ and the density flux must be continuous,

$$P(R,t) = P'(R,t) = \rho \quad (2-9)$$

$$D \frac{\partial P}{\partial r} = D' \frac{\partial P'}{\partial r} \quad (2-10)$$

Where $P(r,t)$ and $P'(r,t)$ are the densities within and outside the periphery, respectively. The solution of $P(r,t)$ and $P'(r,t)$ give exponential integral

functions $Ei(-r^2/4Dt)$ and $Ei(-r^2/4D't)$, respectively. In order to satisfy the first boundary condition for all t , $R(t)$ must satisfy equation 2-11.

$$R(t)^2 = \lambda^2 4Dt \quad (2-11)$$

Assuming a source depositing n ink molecules per unit time, they impose a constant flux, n , at the origin,

$$-2\pi Dr \frac{\partial P}{\partial r} \Big|_{r \rightarrow 0} = n \quad (2-12)$$

Then the number densities inside and outside the boundary are given in equation 2-13 and equation 2-14, respectively.

$$P(r,t) = \rho - \frac{n}{4\pi D} [Ei(-r^2/4Dt) - Ei(-\lambda^2)] \quad (2-13)$$

$$P'(r,t) = \frac{\rho}{Ei(-\lambda^2 D/D')} Ei(-r^2/4D't) \quad (2-14)$$

Due to the continuity of the flux at R , λ^2 should satisfy equation 2-15

$$-\frac{n}{4\pi} e^{-\lambda^2} = D' \rho \frac{e^{-\lambda^2 D/D'}}{Ei(-\lambda^2 D/D')} \quad (2-15)$$

Finally taking the limit $D' \rightarrow 0$ and using the asymptotic expansion of $Ei(-x)$ for large d , $Ei(-x) \approx -e^{-x}/x$, and simplify the above equation to

$$e^{-\lambda^2} = \frac{4D}{(n/\pi\rho)} \lambda^2 \quad (2-16)$$

Equations (2-13), (2-14), (2-15) and (2-16) form the central results of the continuum theory. The circle growth is related to the deposition rate, n , and the diffusion constant, D . In the slow deposition limit ($n/\pi\rho \ll 4D$),

$$R(t)^2 = \frac{n}{\pi\rho} t \quad (2-17)$$

Literature Review

The radial growth is solely determined by the deposition rate. On the other hand, in the fast deposition limit ($n/\pi\rho \gg 4D$), the radial growth is determined by both the deposition rate ($n/\pi\rho$) and the diffusion constant (D)

$$R(t)^2 = 4Dt \ln[(n/\pi\rho)/4D] \quad (2-18)$$

The following simulation results were obtained. The circle growth was largely isotropic, but the periphery was rather noisy due to the diffusional nature of self-assembly. For slow deposition, the periphery propagated step-by-step in time. In contrast, the periphery growth of fast deposition was confined to one fourth of the total time, giving a negligible growth at later times. For transport certain molecules, the growth gets faster with increasing deposition rate. While the tip was in contact with the surface a linear growth of $R(t)^2$, and thereafter a much slower increase in the radius that eventually stopped when all the molecules were adsorbed. The final radius converged to the same value regardless of the deposition rate. For a moving tip to construct lines or structures, high scan speed resulted in less transport.

They further connected the model to DPN experiment with ODT ink. They took the spacing between ODT molecules (5\AA) of ODT monolayer on Au(111) as the grid length l , by assuming the diffusion time step much larger than the velocity relaxation time and thermal equilibrium in the velocity distribution, then

$$\Delta t \gg mD / K_B T \quad (2-19)$$

At room temperature, $\Delta t \gg 2.7$ ps. $4D\Delta t = l^2$, the upper limit of the diffusion constant was estimated to be $2.32 \times 10^{-4} \text{ cm}^2 \text{ s}^{-1}$.

Sheehan and colleague [246] proposed a method to calculate the diffusion coefficient of ODT on gold from DPN experimental data. They assumed the tip as an infinite reservoir of molecules, which allows it to maintain a constant concentration, C_0 , along the perimeter of the tip-surface contact. Deposited molecules diffuse radially outward across the substrate. As the island grew outward, the area within the island, where the concentration was greater than the surrounding concentration (C_s) and the SAM was standing. The diffusion rate across the surface was independent of concentration (Fickian diffusion) because the thiol-gold binding energy was greater than the interaction energy between the alkane backbones. The surface diffusion was radially symmetric from the tip, with the concentration, C , vanishing at infinite radius, $C(r = \infty) \equiv 0$. For Fickian diffusion, the concentration obeyed the 2D diffusion equation,

$$\frac{\partial^2 c}{\partial r^2} + \frac{1}{r} \frac{\partial c}{\partial r} = \frac{1}{D} \frac{\partial c}{\partial t} \quad (2-20)$$

They utilized Smith method [250] to solve the integrate equation and gave the formula:

$$c(r,t) = C_0 \frac{E_1(r^2 / 4Dt)}{\ln(4Dt / a^2 e^{2\gamma})} \quad (2-21)$$

where E_1 is exponential integral and γ is Euler's gamma ($\cong 0.577$). They fitted their experimental data to this model with three parameters, C_s / C_0 , a (contact radius) and D . The values of C_s / C_0 and D were found by nonlinear least-squares fittings. The transition concentration C_s / C_0 and surface diffusion coefficient of ODT deposited on clean gold via DPN to be 0.12 ± 0.02 and $8400 \pm 2300 \text{ nm}^2 \text{ s}^{-1}$, respectively [246].

Literature Review

Schwartz [247] proposed two physical diffusion models to explain his experimental data in DPN with ODT and MHA inks. The first model was non-polar molecules transport via simple molecular surface diffusion. He thought the transport process was a simple molecular diffusion and Arrhenius temperature dependent, not a capillary force-driven transport. He developed a mathematical diffusion model to fit the experimental data with ODT (Figure 2-24).

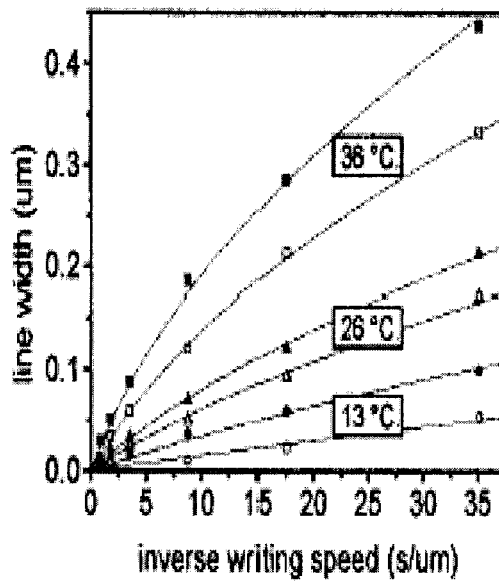


Fig.2-24 Line widths as a function of AFM tip speed with ODT [247].

The rate at which the gold surface covered with monolayer is

$$\frac{y}{x} = wv = \frac{w\Delta l}{\Delta t} = \frac{\Delta area}{\Delta t} \tag{2-22}$$

Where w is the line width, v is the speed of the AFM tip during the patterning process, and l is the distance that the AFM tip has moved. The flux of molecules to the surface F is

$$F = \rho\Delta A / \Delta t = \rho wv \tag{2-23}$$

where ρ is the monolayer surface density.

Literature Review

For a circle pattern, Fick's first law was adopted to calculate the molecular flux

$$F = 2\gamma\pi D \frac{dC}{dr} \quad (2-24)$$

Figure 2-25 is the DPN process in his model, then the above equation can be expressed as

$$F = 2\gamma\pi D \frac{dC}{dr} = 2\lambda\pi D \frac{C}{(w/2) + l_0} = \rho w v \quad (2-25)$$

Rearranging terms gives

$$G \equiv [4\gamma\pi D C / \rho] = v w^2 + 2v w l_0 \quad (2-26)$$

The physically relevant solution to equation (26) gives

$$w = -l_0 + \left(\frac{G}{v} + l_0^2\right)^{1/2} \quad (2-27)$$

Equation (2-27) fits the data in Figure 2-25 [247].

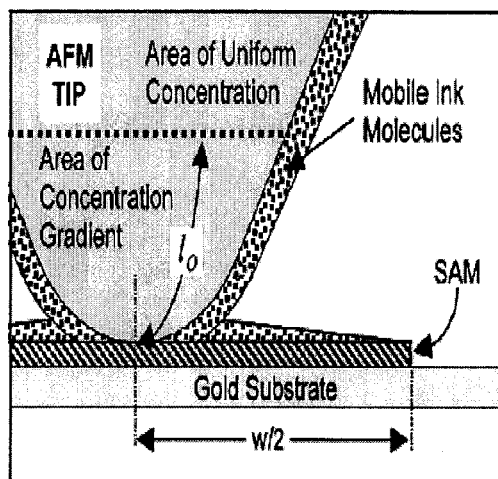


Fig.2-25 DPN process in Schwartz's model [247].

The thiols (ODT and MHA)-gold system is a strong interaction system due to the formation of covalent bond Au-S. The diffusion is isotropic and can be

Literature Review

interpreted with Fickian diffusion theory. But for a weak-binding case, the result is different. Manandhar and colleague [251] studied 1-dodecylamine (DDA) – mica system, which owes weak-binding. They found anisotropic patterns shown in Figure 2-26.

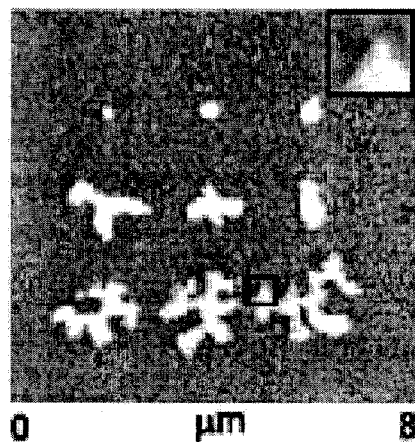


Fig.2-26 LFM image of DDA on mica [251].

They interpreted this as weak-binding between the DDA molecules and mica substrate and developed a diffusion model shown in Figure 2-27. For a strong surface binding, the diffusion was dominated by surface binding event. In contrast, for the case of weak surface binding, the diffusion was determined by interaction between molecules, so the lateral diffusion was probably isotropic or anisotropic. Furthermore, DDA molecules crystallize rapidly on a mica surface, the formed crystalline impede the diffusion of DDA molecules arrived later, so the pattern was more anisotropic at long deposition time.

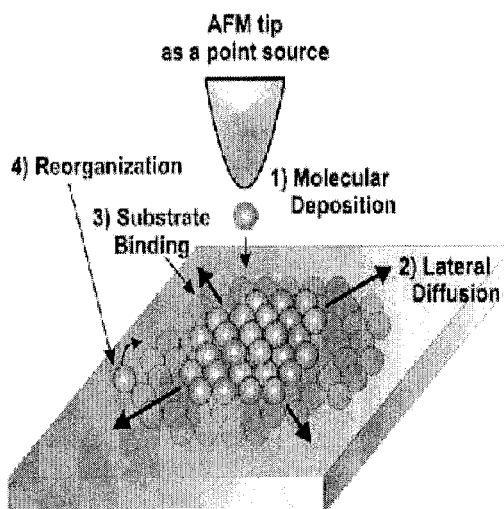


Fig.2-27 DPN process with a weak surface binding [251].

In summary, DPN has been demonstrated to be a promising nanolithography which has potential applications in the fabrication of electric and optic device, sensors and actuators at nanometer scale. However, it is still at an early and experimental stage. Many works both in fundamental and applied research are required in order to develop and commercialize DPN.

Chapter 3 Fabrication of Ferroelectric Micro- to Nanostructures via Dip-pen Nanolithography

3.1 Introduction

As described in Chapter 2, dip-pen nanolithography (DPN) has been used to fabricate micro- and nanostructures with various materials, such as biomolecules [209-232], polymers [199-204], inorganic salts [237-239], metal nanoclusters [236] as well as magnetic materials [233-235]. However, DPN on ferroelectric polymers has not been reported.

Polymers with ferroelectric properties are an important class of functional materials with potential applications in electrical, optical, biomedical, robotic, and sensing devices. Typical ferroelectric polymers contain polyvinylidenedifluoride (PVDF) and its related copolymers and derivatives. Among the known ferroelectric polymers, poly(vinylidene fluoride-trifluoroethylene [P(VDF-TrFE)] shows the highest ferroelectric polarization and electromechanical response; therefore, it is widely used as acoustic sensors and transducers with a thickness of several to tens of microns [252-254]. Thin films of P(VDF-TrFE) is helpful in the investigation of the ferroelectric phenomena in low-dimension system. Furthermore, thin films have potential applications in optical, electronic, and sensing technologies.

The conventional methods to prepare thin films of P(VDF-TrFE) are spin coating and Langmuir-Blodgett Monolayer Transfer Technique (Figure 3-1). Spin coating is used to coat the wafer with material which is originally in the liquid form. The liquid is dispensed onto the wafer surface in predetermined amount and the wafer is rapidly rotated (up to 6000 rpm). During spinning the liquid is uniformly distributed on the surface by centrifugal forces, and the material is then solidified when baked at low temperature (typically <200 °C). However, spin coating is suitable for preparing thin films with a thickness of tens to several hundreds of nanometers, but not suitable for controlling the nanostructure scale. Langmuir-Blodgett monolayer transfer technique is used to deposit an insoluble spread monolayer of atoms or molecules floating at the gas/liquid interface onto a solid substrate by successively dipping a solid substrate up and down through the monolayer, while simultaneously keeping the molecular density or surface pressure constant by a computer controlled feedback system between the electrobalance measuring the surface pressure and a barrier moving mechanism controlling the available area for the monolayer molecules. Consequently, the floating monolayer with precisely controlled properties is adsorbed to the solid substrate. In this way multilayer structures of hundreds of layers can be produced. However, Langmuir-Blodgett monolayer transfer technique can only control the film thickness to a nanometer-scale. It is difficult to control the lateral direction to a nanometer-scale. In this project, we propose DPN to prepare thin film of P(VDF-TrFE). DPN utilizes a coated AFM tip to deposit chemicals to a substrate of interest. DPN has the advantages to control the pattern to a nanometer scale in both spatial and lateral directions. Therefore, DPN is

Fabrication of Ferroelectric Micro- to Nano-structures via DPN

selected to construct micro- and nanostructures composed of the ferroelectric polymer, P(VDF-TrFE).

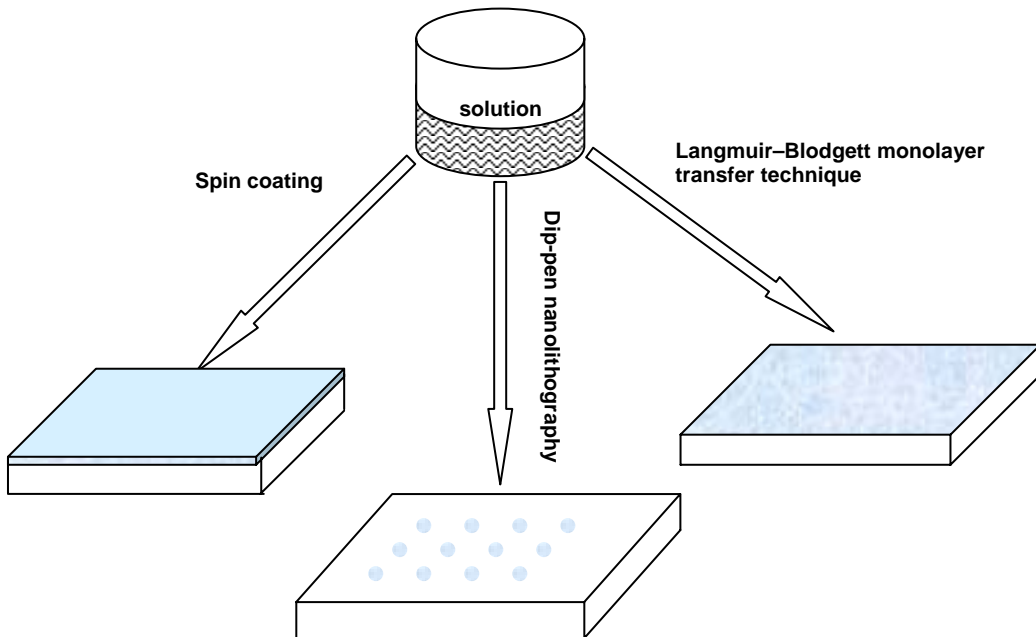


Fig.3-1 Schematic diagram of the methods for the preparation of thin film of P(VDF-TrFE).

3.2 Experimental

P(VDF-TrFE 80:20) with a mole ration of 80/20 for VDF/TrFE was purchased from Piezotech SA, France while acetone (99.5%) was purchased from Ajax Finechem. The two chemicals were used as received.

Contact “golden” silicon cantilevers (CSG11) were purchased from NT-MDT, Russia. The typical spring constant, tip curvature radius and resonance frequency of the contact silicon cantilever was about 0.03 N/m, 10 nm and 10 kHz (provided by the supplier), respectively.

DPN patterning and pattern imaging were conducted using a commercial AFM (Solver P47H, NT-MDT, Russia). A field emission scanning electron microscope (FE-SEM) (JSM-6335F field emission SEM by JEOL, Japan) was used to visualize the AFM tip. Sputtering was conducted using ExplorerTM 14 Denton Vacuum, U.S.A, and X-ray photoelectron spectroscopy (XPS) was measured with Physical Electronics PHI 5600, U.S.A.

3.3 Results and Discussion

3.3.1 Examination of Coated Tip with FE-SEM

The ink solution was prepared as follows: 3.6 mg of P(VDF-TrFE) was dissolved in 5 ml acetone, stirred for 5 minutes to obtain a clear solution, and sealed until it was to be used.

In DPN, the cantilever should be soft enough to avoid the likelihood of scratching the substrate surface. Therefore, very soft cantilevers, CSG11, were used for DPN patterning and AFM imaging. The CSG11 tip was coated by dipping the cantilever in the ink solution for 1 minute, and was dried in air.

Fabrication of Ferroelectric Micro- to Nano-structures via DPN

Acetone is a volatile solvent, hence, P(VDF-TrFE) remained on the cantilever surface after the volatilization of the acetone.

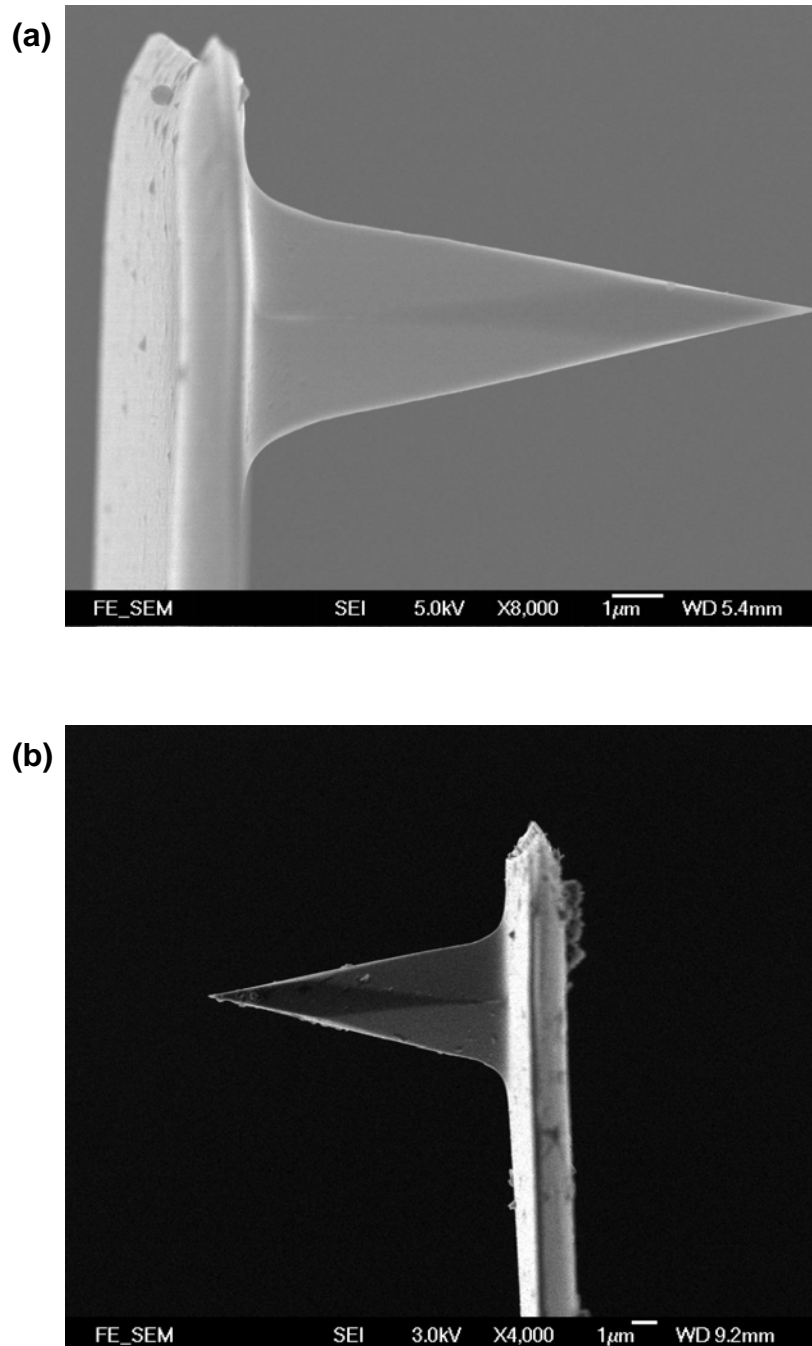


Fig.3-2 FE-SEM micrographs of the AFM before (a) and after (b) coated with P(VDF-TrFE).

The tip was visualized with a field emission scanning electron microscopy at 9.6×10^{-5} Pa. Figure 3-2 shows the comparison of the FE-SEM micrographs of the tip before and after coating with P(VDF-TrFE). For a new Si tip, it is clean (Figure 3-2a). After coating, the surface was covered with a thin film of P(VDF-TrFE) (Figure 3-2b). This demonstrates that we can use the coated silicon tip for DPN.

3.3.2 Fabrication of Micro- to Nano-patterns on Gold Substrate with P(VDF-TrFE) Coated AFM Tip

The polycrystalline gold substrate is prepared by sputtering a layer of 30 nm gold on top of n-doped Si (100) wafer covered with silicon oxide with a thickness of 40 nm (measured via ellipsometry) with a titanium adhesion layer of 10 nm. Figures 3-3a and 3-3b show the surface topography and lateral force microscopy (LFM) images of the gold substrate. LFM measures the frictional forces on a surface. By measuring the “twist” of the cantilever,

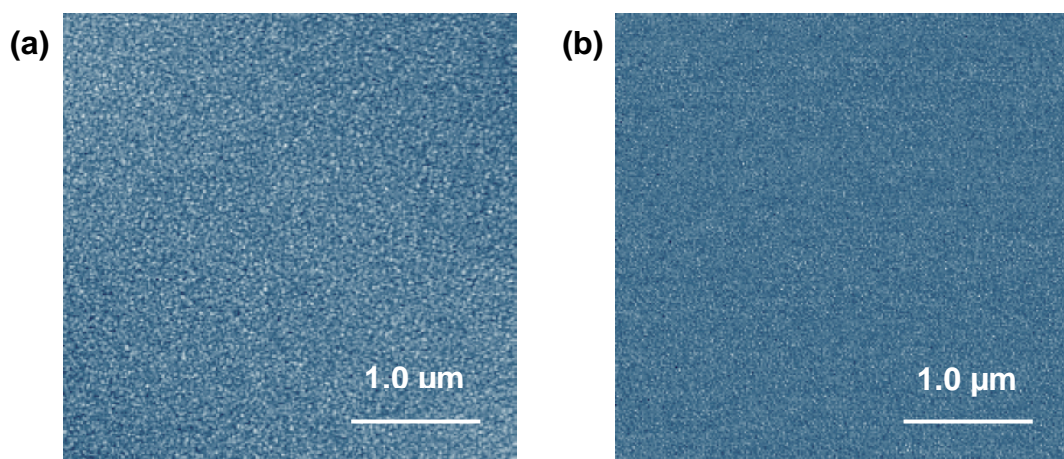


Fig.3-3 Topographic (a) and lateral force microscopy (b) images of the polycrystalline gold.

rather than merely its deflection, areas of higher and lower friction can be qualitatively determined. Both images are uniform. The roughness of the polycrystalline gold film surface is about 0.6 nm.

DPN patterning was operated in contact mode with a contact force of 2.0 nN. The fabricated patterns are viewed via topographic images as well as lateral force microscopy images. Figure 3-4 illustrates micro- and nano-patterns of P(VDF-TrFE) on gold substrate fabricated via DPN. Figure 3-4a is the topographic image written at a different contact time. The areas covered with P(VDF-TrFE) exhibit brighter contrast, which means these areas are higher than the neighboring areas. P(VDF-TrFE) cannot be clearly seen in topographic image for short contact time, e.g., one and two minute(s) in Figure 3-4a. However, the lateral force microscopy image (Figure 3-4b) gives black contrast, demonstrating that polymer has been deposited on gold successfully. Increasing the contact time to longer than two minutes, the polymer can be seen in topographic image. For 3-, 4- and 5 minutes duration, the heights of the points are shorter than those points obtained at a longer duration. For a much longer duration (longer than 5 minutes), the polymer patterns have the same height, about 1.0 nm, illustrating uniform P(VDF-TrFE) pattern formed on gold. This result is similar to the formation of Self-Assembled Monolayer (SAM) of thiol on gold. At low concentrations, the alkane chains maximized their interaction with gold surface by lying prone. The thiol molecules did not densely assemble themselves on gold surface resulting in low spatial resolution. When the concentration reaches a critical value, the thiol molecules densely assemble themselves and align on

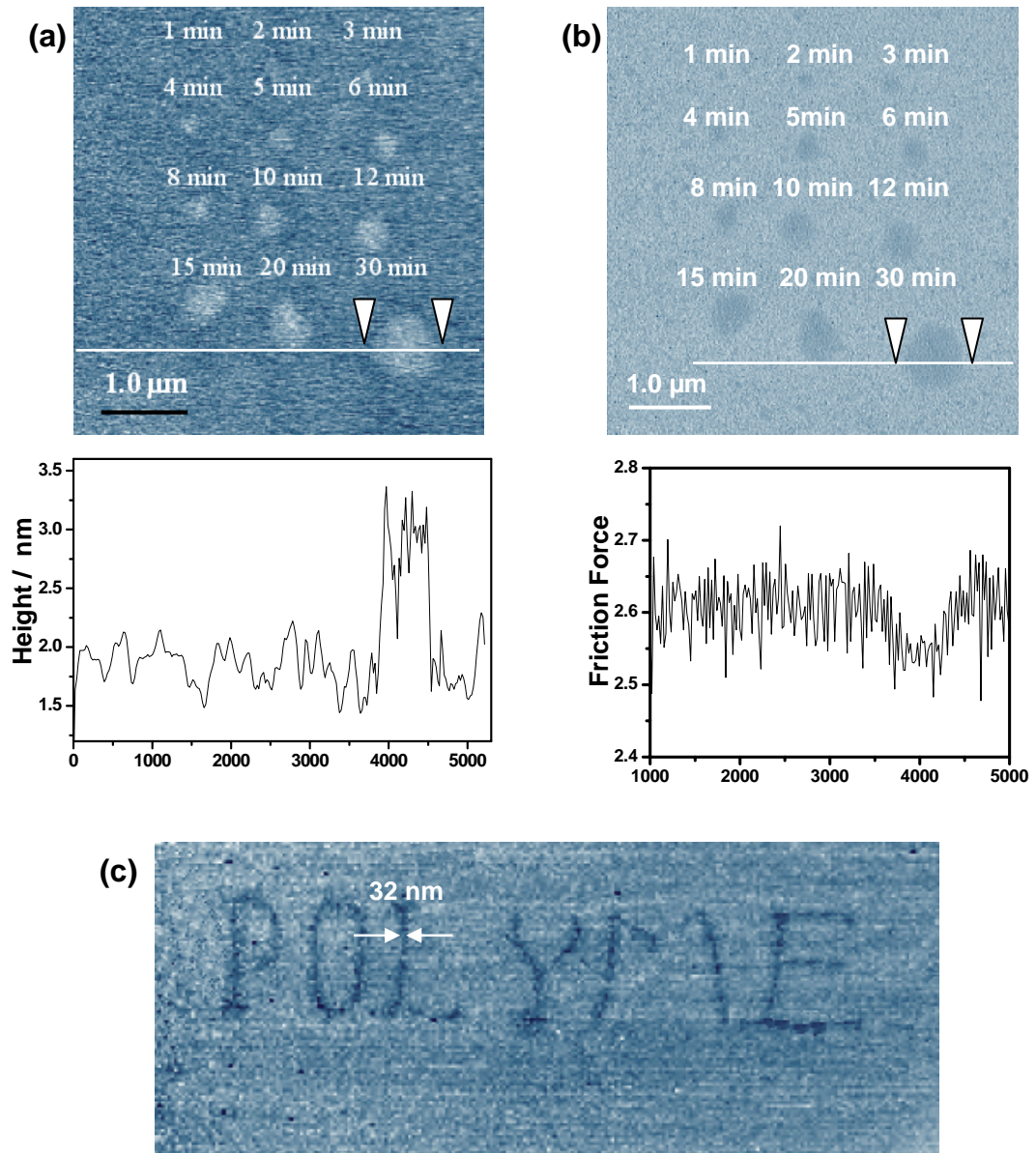


Fig.3-4 Micro and nanopatterns of P(VDF-TrFE) on gold substrate fabricated via DPN at 22°C. (a) Topography of point array written at different contact time at relative humidity of 7%. The contact times for these dots are 1, 2, 3, 4, 5, 6, 8, 10, 12, 15, 20 and 30min, respectively. (b) Lateral force image of the point array obtained simultaneously with (a). (c) Lateral force image of a word "POLYME" written with an AFM tip coated with P(VDF-TrFE) at relative humidity of 64%, writing rate :156 Å/s.

gold surface, forming SAMs [255-257]. Similarly, P(VDF-TrFE) deposited on the gold substrate increases as the contact time increases and then forms patterns with a uniform thickness after a critical concentration (C_r). The density of P(VDF-TrFE) was measured to be 349 kg/m^3 . The dot area was calculated to be 64209 nm^2 when the contact time is 6 minutes. As the thickness is 1 nm, hence the volume of P(VDF-TrFE) was calculated to be 64209 nm^3 . The mass of P(VDF-TrFE) in the pattern was calculated to be $2.24 \times 10^{-17} \text{ g}$. Then surface concentration C_r was calculated to $3.49 \times 10^{-4} \text{ g/m}^2$.

Figure 3-4b shows the corresponding lateral force microscopy (LFM) image obtained at the same time with the topographic image in Figure 3-4a. The P(VDF-TrFE) dark spots created via DPN can be clearly seen. DPN was conducted at 22°C and 7% relative humidity (RH). As compared with the gold substrate, the hydrophobic polymer layer of P(VDF-TrFE) provides a lower friction force to the AFM tip so that a dark contrast appears in the LFM image, giving the same trend as ODT as shown in Figure 2-14b but with a much slower transport rate [194]. The slower transport rate was probably caused by the properties of the polymer and the interaction between the ink and the substrate.

DPN can be used to fabricate arbitrary patterns in addition to dot by controlling the tip motion. Figure 3-4c shows the six letters "POLYME" written with an AFM tip coated with P(VDF-TrFE) at a relative humidity of 64% and writing rate of 156 \AA/s . The line width is about 32 nm, which can be further

reduced by reducing the writing rate during pattern formation or utilizing much sharper tips.

3.3.3 XPS Analysis of DPN-generated P(VDF-TrFE) Patterns

To further prove that the formation of these micro and nanopatterns is caused by the deposition of P(VDF-TrFE) rather than some other contaminants, an additional surface technique, x-ray photoelectron spectroscopy (XPS) was utilized, which was recently used to verify the results of DPN [199]. XPS survey and high resolution scan were collected with Physical Electronics PHI 5600. Figure 3-5a shows the schematic diagram of the sample analyzed by XPS. A rectangular mark was prepared on the silicon wafer covered with thin film of gold. Micrometer-sized patterns of P(VDF-TrFE) were then constructed via DPN within the mark. Finally, XPS analysis focused within the mark to analyze the element contents and the gold valence of the gold surface. Figures 3-5b and 3-5c show the XPS results of the F 1s and Au 4f, respectively. In Figure 3-5b, a weak peak emerged at 687.4 eV, which demonstrates that P(VDF-TrFE) was deposited to gold successfully. Figure 3-5c shows the Au 4f peak. The binding energy (83.7 eV) of gold was almost equal to the binding energy (84.0 eV) at its ground state. It can be concluded that the gold was in the metallic state. This demonstrates that the interaction between the polymer and the gold is Van der Waals' force.

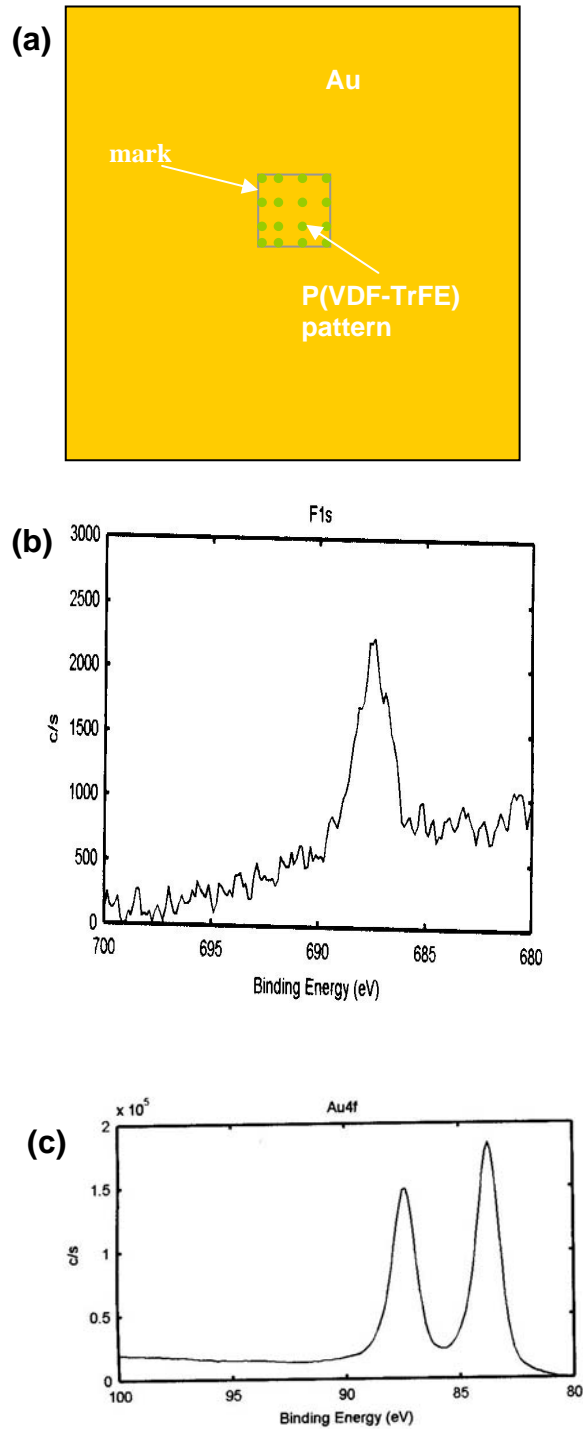


Fig.3-5 (a) Schematic diagram of the sample composed of DPN-generated P(VDF-TrFE) patterns within a mark analyzed with XPS. Results of the XPS for the F 1s (b) and Au 4f (c) spectra of the gold surface patterned with P(VDF-TrFE).

3.3.4 Mechanism of Deposition of P(VDF-TrFE) to Gold

In previous report on DPN, the formation of chemical bonds and electrostatic interaction between the ink and substrate can result in DPN deposition. For example, in the gold (substrate) – thiol (ink) system, there is no doubt that the formation of Au-S covalent bonds is the chemical driving force for the deposition of thiol or thiolated molecules to gold substrate [195,202,211-214], and amine-terminated molecules can be deposited to aldehyde-terminated substrate due to the formation of Schiff base (-C=N-) [215]. In addition to the formation of covalent bond, the electrostatic interaction can also induce the deposition of some charged inks to oppositely charged surface [216]. However, for P(VDF-TrFE)-gold system, no effective chemical bond is formed, and no electrostatic interaction does exist. The deposition of P(VDF-TrFE) to gold via DPN is only due to Van der Waals' interaction between gold and P(VDF-TrFE) molecules. This demonstrates that formation of chemical bond or electrostatic interaction is not the sole requirement for DPN. It is well known that gold easily adsorbs gas, water and other chemicals to its surface, especially in this condition that all the gold particles are at a nanometer scale, which is very active to absorb other chemicals either through physical or chemical interaction. Therefore, most of DPN works utilized gold, as the substrate. Most of all, the gold must be fresh. DPN cannot be realized after the gold exposed to air for more than 60 hours.

3.3.5 Detection of Ferroelectric Properties in DPN-generated P(VDF-TrFE) Patterns

As described above, P(VDF-TrFE) in the DPN-generated patterns is in its molecular state without formation of covalent bond or electrostatic interaction with the gold. Does it have ferroelectricity? This is the key issue for the fabrication of optical/electronic nanodevices and nanosensors. The ferroelectric response is detected with AFM. A varied DC voltage was applied between a conductive AFM tip and the DPN-generated P(VDF-TrFE) pattern to detect the ferroelectric response. A circle was drawn by varying the voltage linearly from -10 V to $+10$ V anti-clockwise from point A, and as shown in Figure 3-6a, an asymmetric polarization was obtained. When a positive voltage was applied on the tip, there was no apparent change on the sample, while a negative voltage produced a protruded pattern on the surface. The greater the applied voltage is, the higher the protrusion is obtained. Figure 3-6b shows the same pattern after one hour, demonstrating that the protruded pattern slowly returned to its original state.

Asymmetric phenomena have been observed by other researchers on very thin P(VDF-TrFE) films. Bune and coworkers [258-261] observed an asymmetric pyroelectricity in ultrathin ferroelectric Langmuir-Blodgett-deposited polymer films on an Al-coated glass. They found that the bistable switching of polarization became monostable when the thicknesses of the films were decreased below 15 monolayers (ML). Chen and coworkers [262] also obtained the asymmetric piezoelectricity when they polarized thin P(VDF-TrFE) films (with thickness about 20 nm) on graphite. However,

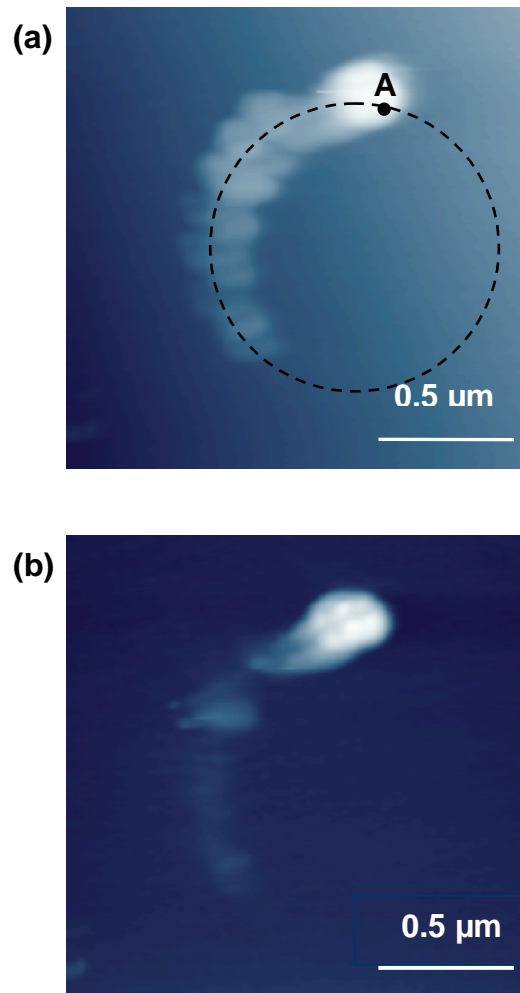


Fig.3-6 The topography image obtained after applying a linearly varied DC voltage from -10V to +10V (between a conductive AFM tip and the sample) to draw a circle from point A counter-clockwise in (a). There was no apparent change in the sample when a positive voltage was applied, while a negative voltage produced a protruded pattern on the surface. The greater the voltage applied, the higher the protrusion obtained. The protruded pattern slowly returned to its original state after a certain time; (b) is the image of the same area after one hour.

symmetric piezoelectricity was obtained on thick film (60 nm in thickness). They believed that this was caused by the substrate induced orientation. A layer of the polymer is oriented at the interface of substrate and polymer layer leading to a significant dipole moment at this interface. From the direction of the dipole, they inferred that this orientation has the hydrogen oriented towards the substrate and the fluorine away.

The P(VDF-TrFE) molecules were oriented on the gold during DPN process and form patterns with the same thickness of about 1 nm after a critical concentration. The thickness of one layer of P(VDF-TrFE) was 0.5 nm [261], hence the P(VDF-TrFE) patterns constructed via DPN should be two layers. Similarly, P(VDF-TrFE) molecules in these DPN-generated patterns were highly oriented on gold substrate due to the substrate effect. From the polarization result, the positive part of the P(VDF-TrFE) came into contact with gold, while the negative part was positioned away from the gold. Therefore, a net dipole moment pointing from the upper part to the gold was formed. A schematic diagram showing the uniform orientation of the P(VDF-TrFE) on the gold is illustrated in Figure 3-7a. This implies that the structures of the P(VDF-TrFE) constructed via DPN possess ferroelectric properties. Though some researchers thought that ferroelectric polymer would lose ferroelectricity with a thin thickness. Bune and colleague [261] detected the polarization hysteresis loop of P(VDF-TrFE 70:30) [2 ML thick] at 25°C, as shown in Figure 3-7b. Saturation for the 2-ML film was incomplete; however, the ferroelectric switching was obtained, demonstrating that the 2-ML film of P(VDF-TrFE) still possessed ferroelectric property.

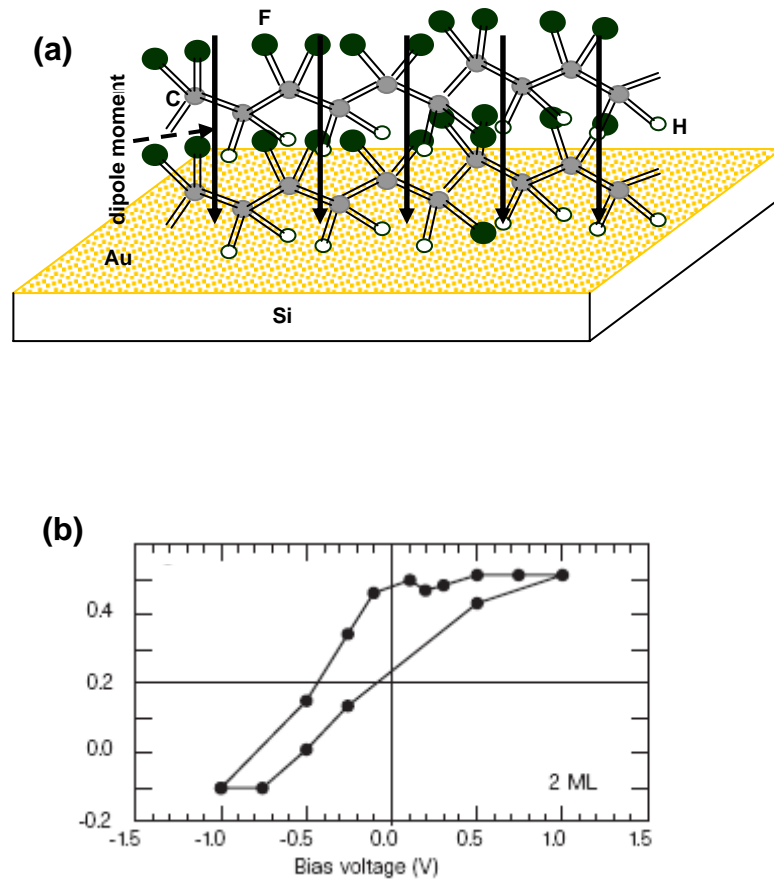


Fig.3-7 (a) Schematic diagram of the orientation of P(VDF-TrFE) on gold. The positive part of the P(VDF-TrFE) contact with gold, while the negative part is positioned far from the gold. Therefore, a net dipole moment pointing from the upper part to the gold is formed. (b) Polarization hysteresis loop of the P(VDF-TrFE 70:30) 2 monolayers at 25°C measured by Bune et al's [259].

3.3.6 Kinetics of Diffusion of P(VDF-TrFE) on Gold

In DPN, there are two steps. The first step is the deposition of the ink to the substrate surface, and the second is ink diffuses on the substrate surface

and forms patterns. It is difficult to visualize the first step; therefore, researchers always utilize the results which are obtained from the second step to assume that the process occurring in the first step [245] or even neglect the first step by assuming the tip as an ink source without depletion during pattern formation [249]. Here the kinetics is studied by adopting the later method, i.e., neglecting the first step.

Figure 3-8a-e are lateral force microscopy images of P(VDF-TrFE) points array at 25°C for 60 s (a), 120 s (b), 180 s (c), 240 s(d), and 300 s (e), respectively. The tests were repeated for five times at the same temperature, relative humidity and with the same ink but with five independent tips and substrates. The averaged data was used to do scaling analysis, and the standard deviations were illustrated as the error bars. Figure 3-8 f shows the curve of dot radius (r) as a function of contact time (t), and the curve of dot area (A) as a function of contact time (t). It is found that $r \propto t^{1/2}$ and $A \propto t$.

Figures 3-9a and 3-9b show the lateral force images of lines written with an AFM tip coated with P(VDF-TrFE) at 25°C and relative humidity of 64%. Figure 3-9c shows the line width (W) versus inverse rate (v^{-1}), and the curve of $W^2 \sim v^{-1}$. Similarly, the data was average from five independent measurements. The error bars in Figures 3-9c are standard deviations. The same trend as for dots pattern was obtained, i. e, $W \propto v^{-1/2}$ and $W^2 \propto v^{-1}$

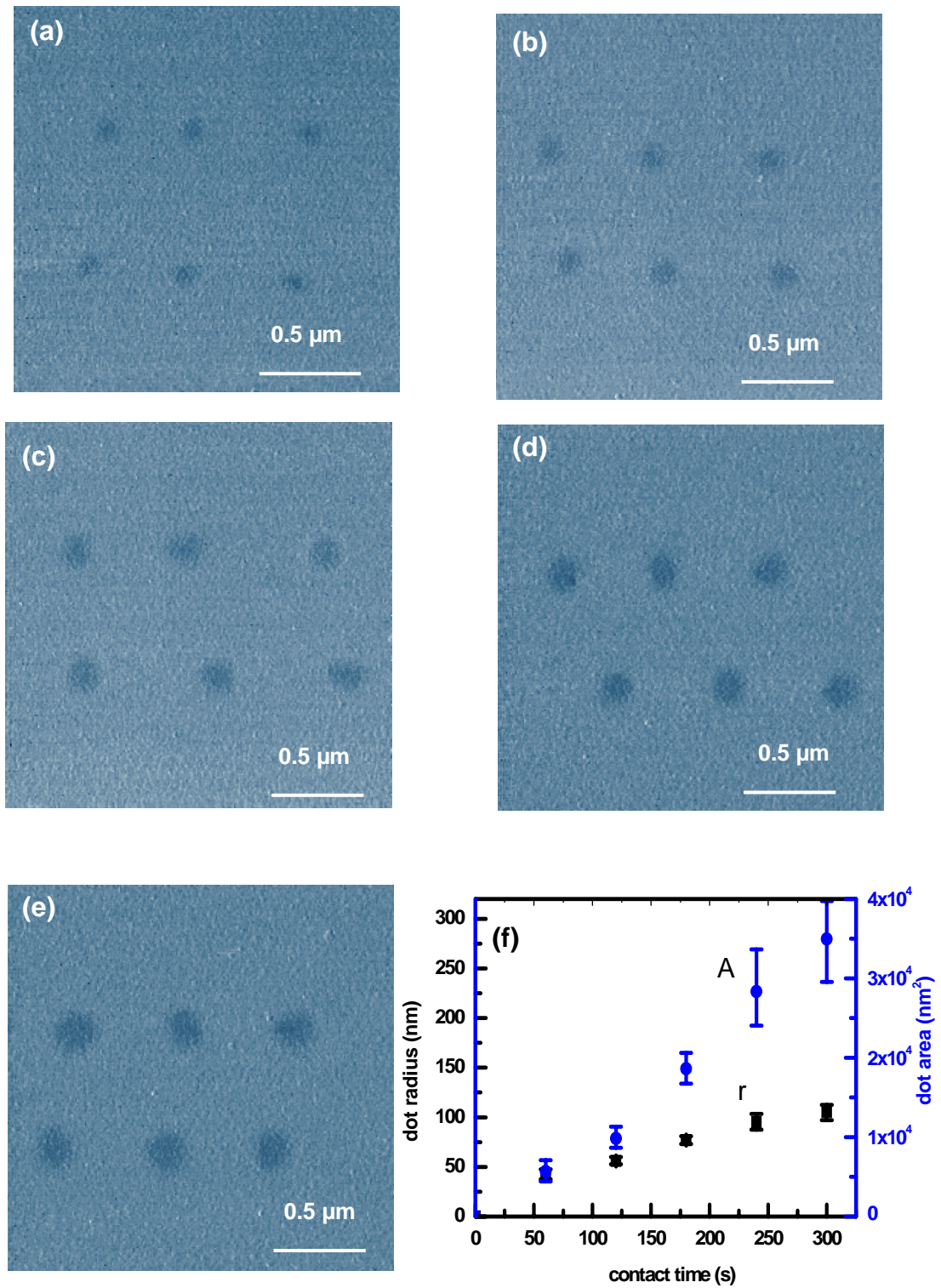


Fig.3-8 Lateral force images of P(VDF-TrFE) points array at 25°C and relative humidity of 64% for 60 s (a), 120 s (b), 180 s (c), 240 s (d) and 300 s (e) respectively. (f) is the curve of dot radius and dot area as a function of

Fabrication of Ferroelectric Micro- to Nano-structures via DPN

contact time averaged from five independent measurements. The error bars are standard deviations.

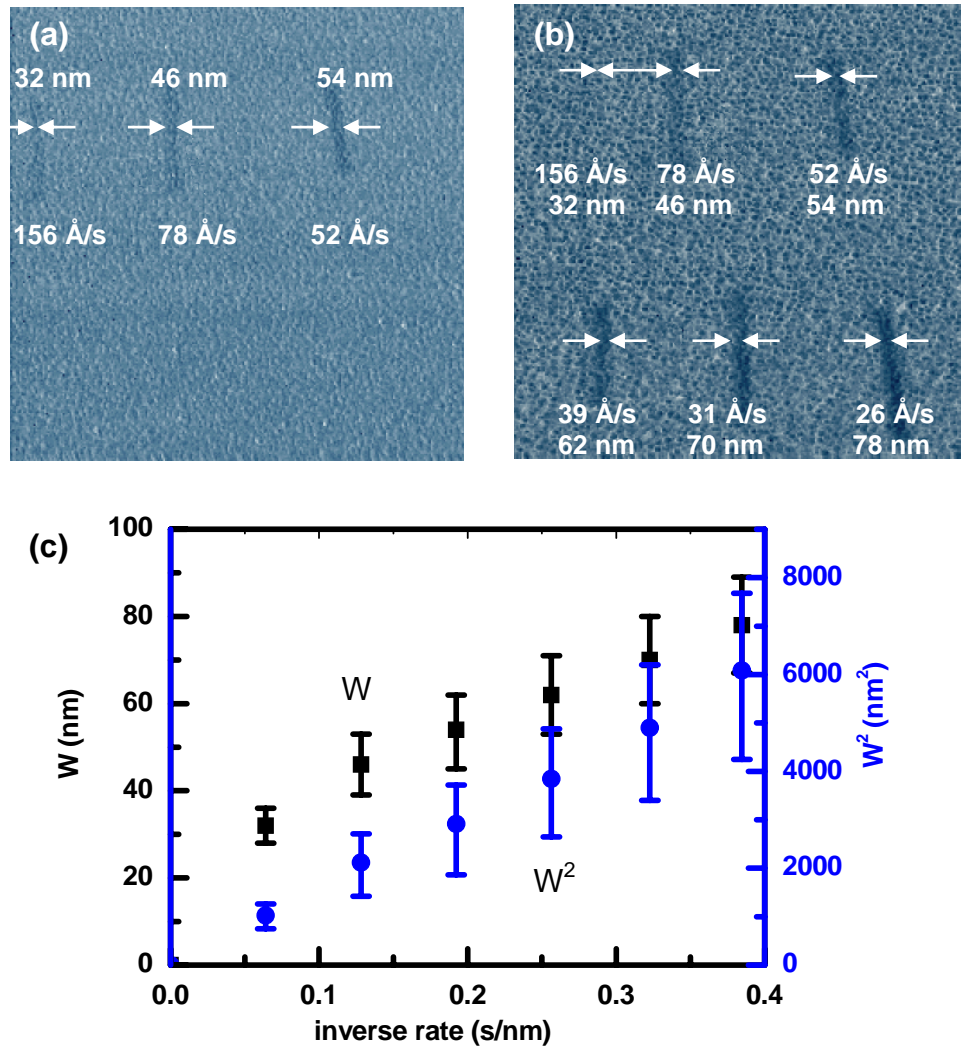


Fig.3-9 Lateral force images of three lines (a) and six lines (b) written with an AFM tip coated with P(VDF-TrFE) at 25°C, relative humidity of 64%. Panel (c) is line width (W) \sim inverse rate (ν^{-1}) and $W^2 \sim \nu^{-1}$. The error bars are standard deviations.

Fabrication of Ferroelectric Micro- to Nano-structures via DPN

As stated above, P(VDF-TrFE) forms patterns on gold with uniform thickness after a critical concentration. It can be deduced that m (mass of polymer deposited on gold) was proportional to contact time. The tip coated with P(VDF-TrFE) can be thought of as a point source providing P(VDF-TrFE) without depletion during the DPN process. A simplified diffusion model adopting Fick's first law to two dimensions was used to derive the relationship between dot radius and contact time. It was assumed:

(1) The tip could provide sufficient P(VDF-TrFE) molecules for surface diffusion, and could model the AFM tip as a point source. P(VDF-TrFE) molecules diffuse radially from the AFM tip.

(2) DPN process was controlled by P(VDF-TrFE) molecules diffusion on the gold surface. Diffusion coefficient (D) at a constant temperature was assumed as a constant.

(3) C_0 was the concentration of P(VDF-TrFE) at the contact point where $r = 0$ when $t = 0$.

(4) C_r was the concentration of P(VDF-TrFE) at a distance of r from the contact point.

(5) The concentration was symmetrical with respect to $r = 0$, tends to 0 when $r \rightarrow \infty$ for $t > 0$.

(6) The concentration gradient was the driving force for the P(VDF-TrFE) molecules diffusion.

Figure 3-10 shows the schematic illustration of this process modified from Schwartz's mathematical model [247]. O was the contact point between the tip and gold substrate.

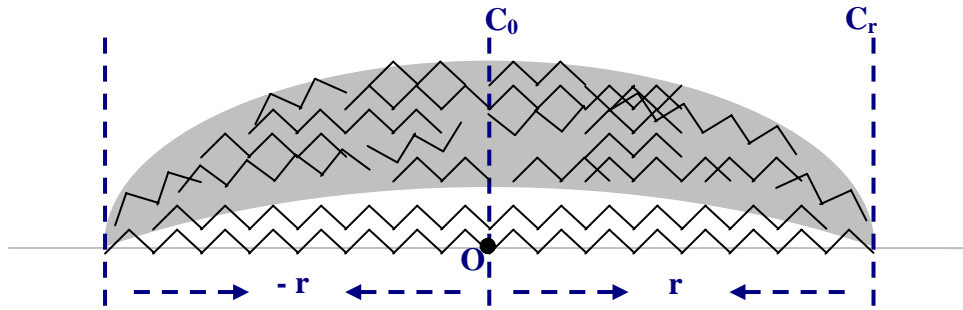


Fig.3-10 The schematic plot of the DPN process with P(VDF-TrFE) ink. O is the contact point between the tip and the gold substrate, and C_0 is the concentration of P(VDF-TrFE) at point O. C_r is the concentration of P(VDF-TrFE) at a distance of r from O. The concentration is symmetrical with respect to $r = 0$, tends to zero when $r \rightarrow \infty$ for $t > 0$. The concentration gradient is the driving force for the P(VDF-TrFE) molecules diffusion.

Fick's first law to two dimensions for a point source was adopted. The molecular flux (F) can be expressed in this equation:

$$F = -2\pi D r \frac{dC}{dr} \quad (3-1)$$

where C is surface concentration of P(VDF-TrFE).

P(VDF-TrFE) formed micro- to nanostructures on gold with uniform thickness, obviously, the P(VDF-TrFE) molecule density (ρ) on gold surface was a constant. F can be also expressed in this equation:

$$F = \rho \frac{dA}{dt} = \rho \frac{2\pi r dr}{dt} \quad (3-2)$$

Then

$$F = 2\pi Dr \frac{dC}{dr} = \rho \frac{2\pi r dr}{dt} \quad (3-3)$$

$$\int_{C_0}^{C_r} dC \int_0^t dt = \int_0^r dr \int_0^r dr \quad (3-4)$$

$$\frac{D(C_0 - C_r)}{\rho} t = r^2 / 2 \quad (3-5)$$

Then the relationship between r and t can be expressed in equation (3-4)

$$r = \sqrt{\frac{2D}{\rho}(C_0 - C_r)t} \quad (3-6)$$

Dot radius r is proportional to $t^{1/2}$.

By fitting to the data obtained at 25°C and a relative humidity of 64% for a P(VDF-TrFE) coated silicon tip, the following relationship can be obtained:

$$r \approx 6.11t^{1/2} \quad (3-7)$$

The unit for r and t is nm and s, respectively.

3.4 Summary

In summary, the following results have been obtained:

- For the first time, the micro- and nanostructures of a ferroelectric polymer, P(VDF-TrFE), were constructed via DPN onto the gold substrate. In LFM images, the hydrophobic polymer produced a black contrast. The thickness of the DPN-generated P(VDF-TrFE) patterns was about 1 nm when the surface concentration $C_r \geq 3.49 \times 10^{-4} \text{ g/m}^2$. Lines as thin as 32 nm and dot radius as small as 20 nm have been obtained.
- The P(VDF-TrFE) molecules in the DPN-generated patterns were well oriented on the gold substrate due to the substrate effect and showed asymmetric properties. It thus held ferroelectric properties. This provides potential new opportunities for nanostructured sensor applications.
- The interaction between the P(VDF-TrFE) and the gold substrate was Van der Waals' interaction rather than electrostatic interaction or the formation of covalent bond.
- The growth rate of dot radii/line-width was proportional to $t^{1/2}$. A simplified diffusion model adopting Fick's first law to two dimensions for a point source was proposed, and $r = \sqrt{\frac{2D}{\rho}(C_0 - C_r)t}$ has been obtained.

Chapter 4 Effects of Experimental Conditions on Dip-pen Nanolithography

4.1 Introduction

Dip-pen nanolithography (DPN) has been demonstrated to be a promising candidate in the manufacturing of biosensor, electrical, optical, and mechanical nanodevices. In addition, the rate and quality of DPN can be affected by many parameters, such as temperature, surface property of the substrate, relative humidity, tip size, and tip components, as well as chemical affinity between the ink and the substrate. Thus, there is a great significance to study the effects of experimental conditions on DPN for good control of the transport rate of inks and quality of patterns or design of a new ink-substrate system.

The influence of temperature on DPN was studied by changing the substrate temperature and keeping the other experimental conditions constant while measuring the relationship between the pattern growth rate and the substrate temperature.

The influence of substrate surface roughness was studied by preparing a series of gold thin films with different roughness that were used as the DPN substrate and using P(VDF-TrFE) and ODT as the DPN inks and similarly keeping the other experimental conditions constant while measuring the

Effects of Experimental Conditions on Dip-pen Nanolithography

relationship between the pattern growth rate and the substrate surface roughness.

The influence of relative humidity was also studied by changing the relative humidity in the DPN system and keeping the other experimental conditions constant while measuring the relationship between the pattern growth rate and relative humidity.

Commercial AFM tips with the same material and force constant but with different tip size could not be obtained. Hence, the influence of tip size was studied by assuming the three types of tips which have the same component of silicon but with different tip sizes (the curvature radius of the three types of tips are 10 nm, 20 nm, and 50 nm, respectively), while calculating the contact radius at ambient conditions (25°C and 50% relative humidity), or when there was no meniscus formed. The influence of tip material was studied by utilizing three types of tips which were composed of Si, Si₃N₄ and Au with curvature radius of 10 nm, 20 nm, and 50 nm, respectively and using ODT and P(VDF-TrFE) as the DPN inks and gold as DPN substrate while measuring the growth rate of pattern as a function of tip materials after deducting the effect of tip size.

The influence of chemical affinity was studied by controlling the ink affinity to the tip and the substrate through the selection of tips (Si, Si₃N₄ and Au), inks (ODT and P(VDF-TrFE)) and substrate (Au, Ag, Pt) materials while measuring the growth rate of ink as a function of chemical affinity.

4.2 Effect of Temperature

4.2.1 Experimental

The gold substrate was placed on a heating stage, and the temperature of the substrate was measured with a thermocouple with an accuracy of ± 1.0 °C (It's difficult to measure the temperature at the AFM tip). At each testing condition, the substrate was first raised to the desired temperature and stabilized for two hours. Then DPN was conducted.

The DSC thermogram was measured in a temperature range of between 30 and 200°C at a heating rate of 10°C min⁻¹ under a nitrogen atmosphere by using a differential scanning calorimeter DSC 7 (Perkin Elmer, U.S.A.).

4.2.2 Results and Discussion

Figures 4-1 to 4-9 show the lateral force images of DPN generated P(VDF-TrFE) patterns and their corresponding scaling analysis at 30°C, 35°C, 40°C, 45°C, 50°C, 55°C, 60°C, 65°C and 70°C, respectively. The results obtained at room temperature (25°C) have been illustrated in Figure 3-8. It is clear that the dot radius strongly depended on the substrate temperature at a constant contact time, and it increased as the temperature increased, i.e., the temperature exhibited a positive effect on the deposition

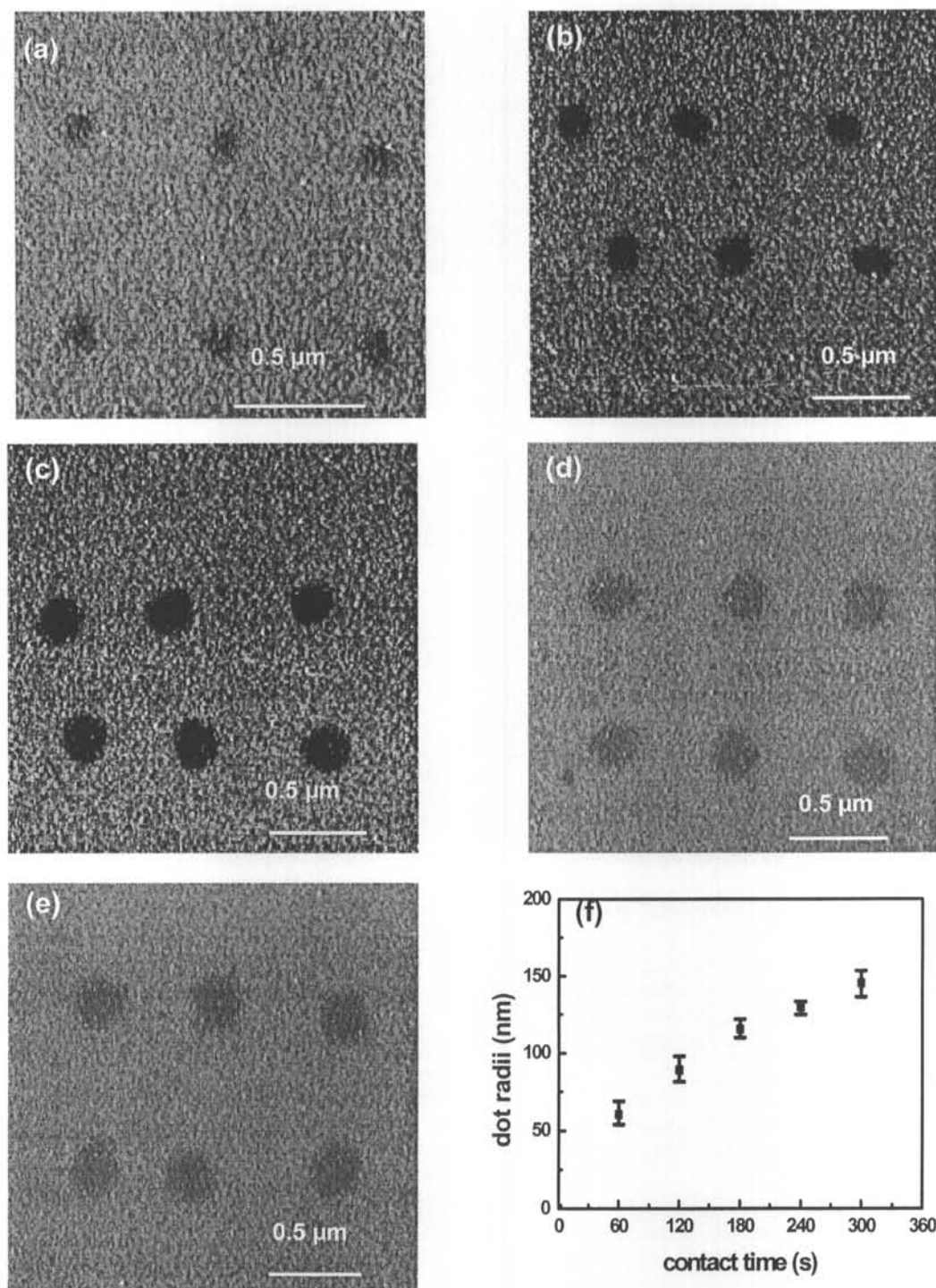


Fig.4-1 Lateral force microscopy images of P(VDF-TrFE) points array at 30°C and relative humidity of 64% for 60 s (a), 120 s (b), 180 s (c), 240 s (d), and 300s (e), respectively, and panel (f) is the curve of dot radius averaged from five independent measurements as a function of contact time. The error bars are standard deviations.

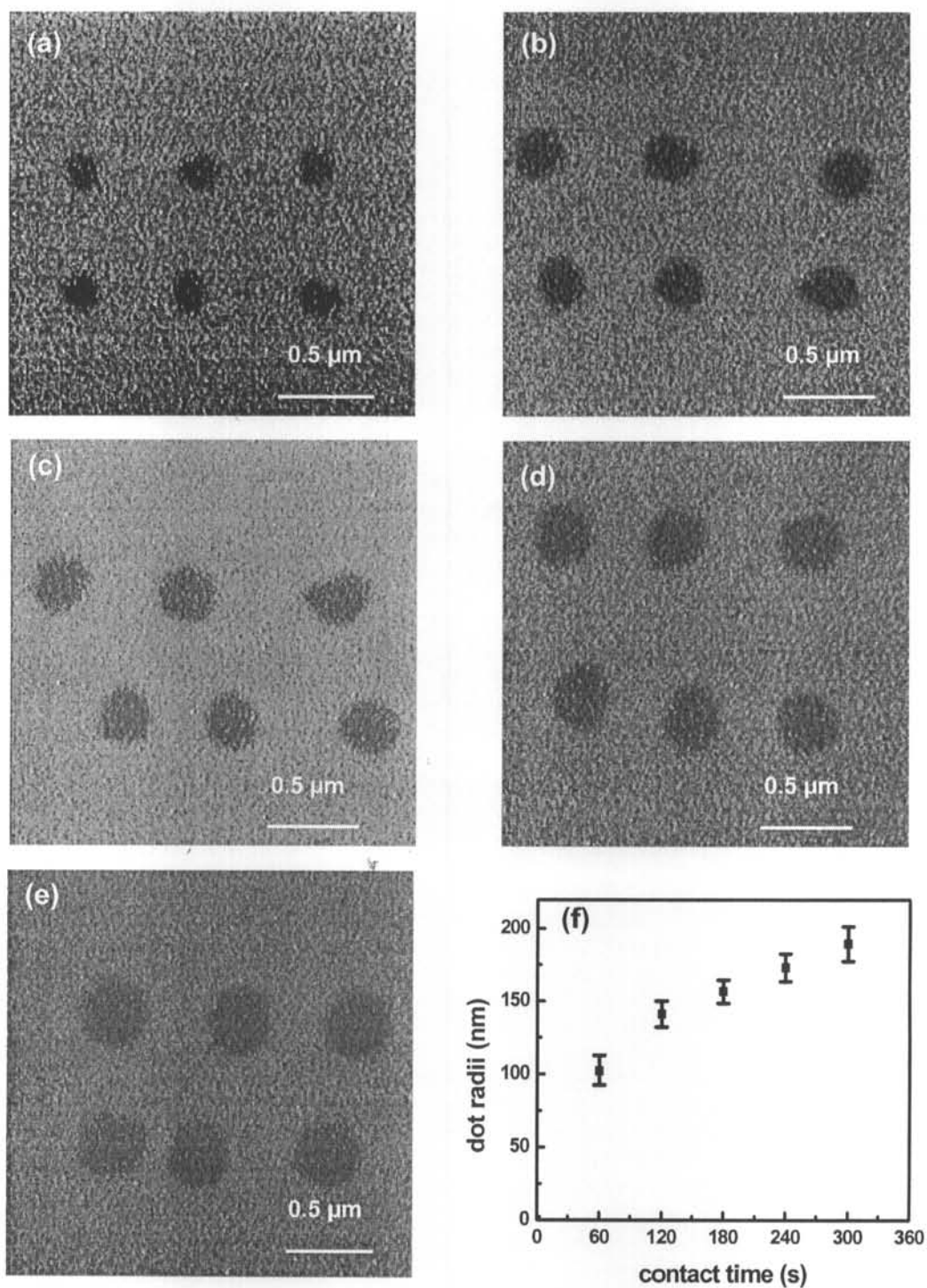


Fig.4-2 Lateral force microscopy images of P(VDF-TrFE) points array at 35°C and relative humidity of 64% for 60 s (a), 120 s (b), 180 s (c), 240 s (d), and 300s (e), respectively, and panel (f) is the curve of dot radius averaged from five independent measurements as a function of contact time. The error bars are standard deviations.

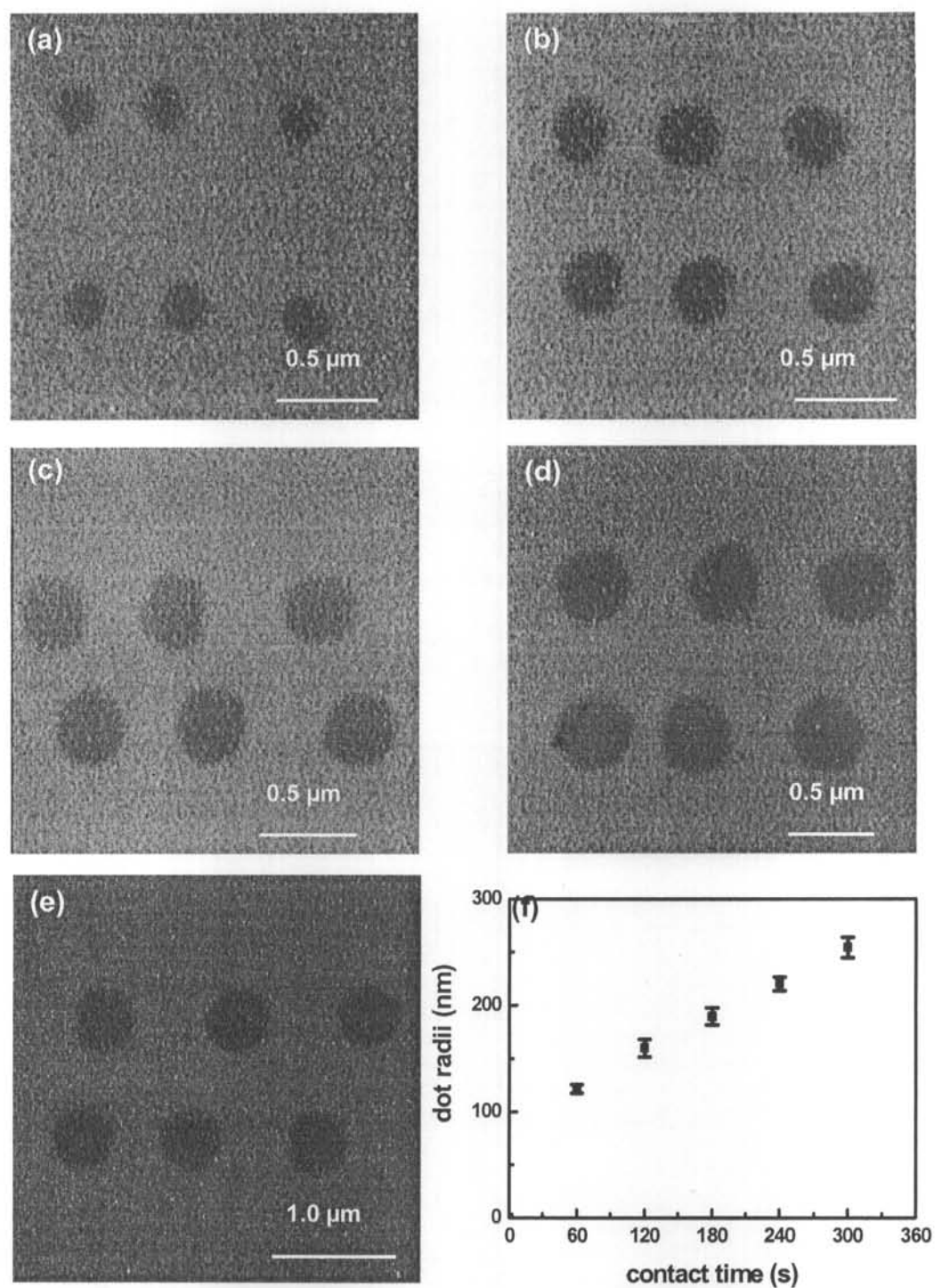


Fig.4-3 Lateral force microscopy images of P(VDF-TrFE) points array at 40°C and relative humidity of 64% for 60 s (a), 120 s (b), 180 s (c), 240 s (d), and 300s (e), respectively, and panel (f) is the curve of dot radius averaged from five independent measurements as a function of contact time. The error bars are standard deviations.

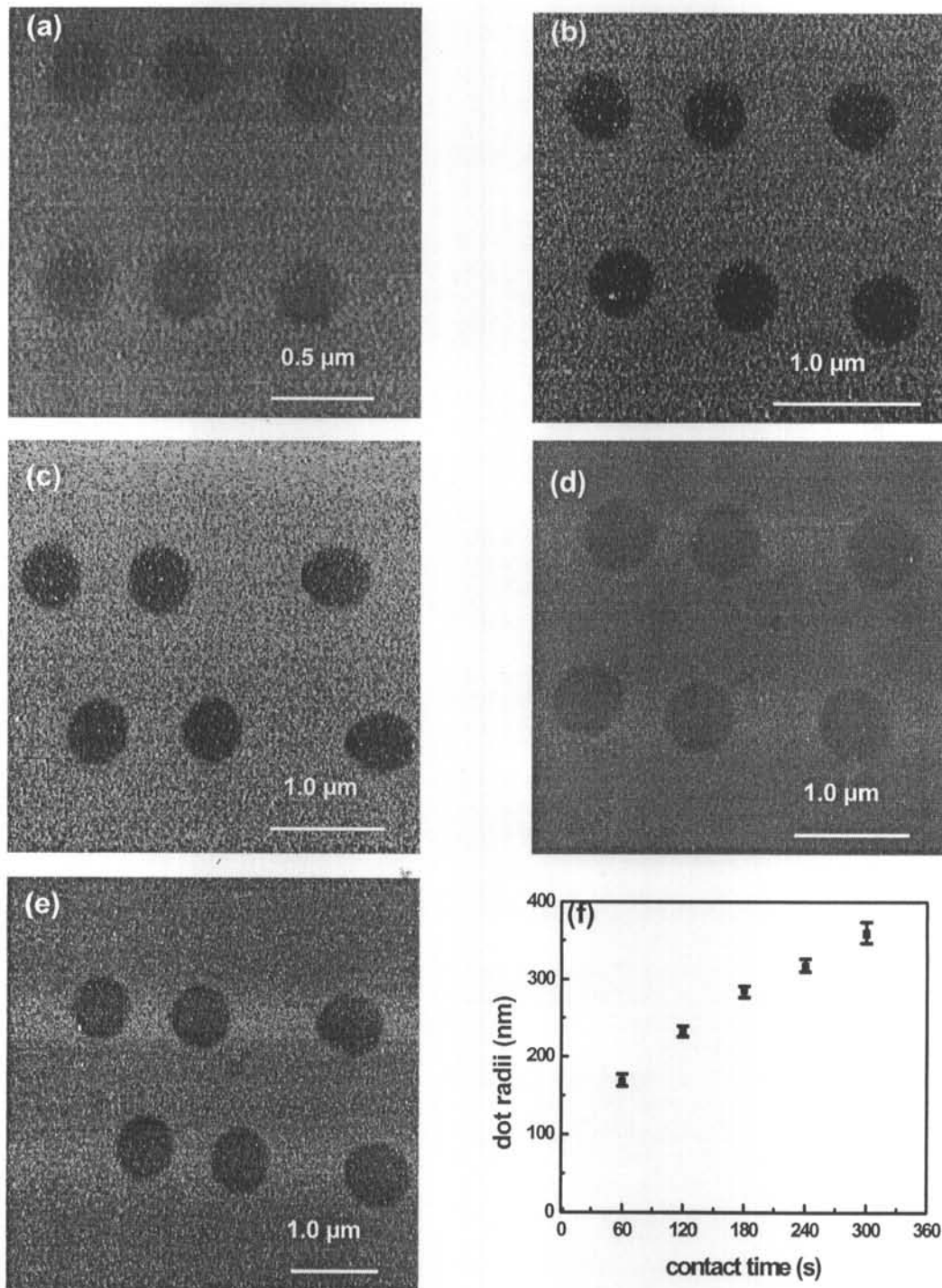


Fig.4-4 Lateral force microscopy images of P(VDF-TrFE) points array at 45°C and relative humidity of 64% for 60 s (a), 120 s (b), 180 s (c), 240 s (d), and 300s (e), respectively, and panel (f) is the curve of dot radius averaged from five independent measurements as a function of contact time. The error bars are standard deviations.

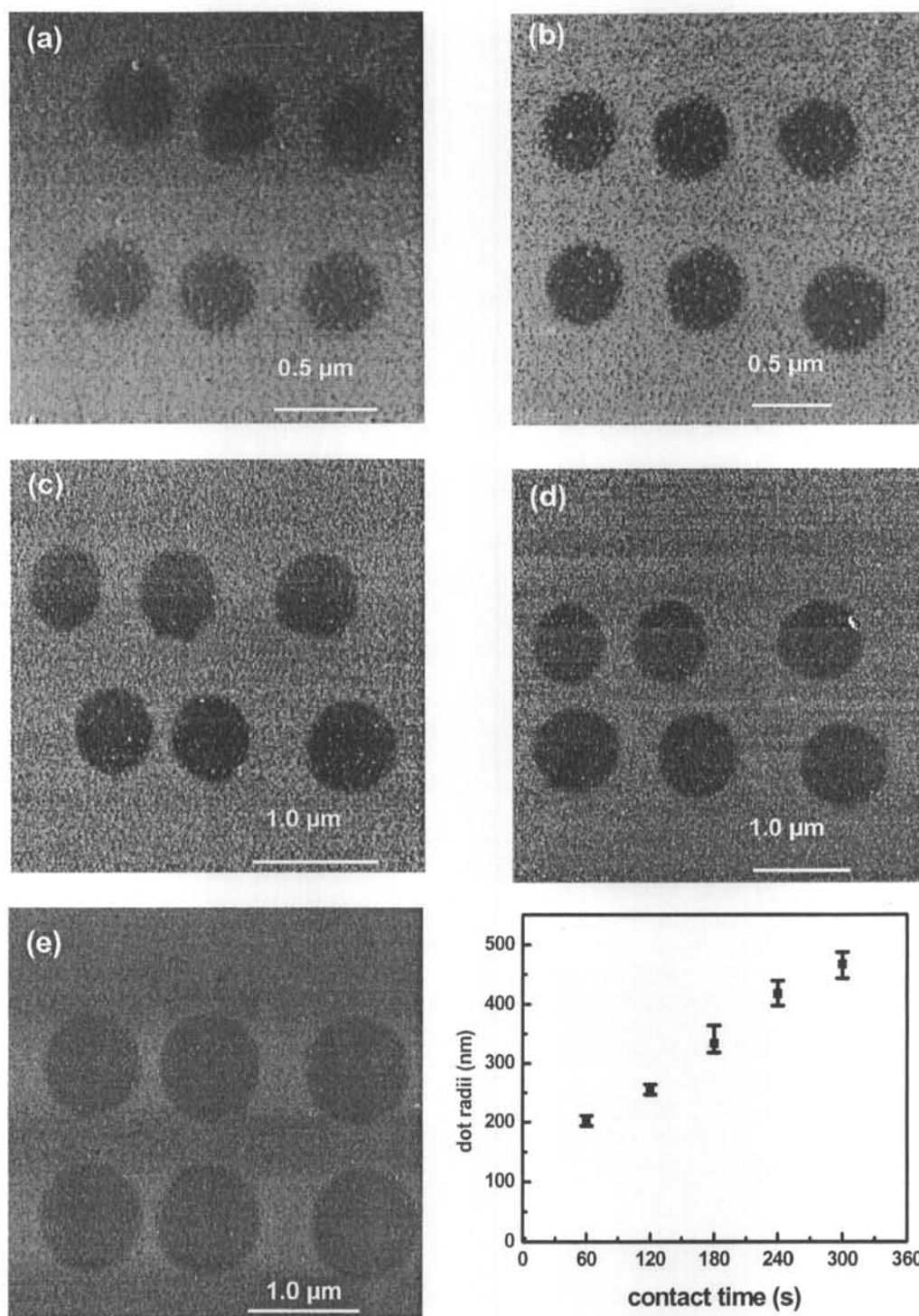


Fig.4-5 Lateral force microscopy images of P(VDF-TrFE) points array at 50°C and relative humidity of 64% for 60 s (a), 120 s (b), 180 s (c), 240 s (d), and 300s (e), respectively, and panel (f) is the curve of dot radius averaged from five independent measurements as a function of contact time. The error bars are standard deviations.

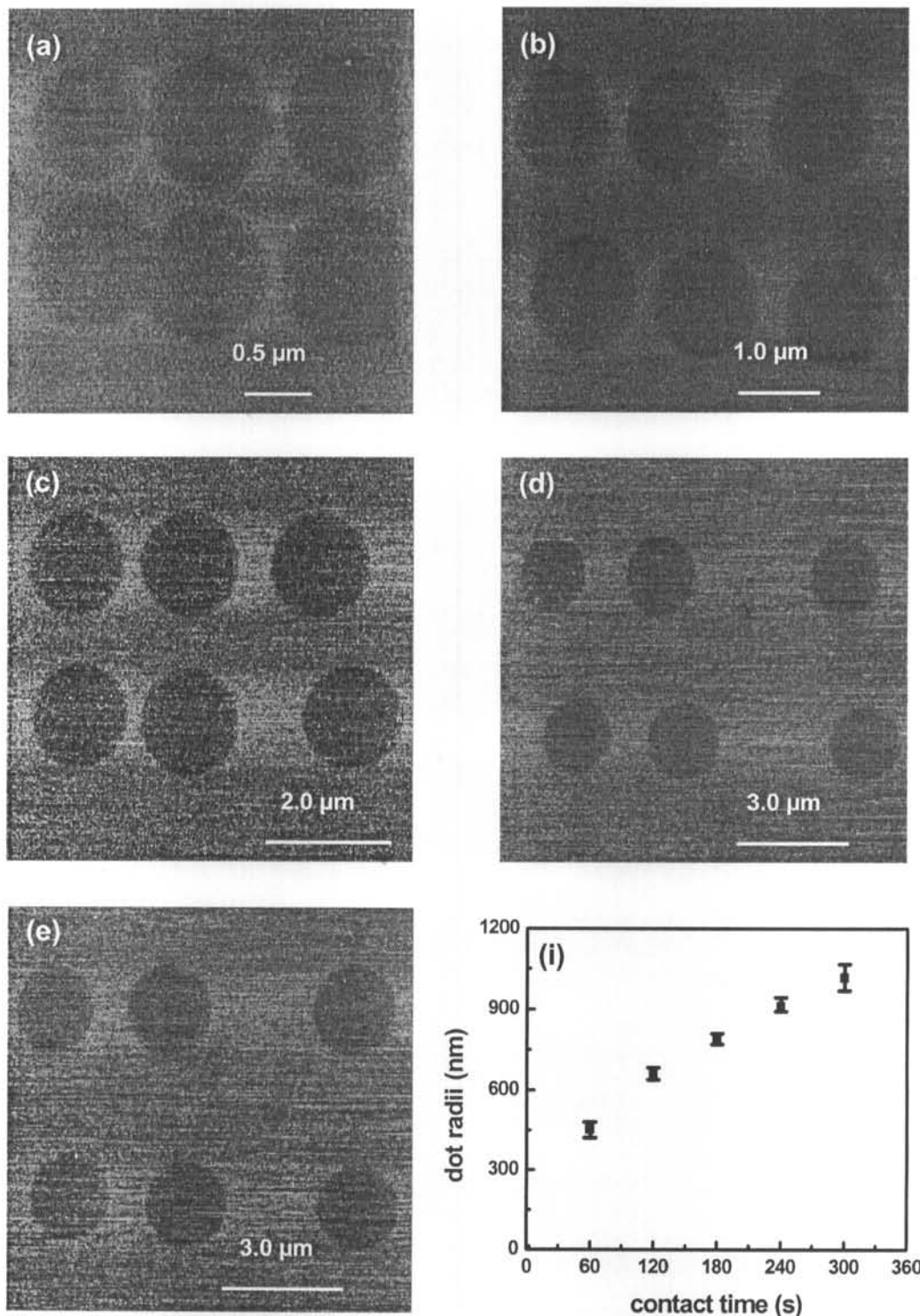


Fig.4-6 Lateral force microscopy images of P(VDF-TrFE) points array at 55°C and relative humidity of 64% for 60 s (a), 120 s (b), 180 s (c), 240 s (d), and 300s (e), respectively, and panel (f) is the curve of dot radius averaged from five independent measurements as a function of contact time. The error bars are standard deviations.

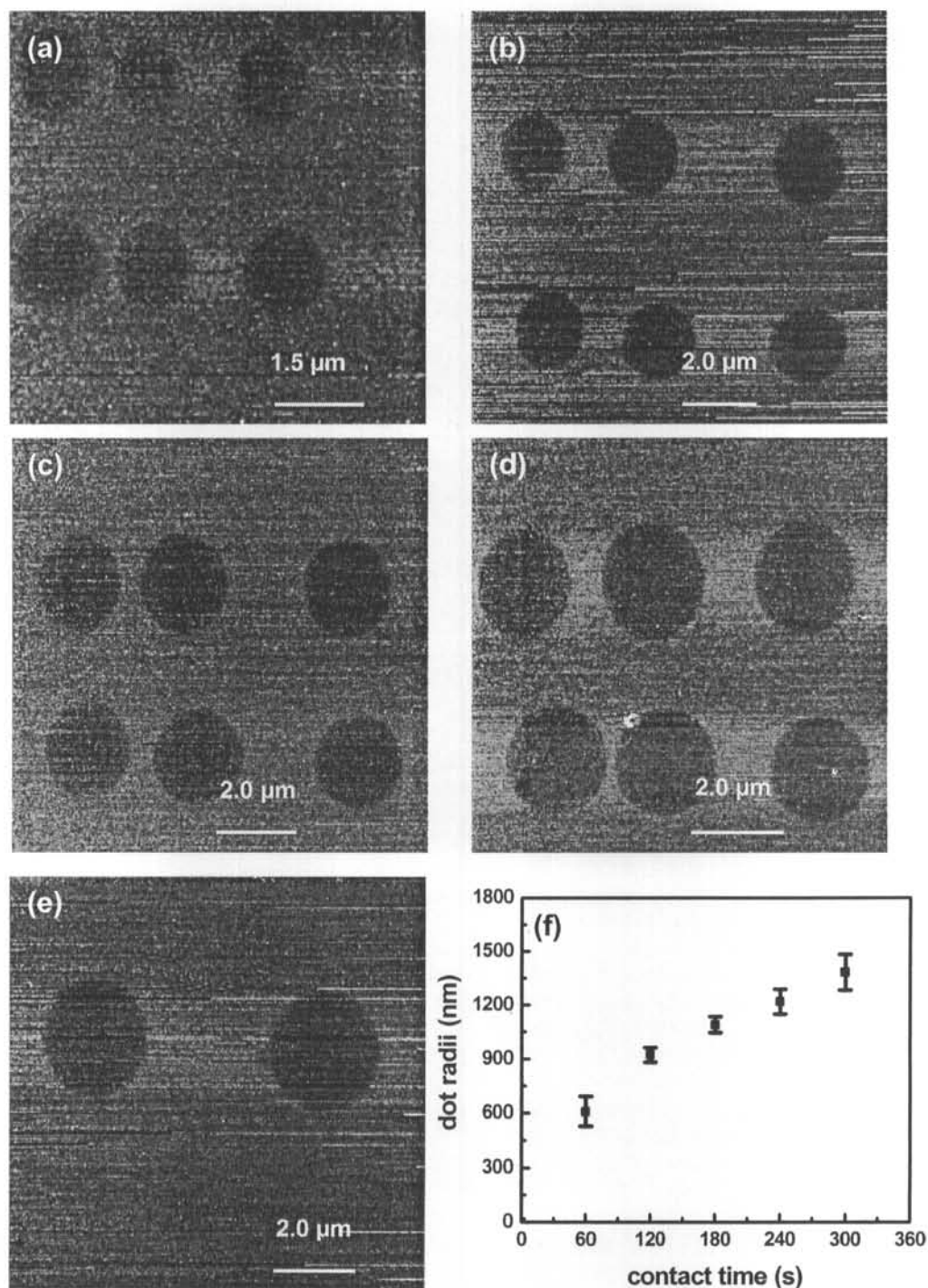


Fig.4-7 Lateral force microscopy images of P(VDF-TrFE) points array at 60°C and relative humidity of 64% for 60 s (a), 120 s (b), 180 s (c), 240 s (d), and 300s (e), respectively, and panel (f) is the curve of dot radius averaged from five independent measurements as a function of contact time. The error bars are standard deviations.

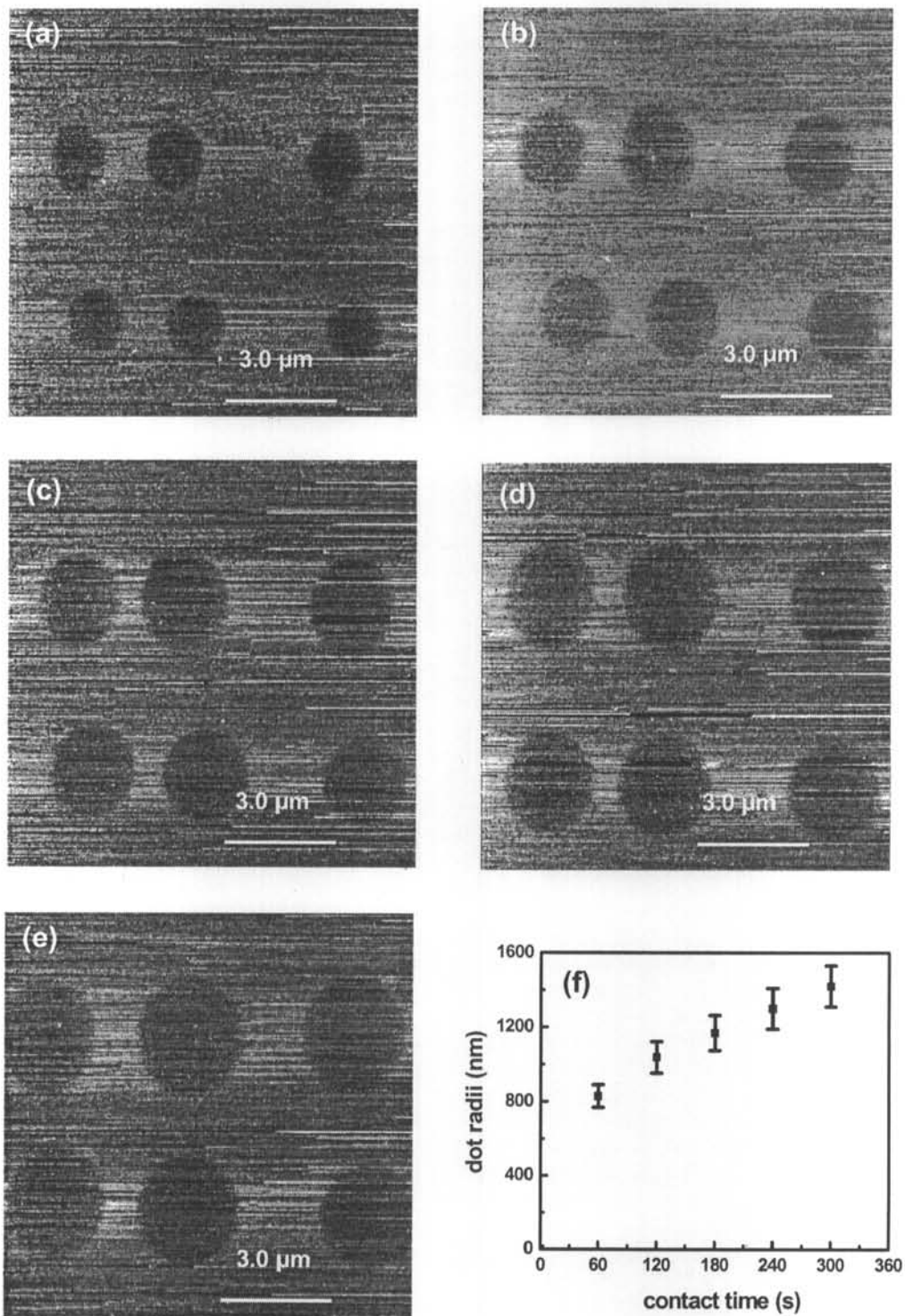


Fig.4-8 Lateral force microscopy images of P(VDF-TrFE) points array at 65°C and relative humidity of 64% for 60 s (a), 120 s (b), 180 s (c), 240 s (d), and 300s (e), respectively, and panel (f) is the curve of dot radius averaged from five independent measurements as a function of contact time. The error bars are standard deviations.

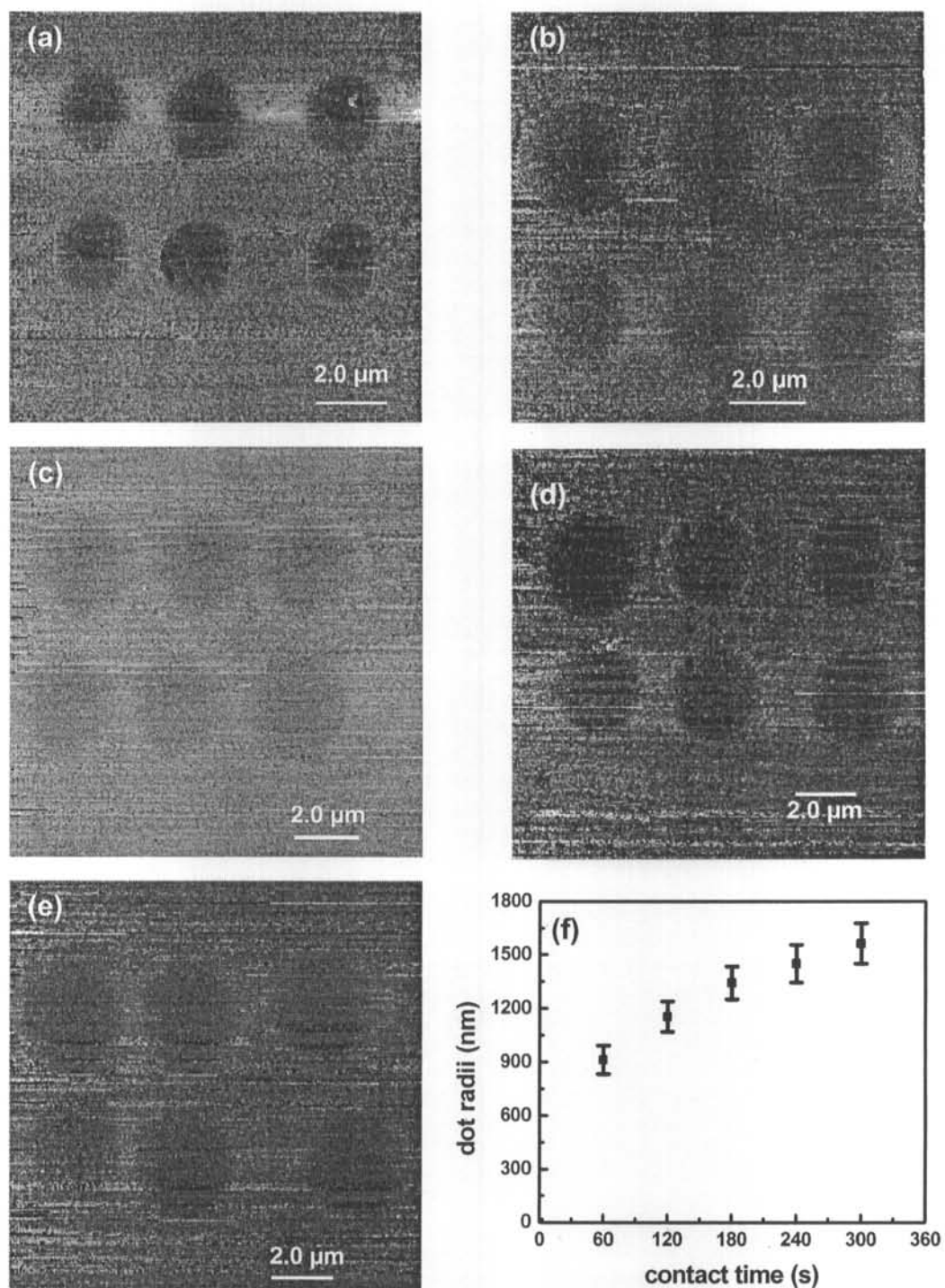


Fig.4-9 Lateral force microscopy images of P(VDF-TrFE) points array at 70°C and relative humidity of 64% for 60 s (a), 120 s (b), 180 s (c), 240 s (d), and 300s (e), respectively, and panel (f) is the curve of dot radius averaged from five independent measurements as a function of contact time. The error bars are standard deviations.

rate of P(VDF-TrFE). But the images became unclear when the temperature was above 70°C due to the vibration of the tip.

A nonlinear fitting of the r versus t with the function $y = ax^b$ using the experimental data shown in Figures 3-8f, 4-1f, 4-2f, 4-3f, 4-4f, 4-5f, 4-6f, 4-7f, 4-8f, and 4-9f was conducted. The relationship between a and T is shown in Figure 4-10a. It demonstrates that a is a temperature-dependent parameter. a increased as the temperature increased. As expressed in equation 3-6, a is diffusion constant-dependent parameter. A jump is observed from 50°C to 55°C, this demonstrate that diffusion constant may experience a change at about 55°C. Figure 4-10b illustrates the relationship between b and temperature. It was found that b was roughly close to 0.5 for all of the measured temperatures, which demonstrated that the dot radius of P(VDF-TrFE) grew linearly with $t^{1/2}$ in the measured temperature range (25~70°C).

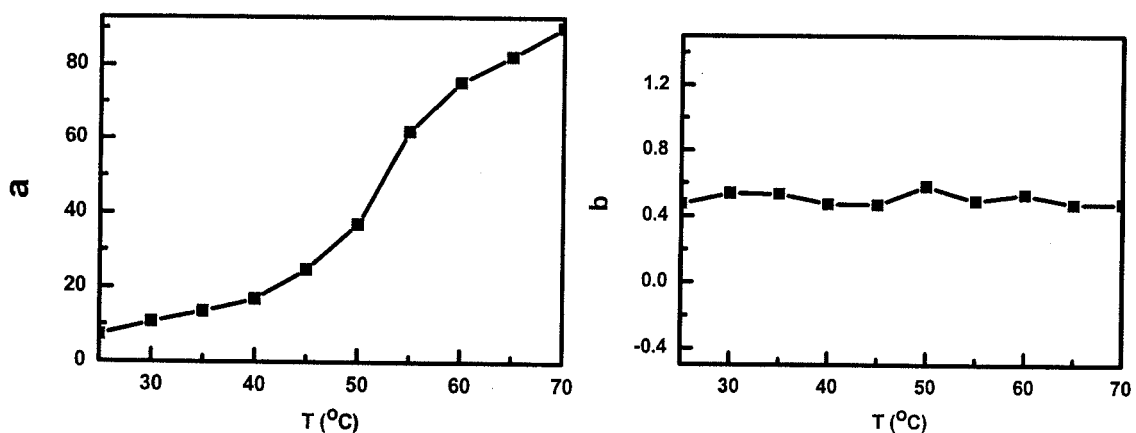


Fig.4-10 The relationship between the a and temperature (a), the b and temperature (b).

Effects of Experimental Conditions on Dip-pen Nanolithography

Therefore, dot area (A) scaled linearly with t in the range of the measured temperature. Here, the slope of the A - t curve was defined as the transport rate of P(VDF-TrFE) (ν), i.e., $\nu = \frac{dA}{dt}$. The plot of $\ln \nu$ versus the inverse temperature $\frac{1}{T}$ (Arrhenius plot) is shown in Figure 4-11a. There was an obvious deviation from the linear curve at about 55°C. The transport rate of the P(VDF-TrFE) molecules increased exponentially with temperatures of below 55°C, which conformed to the Arrhenius plot; however, the transport rate of P(VDF-TrFE) exceeded the expected value according to the Arrhenius plot at above 55°C. The result was different from the result of octadecanethiol (ODT) reported by Schwartz, where $\ln \nu$ was proportional to $\frac{1}{T}$ in all of the measured temperature ranges, as illustrated in Figure 4-11b [247]. Below 55 °C, the activation energy Q was calculated to be 0.98 eV, which was greater than the reported Q (0.74 eV) of ODT [247]. This means that the energy barrier to the diffusion of P(VDF-TrFE) on gold was higher than that of ODT, namely, the diffusion of P(VDF-TrFE) molecules on gold is more difficult than ODT. In fact, we obtained that the transport rate of P(VDF-TrFE) to gold was lower than that of ODT at the same experimental conditions (Figure 4-11c). This conclusion is also consistent with the reported experimental results [202].

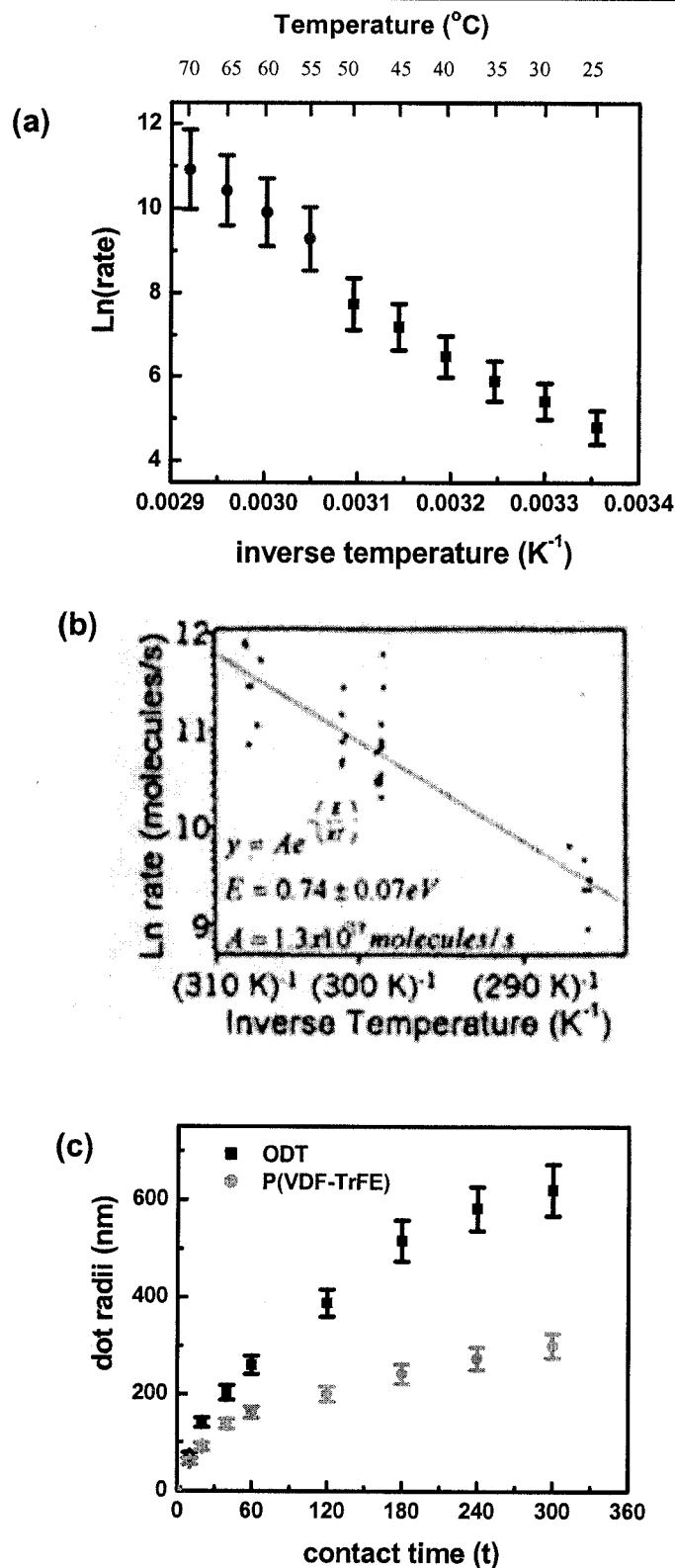


Fig.4-11 (a) Plot of $\ln v$ versus the inverse temperature $\frac{1}{T}$ (Arrhenius plot) for P(VDF-TrFE). (b) Arrhenius plot of ODT measured by Schwartz [247]. (c) Comparison of transport rate of ODT and P(VDF-TrFE) to gold at the same experimental conditions (25°C and relative humidity of 50%).

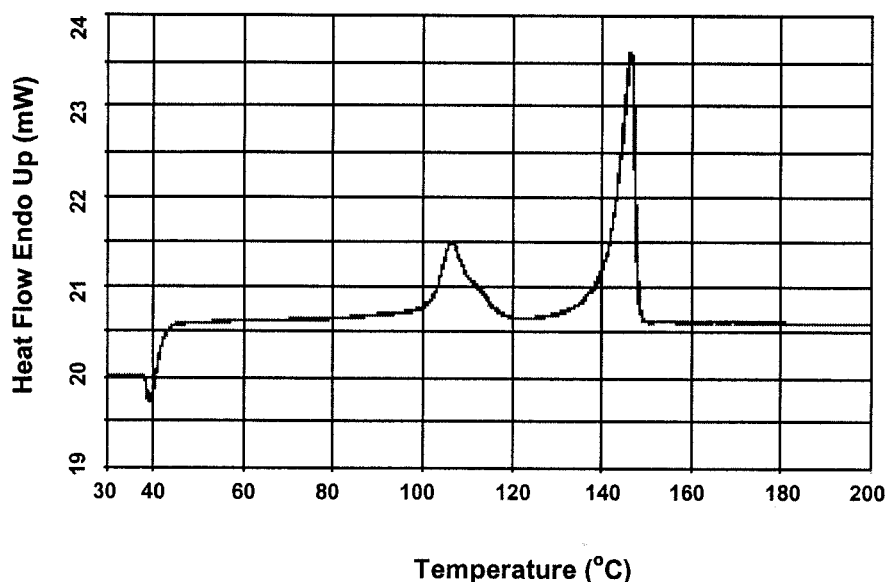


Fig.4-12 Heating DSC thermograms of the P(VDF-TrFE 80:20).

Figure 4-12 shows the DSC thermogram of the P(VDF-TrFE). The peak at 106°C was the first-order ferroelectric-paraelectric phase transition point, namely the Curie temperature (T_c) for bulk P(VDF-TrFE 80:20). This was consistent with the values measured by Bune [261] and Ohigashi [273]. However, some properties different from the bulk occur at a nanometer scale. Bune and colleague measured the dielectric properties of the ferroelectric Langmuir-Blodgett-deposited polymer films (P(VDF-TrFE 70:30)) with a thickness of about 15 nm (30 monolayers), 3.5 nm (7 monolayers), and 1 nm (2 monolayers) on an Al electrode (Figure 4-13). They found a new and unexpected phase transition at a lower temperature of about 30 °C on heating for these thin P(VDF-TrFE) films, and the film with 2 monolayers had the strongest change in dielectric constant at this point than the other two thick films. They attributed this behavior to a new first-order ferroelectric

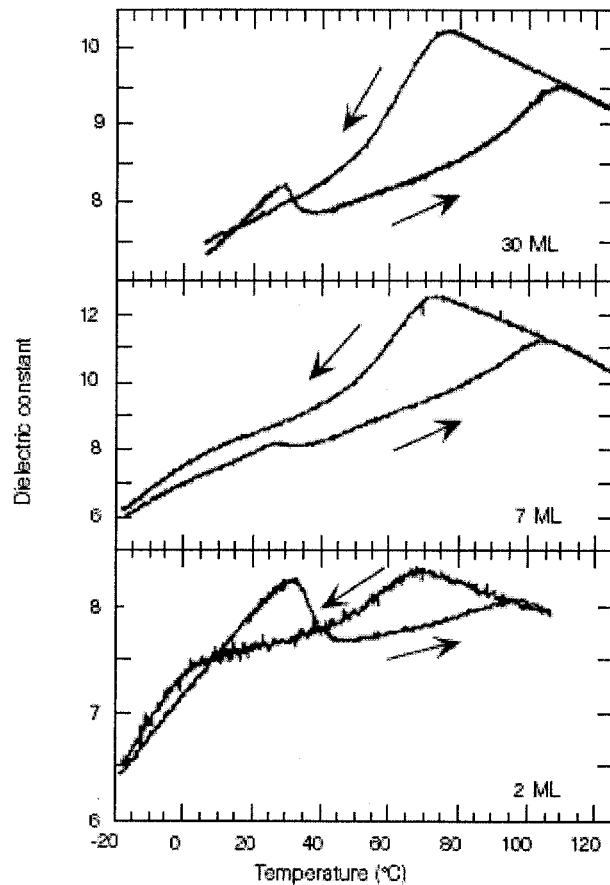


Fig.4-13 Dielectric properties of the ferroelectric Langmuir-Blodgett-deposited P(VDF-TrFE 70:30) films with different thickness measured by Bune [261]. The arrows show the direction of temperature change.

phase transition in the surface layers [261]. The DPN generated P(VDF-TrFE) patterns have a thickness of about 1 nm, it is reasonable to attribute the deviation from the Arrhenius plot at about 55°C to a first-order ferroelectric phase transition. The difference in temperature probably arises from the different electrodes, the different VDF-contents in the polymer, different measuring methods, and especially the difference in temperature between the substrate and the tip. Because we measured the temperature of

Effects of Experimental Conditions on Dip-pen Nanolithography

the substrate other than the temperature of the tip, while the ink was deposited from the tip to the substrate, the temperature of the tip should be lower than that of the substrate.

To further verify our hypothesis, the force-distance curves as a function of temperature were measured with AFM. It is well known that AFM is highly sensitive in measuring weak forces as low as piconewton. The information about biomolecular interactions [12] and capillary force [263] have been obtained by measuring the force-distance curves. The same type of cantilever, CSG11, which is highly sensitive to force with a low spring constant, was used to measure the force-distance curves, and the spring constant was determined according to Sader's method [264]. Three interactions (named the tip-substrate interaction, the tip-ink interaction, and the ink-substrate interaction) were measured at various temperatures. A calibrated cantilever and gold substrate were used to measure the tip-substrate interaction, and the heating procedure was as the same as that described in the experimental section. The force-distance curves (retraction curves) as a function of temperature are shown in Figure 4-14a.

As described in a previous report [263], the absolute value of the pull-off point varies from experiment to experiment for different tips. Therefore, we used the relative values for comparison unless otherwise stated. To measure the tip-ink interaction, a thin film of P(VDF-TrFE) (about 5 nm) was coated on

Effects of Experimental Conditions on Dip-pen Nanolithography

a gold surface by spin coating, and the force-distance curves between the calibrated cantilever and the coated gold substrate at various temperatures were measured. The results are illustrated in Figure 4-14b. To measure the

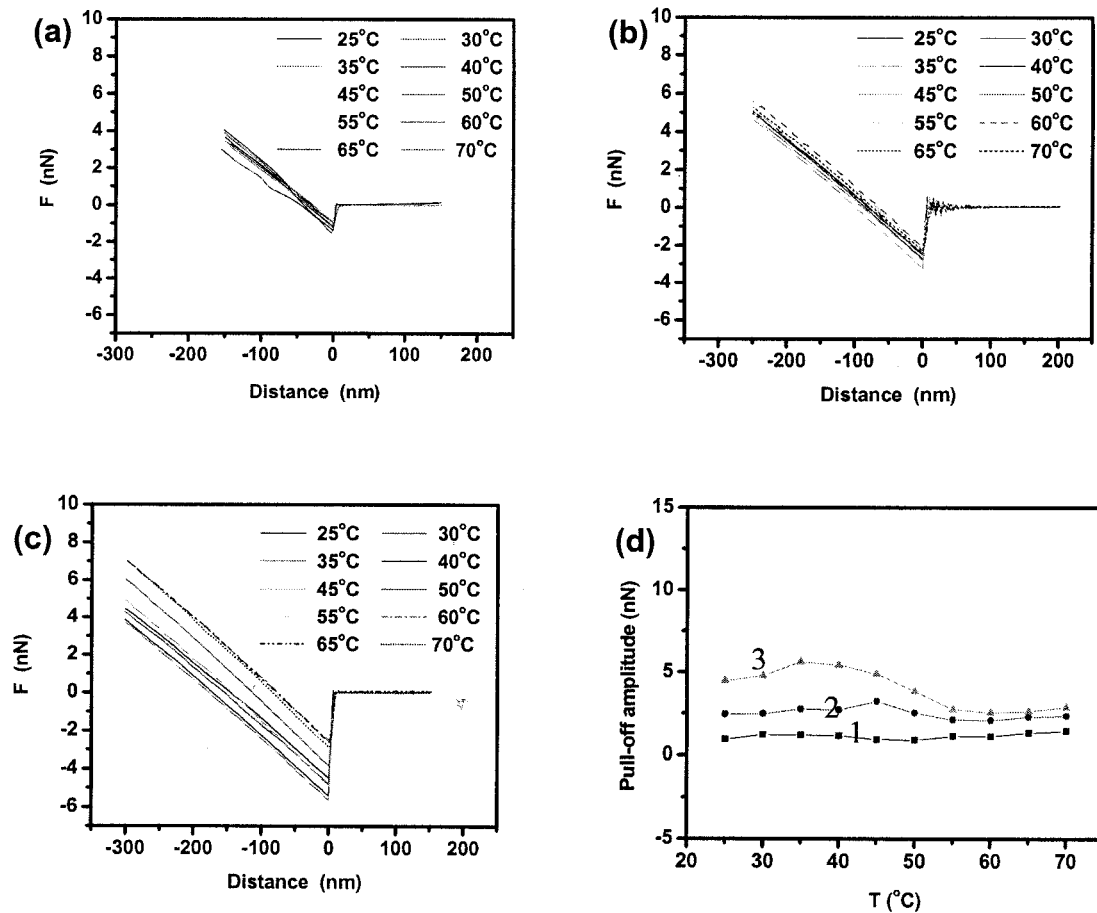


Fig.4-14 Force –distance curves measured as a function of the substrate temperature between (a) a bare tip and gold substrate (b) a bare tip and a thin film of P(VDF-TrFE) coated on gold substrate, and (c) a tip coated with a thin film of P(VDF-TrFE) and gold substrate. (d) is the plot of the relative pull-off amplitude as a function of temperature from a (curve 1), b (curve 2), and c (curve 3).

Effects of Experimental Conditions on Dip-pen Nanolithography

ink-substrate interaction, a thin film of P(VDF-TrFE) was coated on the tip using the same procedure as described in chapter 3, and the force-distance curves between the coated tip and gold substrate were determined. The results are shown in Figure 4-14c. The curves of the relative pull-off amplitude as a function of temperature from the data represented in Figures 4-14a, 4-14b, and 4-14c are illustrated in Figure 4-14d, where curves 1, 2, and 3 denote the tip-substrate interaction, the tip-ink interaction, and the ink-substrate interaction, respectively. Figure 4-14d reveals the following conclusions, the interactions increased according to the following sequence: the tip-substrate interaction < the tip-ink interaction < the ink-substrate interaction. The tip-substrate interaction experienced little change as the temperature increased, while the tip-ink interaction and the ink-substrate interaction experienced an increase (from room temperature to 45°C for the former, and to 40°C for the later) then a decrease, and minimum values were obtained at about 55°C. Little change was then experienced at above 55°C. Nevertheless, the effect of temperature on the ink-substrate interaction was more remarkable. The weakened tip-ink interaction and ink-substrate interaction was caused by the ferroelectric phase transition. The weakened tip-ink interaction sped up the deposition of P(VDF-TrFE) molecules to the gold substrate, and the weakened ink-substrate interaction made the polymer molecules diffuse on the gold surface in a more facile manner, resulting in a significant increase in the transport rate of ink and a deviation from the Arrhenius plot at about the transition point of 55°C.

4.3 Effect of Surface Roughness

Dip-pen nanolithography has attracted a great deal of attention due to its potential applications in the following areas: (1) the fabrication of micro- to nanostructures of biomolecules; (2) the building of tailored chemical surfaces for studying and controlling biorecognition processes from the molecular to the cellular level; (3) the construction of chemical templates for the controlled orthogonal assembly of materials on surfaces; (4) the generation of hard nanostructures using chemical etching, and (5) the in situ investigation of surface reactivity and exchange chemistry [265]. More than 250 papers on DPN have been published since its invention in 1999. However, only one report mentioned the effect of surface roughness but without detailed and systematic study [266]. In fact, the diffusion of ink molecules on a substrate surface is strongly dependent on the properties of the surface.

The present work was mainly motivated by one of our experiments. Two types of gold substrates were used to fabricate the micro- to nanostructure of a ferroelectric polymer, P(VDF-TrFE). One was a thin film prepared by sputtering, and one was a gold ball with many atomic flat facets. It was found that the transport rate of P(VDF-TrFE) to the two types of gold surfaces is different. The transport rate of P(VDF-TrFE) to the flat surfaces on the gold ball is greater than that of the gold thin film. The main difference between the two substrates is that the latter has a rougher surface than the former. Therefore, effect of roughness on DPN is studied by preparing a series of

Effects of Experimental Conditions on Dip-pen Nanolithography

gold thin films with various surface roughness by controlling the experimental conditions during sputtering, and selecting ODT and P(VDF-TrFE) as the DPN inks.

4.3.1 Experimental

All chemicals were used as received, i.e., 30% hydrogen peroxide solution (BDH Laboratory), concentrated sulfuric acid (Aldrich), 98% ODT (Aldrich), and 99.7% acetonitrile (Lab-Scan).

A gold wire (99.99%) with a diameter of 0.15 mm was rinsed with acetone and dipped in a piranha solution (the volume ratio of concentrated sulfuric acid and 30% H₂O₂ is 7:3) for 15 min to remove the organic materials on the surface of the gold. The wire was melted in a CH₄ flame. A small ball of about 3 mm in diameter was formed, and then re-solidified in the atmosphere [267-268].

1mM solution of ODT in acetonitrile was used as the ink. The same type of tip, CSG11 was coated with ODT by immersing the cantilever in the solution for 1 minute and was blown dry with pure nitrogen. The methods of DPN patterning and AFM imaging were the same as those described in the patterning of P(VDF-TrFE) on gold substrate via DPN.

4.3.2 Results and Discussion

4.3.2.1 Characterization of the Gold Ball and the Gold Thin Film with AFM

The gold ball and gold thin film were characterized with AFM, as illustrated in Figure 4-15. Some surface steps illustrated as 1, 2, 3, 4, 5, can be seen clearly in the topography of the facets on the gold ball by the tapping mode (Figure 4-15a). Within each step the surface is flat with a roughness of less than 1 Å. Figure 4-15b shows the profile of the line scan in Figure 4-15a. The height of the steps was in the range of 0.25 to 0.30 nm, near the theoretical inter-atomic distance of gold (0.288 nm) [269]. The topographic and LFM images of the facets on the gold ball measured by the contact mode are shown in Figure 4-15c and Figure 4-15d, respectively. Surface steps in topography (Figure 4-15c) cannot be shown in a LFM image (Figure 4-15d) because the substrate is composed of a single component. The topography and LFM images of a gold thin film measured by the contact mode are illustrated in Figure 4-15e and Figure 4-15f, respectively. The surface of polycrystalline gold was composed of gold particles with an average diameter of about 4 nm. Many crystalline grain boundaries exist on the surface (Figure 4-15e). The roughness was 0.673 nm as measured with AFM. A crystalline boundary can also be seen in the LFM image (Figure 4-15f).

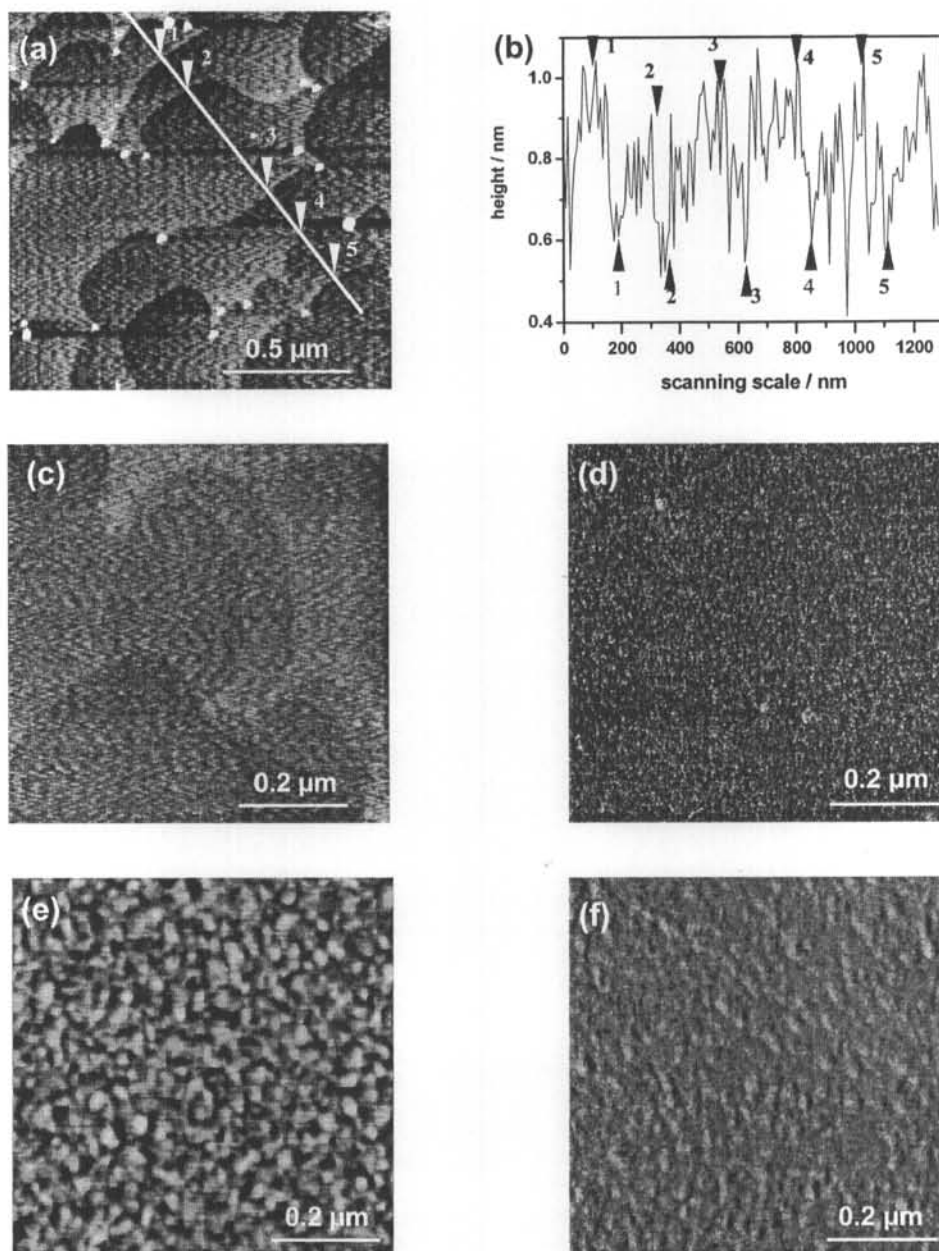


Fig.4-15 Characterization of the facets on a gold ball and on a polycrystalline gold thin film with AFM: (a) Topographic image of the facets on a gold ball in the tapping mode. (b) Profile of the line scan in (a), demonstrating that the surface steps are 0.25~0.3 nm. Topography (c) and lateral force image (d) of the facets on a gold ball in the contact mode. The lateral force image shows no information about the surface steps. Topography (e) and lateral force image (f) of the gold thin film in the contact mode. A crystalline boundary exists both in the topography and the LFM image.

4.3.2.2 Comparison of the DPN Patterning of P(VDF-TrFE) on the Gold Ball and Gold Thin Film

DPN was conducted using P(VDF-TrFE) as ink. Point arrays were fabricated by keeping contact between the coated tip and the gold substrate for different periods of time. P(VDF-TrFE) deposited on the gold ball can be seen clearly in both the topographic and LFM images (Figure 4-16). Figure 4-16a shows the topography of two points of P(VDF-TrFE) on the gold ball with a contact time of 30 s and 60 s at a relative humidity (RH) of 64% and 22°C. Figure 4-16b shows the profile of the line scan in Figure 4-16a, indicating that the thickness of P(VDF-TrFE) in the two points was about 1nm. This means that P(VDF-TrFE) patterns on the gold ball fabricated via DPN contained two layers of molecules, the same as on the gold thin film. In the LFM image (Figure 4-16c), the hydrophobic polymer P(VDF-TrFE) on the gold ball exhibited a darker contrast, i.e., a smaller friction force between the tip and the substrate was produced as illustrated in Figure 4-16d.

The dependency of the dot area (A) as a function of contact time (t) for P(VDF-TrFE) patterns on the gold ball and the gold thin film is shown in Figure 4-17. It can be found that A scales linearly with t for both the gold ball and the gold thin film, but at different rates. The slope of the $A-t$ curve was defined as the transport rate of ink, v , and $v = \frac{dA}{dt}$. Then the transport rate of P(VDF-TrFE) to the gold ball was greater than that of the gold thin film. The reason for such a difference is believed to lie in the substrate surface topography. As described above, the roughness of the polycrystalline gold

film (0.673 nm) is greater than the roughness of the facets on the gold ball (less than 0.1 nm).

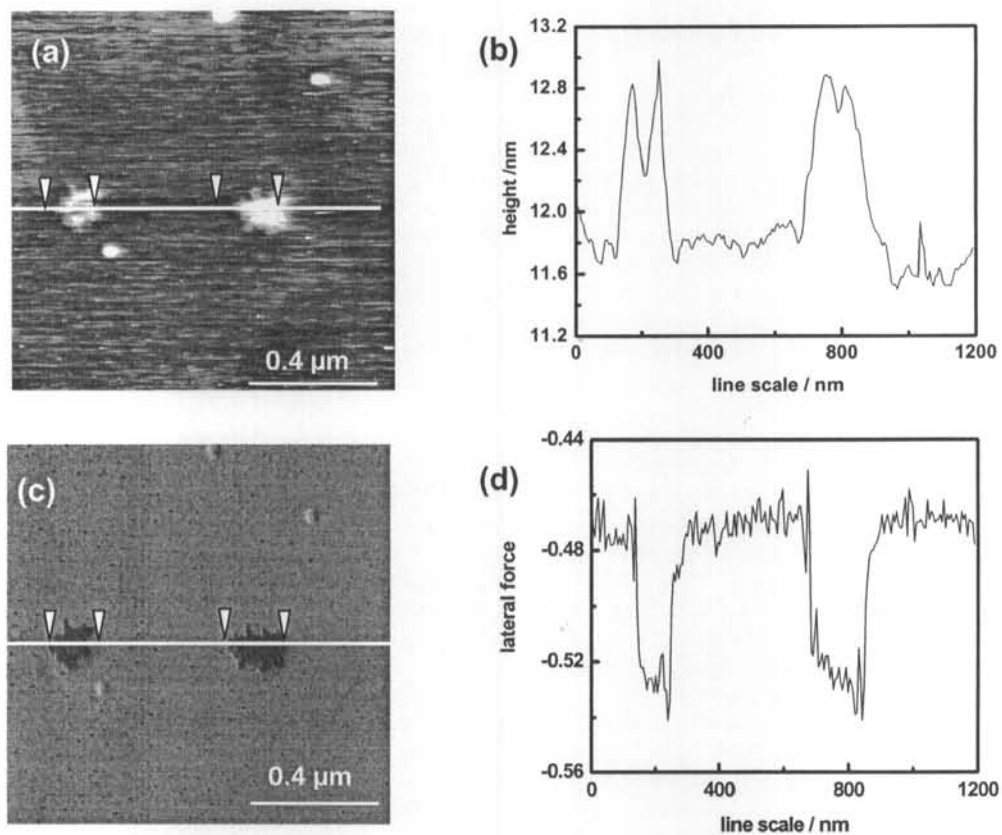


Fig.4-16 Patterns of P(VDF-TrFE) on the gold ball fabricated via DPN: Topography (a) and LFM image (c) of two points of P(VDF-TrFE) on a gold ball (relative humidity of 64%, 22°C, contact time: 30s for the left dot and 60s for the right dot in air). (b) and (d) are profiles of the line scans in (a) and (c).

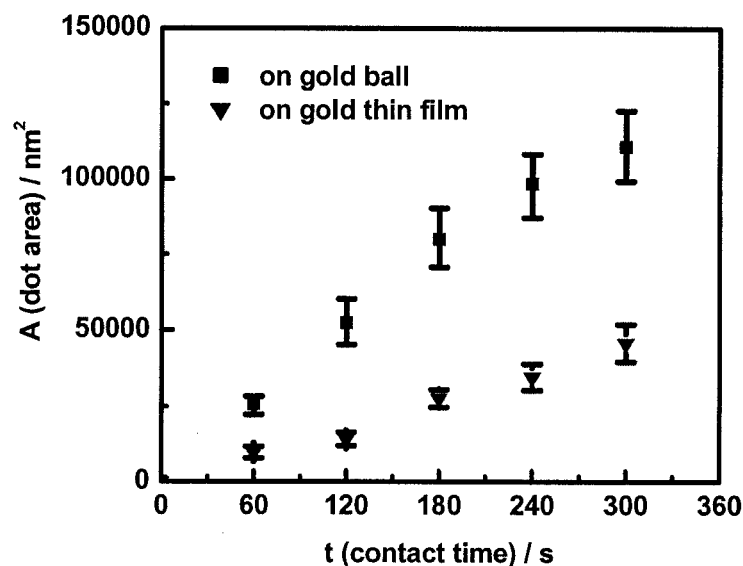


Fig.4-17 The dependency of the dot area (A) versus the contact time (t) curves for P(VDF-TrFE) patterns on a gold ball and a gold thin film via DPN at 22°C and a relative humidity of 80%.

4.3.2.3 Effect of Surface Roughness on DPN

Similar to the above method, Haaheim and coworkers [266] briefly studied the effect of roughness on the transport of MHA via DPN by using three gold substrate with varied roughness prepared by three different methods (i.e., evaporated gold, sputtered gold, and mica-peeled gold). To test our hypothesis and to exclude the cause by different preparing methods, five gold thin films of different roughness were prepared using the same method (sputtering) by controlling the experimental conditions. The five substrates were named 1#, 2#, 3#, 4# and 5#, respectively. Their surface properties are listed in Table 4-1.

Table 4-1 The surface properties of five gold thin films

No	Root mean square (nm)	Roughness (nm)	Peak to peak (nm)
1 [#]	0.865	0.673	8.178
2 [#]	0.999	0.787	10.324
3 [#]	1.316	1.036	10.614
4 [#]	2.061	1.646	13.804
5 [#]	2.361	1.886	15.892

ODT was used as the ink, and point arrays of ODT were fabricated on the five substrates via DPN. The LFM images are shown in Figures 4-18a to 4-18e. Figure 4-18f shows the time dependency of the dot area measured as a function of roughness. It is obvious that the surface roughness affected both the contrast in lateral force images and the transport rate of ODT. The surfaces that are less rough (1[#], 2[#], and 3[#]) provide good contrast as shown in Figures 4-18a to 4-18c, while the contrast on the rough surfaces (4[#] and 5[#]) was not clear as shown in Figures 4-18d and 4-18e, they are not suitable for DPN. The transport rate increases as roughness decreases (Figure 4-18f), i.e., a flat surface facilitates the diffusion of ink molecules.

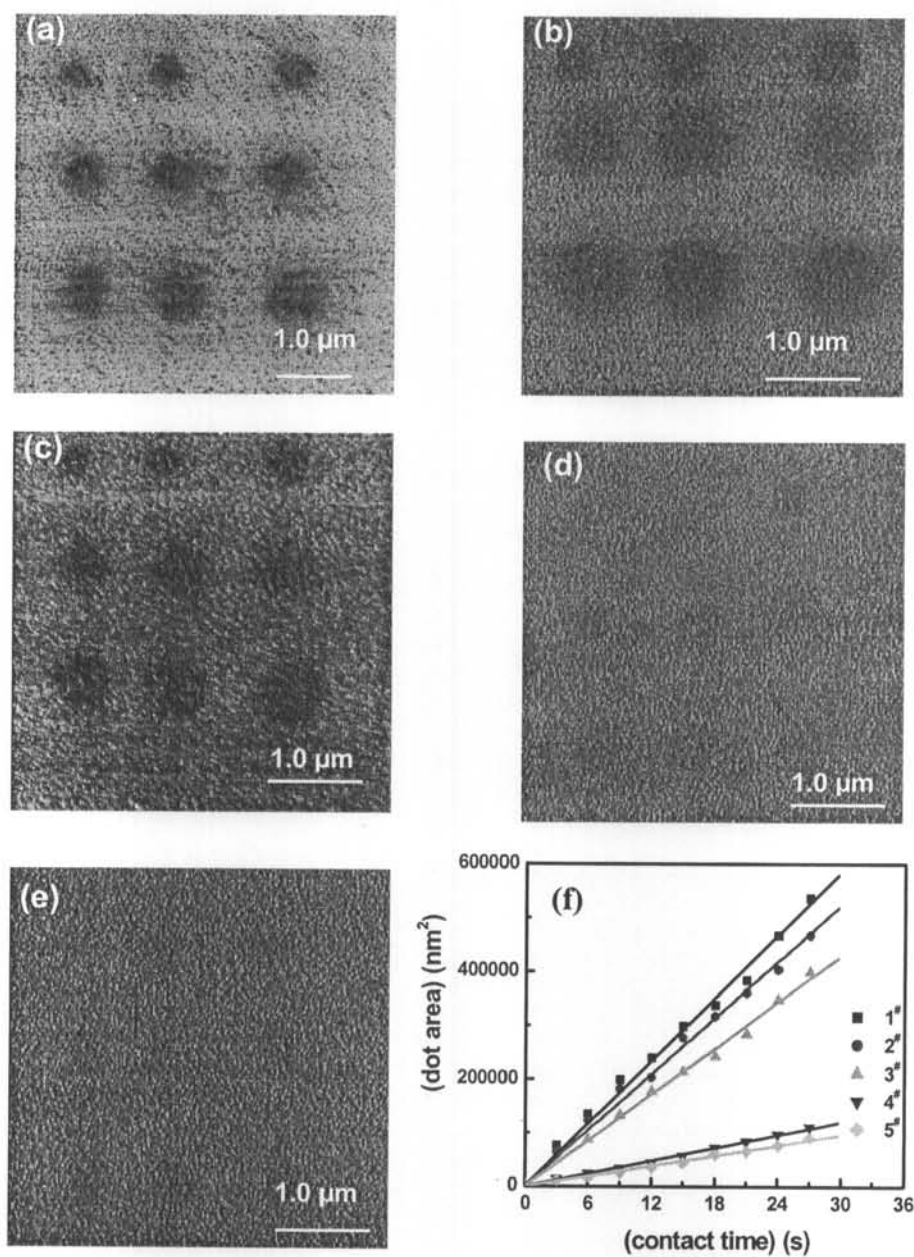


Fig.4-18 Effect of roughness on DPN with ODT ink at 22°C and a relative humidity of 50%: The LFM images of an ODT point array on 1[#] (a); 2[#] (b); 3[#] (c); 4[#] (d); and 5[#] (e). The contact times for the dots are 3, 6, 9, 12, 15, 18, 21, 24, and 27s, respectively. (f) is the dependency of the dot area (A) versus the contact time (t) measured as a function of roughness.

Effects of Experimental Conditions on Dip-pen Nanolithography

P(VDF-TrFE) was also used as the DPN ink to study the effect of roughness, and the results are shown in Figure 4-19. The same trend as that for ODT was obtained. Flat surfaces (1[#], 2[#], and 3[#]) give good contrast in lateral force images, as shown in Figures 4-19a to 4-19c. The two dots with short contact times of 60 and 120 seconds can not be recognized in the LFM image on 4[#] (Figure 4-19d), while the four dots with a short contact times of 60, 120, 180, and 240 seconds can not be differentiated in the LFM image on 5[#] (Figure 4-19e). The transport rate of P(VDF-TrFE) decreases as the roughness increases, as shown in Figure 4-19f.

There is no doubt that the roughness of the surface of the substrate played an important role in DPN. However, the extent of the influence was not the same for different inks (see Figures 4-18 and 4-19), namely the influence is strongly ink-dependent. Figure 4-20 shows the curve of the transport rate of ink as a function of roughness. The transport rate of ODT decreased linearly as the roughness increased (Figure 4-20a). The inset plot was diffusion constant as a function of substrate roughness for MHA, which was reported by Haaheim and coworkers. It also showed a rough linear fit [266]. However, the transport rate of P(VDF-TrFE) was not proportional to the roughness (Figure 4-20b). When the roughness was less than 1 nm, the transport rate of P(VDF-TrFE) decreased rapidly as the roughness increased. When the roughness was greater than 1 nm, the transport rate of P(VDF-TrFE) experienced a small change as the roughness increased. This difference may be caused by the ink-substrate interaction. Both ODT and MHA are thiols, they have strong chemical affinity to gold due to the formation of Au-S

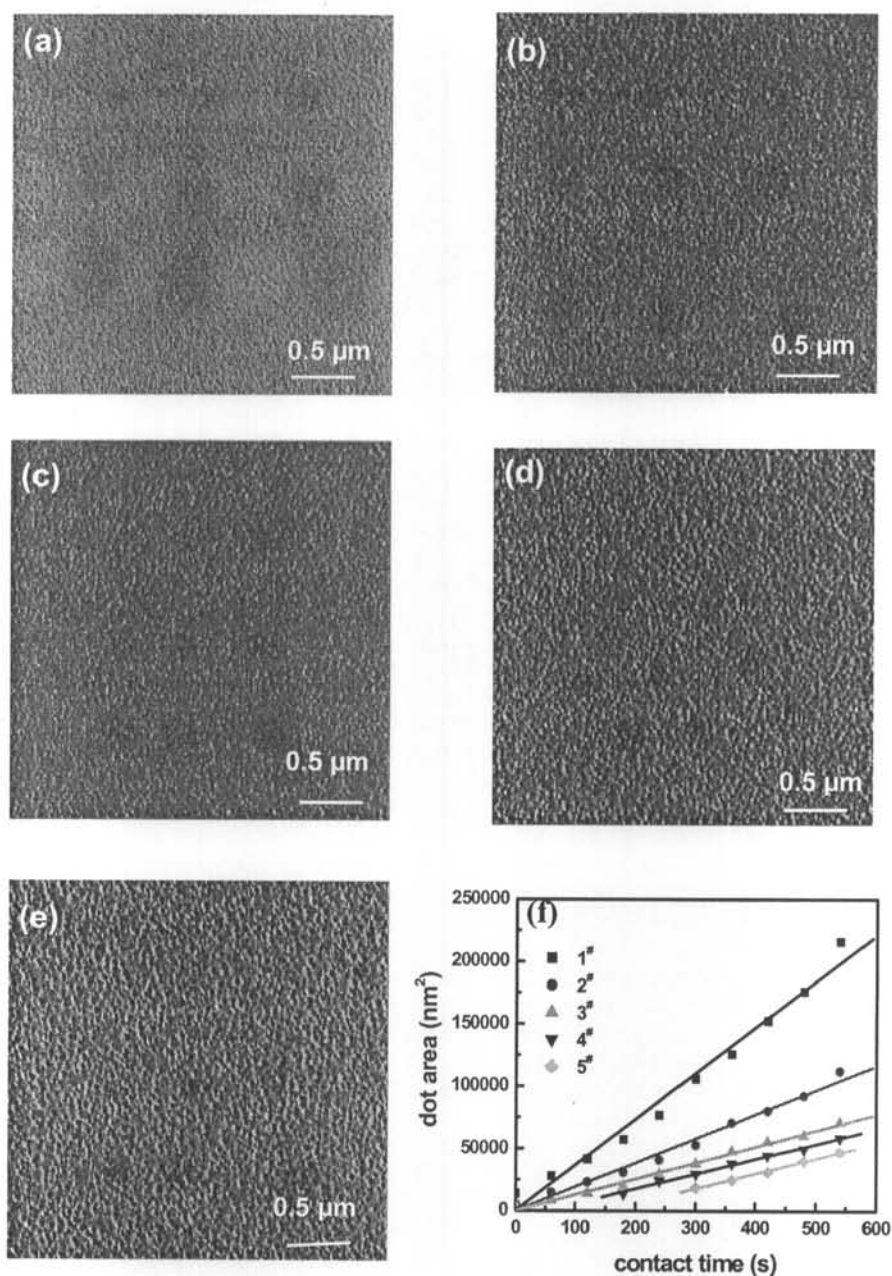


Fig.4-19 Effect of roughness on DPN with P(VDF-TrFE) ink at 22°C and a relative humidity of 50%: LFM images of a P(VDF-TrFE) point array on 1[#] (a); 2[#] (b); 3[#] (c); 4[#] (d); and 5[#] (e). The contact times for the dots are 1, 2, 3, 4, 5, 6, 7, 8, and 9min, respectively. (f) is the dependency of the dot area (A) versus the contact time (t) measured as a function of roughness.

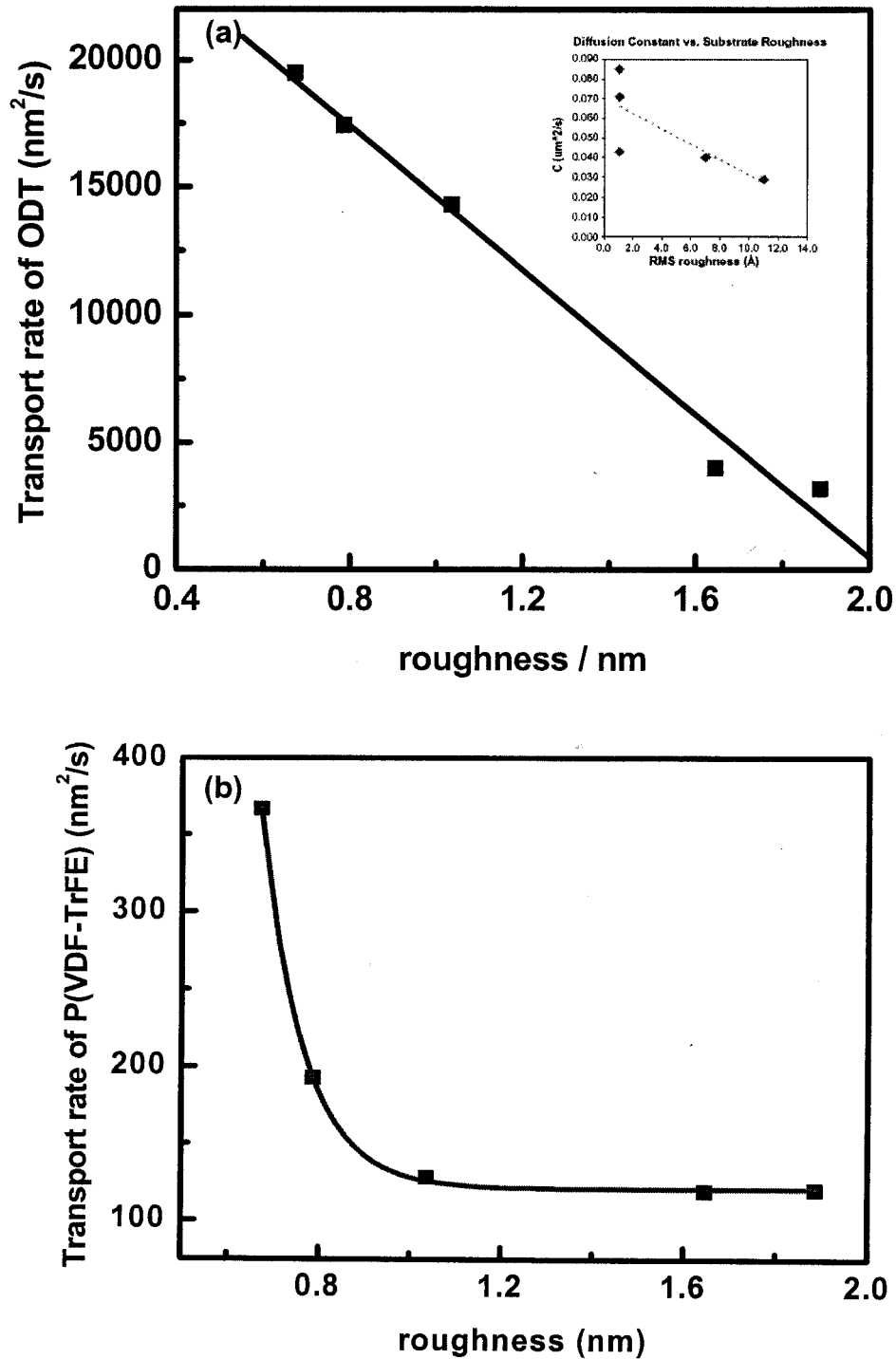


Fig.4-20 The dependency of the transport rate on the surface roughness: (a) ODT. Inset plot is diffusion constant versus substrate RMS [266]. (b) P(VDF-TrFE).

covalent bond, while P(VDF-TrFE) was deposited to gold due to Van der Waal's interaction.

The transport rate of ink decreased as the roughness increased. This is probably caused by the increased interaction between ink molecules and the rough surface. It has been proven that roughness strongly influenced the sticking coefficient (S_0) of molecules on a solid surface, and increased greatly as the roughness of the surface increased [270]. Daikhin and Urbakh also reported that roughness increased the frictional force in a confining system [271]. The increased interaction made it more difficult for ink molecules to diffuse on the rough surface, resulting in a slow transport rate compared to a less rough surface. The interactions between ink molecules and the substrate were different for different systems. Therefore, the influence of roughness was different for different systems, i.e., the influence of roughness was strongly ink-dependent.

It is easy to understand the poor contrast in LFM images on rough surfaces (4[#] and 5[#]). Because the thickness of ODT in the patterns fabricated via DPN was about 1.1 nm [246], and the thickness of P(VDF-TrFE) was about 1.0 nm, both were less than the surface roughness of 4[#] and 5[#]. Therefore, a good contrast can not be obtained on the two substrates.

4.4 Effect of Relative Humidity

Inconsistent conclusions about the effect of relative humidity on the transport rate of thiols have been obtained from different research groups. Schwartz [247] and Sheehan [246] thought that surface diffusion was independent of relative humidity; therefore, water meniscus was not required in DPN. However, Mirkin and colleague thought that the capillary force, which existed even at 0% relative humidity, was the driving force for the deposition of the ink from the tip to the substrate [202, 248,263].

The DPN is generally conducted in ambient conditions where a meniscus is formed between the AFM tip and the substrate, to study the influence of the relative humidity on DPN would benefit the controlling of the transport rate and the pattern quality.

4.4.1 Experimental

The AFM system was placed in a chamber and the relative humidity was controlled by purging dry N₂ into the system to obtain low relative humidity, while let N₂ pass through a water bottle to obtain high relative humidity. The rate of N₂ is 0.2 L/min. The relative humidity is measured with a humidity sensor (Cole-Parmer Instrument Company, U.S.A.) with an accuracy of $\pm 2\%$, as illustrated in Figure 4-21.

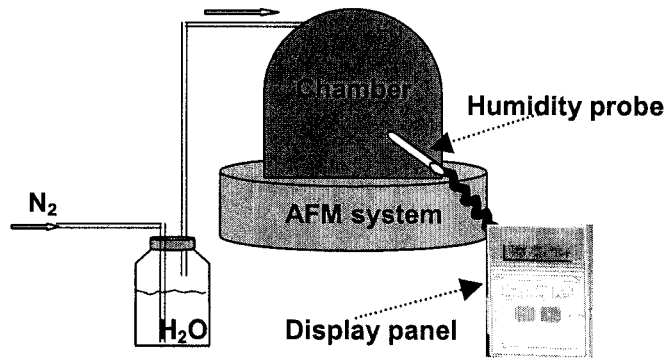


Fig.4-21 Schematic illustration of the AFM experimental system for DPN. AFM was placed in a chamber. Purge dry N₂ in to the system to obtain low relative humidity, while let N₂ pass through a water bottle to obtain high relative humidity.

4.4.2 Results and Discussion

The influence of relative humidity on the transport rate of the hydrophobic P(VDF-TrFE) via the DPN process was studied by changing the humidity in the AFM system. The relative humidity can be reduced to a minimum and stable value of 7% with dry N₂. Figures 4-22 and 4-23 show the DPN results at 7% and 17%, respectively.

Figure 4-24a shows the curves of $A-t$ for the P(VDF-TrFE) patterns measured as a function of relative humidity. The transport rate at a lower relative humidity was slightly greater than the transport rate at higher humidity, therefore, the relative humidity produces a slightly negative effect on the transport rate of the hydrophobic P(VDF-TrFE).

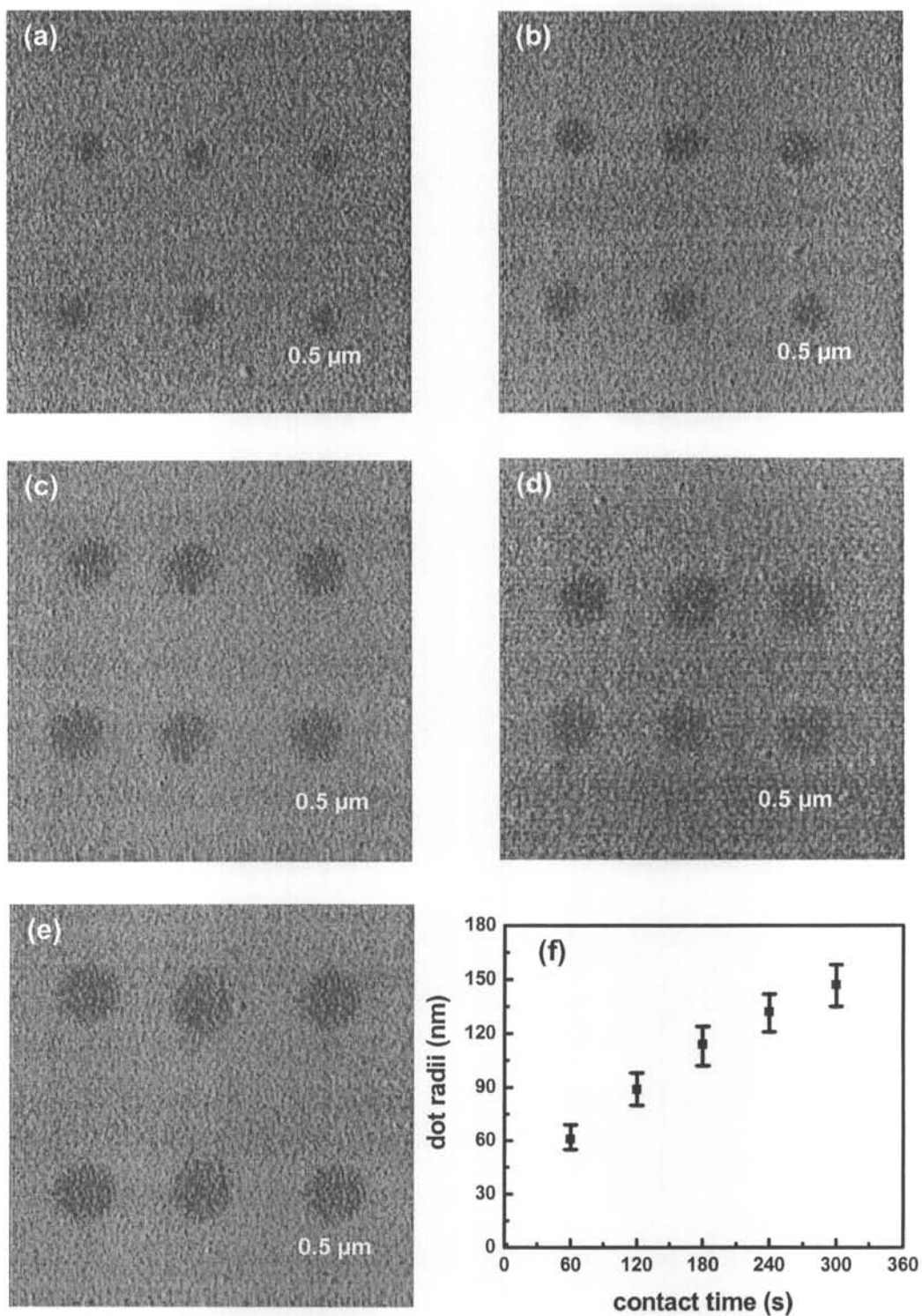


Fig.4-22 Lateral force images of P(VDF-TrFE) points array at 30°C and relative humidity of 7% for 60 s (a), 120 s (b), 180 s (c), 240 s (d), and 300s (e), respectively, and panel (f) is the curve of dot radius averaged from five independent measurements as a function of contact time. The error bars are standard deviations.

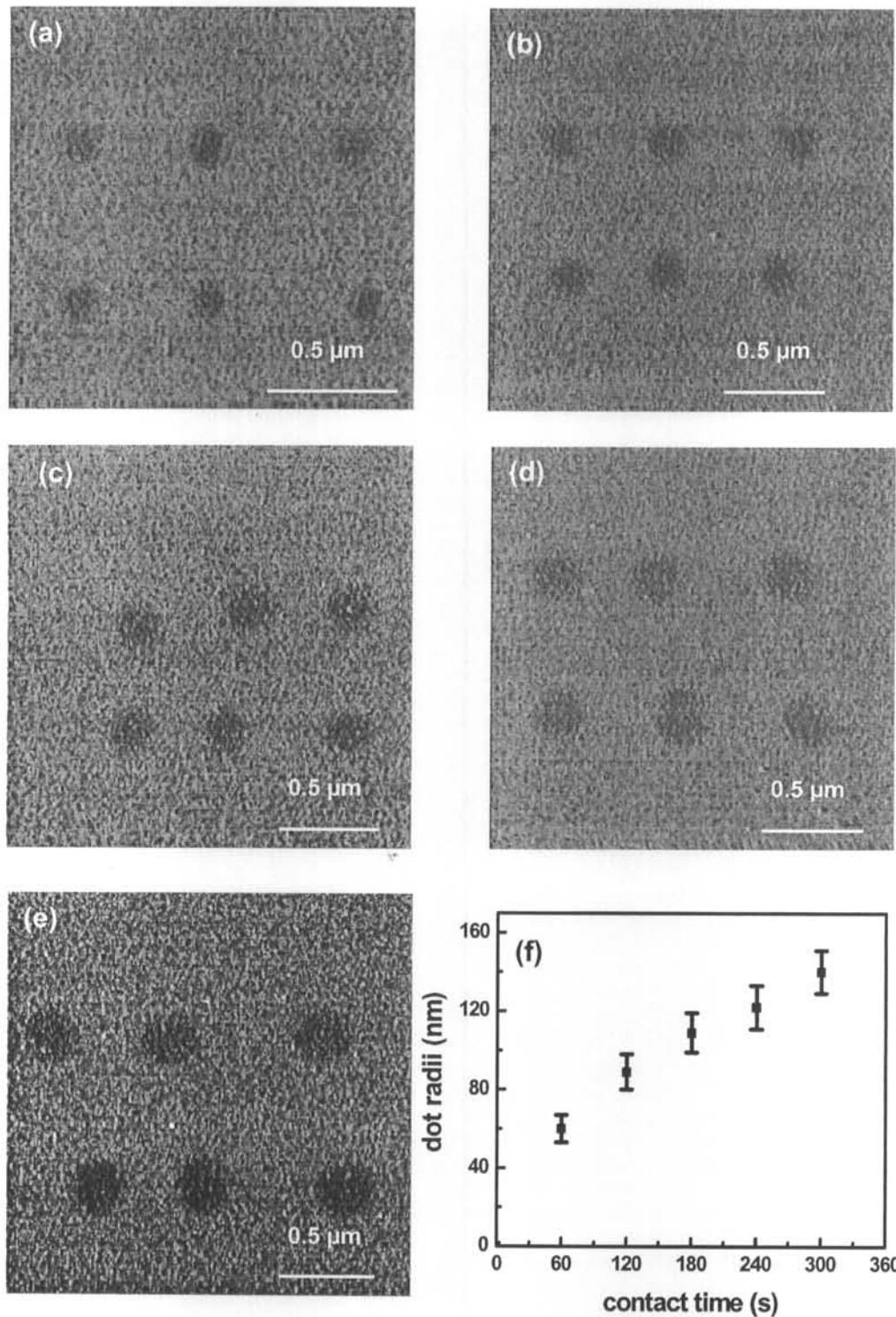


Fig.4-23 Lateral force images of P(VDF-TrFE) points array at 30°C and relative humidity of 17% for 60 s (a), 120 s (b), 180 s (c), 240 s (d), and 300s (e), respectively, and panel (f) is the curve of dot radius averaged from five independent measurements as a function of contact time. The error bars are standard deviations.

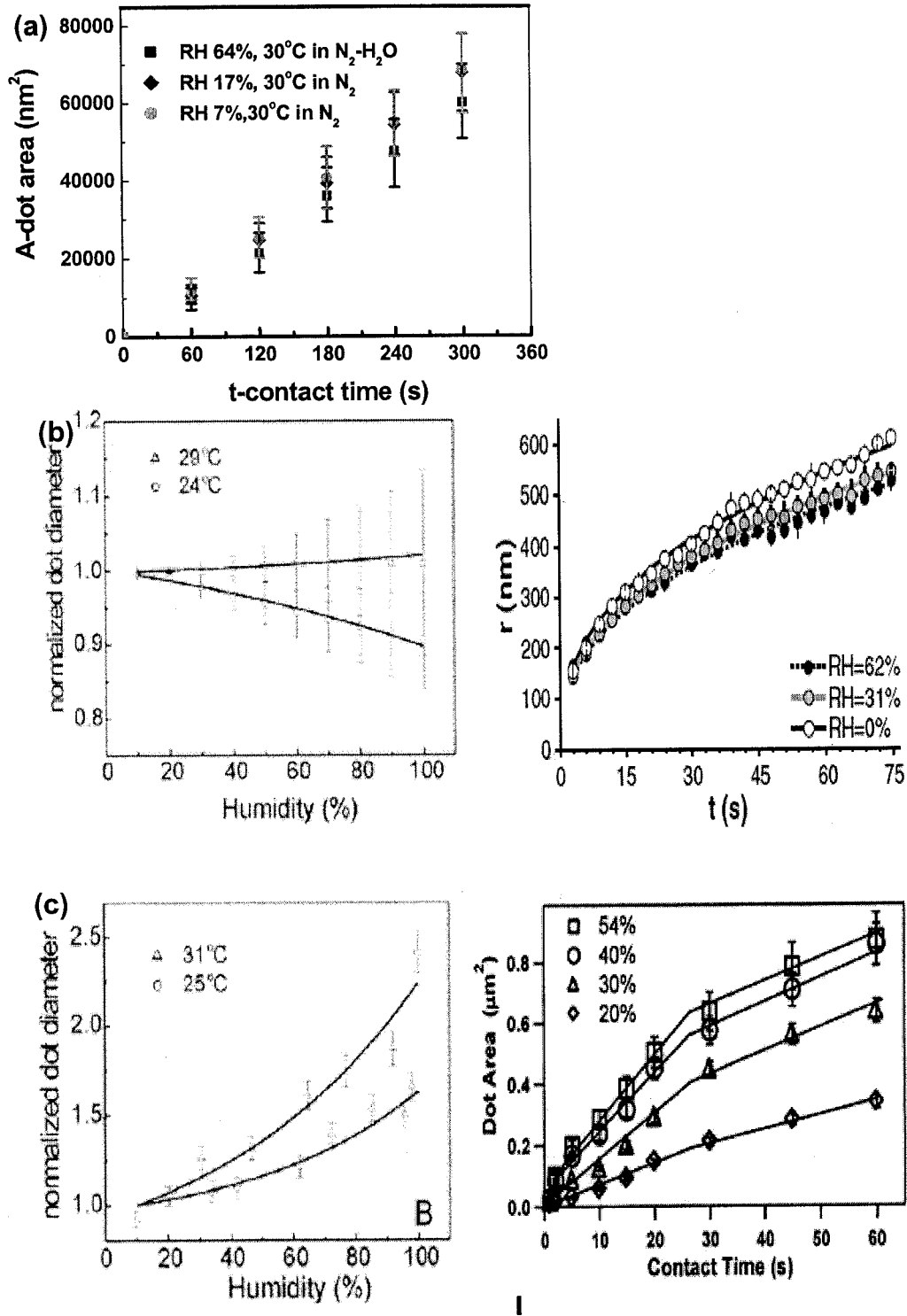


Fig.4-24 (a) $A-t$ curves measured as a function of relative humidity for P(VDF-TrFE). A is averaged from three independent measurements, and the error bars are standard deviations. The humidity dependencies of the growth rate of ODT (b) [246,248] and MHA (c) [245,248].

Figure 4-24b shows the humidity dependencies of the growth rate of another hydrophobic ink, 1-octadecanethiol (ODT) reported by P. E. Sheehan et al. [246] and S. Rozhok [248]. The relative humidity produced a slight effect on the deposition of ODT.

Figure 4-24c shows the humidity dependencies of the growth rate of a hydrophilic ink, 16-mercaptohexadecanoic acid (MHA) [247,248,263]. Different from the above two hydrophobic inks, the transport rate increased as the relative humidity increased.

ODT and MHA have many similar properties: both ODT and MHA are thiols, they have nearly the same molecular weight (about 286 g/mol) and chain length (about 3nm) [272], and they form self-assembled monolayers on gold due to the formation of Au-S covalent bond. The only difference between ODT and MHA is the hydrophilicity. When ODT and MHA were used as DPN inks, two different results were observed. The first was the different influence of relative humidity as described above. The second was that the transport rate of ODT was lower than that of MHA, which has been illustrated in Figure 2-14 and in other groups' work [194,247-248].

In addition, relative humidity played a significant role on DPN for water-sensitive inks. For example, trichlorosilanes and trialkoxysilanes were very sensitive to relative humidity due to the polymerization which would result in heterogeneous and highly polymeric network. DPN with trialkoxysilanes even became unsuccessful when the relative humidity was above 30% [274-276].

Effects of Experimental Conditions on Dip-pen Nanolithography

It is thus reasonable to deduce the following conclusions: (1) For water-sensitive inks, relative humidity must be controlled to a proper range for realizing successful DPN. The range is ink-dependent. (2) For water-insensitive inks, the influence of relative humidity depends on the solubility of the ink molecules in water. Schwartz [247] suggested the following three transport styles for a hydrophobic ink as illustrated in Figure 4-25. When there is no meniscus, the ink molecules are deposited from the AFM tip to the substrate and then

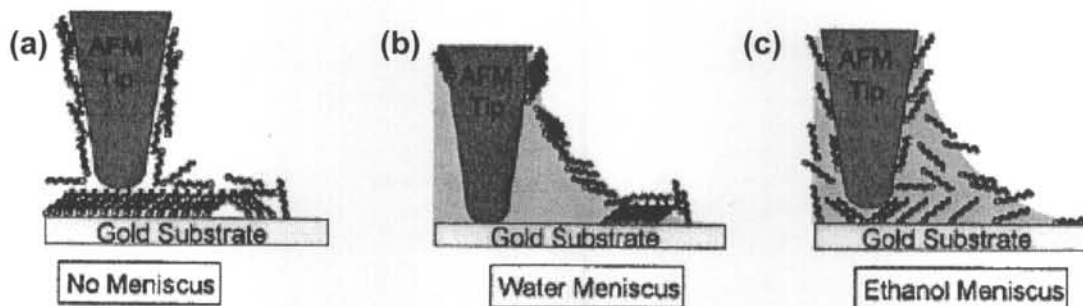


Fig.4-25 Schematic diagram of the ODT distribution at three conditions: (a) there is no meniscus, (b) Water meniscus exists, and (c) Ethanol meniscus exists. ODT dissolved in the ethanol meniscus and then deposited on gold [247].

diffuse radially (Figure 4-25a). When water meniscus exists, ink molecules transfer from the water surface and then deposited on the surface from the periphery of the meniscus (Figure 4-25b). If this were true, then there would be no ink molecules to exist at the center of the DPN-generated features at high relative humidity. However, we have not observed this phenomenon, and no other research groups reported similar results. Therefore, we proposed a deposition style for hydrophobic inks as illustrated in Figure 4-

26a. The AFM tip coated with hydrophobic molecules could suppress the formation of a meniscus, and the ink molecules were deposited to the substrate by pushing the water film on the gold surface away. To verify our hypothesis, we measured the capillary force sensed by the tip, which was coated with different inks. The results are shown in Table 4-2 and Table 4-3. In Table 4-2, the same gold sample was used for measurement, and the relative humidity was controlled at the same value. The capillary forces sensed by a clean tip (CSG 11), a tip coated with hydrophobic P(VDF-TrFE), and a tip coated with hydrophilic MHA are about 0.061 nN, 0.041 nN, and 0.098 nN, respectively. Similarly, in Table 4-3, at the same condition, the capillary force sensed by a clean tip (CSG 11), a tip coated with hydrophobic ODT, and a tip coated with hydrophilic MHA are about 0.196 nN, 0.162 nN, and 0.822 nN, respectively. Namely the hydrophobic coating can suppress the formation of a meniscus, and the hydrophilic coating can improve the formation of a meniscus. Two other research groups obtained the same trend either from computer simulation or from experimental results [243, 277].

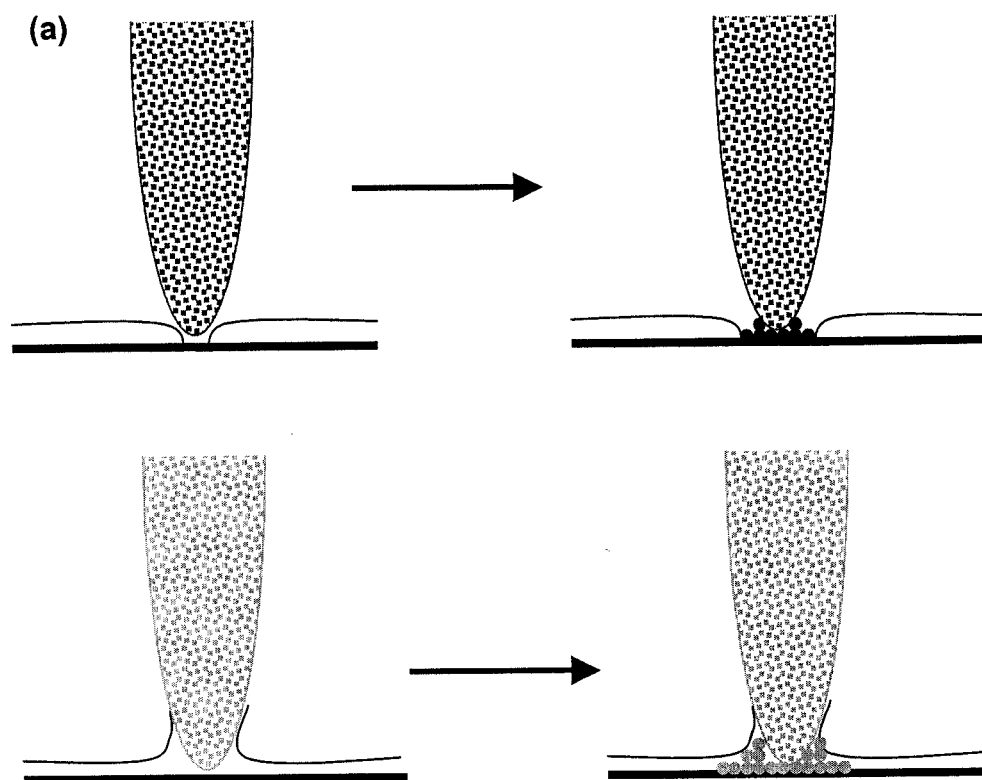


Fig.4-26 Schematic diagram for the deposition of ink

(a) hydrophobic ink, (b) hydrophilic ink

Table 4-2 The capillary force sensed by an AFM tip coated with inks which have different solubilities

relative humidity	substrate	tip	capillary force (nN)
48%	Gold	clean tip	0.061 ± 0.025
48%	Gold	tip coated with P(VDF-TrFE)	0.041 ± 0.007
48%	Gold	tip coated with MHA	0.098 ± 0.012

Table 4-3 The capillary force sensed by an AFM tip coated with inks which have different solubilities

relative humidity	substrate	tip	capillary force (nN)
68%	Gold	clean tip	0.196±0.074
68%	Gold	tip coated with ODT	0.162±0.054
68%	Gold	tip coated with MHA	0.822±0.101

In terms of energy, it is beneficial to form ink patterns rather than keep the water film on the substrate surface. For example, in the generally used gold (substrate)-thiol (ink) system, the binding energy of H₂O-gold is 40-65 KJ/mol [278], while the binding energy of thiol-gold is 184 KJ/mol. For hydrophilic inks, which were similar to those shown in Figure 4-25c, the ink molecules dissolved in the meniscus and were deposited on the substrate surface, as illustrated in Figure 4-26b. The width and thickness of the meniscus increased as the relative humidity increased, therefore, the dissolved ink molecules increased as the relative humidity increased, namely relative humidity played a positive effect on the deposition of hydrophilic inks. The meniscus that was formed between the hydrophilic tip (a tip coated with MHA) and the substrate increased the contact area between the ink and the substrate, resulting in a greater speed than a hydrophobic ink (ODT).

4.5 Effect of Tip Size

The commercial tips, which have the same material, the same force constant and different curvature radii could not be obtained. However, three types of tips that have the same force constant and different curvature radii but with different components were obtained. The three types of tips were: (1) contact silicon cantilever, (2) contact silicon nitride cantilever, and (3) contact Au cantilever. All of them have a force constant of 0.03 N/m, which are suitable for DPN. Therefore, we studied the effect of tip size using the parameters of the three types of tips by assuming they were composed of the same material. The curvature radii and the cone angles for the three tips were 10 nm, 20 nm, 50 nm, 22°, 30° and 30°, respectively. We assumed DPN was conducted at ambient condition (25°C, and relative humidity of 50%). When there was no meniscus formed between a hydrophobic tip and the substrate, the ink molecules diffused radially from the periphery of the contact point, as illustrated in Figure 4-27a. Apparently, a tip with a bigger curvature radius caused a larger contact point, and generated nanopatterns with a larger size. Though there was no meniscus formed, a water film existed on the gold surface. According to Lee and Staehle's report, at 25°C and a relative humidity of 50%, the thickness of water on gold was about three layers [279]. It is well known that the diameter of water molecule is $3.10 \times 10^{-10} \text{ m}$; therefore, the thickness of the water film (h) was calculated to be 0.93 nm . The contact radii (r') for the three types of tips were calculated using the equation $r' = \sqrt{r^2 - (r - h)^2}$, which were calculated to be 4.75 nm , 6.82 nm , and 10.89 nm , respectively. The contact radius r' increased as the

curvature radius of the AFM tip increased. The relationship between the water thickness on gold and relative humidity at room temperature is shown in Figure 4-27b [279]. One can calculate the contact radius under other relative humidity conditions using this relationship.

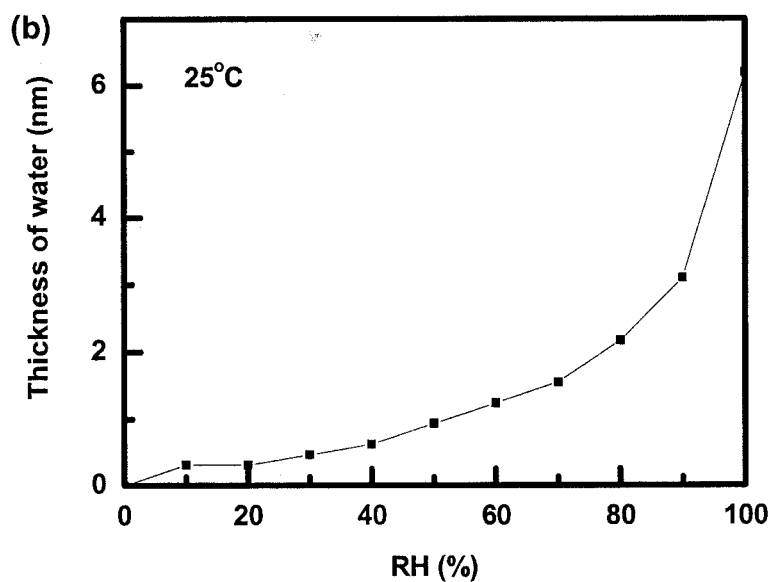
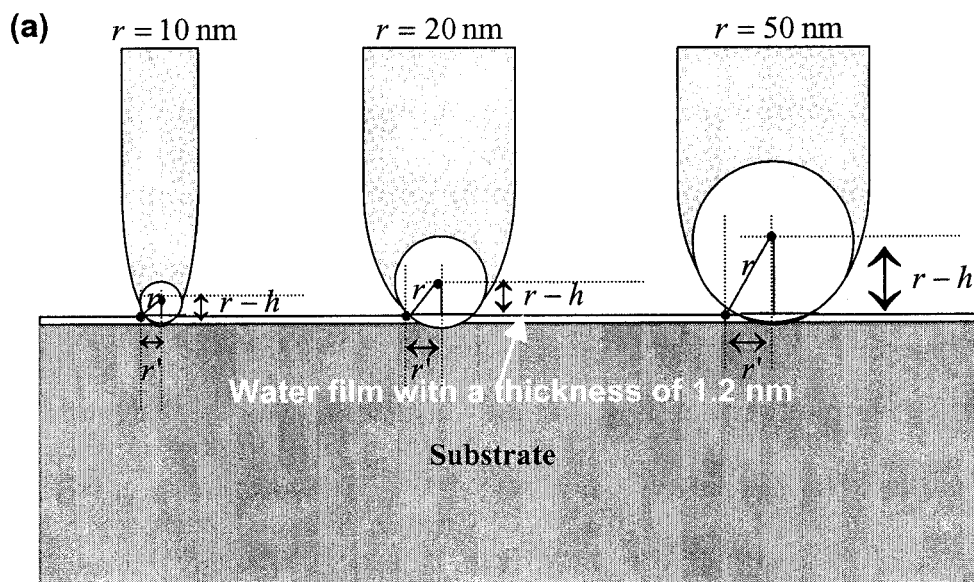


Fig.4-27 (a) Schematic diagram of the calculation of contact radius for tips which have different curvature radius when no meniscus is formed between the tip and the substrate. (b) The relationship between water thickness on gold and the relative humidity at 25°C (derived from [279]).

Effects of Experimental Conditions on Dip-pen Nanolithography

For most of the inks (such as thiols [202], P(VDF-TrFE), conducting polymer [201], 1-dodecylamine [251]), the time-dependencies of the size of the DPN-generated patterns can be resolved successfully using a diffusion model [249]. The DPN process, which contained two steps (i.e., the ink molecules are transported from the coated tip to the substrate and then form desired nanopatterns), was simplified as the diffusion of ink molecules on the substrate surface to form patterns. The driving force was the concentration gradient and the chemical affinity between the ink and the substrate. In our assumption, the DPN was conducted using the same ink, the same substrate, and the same tip material under the same experimental conditions (i.e., temperature, relative humidity). The only difference was the curvature radius of the tip. Therefore, the diffusion constant (D) and starting concentration (C_0) were the same for the three tips, thus results in the same diffusion length, l . However, the measured diffusion length l' contained the contact radius r' , i.e., $l' = l + r'$. At the same conditions, l' increased as the curvature radius of the AFM tip increased.

However, when a meniscus was formed between the tip and the substrate, the contact radius depended on the width of the meniscus (w). Utilizing the grand canonical Monte Carlo simulation of a two-dimensional lattice gas model, Jang and colleague calculated the width of meniscus of four tips, which have a curvature radius of 8 nm, 12 nm, 23 nm, and 46 nm, respectively. In their report, the width of the meniscus of the four tips at 25°C and a relative humidity of 50% is 18 nm, 24 nm, 36 nm, and 48 nm, respectively. Thus, the width of the meniscus increased as the curvature

radius of the tip increased [243]. At the same temperature and relative humidity, the width of the meniscus is estimated to be about 20 nm, 34 nm, and 52 nm for the tips which have a curvature radius of 10 nm, 20 nm, and 50 nm, respectively. A schematic diagram is illustrated in Figure 4-28a. The meniscus was symmetric around the tip, but only half of the meniscus was drawn for simplification. Here, the contact radius (r') was half of the width of the meniscus ($w/2$). Specifically, the contact radius for the three types of tips was about 10 nm, 17 nm, and 26 nm, respectively. Similar to the condition where no meniscus was formed, the diffusion length of ink molecules, l' , can be expressed as: $l' = w/2 + l$ or $l' = r' + l$. Figure 4-28b is the relationship between meniscus width and tip curvature radius derived from reference [243] at 25°C and 50% RH for a completely wetting tip. The meniscus width grows roughly with square root of curvature radius of tip. The trend may be different for an incompletely wetting tip.

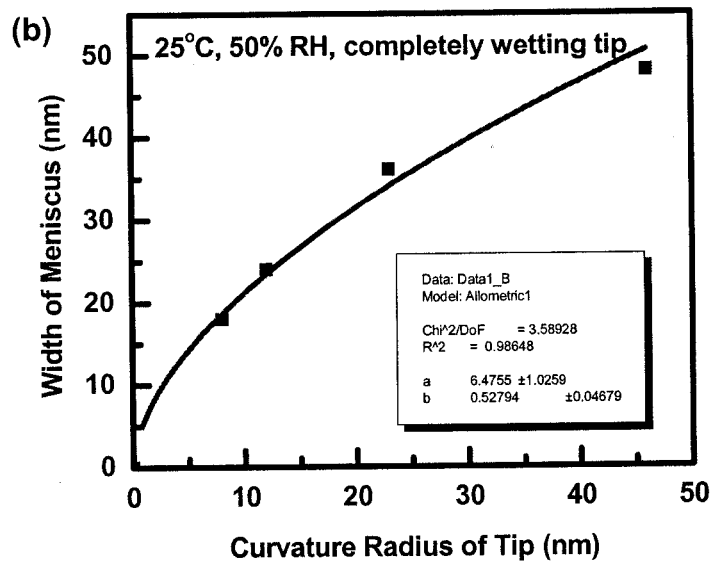
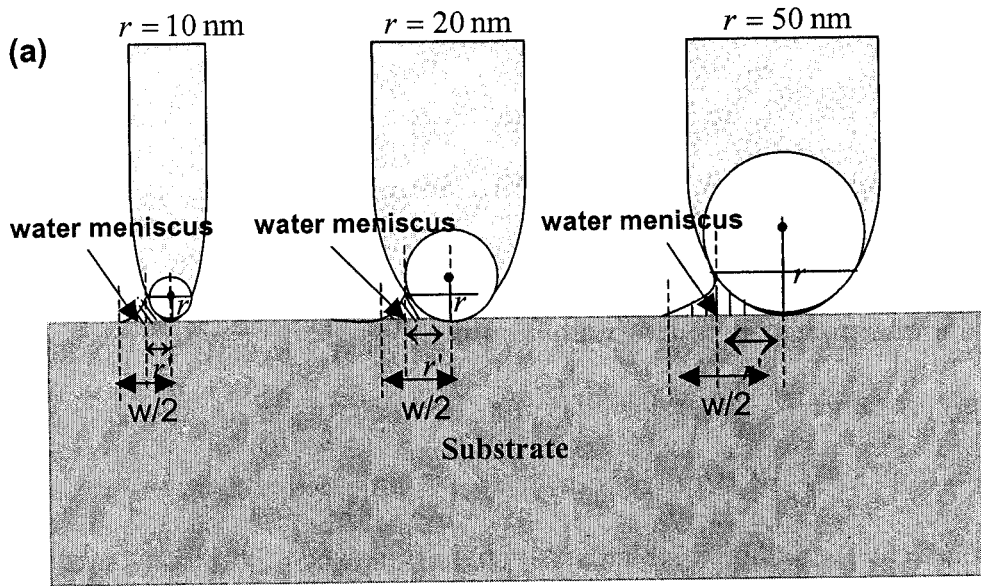


Fig.4-28 (a) Schematic diagram of the calculation of contact radius for tips with different curvature radius when meniscus is formed between the tip and the substrate. (b) The relationship between meniscus width and curvature radius of tip at 25°C and 50% RH for a completely wetting tip.

The comparison of the contact radius with/without meniscus is shown in Table 4-4. Where meniscus is formed, the contact radius is much larger than the contact radius where no meniscus is formed.

Table 4-4 Comparison of the contact radius with/without meniscus at 25°C and 50% relative humidity for the three types of tips

Curvature radius \ Contact radius	No meniscus	Meniscus is formed
10	4.75 nm	10 nm
20	6.82 nm	17 nm
50	10.89 nm	26 nm

4.6 Effect of Chemical Affinity

Since its invention, dip-pen nanolithography (DPN) has been proven to be a promising nanolithography which has potential applications in biosensor, gas sensor, electrical and optical nanodevices. In a DPN process, one special functional material is deposited onto a substrate of interest via an AFM tip. It is important to identify the controlling parameters that would improve the rate and quality of DPN patterning. As illustrated above, many parameters, such

as temperature, substrate roughness, relative humidity, properties of ink, and the geometry and material of the tip would all produce some effect on DPN. However, the effect of chemical affinity has not been systematically studied. In the early days, capillary force was considered to be the driving force for DPN process [202], which stimulated hot discussions in the literature. Some researchers functionalized the ink molecules with a functional group such as $-SH$ for gold substrate [144] or trichlorosilane for SiO_2 substrate [276] in order to increase the ink affinity to the substrate. However, the ink-tip affinity is usually neglected, and there has thus far been no conclusion on what is the key parameter in DPN. Here, we probed this question by controlling the ink affinity to the tip and substrate through the selection of tips, inks and substrate materials, and comparing with other controlling parameters during the DPN process.

4.6.1 Experimental

The substrates used in this study were 30 nm of polycrystalline thin films of Au, or Ag, or Pt on 10 nm of Ti adhesive layer that was deposited on Si(100) wafer by sputtering.

The inks were 1 mM 1-octadecanethiol (ODT)/acetonitrile solution, and 0.72 mg/mL of P(VDF-TrFE)/acetone solution. Three types of contact tips, made by Si, or Si_3N_4 , or Au, with a force constant of 0.03 N/m were used for DPN. The curvature radius for a Si tip, Si_3N_4 tip and Au tip are of 10 nm, 20 nm and 50 nm.

The tip coating method, the controlling of relative humidity and temperature, DPN patterning and AFM imaging were the same as the methods described previously.

4.6.2 Results and Discussion

The DPN patterning results on Au are summarized in Table 4-5. Here, “+” and “-” denote successful and unsuccessful patterning processes, respectively. It was reported that the transport rate of ODT increased exponentially as the temperature increases [247]. In section 4.3, we have demonstrated that a rough gold surface (roughness > 1.1 nm) can give poor contrast in lateral force microscopy (LFM) images. We took the following measures for the failed cases in order to clarify the effects of different parameters: (1) elevating the substrate temperature to as high as 60°C; (2) changing the relative humidity from 5% to 80%; (3) checking the coated tips using SEM; (4) using the substrate with flat surface (roughness was about 0.6 nm); (5) prolonging the contact time between the tip and the substrate. DPN was still unsuccessful with the Au tip.

Effects of Experimental Conditions on Dip-pen Nanolithography

Table 4-5 DPN results on gold substrate with ODT and P(VDF-TrFE) as ink using Si, Si₃N₄ and Au tips

Tip	Si	Si ₃ N ₄	Au
Ink1		ODT	
DPN result	+	+	-
Ink2		P(VDF-TrFE)	
DPN result	+	+	+

“+” means successful and “-” means unsuccessful

First, ODT was used as the DPN ink for a gold substrate. The three types of tips were coated with ODT by immersing the cantilevers into a solution of 1 mM ODT in acetonitrile, and gently blown dry with N₂. Then the coated tips were visualized with a FE-SEM. Figures 4-29a, 4-29c, and 4-29e show new Si tip, Si₃N₄ tip and Au tip, and Figures 4-29b, 4-29d and 4-29f show the corresponding coated tips. For all of the three types of tips, the new tips were clean without anything adsorbed on the surface; while ODT were left on the tip surface after coating and evaporation of the solvent.

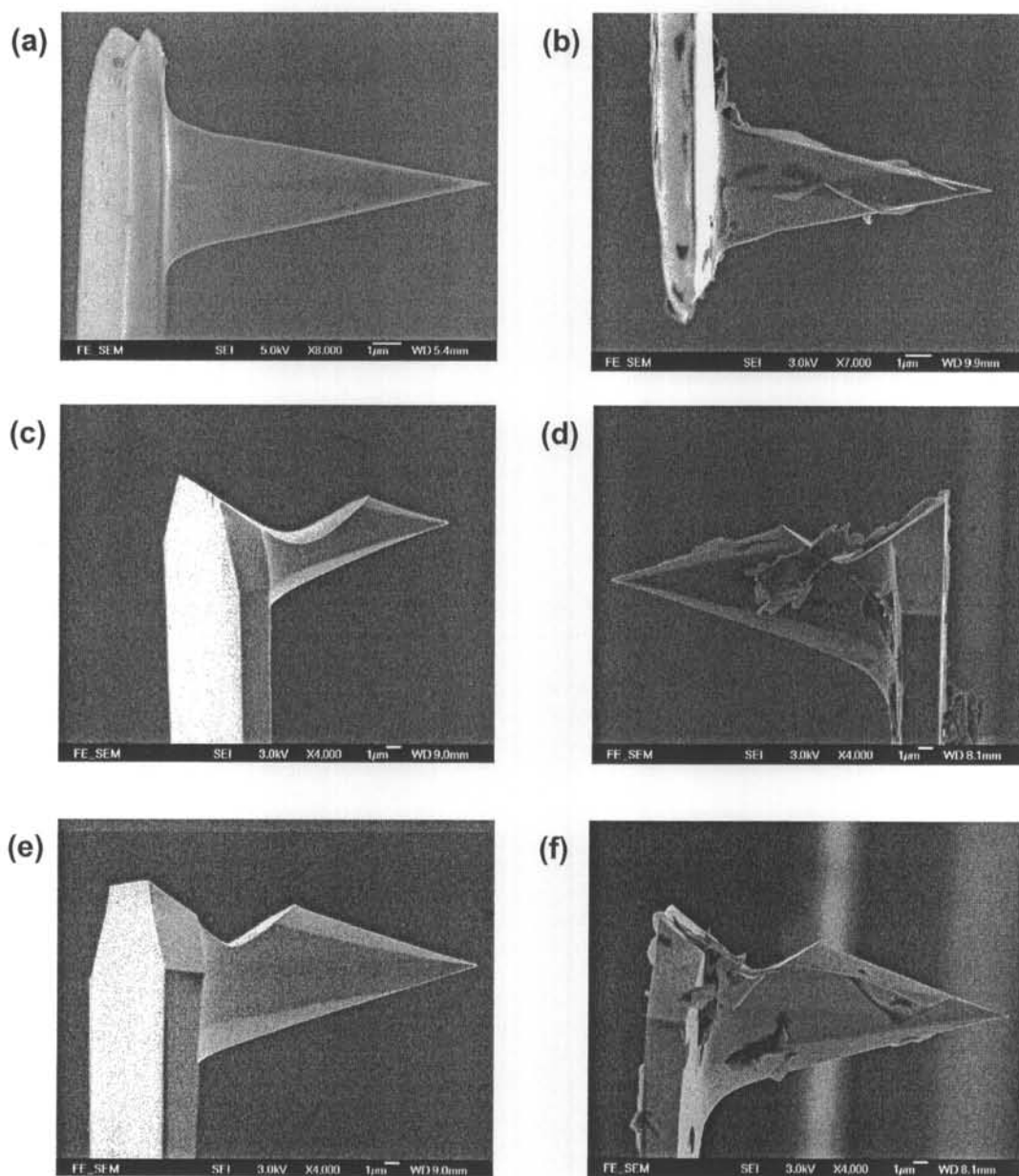


Fig.4-29 SEM micrographs of (a) clean Si tip, (b) Si tip coated with ODT, (c) clean, (d) Si₃N₄ tip coated with ODT, (e) clean Au tip and (f) Au tip coated with ODT.

Although ODT had been coated on Au tip as visualized by FE-SEM (Figure 4-29f), we failed to deposit ODT to the Au substrate using an ODT coated Au tip by trying five independent tips. The Si tip and Si₃N₄ tip that were coated

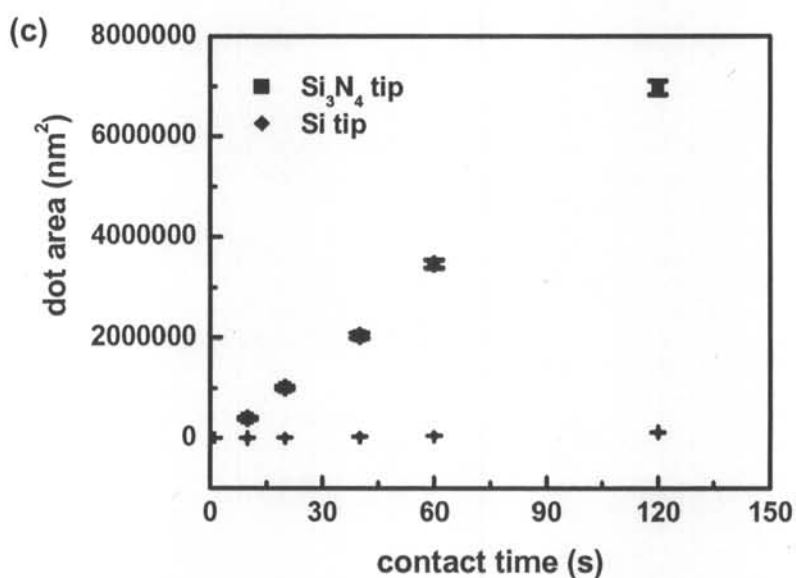
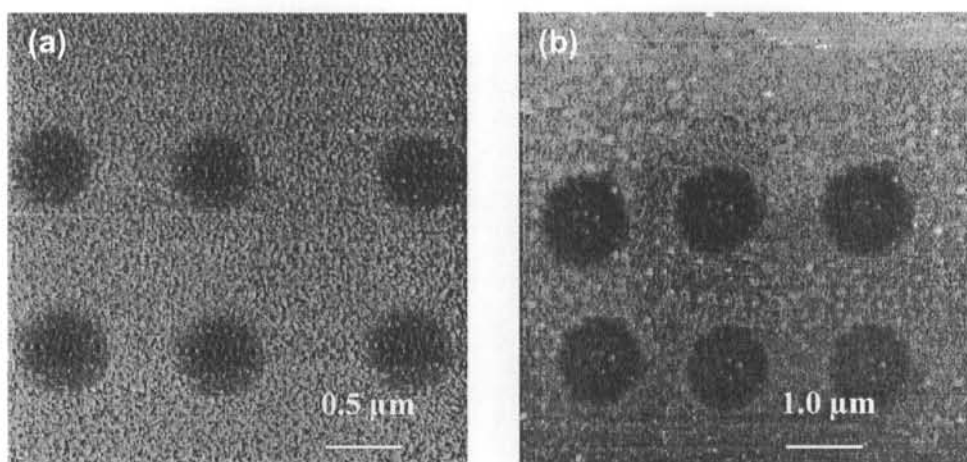


Fig.4-30 (a) LFM image of an ODT point array fabricated with a Si tip coated with ODT at 25°C and a relative humidity of 50%. Contact time: 180s. (b) LFM image of an ODT point array fabricated with a Si₃N₄ tip coated with ODT at 25°C and a relative humidity of 50%. Contact time: 20s. (c) Comparison of the transport rate of ODT to gold using a Si tip and a Si₃N₄ tip at the same experimental conditions (25°C and a relative humidity of 50%). The effect of tip size is deducted.

with ODT can be used to deposit ODT to a gold substrate easily. Both of the patterns fabricated with a coated Si tip and a coated Si₃N₄ tip produced black contrast in LFM images, independent of the tip materials (see Figures 4-30a and 4-30b); However, the transport rate of ODT was different (see Figure 4-30c). The transport rate of ODT with a Si₃N₄ tip was much faster than that with a Si tip. The transport rate (v) was defined as $v = \frac{dA}{dt}$. The transport rate of ODT with a Si tip (v_{Si}) and a Si₃N₄ tip ($v_{Si_3N_4}$) was about =1001 nm²/s and 59036 nm²/s by linear fitting the corresponding $A \sim t$ curves. Therefore the transport rate of ODT with a Si₃N₄ tip is about 59 times of that with a Si tip.

Second, P(VDF-TrFE) was used as the DPN ink. The coated tips were also visualized with a FE-SEM. Figures 4-31a to 4-31c show Si tip, Si₃N₄ tip, and Au tip coated with P(VDF-TrFE). For all of the three types of tips, P(VDF-TrFE) were left on the tip surface after coating and evaporation of the solvent.

Similar to ODT, P(VDF-TrFE) can not be transported to the Au substrate using a P(VDF-TrFE) coated Au tip by trying five independent tips. The Si tip and Si₃N₄ tip coated with P(VDF-TrFE) can be used to deposit P(VDF-TrFE) to a gold substrate easily. Both of the patterns fabricated with a coated Si tip and a coated Si₃N₄ tip produced black contrast in LFM images, independent of the tip materials (see Figures 4-32a and 4-32b); However, the transport rate of P(VDF-TrFE) was different (see Figure 4-32c). The transport rate of

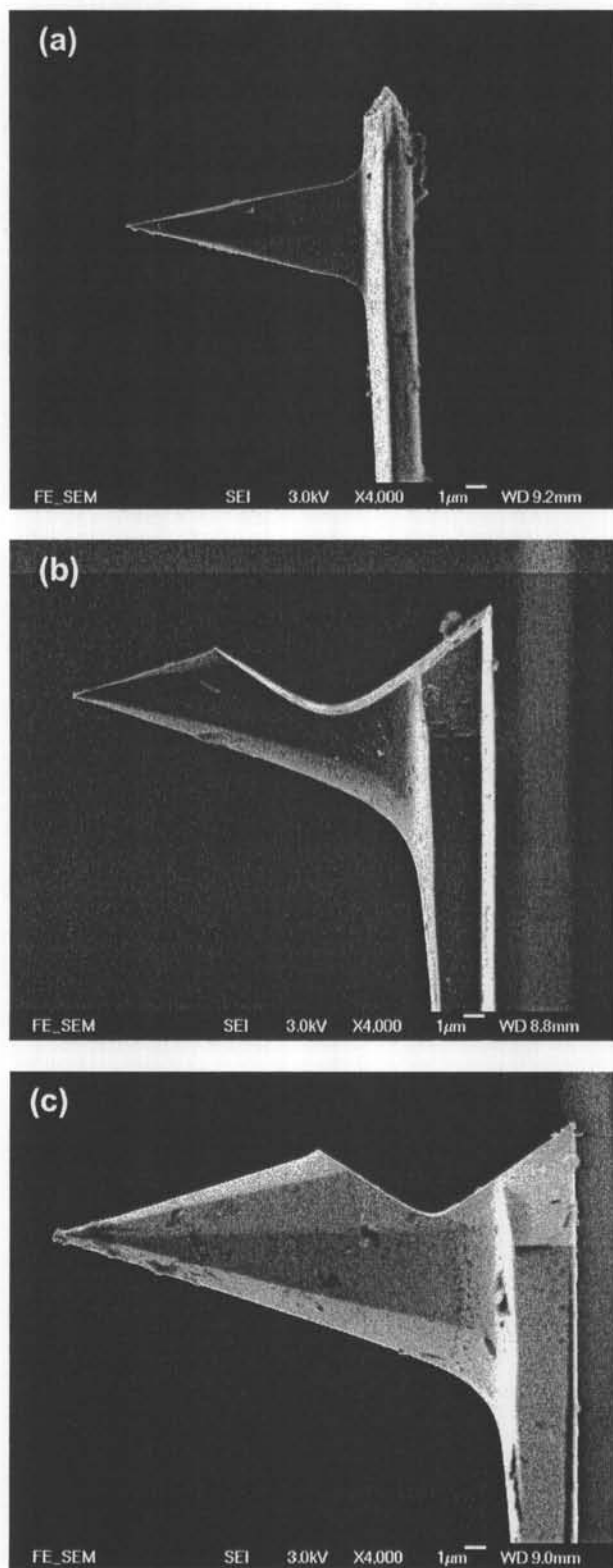


Fig.4-31 SEM micrographs of tips coated with P(VDF-TrFE): (a) Si tip, (b) Si₃N₄ tip, and (c) Au tip.

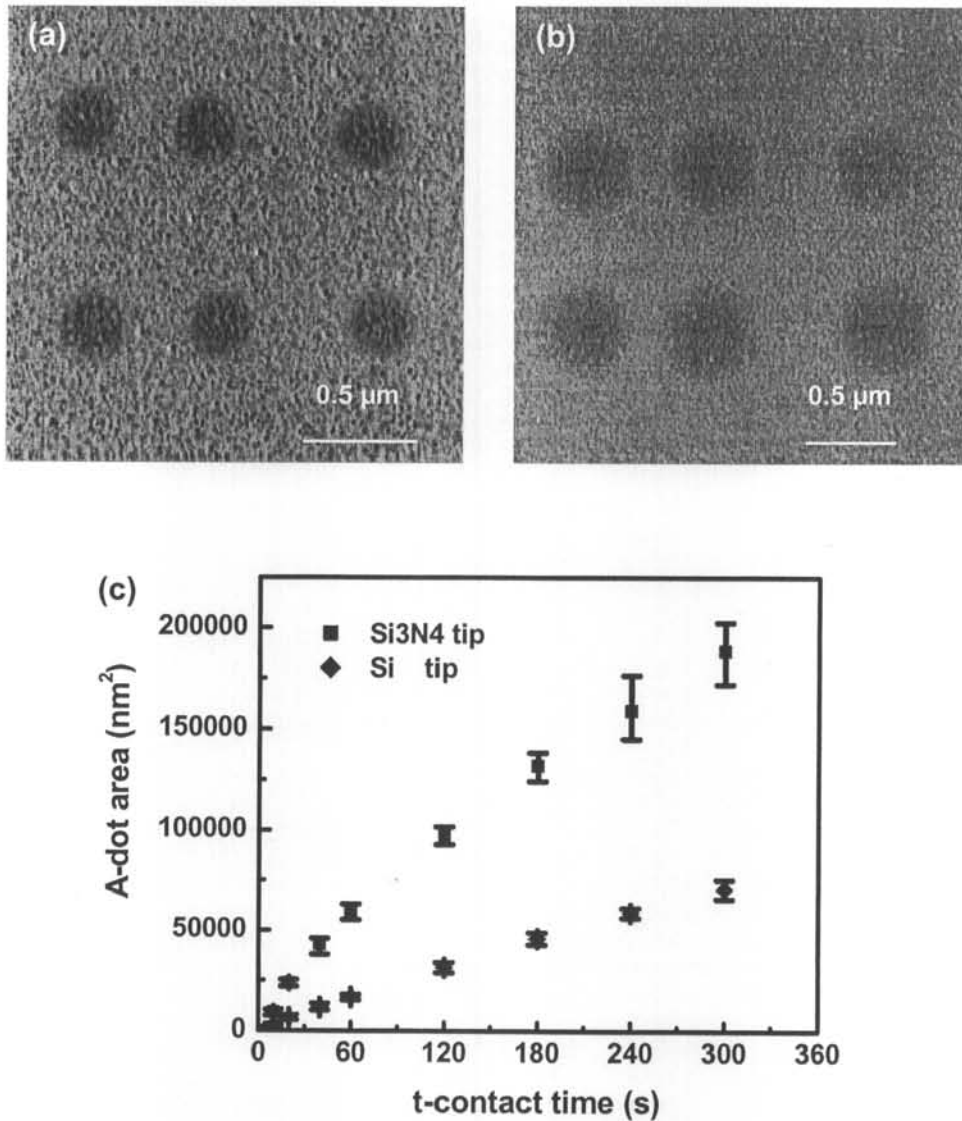


Fig.4-32 (a) LFM image of a P(VDF-TrFE) point array fabricated with a Si tip coated with P(VDF-TrFE) at 25°C and a relative humidity of 50%. Contact time: 240s. (b) LFM image of an P(VDF-TrFE) point array fabricated with a Si₃N₄ tip coated with P(VDF-TrFE) at 25°C and a relative humidity of 50%. Contact time: 20s. (c) Comparison of the transport rate of P(VDF-TrFE) to gold using a Si tip and a Si₃N₄ tip at the same experimental conditions (25°C and a relative humidity of 50%). The effect of tip size is deducted.

Effects of Experimental Conditions on Dip-pen Nanolithography

P(VDF-TrFE) with a Si_3N_4 tip was much faster than that with a Si tip. The transport rate of P(VDF-TrFE) with a Si tip (v_{Si}) and a Si_3N_4 tip ($v_{\text{Si}_3\text{N}_4}$) was about $\approx 237 \text{ nm}^2/\text{s}$ and $620 \text{ nm}^2/\text{s}$ respectively by linear fitting the corresponding $A \sim t$ curves. Therefore the transport rate of P(VDF-TrFE) with a Si_3N_4 tip is about 2.6 times of that with a Si tip.

Furthermore, the same DPN results were obtained on a silver substrate as on a gold substrate (Figure 4-33), but DPN failed on a platinum substrate with all three types of tips. Ag has most of same chemical properties as Au. ODT can form self-assembled monolayers on Ag [280]. Therefore, ODT can be transferred to Ag with Si and Si_3N_4 tips, while the two inks do not have strong chemical affinity to Pt, DPN can not be realized. Moreover, the repeatability on Ag is not as good as on Au, DPN can not realized on Ag after the Ag substrate exposed to air for about two hours. Because Ag is easily oxidized under ambient condition, a thin film of silver oxide layer covers the Ag surface, thus changing the chemical interaction between the ink molecules and the substrate.

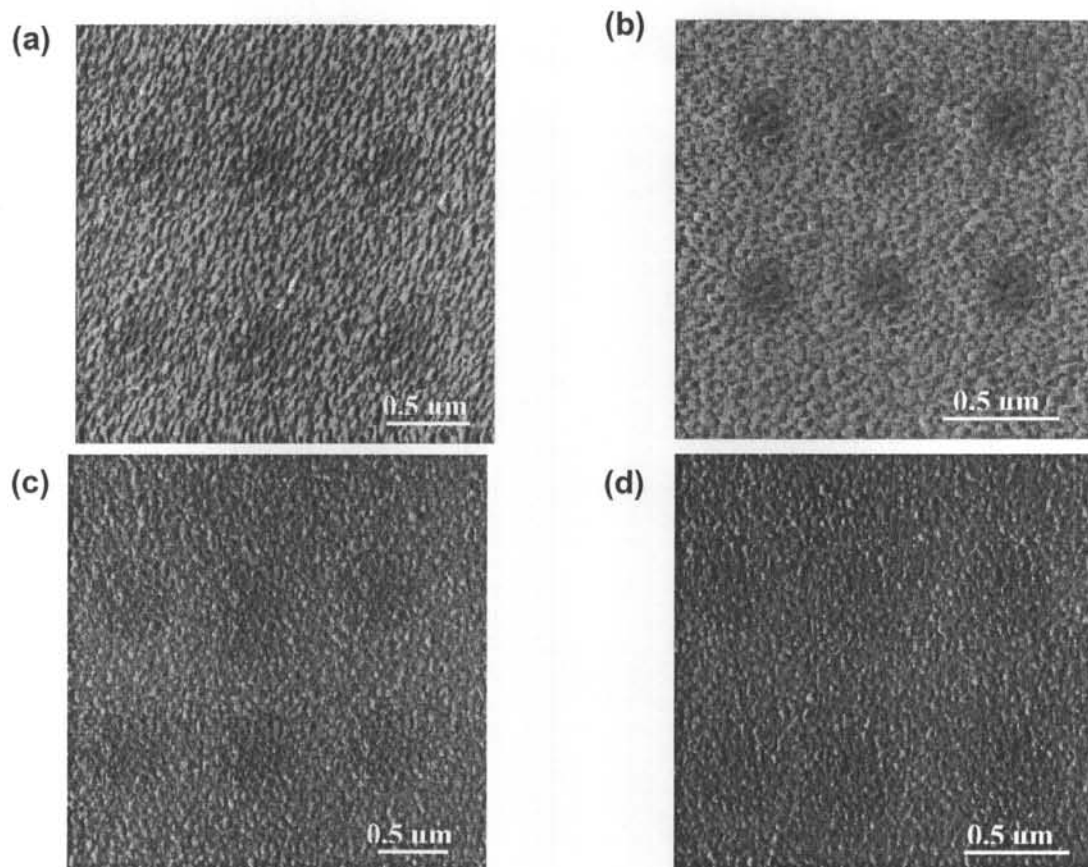


Fig.4-33 Lateral force microscopy images of points array on silver substrate (25°C, RH 50%). (a) and (b) is a point array of P(VDF-TrFE) fabricated with Si_3N_4 tip and Si tip for 180 s per dot, respectively. (c) and (d) is a point array of ODT fabricated with Si_3N_4 tip and Si tip for 20 s per dot.

This reminded us that the possible reason may lie in the difference in chemical affinity. It is well known that there exists strong chemical affinity between thiol and gold through the formation of Au-S covalent bond [195]. ODT has a stronger chemical affinity to the Au substrate than to the tip made of Si or Si₃N₄. If we denote f_{A-B} as the chemical affinity between A and B, then when $f_{ink-tip} < f_{ink-substrate}$, DPN can be realized. When the tip is Au, i.e., $f_{ink-tip} = f_{ink-substrate}$, DPN can not be realized. This indicates that the chemical affinity plays an important role in DPN. It might be reasonable to assume that DPN can not be realized when $f_{ink-tip} \geq f_{ink-substrate}$. Our hypothesis has been supported by the second type of ink, P(VDF-TrFE), which can not form effective chemical covalent bond with either the tips or the substrate. Since P(VDF-TrFE) molecules have a stronger affinity to gold than to Si and Si₃N₄. The DPN results with P(VDF-TrFE) ink were the same as for ODT, as described above.

Figure 4-34 shows how the chemical affinity controls DPN: ink can not be transferred to a substrate via DPN if $f_{ink-tip} \geq f_{ink-substrate}$, and can be transferred to the substrate if $f_{ink-tip} < f_{ink-substrate}$.

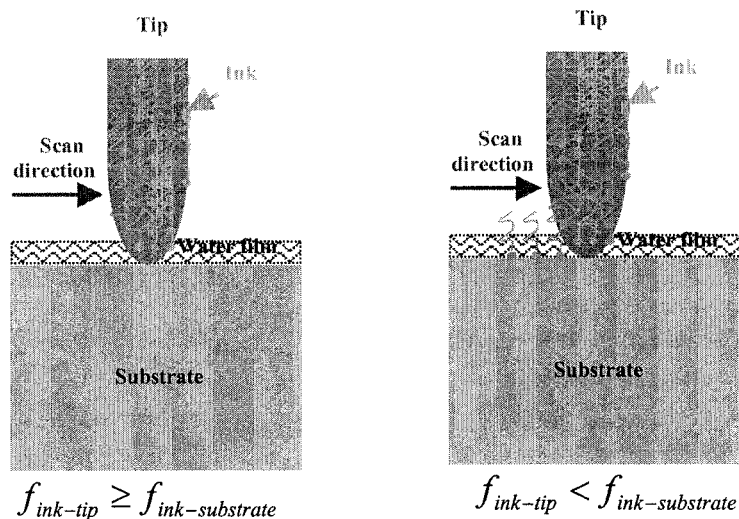


Fig.4-34 The influence of chemical affinity on dip-pen nanolithography.

Chemical affinity is also an important parameter for DPN. Chemical affinity, relative humidity, temperature, coating method, and surface properties of substrate not only influence the transport rate of ink, but also lead to unsuccessful DPN at special conditions. For example, high hydrophilic inks are very sensitive to relative humidity; an ink will become frozen and can not be transported to the substrate below a critical temperature, etc [281]. It was also found that the coating method [282] and the surface roughness of substrate influenced the transport rate of ink.

4.7 Summary

In summary, the effect of temperature, surface roughness of the substrate, relative humidity, tip size as well as chemical affinity on the DPN have been studied:

- The transport of ink increases as the temperature increases. For P(VDF-TrFE), the relationship between r and t is $r = at^{1/2}$ form 25~70°C. a is temperature-dependent. It is related to diffusion constant. A deviation from Arrhenius plot at about 55°C is observed. This may be caused by a ferroelectric phase transition for such thin ferroelectric film or the shift of the ferroelectric phase transition under the special conditions. When the temperature is below 55°C, the transport rate of the P(VDF-TrFE) molecules increases exponentially with temperatures, which conforms to the Arrhenius plot. The activation energy (Q) was calculated to be 0.98 eV.

- Surface roughness influences both the contrast in LFM images and the transport rate of ink. Surfaces with less roughness give good contrast in LFM images, while rough surfaces give poor contrast. Rough surface (i.e., roughness is greater than 1.65 nm) was not suitable for DPN. For both ODT and P(VDF-TrFE), the dot area grew linearly with t in all the measured roughness ranges. The transport rate of ink increased as the roughness decreased. It may be caused by the increased friction force or the decreased diffusion constant. However, the extent of the influence was strongly ink-dependent. For ODT, the transport rate of ink decreased linearly as the roughness increased. For P(VDF-TrFE), the transport rate of ink

decreased rapidly as the roughness increased when the roughness was less than 1.0 nm, while the roughness produced a little effect on the transport rate of ink when roughness was greater than 1.0 nm. This is probably caused by the different ink-substrate interaction. In this project, a general theory about the transport rate of ink and surface roughness has not been obtained. In future, a quantitative theory may be obtained through more detailed study using various ink-substrate systems and a broad surface roughness range.

- The influence of relative humidity depended on the solubility of the ink in water. The transport rate of hydrophilic ink increased as the relative humidity increased due to the increased meniscus width, while the transport rate of hydrophobic ink experience small change as the relative humidity increased, because the hydrophobic molecules does not deposited to the substrate through the meniscus but directly to the substrate surface. It is difficult to obtain a quantified equation for inks with different solubility.

- When no meniscus was formed between the substrate and the tip for a hydrophobic tip, the effect of tip size depended on the tip contact radius. The tip contact radius can be calculated using $r' = \sqrt{r^2 - (r - h)^2}$. Obviously, the contact radius increased as the tip curvature radius increased. When meniscus was formed, the effect of tip size depended on the size of the meniscus width, because under ambient conditions (at 25°C and 50% RH), the width of the meniscus is larger than the tip contact radius. The meniscus width is roughly proportional to square root of tip curvature radius. Then at

Effects of Experimental Conditions on Dip-pen Nanolithography

the same conditions, a tip with a larger curvature radius can generate a larger pattern than a tip with a smaller curvature radius due to a bigger contact point or the formation of a meniscus with a larger size.

- Chemical affinity is an important controlling parameter for DPN. It is necessary to consider the ink affinity to the substrate as well as to the tip when designing a new DPN system. DPN cannot be realized when chemical affinity between the ink and tip was larger or equal to the chemical affinity between the ink and substrate. It is difficult to obtain a quantified equation on the effect of chemical affinity on DPN, because it is difficult to measure the definite values of chemical affinity between different materials.

Chapter 5 Anodic Nanooxidation, Force Nanolithography and Characterization of Protein Patterns with AFM

5.1 Anodic Nanooxidation with AFM

Local oxidation of semiconductor and metallic surfaces by atomic force microscopy (AFM) is a promising method to fabricate nanostructures for nanoelectric applications [177,192]. There are two methods to apply voltage, one is to apply a positive voltage to the sample, the other is to apply a negative voltage to the tip. Either tip negatively biased or sample positively biased depends on the AFM system. The formed oxide becomes protruded, with higher features on the sample surface. This method is also named as anodic oxidation.

5.1.1 Nanooxidation of silicon

5.1.1.1 *Experimental*

The samples are n-type Si(100) wafers with a resistance of 6 Ω -cm and thickness of 0.5 mm (Tianjin, China). Before use, the Si wafer was cleaned in clean room according to the following procedure: rinsed in deionized water (DI water) for 10 minutes and in CH₃OH bath for 5 minutes with ultrasonic agitation to remove inorganic contaminants; then rinsed in acetone bath with ultrasonic agitation for 10 minutes to remove some organic materials, and rinsed with DI water again; followed dipping in Piranha solution

Anodic Nanooxidation, Force Nanolithography and Characterization of Protein Patterns with AFM

(H_2SO_4 :30% H_2O_2 =3:1 (v:v)) at 90°C for 20 minutes, and rinsed with DI water; finally dipped in HF solution [DI water:HF(w/w)=50:1] for 45 seconds to etch the native silicon oxide film, copiously rinsed with DI water for 10 minutes, and blown dry with ultrapure N_2 .

The silicon cantilevers were coated with 25 nm TiN (MikroMasch). The typical force constant and resonance frequency of the cantilevers were about 6 N/m and 155 kHz, respectively. Negative voltage was applied to the conduct tip with respect to the silicon substrate in semi-contact mode.

5.1.1.2 Results and Discussion

The typical surface morphology of Si wafer after the tip-induced oxidation by the application of -4, -5, -6, -7, and -8 V for 2 milliseconds is shown in Figure5-1a. An appreciable morphology change was observed only when the

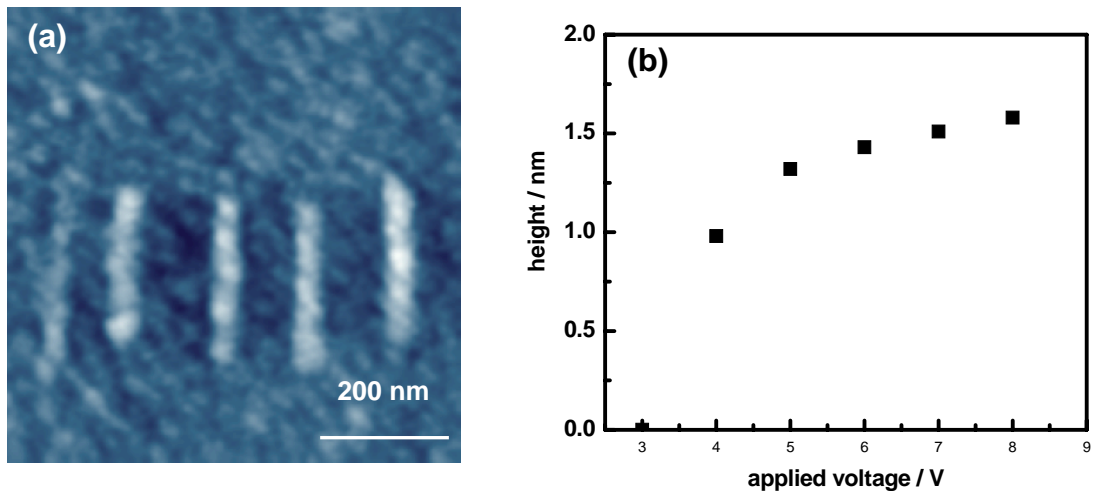


Fig.5-1 The effect of applied voltage on the oxidation of Si. (a) AFM topographic image of silicon after nanooxidation (From left to right: -4 V, -5 V, -6 V, -7 V, and -8 V applied to the tip for 2 milliseconds at a relative humidity of 28% and 20°C. (b) The dependence of oxide height versus voltage.

Anodic Nanooxidation, Force Nanolithography and Characterization of Protein Patterns with AFM

sample bias value was above 4 V. A threshold voltage existed, which was consistent with Yashtake et al's observation [191]. They obtained a threshold voltage of -5 V. The difference in threshold voltage arose from the sample. In their method, the silicon wafer was passivated with a native oxide layer; therefore, a higher threshold electric field was required. Figure 5-1b shows the dependence of silicon oxide height as a function of voltage. The height increased as the applied voltage increased. Hence, the electric field enhanced the tip-induced oxidation.

Figure 5-2a shows the silicon wafer modified by the application of -8 V to the tip for 5, 10, 20, 40, and 80 milliseconds. Figure 5-2b shows the dependence

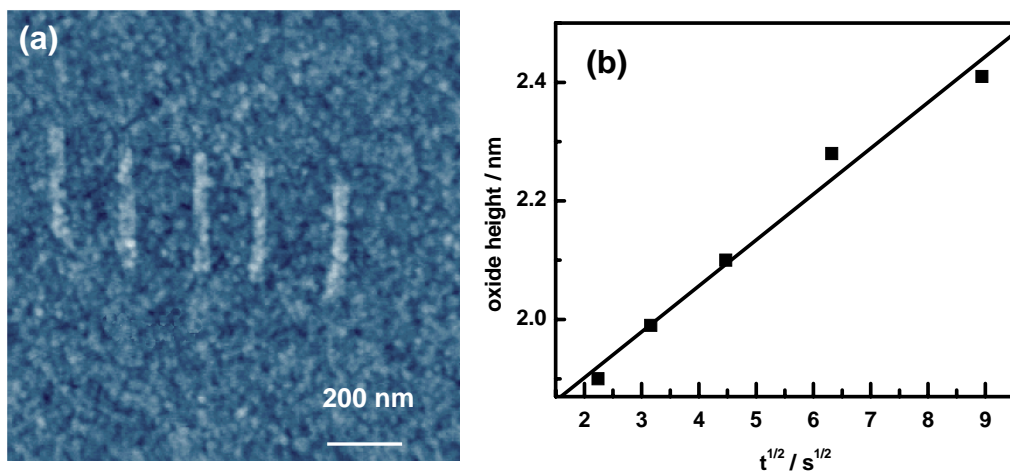


Fig.5-2 The effect of duration on the oxidation of Si. (a) AFM topographic image of silicon after nanooxidation by the application of -8 V at 20°C and at a relative humidity of 28% for 5, 10, 20, 40 and 80 milliseconds (from left to right), respectively. (b) The dependence of oxide height versus $t^{1/2}$.

Anodic Nanooxidation, Force Nanolithography and Characterization of Protein Patterns with AFM

of oxide height versus $t^{\frac{1}{2}}$. The oxide height was roughly proportional to the square root of duration with 0.99 for R by linear fitting. That means the oxidation was limited by the diffusion of oxidizing products.

Figure 5-3a shows the silicon wafer modified by the application of -10 V to the tip for 1 millisecond at a relative humidity of 54%, 44%, 34%, and 29% (from left to right), respectively, and Figure 5-3b shows the lateral contour of the lines. Both of the line width and line height increased as the relative humidity increased. The aspect ratios (height/width) for the four lines were 0.051, 0.054, 0.063, and 0.069, which means that a reduced relative humidity can improve the aspect ratio. This result proved that water takes part in the electrochemical reaction during the tip-induced oxidation. The intense electric field produced O^- ions, which oxidized silicon to form

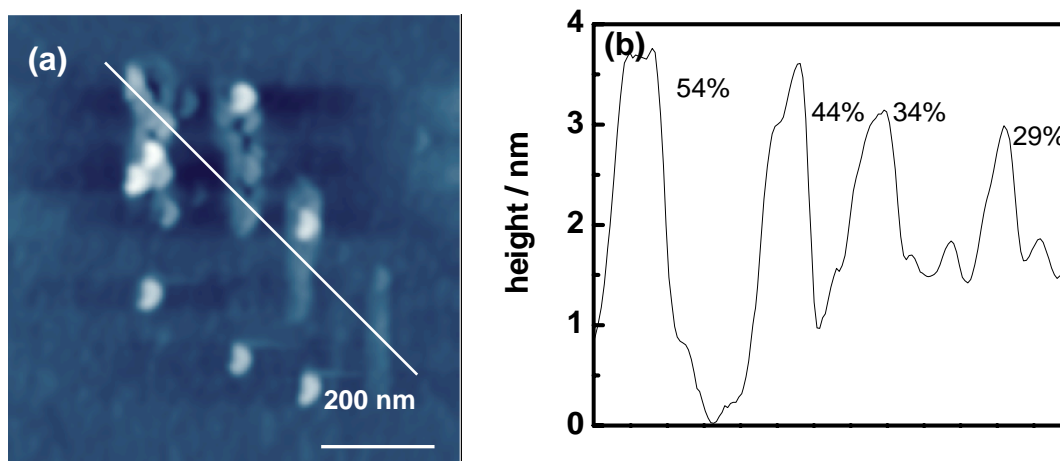


Fig.5-3 The effect of relative humidity on the oxidation of Si. (a) AFM topographic image of silicon after nanooxidation by the application of -10 V for 1 millisecond at 20°C and at a relative humidity of 54%, 44%, 34% and 29% (from left to right), respectively. (b) Lateral contour of the lines.

Anodic Nanooxidation, Force Nanolithography and Characterization of Protein Patterns with AFM

protruded silicon oxide [189]. Water, acting as a medium, could transport the ions to the silicon surface. The meniscus width increased as the relative humidity increased [243], and thus increased the reaction area. Therefore, the line width obtained at higher relative humidity was wider than that obtained at a lower relative humidity. The mechanism and kinetics about the local anodic oxidation have been studied by several research groups [166,173,174,179]. In this study, we did not focus on this field. Instead, we exploited the possibility in fabricating more complicated nanostructures by utilizing the obtained conditions. Complicated and three-dimensional structures were required in nanodevices in order to realize some special

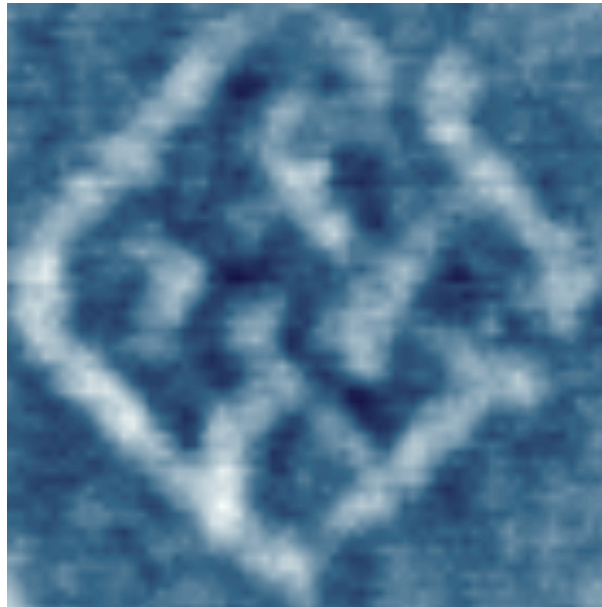


Fig.5-4 The Hong Kong Polytechnic University Logo (300 nm × 300 nm) fabricated using raster lithography at 20°C and a relative humidity of 28% by the application of voltage from -4 V to -8 V to the tip for 2 milliseconds to 5 milliseconds.

Anodic Nanooxidation, Force Nanolithography and Characterization of Protein Patterns with AFM

functions. To fabricate complicated nanostructures has great significance. However, it is difficult to do so in a vector lithography, where oxidation is conducted by applying an equal voltage to the selected area, thus producing nanopatterns with the same thickness. Raster lithography method can realize this requirement by applying different voltage to different areas, thus producing nanopatterns which would contain features with different thickness. The value of the applied voltage to a definite site depends on its contrast in the given picture. Figure 5-4 shows a 300 nm × 300 nm POLYU Logo using a raster lithography at 20°C and a relative humidity of 28% by the application of voltage from -4 V to -8 V to the tip for 2 milliseconds to 5 milliseconds. It is possible to fabricate more complicate nanostructures by designing a picture with proper contrast.

5.1.2 Nanomodification of Au

It is well known that a negatively biased conductive AFM tip would oxidize semiconductors (Si, Ga, Ge) [163,166,168-172,190], and some transition metals (Ti, Al) [169,190]. However, for those noble metals such as Au and Pt which are not easily oxidized, would a biased AFM tip chemically modify their surfaces? We studied this using gold thin films prepared by sputtering and gold ball prepared by melting method. The modification method was the same as for nano-oxidation.

Similar to semiconductors and transition metals, the negatively biased tip could modify the gold surface, and the modified areas became protruded. Figure 5-5a shows a line that was fabricated on a gold thin film by the

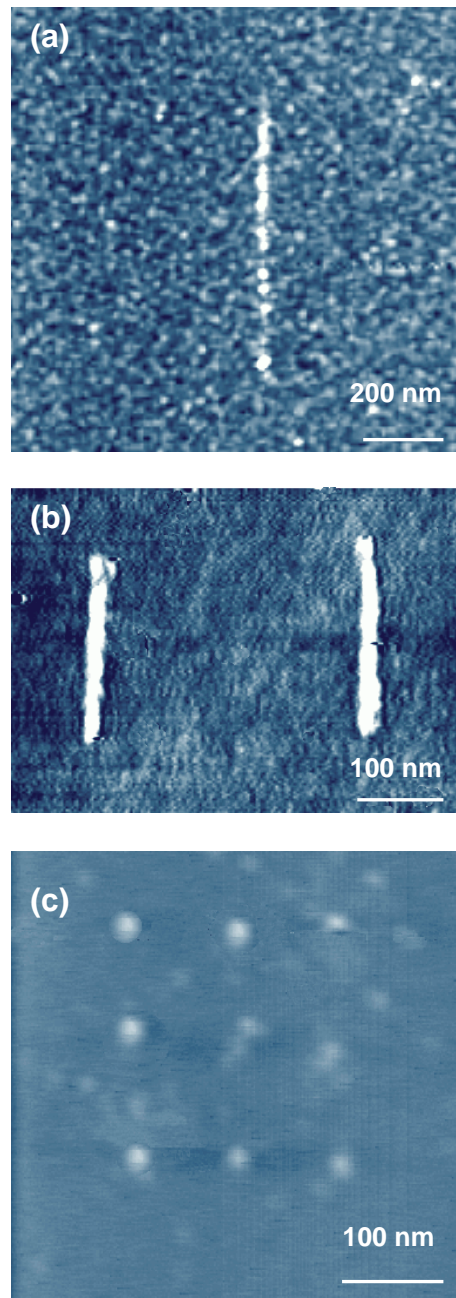


Fig.5-5 Nanopatterns on Gold film and gold ball by the application of certain voltage on a conductive AFM tip. (a) A line constructed on gold film with -6 V applied to the tip for 1 millisecond per point. (b) Two lines constructed on gold ball with -4 V applied to the tip for 0.15 and 0.2 milliseconds per point. (c) A 3×3 point array on gold ball constructed with -5 V applied to the tip for 0.1 milliseconds per point.

Anodic Nanooxidation, Force Nanolithography and Characterization of Protein Patterns with AFM

application of -10 V to the conductive AFM tip for 1 millisecond per point. The thickness of the line ranges in 2~5 nm and the line width was about 37 nm. Nanofeatures can also be fabricated on a gold ball. Figure 5-5b shows two lines fabricated on a gold ball by the application of -4 V to the conductive AFM tip for 0.15 and 0.2 milliseconds per point. The averaged line thickness were about 2.2 and 2.5 nm, and the averaged line width were about 23 nm and 27 nm, respectively. Compared to the lines on the gold ball, the line on the gold thin film was not consecutive due to a much rougher surface. Figure 5-5c shows a 3x3 point array on the gold ball fabricated by the application of -5 V to the conductive AFM tip for 0.1 milliseconds per point. The height of the dots ranged from 2 to 3 nm, and the diameter of the dots ranged from 22 to 26 nm. There was no any cavity left after the modification.

Figure 5-6 shows the dependence of the pattern height versus voltage. There also existed a threshold voltage. There was no any appreciable morphology change when the applied voltage was below -4 V. The pattern height increased linearly as the voltage increased when the electric field was above 4 V.

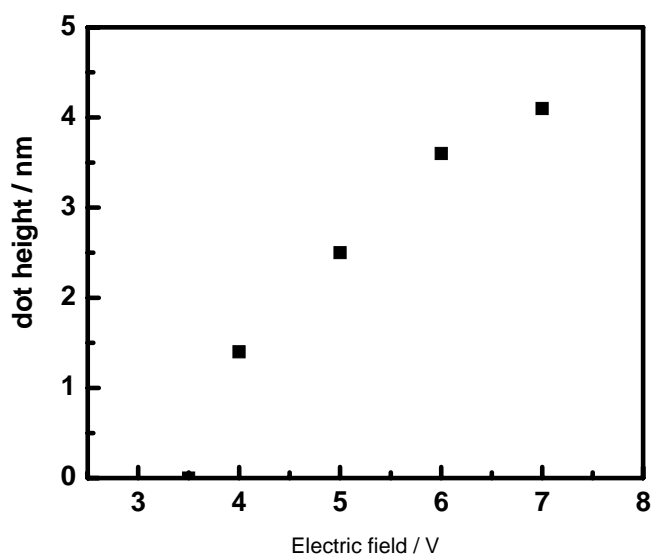


Fig.5-6 The dependence of pattern height versus voltage.

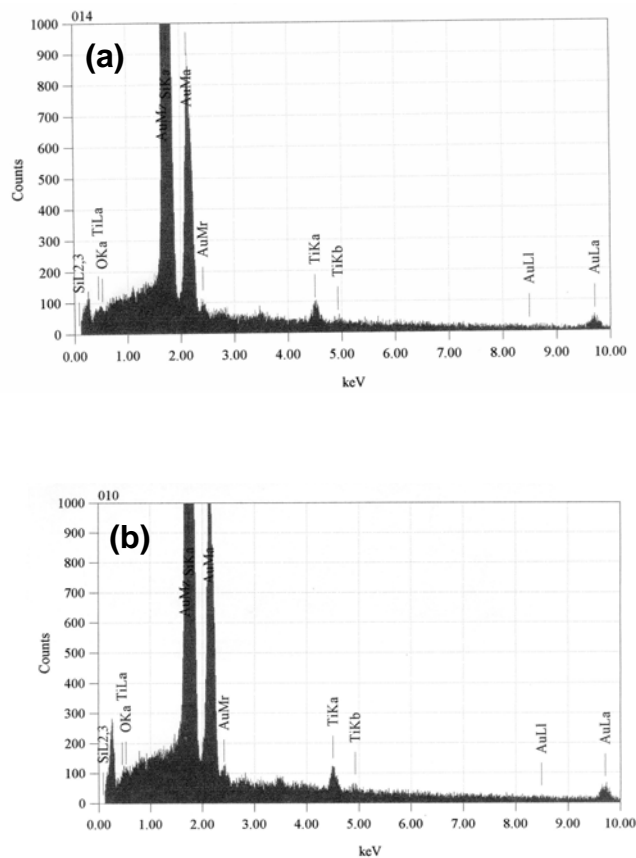


Fig.5-7 EDX spectra outside (a) and inside (b) the patterned area.

Anodic Nanooxidation, Force Nanolithography and Characterization of Protein Patterns with AFM

To check that the gold was oxidized or only physically changed due to the applied intense electric field, chemical composition inside and outside the patterned area was analyzed by EDX. The patterns were first found by FE-SEM, then EDX analysis focused on these areas. Figure 5-7 shows EDX spectra outside (a) and inside (b) the patterned area. The oxygen content inside the patterned area (1.86%) was a little greater than that outside the patterned area (1.33%). Therefore, this is not convincing. Detailed works, such as XPS, should be conducted to clarify this process.

5.2 Force Nanolithography with AFM

Force nanolithography is different from dip-pen nanolithography and nanooxidation, where the sample surface is mechanically modified by an AFM tip. This direct mechanical modification of a sample structure has proven to be very useful in the fabrication of nanodevices. Force nanolithography is usually done by using an AFM tip to scribe some patterns in a soft sample surface such as soft metals or polymers. For some hard samples, a thin layer of soft material on the hard sample can be used as a sacrificial layer. Nanopatterns were first fabricated on the soft layer by force nanolithography. Then the patterns were transferred to the hard samples with the combination of an appropriate etching process.

5.2.1 Experimental

The same AFM (Solver P47) was used to scribe the samples and subsequently to measure the topographic images of the patterned surface. The cantilever for force nanolithography was noncontact silicon cantilevers (NSC11) from NT-MDT Company, which have a pyramidal diamond tip. The typical force constant, radius of curvature, and full tip cone angle are 48 N/m, 10 nm, and 20°.

Thin layers of a polymer PMMA (AZ1500, Korea) and PZT were prepared by spin coating onto silicon substrate. The thickness of the film can be controlled by the experimental conditions, and are measured with ellipsometry. The roughness of the prepared film is less than 0.1 nm.

5.2.2 Force Nanolithography on PMMA

Figure 5-8a shows the AFM topographic image of a point fabricated on a PMMA surface with a thickness of 200 nm by the application of 1.0 μN to the tip for 20 milliseconds. The modified area shows a triangular shape, which was caused by the tip shape. Figure 5-8b shows the section profile along the AA' direction. The pattern depth was about 90 nm.

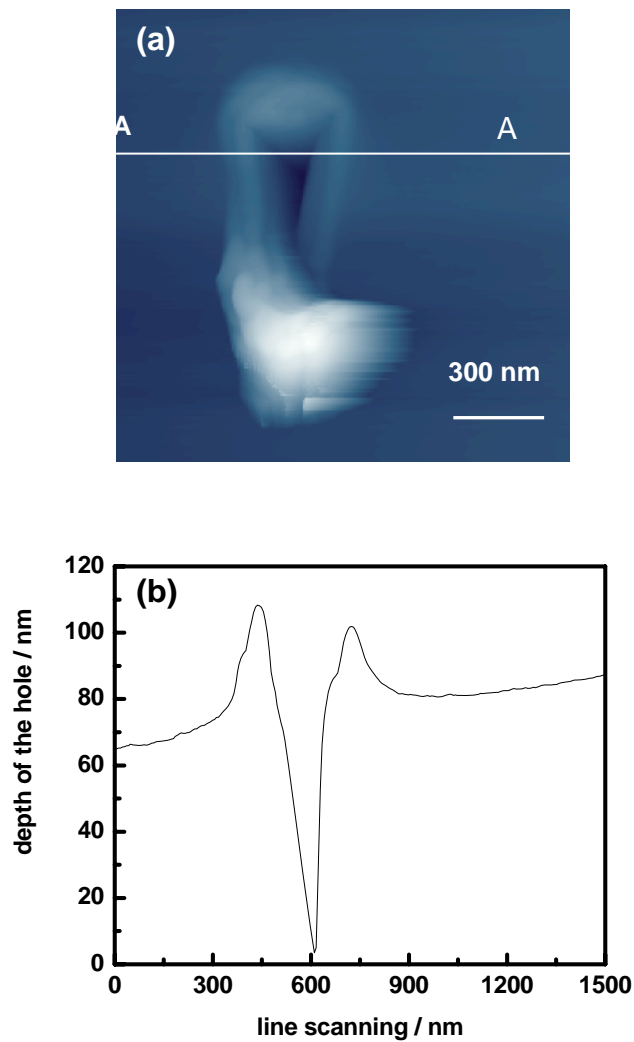


Fig.5-8 AFM topographic image of a point fabricated with $1.0 \mu\text{N}$ applied to the tip for 20 ms (a) and the section profile along the AA' direction (b).

Reducing the applied load to $0.6 \mu\text{N}$, the created pattern is shown in Figure 5-9a. The modified area also shows a triangular shape, which was caused by the tip shape. Figure 5-9b shows the section profile along the AA' direction. The pattern depth was about 70 nm.

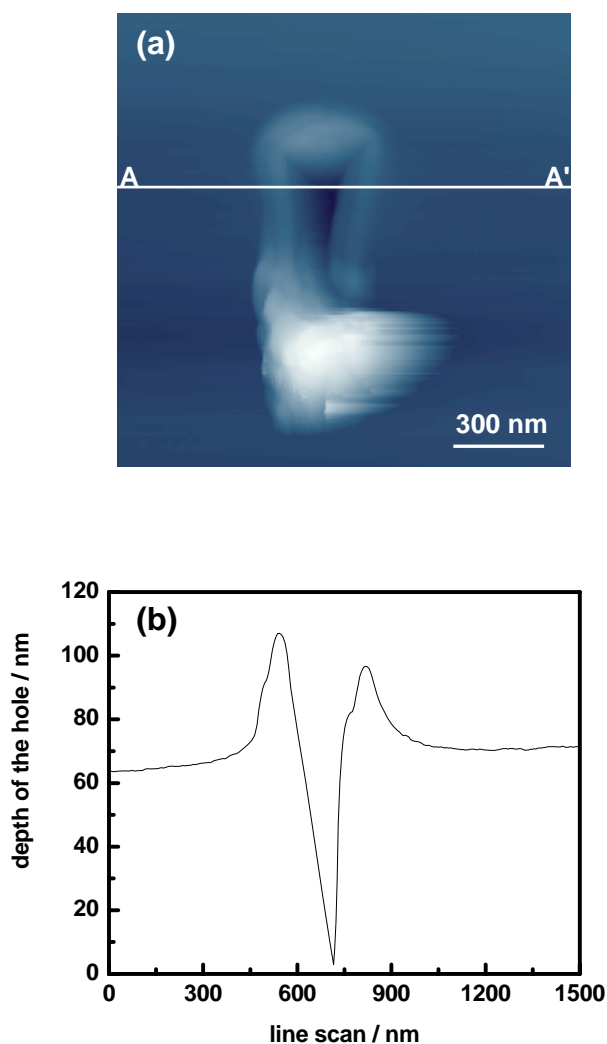


Fig.5-9 AFM topographic image of a point fabricated with $0.6 \mu\text{N}$ applied to the tip for 20 ms (a) and the section profile along the AA' direction (b).

Further reducing the applied load to $0.25 \mu\text{N}$, the created pattern is shown in Figure 5-10a. The modified area does not show a triangular shape, but looks like a short line. Figure 5-10b shows the section profile along the AA' direction. The pattern depth decreased to about 30 nm.

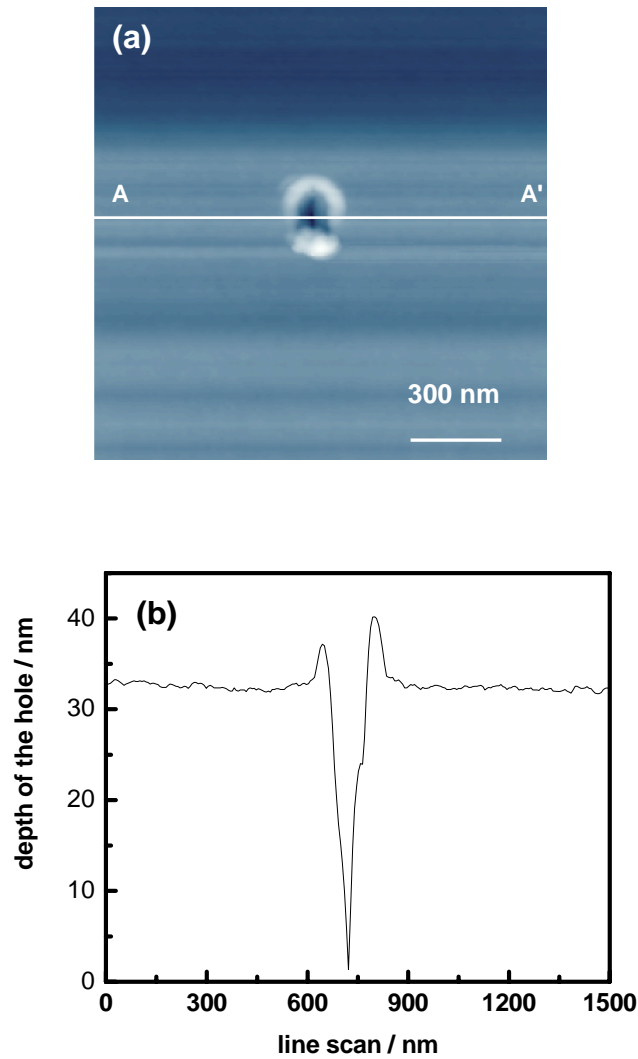


Fig.5-10 AFM topographic image of a point fabricated with 0.25 μN applied to the tip for 20 ms (a) and the section profile along the AA' direction (b).

When the applied load is further reduced to 0.15 μN , the created pattern shows a regular hole, as shown in Figure 5-11a. Figure 5-11b shows the section profile along the AA' direction. The pattern depth decreased to about 15 nm. The HFW of the hole was 32 nm.

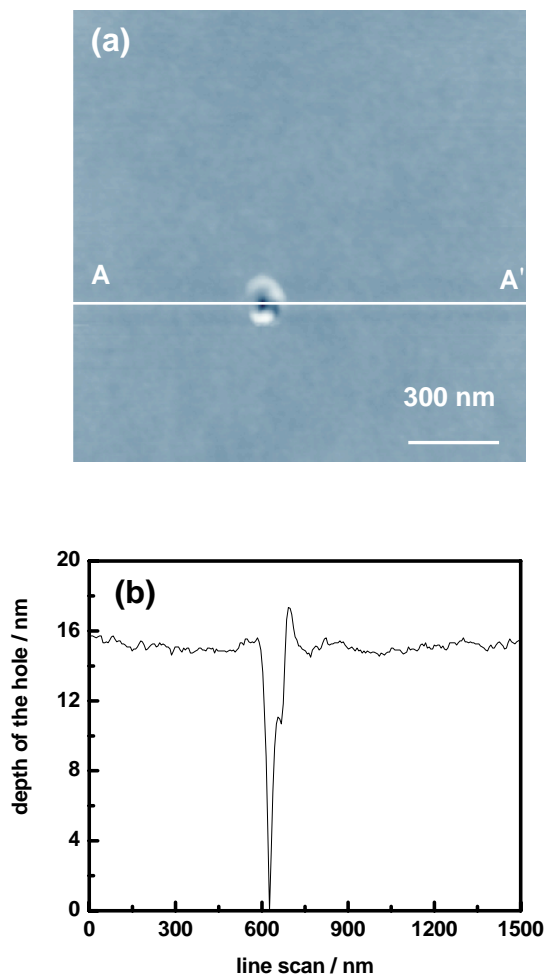


Fig.5-11 AFM topographic image of a point fabricated with $0.15 \mu\text{N}$ applied to the tip for 20 ms (a) and the section profile along the AA' direction (b).

Figure 5-12 shows the relationship between the loading force and the pit depth. The pit depth increased linearly with increasing loading force.

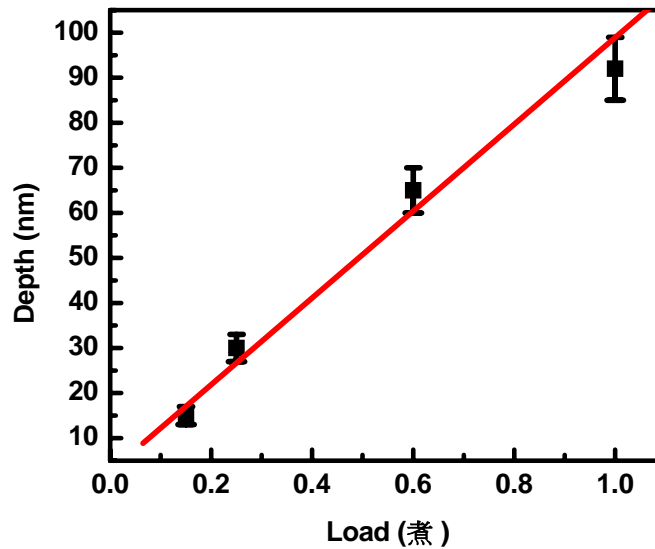


Fig.5-12 Relationship between the loading force and the pit depth, showing a roughly scaling behavior. The data are averaged from 5 independent measurements, and the error bars are standard deviations.

A PMMA film with a thickness of 16 nm was prepared, and a 4×4 point array was created by utilizing a load of 0.15 μN and duration of 20 milliseconds, as shown in Figure 5-13a. Figures 5-13b to 5-13f show the section profile along the line 1, 2, 3, 4, and 5, respectively. The repeatability is good. Real data storage density was of about **18 Gbit/inch²**, which can be further improved by increasing the density and decreasing the tip radius.

Anodic Nanooxidation, Force Nanolithography and Characterization of Protein Patterns with AFM

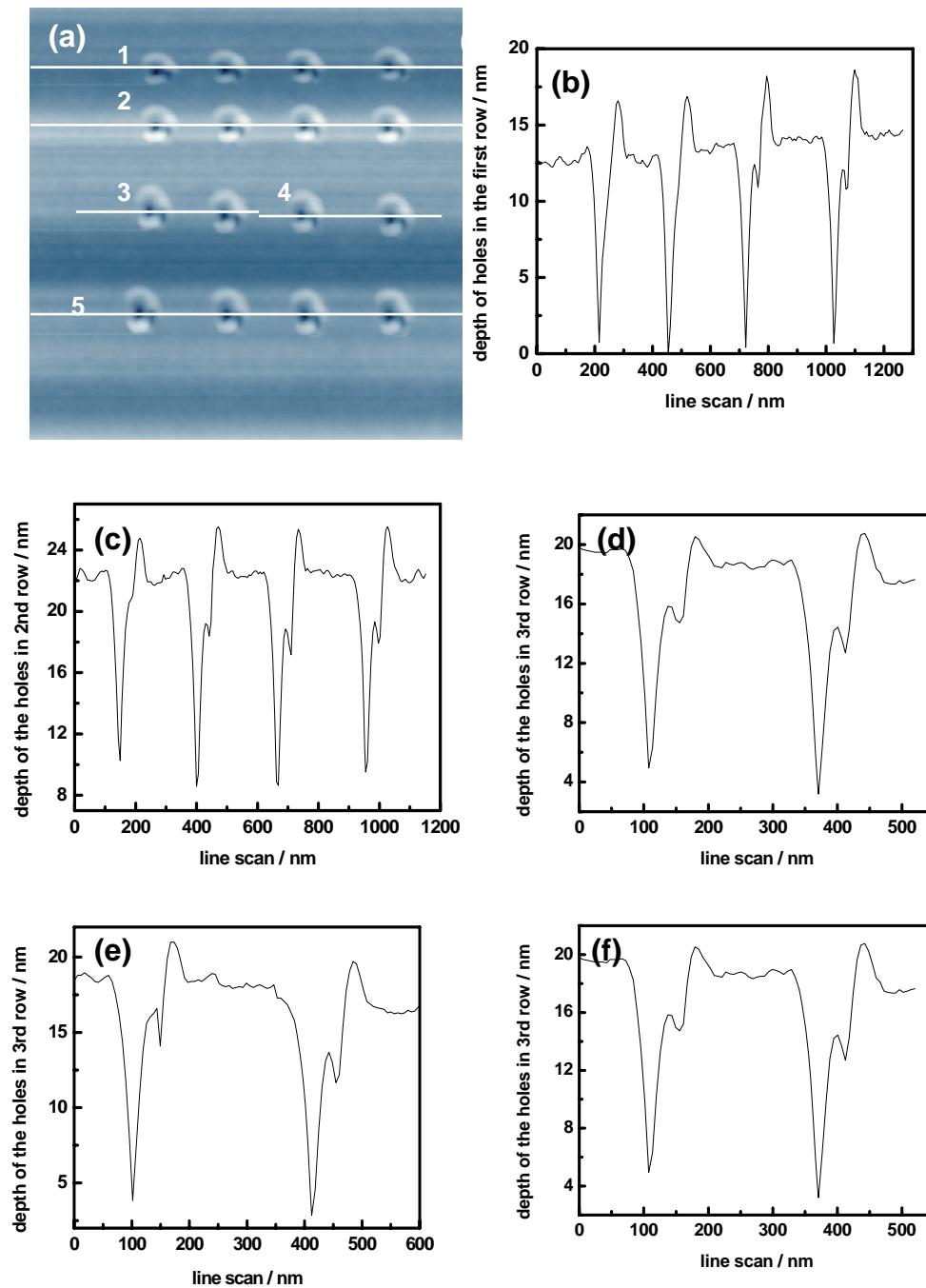


Fig.5-13 (a) topographic image of a 4×4 point array created on a PMMA film with a thickness of 16 nm with 0.15 μN applied to the tip for 20 ms, and lateral contour of line 1 (b), line 2 (c), line 3 (d), line 4 (e) and line 5 (f).

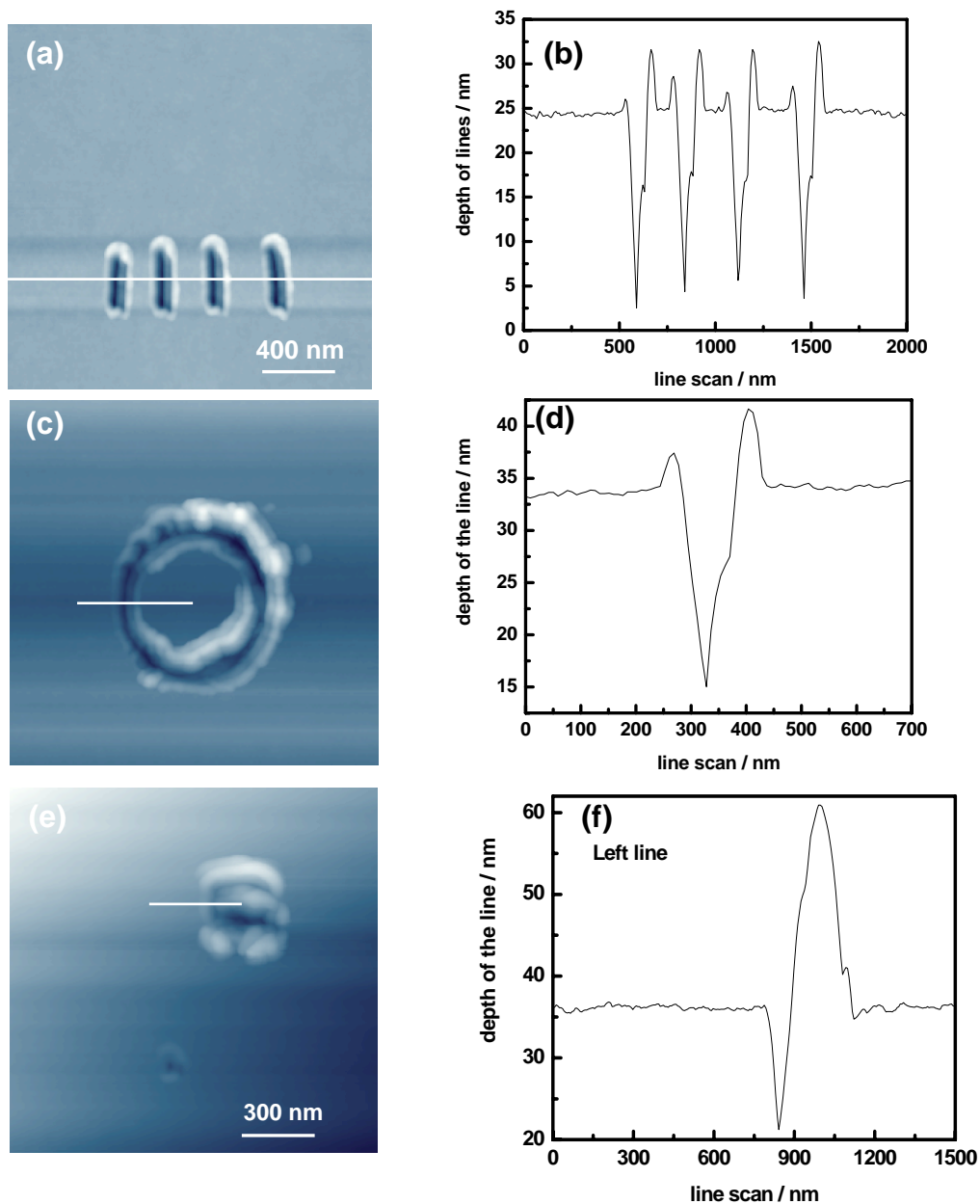


Fig. 5-14 (a) A topographic image of four lines fabricated on a PMMA film with a thickness of 20 nm with 0.20 μN applied to the tip for 20 ms. (b) Lateral contour of line in (a). (c) A topographic image of a circle fabricated on a PMMA film with a thickness of 20 nm with 0.20 μN applied to the tip for 15 ms. (d) Lateral contour of line in (c). (e) A topographic image of a rectangular fabricated on a PMMA film with a thickness of 16 nm with 0.15 μN applied to the tip for 20 ms, and (f) Lateral contour of line in (e).

Anodic Nanooxidation, Force Nanolithography and Characterization of Protein Patterns with AFM

In addition to fabricating point array, force nanolithography can also be used to fabricate random pre-designed patterns on this soft polymer. Figure 5-14 gives some examples.

5.2.3 Force Nanolithography on PZT film

The lead zirconate titanate (PZT) system has been subjected to intensive studies worldwide since its discovery. Advances in modern technology has already set this ferroelectric material at the center stage for application to piezoelectric, pyroelectric, non-volatile random access memory devices, imaging systems sensors and actuators in smart and very smart structures due to its large remanent polarization, strong temperature dependence property of the spontaneous polarization below the Curie temperature T_C , and relatively low temperature deposition process. As the sensors/actuators are becoming smaller and smaller, corresponding nanotechnologies to fabricate smaller nanostructures are required. PZT is a hard ceramic; therefore, direct fabrication of nanopatterns via force nanolithography on its surface is difficult, which would degrade the tip easily. Sol-gel is commonly used to produce PZT thin films for their easy composition control and low processing temperatures when compared with other techniques. In this study, we tried to construct nanopatterns on the PZT thin film before it is sintered.

Anodic Nanooxidation, Force Nanolithography and Characterization of Protein Patterns with AFM

Figures 5-15a and c show topographic images of PZT film after it was modified by force lithography. Holes and trenches can be fabricated on the surface as easily as that on the PMMA film. Force nanolithography on PZT sol-gel film may have potential applications in the fabrication of piezoelectric, pyroelectric, non-volatile random access memory nanodevices, and to study the piezoelectric properties at a nanometer scale.

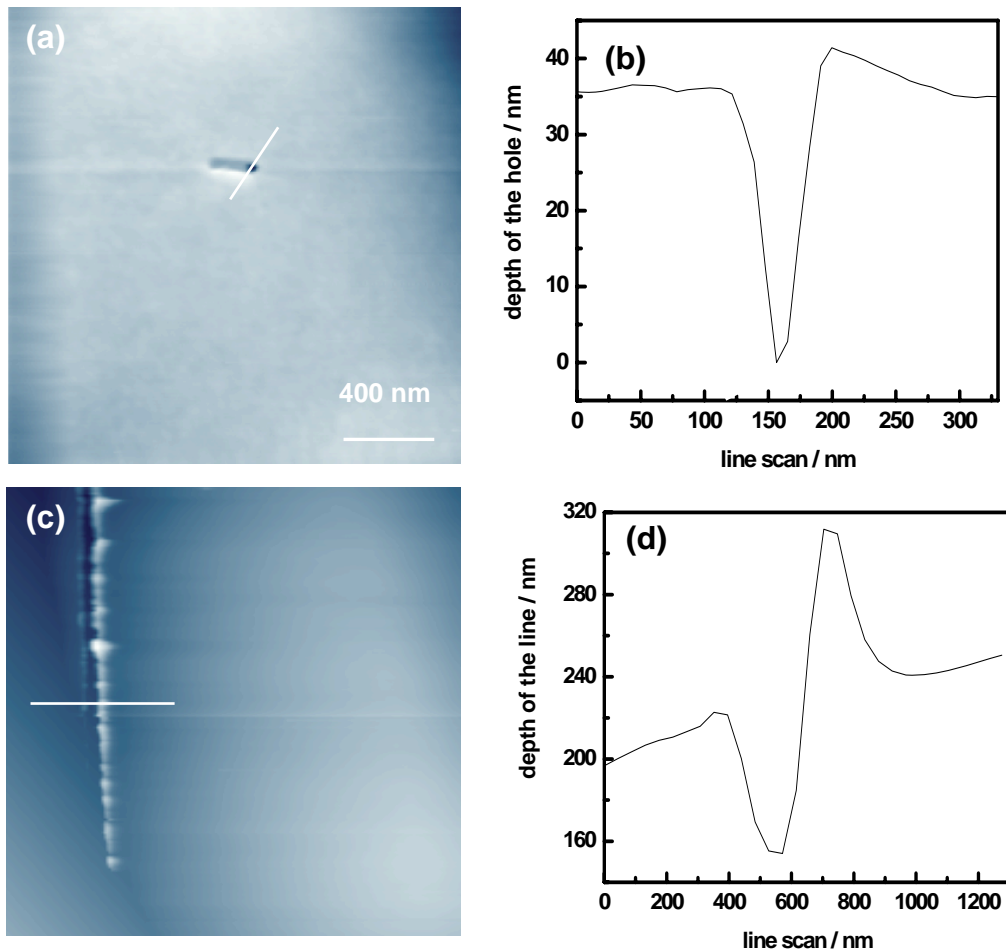


Fig.5-15 (a) The topographic image of a hole fabricated on PZT thin film with a thickness of 400 nm by the application of $0.5 \mu\text{N}$ for 10 ms, and (b) lateral contour of the line in (a). (c) The topographic image of a line fabricated on PZT thin film with a thickness of 400 nm by the application of $0.5 \mu\text{N}$ for 10 ms, and (d) lateral contour of the line in (c).

Anodic Nanooxidation, Force Nanolithography and Characterization of Protein Patterns with AFM

In summary, force nanolithography can be used to fabricate nanopatterns on PMMA and an un-sintered PZT surface easily. Real data storage density of about 18 Gbit/inch² has been obtained on PMMA. The pit depth increased linearly with the increasing applied load for PMMA. By controlling the film thickness and the applied load, the film can be scratched and the bottom substrate can be exposed. With the combination of a proper etching method, nanopatterns can be transferred into the bottom substrate.

5.3 Characterization of protein patterns with AFM

5.3.1 Introduction

Protein adsorption on solid surface is a very important and active area of research due to its potential applications from fundamental studies in cell biology to the development of various “biochip” platforms [283,284]. There are mainly two types of methods to study about protein adsorptions. The first type is to fabricate selective templates for protein adsorption to form micro to nanoscale protein patterns using techniques such as photolithography [285], micromaching [286], microfluidic channel networks [287,288], microcontact printing [148,289] and AFM-based nanotechnology, nanografting [149,150] and dip-pen nanolithography [202,211,213,215,227,228]. The second type for immobilizing protein in micro- or nanoscales is self-assembled monolayers (SAMs) [290,291]. Both types of methods are based on the modification of substrate surface property to realize selective adsorption.

Gold, mica, glass and SiO₂ are most often used as substrate materials for protein adsorption because their surface properties are easily modified by forming SAMs with high degree organization and physical robustness. Materials used to prepare SAMs on gold contain two terminated groups. One is ~SH, which forms Au-S covalent bond on gold [195]. The other terminated group with special property is exposed to the surface for protein adsorption due to the electrostatic interaction, hydrophobic interaction or formation of chemical bond between protein and the other terminated group. George and

Anodic Nanooxidation, Force Nanolithography and Characterization of Protein Patterns with AFM

colleague firstly reported the preparation of mixed SAMs by immersing gold in the solution containing two types of thiols [292–296]. They further studied the protein adsorption on the mixed SAMs and found the SAMs of thiol containing oligo(ethylene glycol) have high resistance to protein adsorption. They prepared mixed SAMs containing oligo(ethylene glycol) moiety to selectively immobilize protein [297–299]. Chemically immobilizing protein on mixed carboxylate-terminated (COOH) SAMs through chemical reactions to form S-RCO-NH-protein covalent bond was also reported [300,301]. Serum albumin is one of the most abundant proteins in blood, and it is capable of affecting blood coagulation [302]. Therefore, serum albumin adsorption on self-assembled monolayers [303,304], mica [305], chemically modified silicon [306], titanium oxide film [307] and polymer surfaces [308] was extensively studied.

Here, SAMs and mixed SAMs with two long chain thiols, CH₃-terminated 1-octadecanethiol (ODT) and carboxylate-terminated 16-mercaptohexadecanoic acid (MHA) at various molar ratios were prepared. The adsorption of a protein, bovine serum albumin, on gold film and the prepared SAMs were studied with AFM, and the mechanism for the protein adsorption on these surfaces which have different chemical properties was also discussed.

5.3.2 Experimental

1-Octadecanethiol (Aldrich), 16-mercaptohexadecanoic acid (Aldrich), 2-butanol (International Laboratory), and bovine serum albumin (BSA) (Sigma) were used as received.

A 10 nm Ti and then a 30 nm gold are coated on *n*-Si(1 0 0) wafer by sputtering with ExplorerTM 14 Denton Vacuum.

Fresh gold surfaces were immersed in one of the five solutions: 1mM ODT in 2-butanol, 1mM MHA in 2-butanol, the mixture of the above solutions with the mole ratios of MHA to ODT as 1:10, 1:1, 10:1) for 48 h. Then the samples were taken out and copiously rinsed with 2-butanol and ethanol followed by distilled de-ionized water and blown dry with pure nitrogen to form different SAMs on gold surfaces. We named the three mixtures of SAMs as: the mixture 1:10 SAMs, 1:1 SAMs, and 10:1 SAMs, respectively.

SAMs on gold were immersed into aqueous BSA solution (2.5 $\mu\text{g}/\mu\text{l}$) for 1 h, copiously rinsed with distilled de-ionized water to remove weakly adsorbed BSA and blown dry with pure argon.

The adsorbed protein was characterized with a commercial AFM (Solver P47H, NT-MDT, Russia) in tapping mode. The typical force constant, tip curvature radius and resonance frequency of the silicon cantilever are about 0.30 N/m, 10 nm, 21 kHz (MicroMasch), respectively. AFM images were obtained in ambient condition (about 20°C and at relative humidity of 50%) and at a scan rate of 2 Hz.

5.3.3 Results and Discussion

5.3.3.1 Gold film and SAMs

The surfaces of gold film and SAMs are shown in Figure 5-16. All surfaces are very flat and the roughness of all surfaces is less than 0.5 nm. Figures 5-16a, 5-16b, and 5-16c show the typical topography of gold surface, ODT SAMs and the mixture 1:1 SAMs, respectively. The MHA and ODT form uniform SAMs on gold through S~Au covalent bond [195], exposing hydrophilic ~COOH group and hydrophobic ~CH₃ group on the surface, respectively. Nearly the same chain length, 3 nm of MHA and ODT [250] results in a flat surface of mixture SAMs.

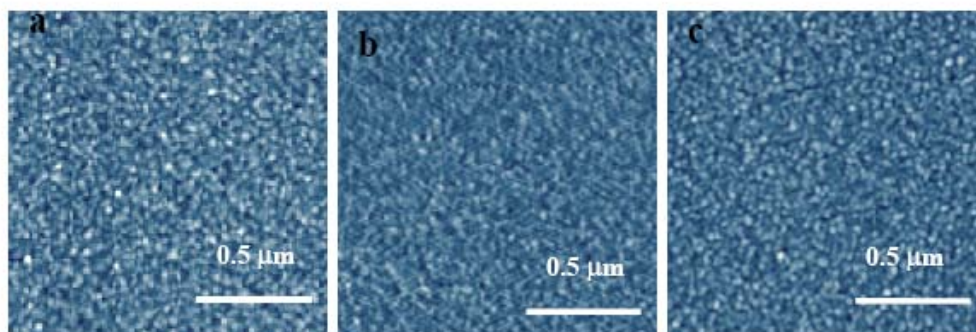


Fig.5-16 Topographies of gold film (a), ODT SAMs (b), and the mixture 1:1 SAMs (c).

5.3.3.2 Protein Patterns and the mechanism for protein adsorption

(a) On gold film

Figure 5-17 shows the protein pattern immobilized on gold film. Figure 5-17a shows the topography of the adsorbed protein. The protein densely adsorbed on gold has the shape of belts, lines and points. The width of the belts and lines is in the range of 80 ~ 700 nm and the diameter of the points is in the range of 30 ~ 250 nm. Densely coalesced streptavidin pattern on gold was also obtained by Kim et al [309]. The protein pattern is probably caused by the solution concentration, adsorption time, the interaction between protein molecules and between protein molecules and gold substrate [304,308]. Each BSA molecule contains 582 amino acids. It is a prolate ellipsoid. The major and minor axes of the ellipsoid are 14 nm and 4 nm, respectively [310]. BSA molecules adsorb on solid surface by "side-on" or "end-on" orientation with minor or major axes perpendicular to the surface [305]. The surface coverage of the protein is about $81 \pm 2\%$, estimated by an image analyzer (Clemex Technologies Inc.). Figure 5-17b is the line cross section in Figure 5-17a. The height of the patterns in Figure 5-17a is about 4 ± 0.5 nm, which is close to the minor axes of BSA molecule. The result suggests that BSA monolayer is formed on gold surface by side-on orientation. BSA molecule contains 17 disulfide valences (R-S-S-R') and one free ~SH [310]. Both disulfide and free ~SH have strong affinity with gold through formation of Au-S covalent bond [195]. The Au-S bond is illustrated in Figure 5-17c. The covalent Au-S bond is much more stable than intermolecular interaction, resulting in protein immobilization on gold surface with single layer.

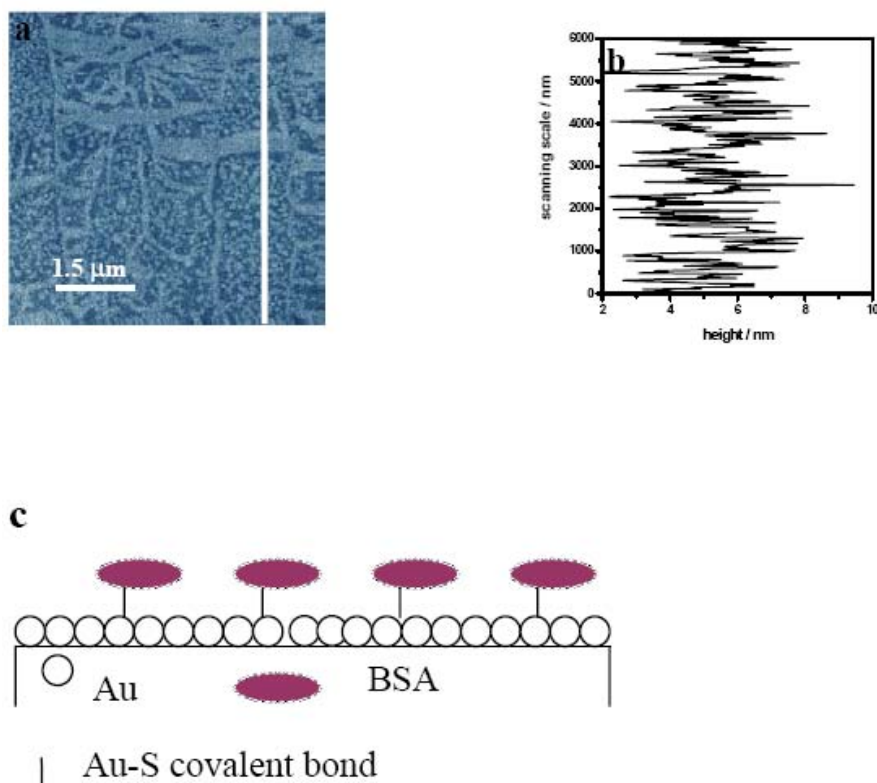


Fig.5-17 Protein immobilization on gold film

- (a) Topography of gold after absorb BSA. (b) Cross section of the line in (a)
- (c) Schematic illustration for the protein immobilization on gold film

(b) On MHA SAMs

Figure 5-18 shows the protein pattern absorbed on MHA SAMs. Figure 5-18a is the topography of the protein absorbed on MHA SAMs. As shown in Figure 5-18b, some spherical patterns with the height of about 4 ± 0.5 nm and lateral dimension of about 18 ± 2 nm sparsely distribute on the surface, demonstrating individual BSA molecules on the MHA SAMs. The spherical pattern other than ellipsoid [310] is caused by the convolution effect of the tip. The typical radius of the tip used in the present study is about 10 nm, greater than the BSA molecular scale. Therefore, the BSA molecule is extended [32].

Anodic Nanooxidation, Force Nanolithography and Characterization of Protein Patterns with AFM

Globular structures of albumin were also obtained with AFM by other research groups [308,311]. The surface coverage of the protein on MHA SAMs is very low, about 2 ± 0.4 %. The absorption of protein on MHA SAMs is probably due to repulsive electrostatic interaction between COO^- and protein molecules [286]. The pH of the used aqueous BSA solution in the

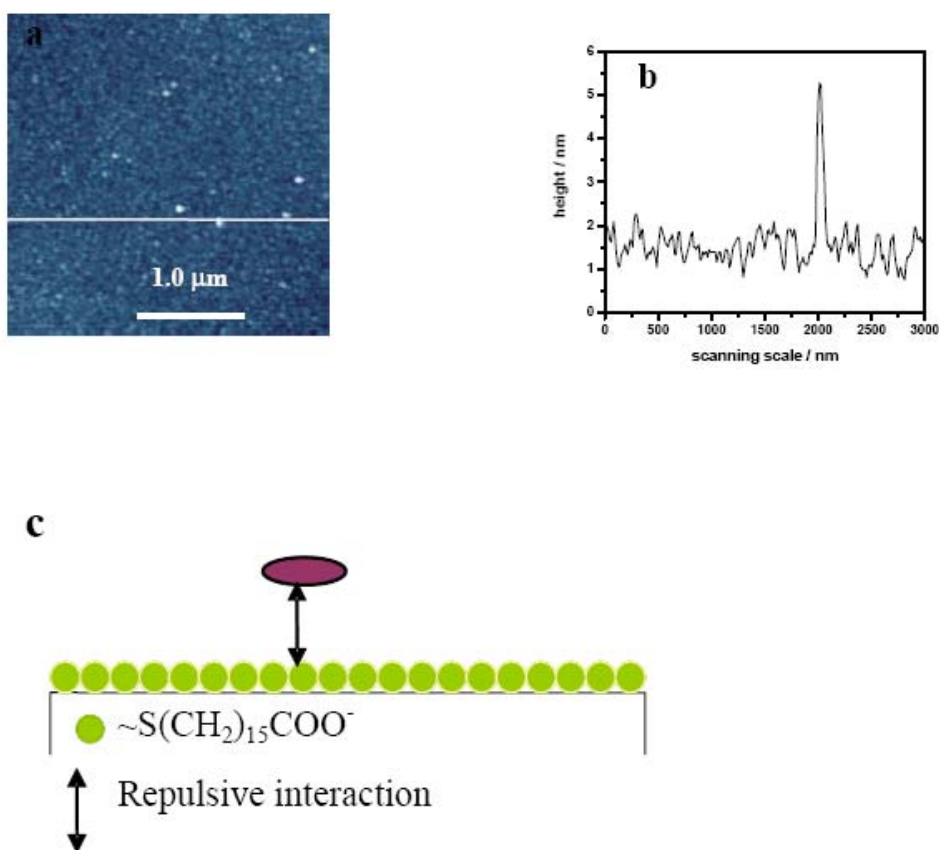


Fig.5-18 Protein adsorption on MHA SAMs

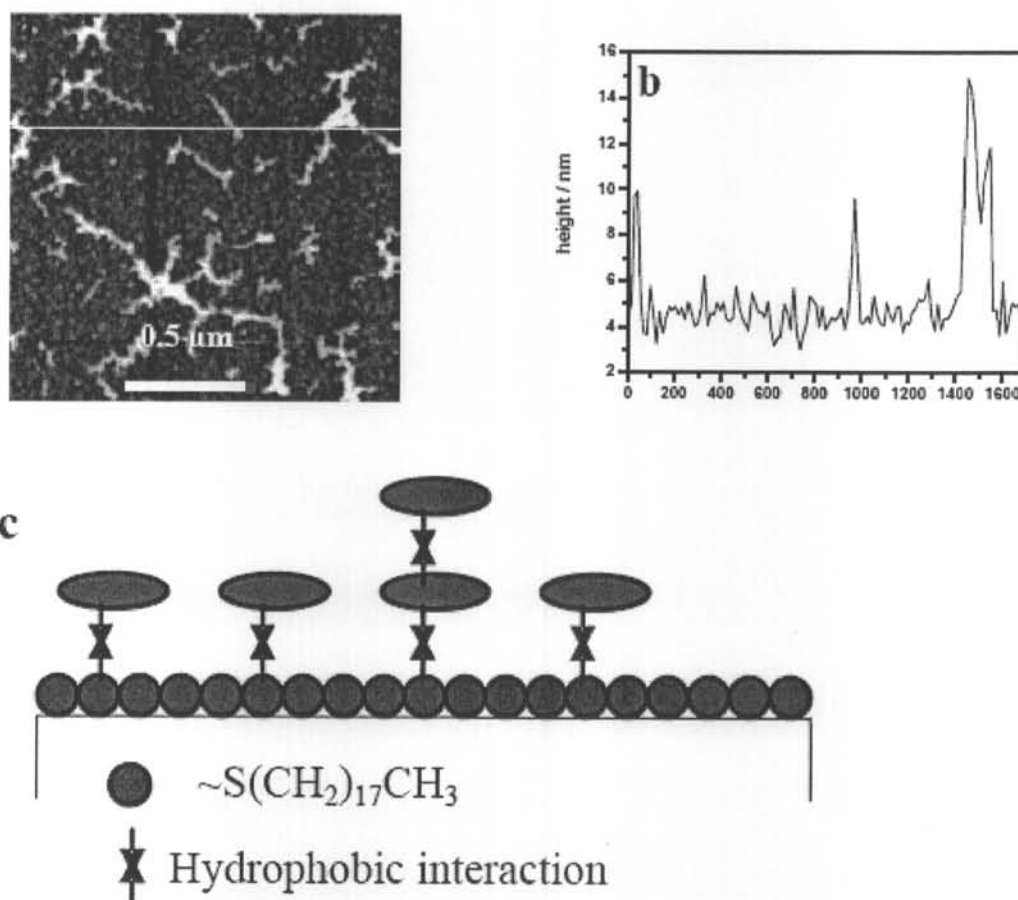
(a) Topography of protein pattern on MHA SAMs. (b) Cross section of the line in (a). (c) Schematic illustration for the adsorption of protein on MHA SAMs.

present experiment is about 6, higher than the reported isoelectric point (pI) of BSA (4.6~4.7) [312], therefore, the protein molecules have net negative

charge. MHA SAMs surface is also negatively charged due to ionization [313], thus producing repulsive electrostatic interaction between BSA molecules and MHA SAMs. Protein adsorption on MHA SAMs is illustrated in Figure 5-18c.

(c) On ODT SAMs

Figure 5-19 shows the protein pattern absorbed on ODT SAMs. Figure 5-19a shows the topography of protein adsorbed on ODT SAMs. Protein molecules form non-uniform and branched patterns. The heights are nearly 8 ± 1.0 nm at the knot of the branches and about 4 ± 0.5 nm at the branches, shown in Figure 5-19b, indicating that two protein molecules aggregate at the knots. The surface coverage of protein on ODT SAMs is about $9 \pm 1\%$, which is greater than that on MHA SAMs. This result confirms the observations from previous reports [306,308,314], i.e., that the amount of BSA adsorbed on CH_3 -terminated surface is greater than that on COOH -terminated surface. Protein adsorption on ODT SAMs is mainly due to hydrophobic interaction between hydrophobic moiety of protein molecule and the hydrophobic surface through reverse phase chemistry [297,315], as illustrated in Figure 5-19c. Protein aggregation formed at the knot is probably caused by the hydrophobic interaction, which further increases the hydrophobic interaction between protein molecules.



(a) Topography of protein pattern on ODT SAMs. (b) Cross section of the line in (a). (c) Schematic illustration for the adsorption of protein on MHA SAMs.

(d) On the Mixture 1:1, 1:10 and 10:1 SAMs

Figure 5-20 shows the protein pattern absorbed on the SAMs with the mixture 1:1 SAMs. Figure 5-20a shows the topography of the SAMs after the adsorption of protein. Protein on the SAMs with the mixture also formed branched but much dense patterns. The surface coverage of protein was about $28 \pm 1.5\%$. As shown in Figure 5-20b, the pattern height was about 4 ± 0.5 nm, indicating a monolayer of protein molecules on the mixture 1:1

Anodic Nanooxidation, Force Nanolithography and Characterization of Protein Patterns with AFM

SAMs. The sum of the coverage of proteins on ODT SAMs and MHA SAMs was about 11%, which was less than that on the mixture 1:1 SAMs (28%). This result indicates that the protein adsorption on mixed SAMs is not a simply mathematical sum of MHA SAMs and ODT SAMs. The increased adsorption of protein on mixed SAMs was probably due to coordination of hydrophobic group ($\sim\text{CH}_3$) and hydrophilic group ($\sim\text{COOH}$). The pKa of carboxylic acids in mixed SAMs where the other component was hydrophobic can be shifted to much higher values [316]. At pH 6, the carboxylic acid groups in the mixed SAM are likely to be predominantly protonated and repulsive interactions

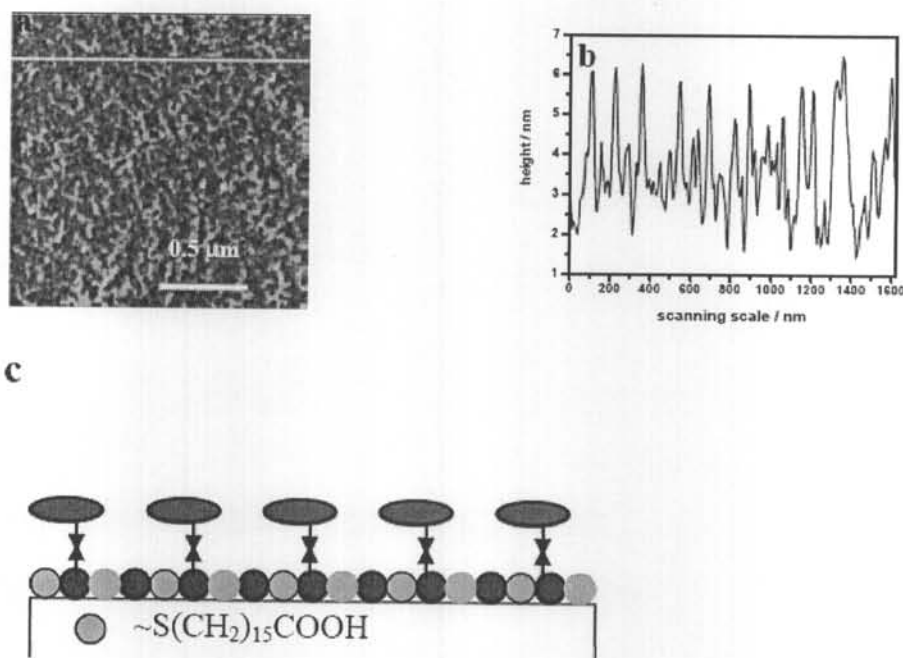


Fig. 5-20 Protein adsorption on the mixture 1:1 SAMs

(a) Topography of protein pattern on the mixture 1:1 SAMs. (b) Cross section of the line in (a). (c) Schematic illustration for the protein adsorption on the mixture 1:1 SAMs.

Anodic Nanooxidation, Force Nanolithography and Characterization of Protein Patterns with AFM

between BSA and the SAM should decrease, which leads to the increased protein adsorption. The adsorption of proteins on the mixture 1:1 SAMs is illustrated in Figure 5-20c.

Figure 5-21 shows the protein pattern absorbed on the mixture 1:10 SAMs. Figure 5-21a shows the topography of the protein pattern on the mixture 1:10 SAMs. Network pattern of protein was obtained. Dupont-Gillain and

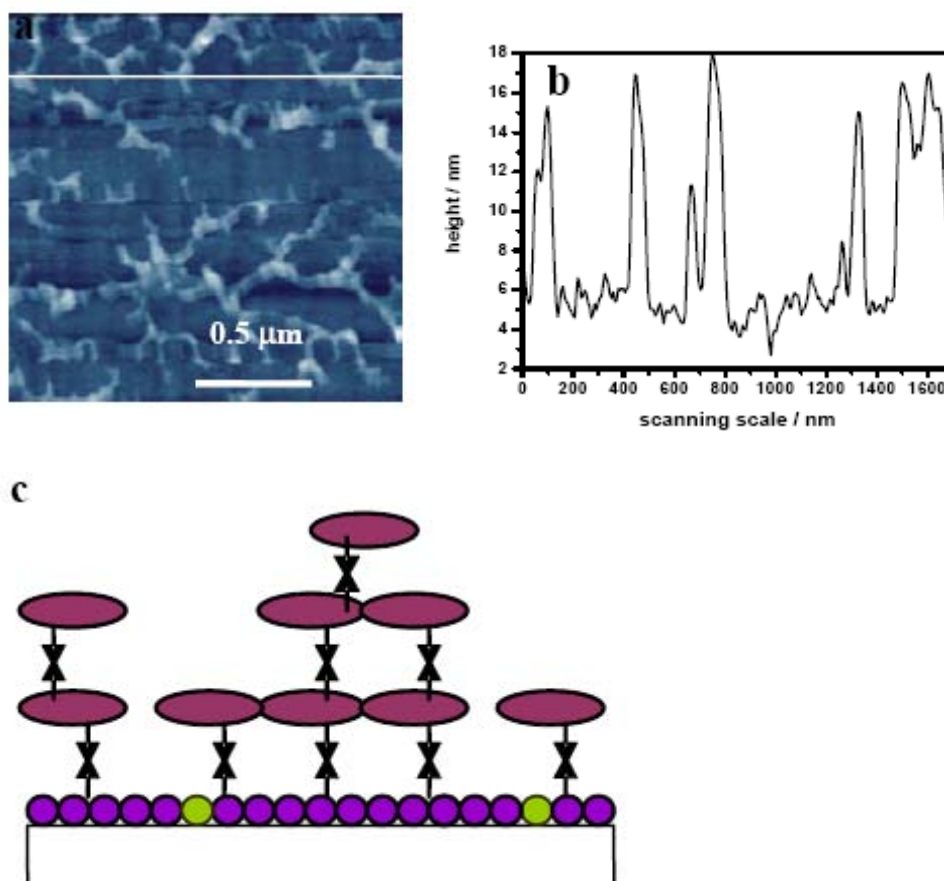


Fig.5-21 Protein adsorption on the mixture 1:10

(a) Topography of protein pattern on the mixture 1:10. (b) Cross section of the line in (a). (c) Schematic illustration for the protein adsorption on the mixture 1:10 SAMs.

Anodic Nanooxidation, Force Nanolithography and Characterization of Protein Patterns with AFM

colleague obtained a net-like structure of collagen adsorbed on poly(methyl methacrylate) with slow drying procedure, they thought a chemically heterogeneous surfaces are produced at slow drying rates [317]. In present study, the mixed SAMs surface was blown dry with argon, which has a faster drying rate. The net-like protein pattern was mainly caused by the mixed SAMs surface properties and the interplay between protein-SAMs interaction and protein-protein interaction. Surface coverage of protein on the mixture 1:10 SAMs is about 19 ± 1.5 %. As shown in Figure 5-21b, the heights of network are about 4, 8 and 12 nm, integer increments of the protein molecule size. The protein pattern on the mixture 1:10 SAMs in Figure 5-21a is similar to that on ODT SAMs in Figure 5-19a. Nevertheless, the amount of proteins absorbed on the surface of the mixture 1:10 SAMs increased, and proteins coalesced to form networks. The line width and height of the network on the mixture 1:10 SAMs (Figure 5-21b) are greater than those on ODT SAMs (Figure 5-19b). The amount of protein molecules on the mixture 1:10 SAMs is greater than that on the mixture 1:1 SAMs. Adsorption of protein on the mixture 1:10 SAMs is illustrated in Figure 5-21c. The protein pattern on the mixture 10:1 is similar to that on MHA SAMs in Figure 5-18a, indicating that the high concentration of MHA has the dominant effect on adsorption patterns of protein.

5.3.4 Summary

The various protein patterns with different coverage on six different surfaces were formed and characterized with AFM. Dense but non-uniform protein pattern with single layer was immobilized on gold film through formation of Au-S covalent bond. Sparsely distributed, individual protein molecules were adsorbed on MHA SAMs surface due to repulsive electrostatic interaction. Branched protein pattern was formed on ODT SAMs with aggregates at knots via hydrophobic interaction. In the mixed SAMs of MHA and ODT with large concentration differences, the adsorption properties of the mixture SAMs were close to that of the dominant component. In the mixed SAMs of MHA and ODT with little concentration difference, the combination properties of the mixture SAMs were significantly changed. The amount of protein adsorbed on mixed SAMs was greater than that on the SAMs with single component due to coordination. The amount of protein adsorbed on six different surfaces decrease according to the following order: gold film > the mixture 1:10 SAMs > the mixture 1:1 SAMS > ODT SAMs > MHA SAMs (the mixture 10:1 SAMs).

Chapter 6 Conclusion and Recommendation for Future Work

In this work, nanopatterning of a ferroelectric polymer [P(VDF-TrFE)] via dip-pen nanolithography, the influence of experimental conditions on dip-pen nanolithography, fabrication of nanostructures on Si and Au via anodic nanooxidation, fabrication of nanostructures on a polymer (PMMA) and PZT sol film via force nanolithography, as well as the formation and characterization of protein patterns via atomic force microscopy have been studied. The major conclusions are summarized in the following sections. The limitations of AFM nanopatterning and recommendations for future work are also discussed in this chapter.

6.1 Major Conclusions

6.1.1 Fabrication of Ferroelectric Micro- to Nanostructures via Dip-pen Nanolithography

A ferroelectric polymer, P(VDF-TrFE), was used as the DPN ink. The following conclusions have been obtained:

- For the first time, the micro- to nanostructures of a ferroelectric polymer, P(VDF-TrFE) were constructed via DPN onto the gold substrate. Line as thin as 20 nm and dot radius as small as 20 nm have been fabricated.

Conclusion and Recommendation for Future Work

- The P(VDF-TrFE) molecules were well oriented on the gold substrate giving the uniform thickness (1 nm) regardless of the pattern size when the surface concentration was greater than $3.49 \times 10^{-4} \text{ g/m}^2$.
- The DPN-generated P(VDF-TrFE) features held ferroelectric properties, and thus provide new opportunities for nanostructured sensor applications.
- The interaction between the P(VDF-TrFE) and the gold substrate was Van der Waals' interaction rather than electrostatic interaction or formation of covalent bond.
- The growth rate of dot radii/line-width was proportional to $t^{1/2}$. A simplified diffusion model adopting Fick's first law to two dimensions for a point source was proposed, and $r = \sqrt{\frac{2D}{\rho}(C_0 - C_r)t}$ has been obtained.

6.1.2 Effects of Experimental Conditions on Dip-pen Nanolithography

The effect of temperature, surface roughness of the substrate, relative humidity, tip size and tip material as well as chemical affinity on the DPN have been studied, and the following conclusions have been obtained:

- The transport of ink increases as the temperature increases. For P(VDF-TrFE), the relationship between r and t is $r = at^{1/2}$ from 25~70°C. a is temperature-dependent. It is related to diffusion constant. A deviation from Arrhenius plot at about 55°C is observed. This may be caused by a ferroelectric phase transition for such thin ferroelectric film or the shift of the ferroelectric phase transition under the special conditions. When the temperature is below 55°C, the transport rate of the P(VDF-TrFE) molecules

Conclusion and Recommendation for Future Work

increases exponentially with temperatures, which conforms to the Arrhenius plot. The activation energy (Q) was calculated to be 0.98 eV.

- Surface roughness influences both the contrast in LFM images and the transport rate of ink. Surfaces with less roughness give good contrast in LFM images, while rough surfaces give poor contrast. Rough surface (i.e., roughness is greater than 1.65 nm) was not suitable for DPN. For both ODT and P(VDF-TrFE), the dot area grew linearly with t in all the measured roughness ranges. The transport rate of ink increased as the roughness decreased. It may be caused by the increased friction force or the decreased diffusion constant. However, the extent of the influence was strongly ink-dependent. For ODT, the transport rate of ink decreased linearly as the roughness increased. For P(VDF-TrFE), the transport rate of ink decreased rapidly as the roughness increased when the roughness was less than 1.0 nm, while the roughness produced a little effect on the transport rate of ink when roughness was greater than 1.0 nm. This is probably caused by the different ink-substrate interaction.

- The influence of relative humidity depended on the solubility of the ink in water. The transport rate of hydrophilic ink increased as the relative humidity increased due to the increased meniscus width, while the transport rate of hydrophobic ink experience small change as the relative humidity increased, because the hydrophobic molecules does not deposited to the substrate through the meniscus but directly to the substrate surface.

- When no meniscus was formed between the substrate and the tip for a hydrophobic tip, the effect of tip size depended on the tip contact radius. The tip contact radius can be calculated using $r' = \sqrt{r^2 - (r - h)^2}$. Obviously, the

Conclusion and Recommendation for Future Work

contact radius increased as the tip curvature radius increased. When meniscus was formed, the effect of tip size depended on the size of the meniscus width, because the width of the meniscus is larger than the tip contact radius under ambient conditions (at 25°C and 50% RH). The meniscus width is roughly proportional to square root of tip curvature radius. Then at the same conditions, a tip with a larger curvature radius can generate a larger pattern than a tip with a smaller curvature radius due to a bigger contact point or the formation of a meniscus with a larger size.

- Chemical affinity is an important controlling parameter for DPN. It is necessary to consider the ink affinity to the substrate as well as to the tip when designing a new DPN system. DPN cannot be realized when chemical affinity between the ink and tip was larger or equal to the chemical affinity between the ink and substrate.

6.1.3 Anodic Nanooxidation, Force Nanolithography, and Characterization of Protein Patterns with AFM

(1) Anodic Nanooxidation was used to chemically modify Si, and the following conclusions have been obtained:

- A threshold voltage and protruded nanopatterns were observed on Si.
- The electric field enhanced the tip-induced oxidation.
- The oxidation of Si was limited by the diffusion of oxidizing products.
- Oxidation growth rate increased as the relative humidity increased.

However, reducing the relative humidity could improve the aspect ratio.

- Three-dimensional and complicated nanostructures could be fabricated in a single scan via raster lithography.

Conclusion and Recommendation for Future Work

- Gold could also be nanomodified by a negatively biased AFM tip.

(2) Force Nanolithography was used to create nanostructures on a soft polymer PMMA surface and an unsintered PZT sol surface. The following conclusions have been obtained:

- Force nanolithography could be used to fabricate nanopatterns on PMMA and an un-sintered PZT surface easily.
- Real data storage density of about 18 Gbit/inch² has been obtained on PMMA.
- The pit depth increased linearly with the increasing applied load for PMMA.
- By controlling the film thickness and the applied load, the film could be scratched and the bottom substrate was exposed. With the combination of a proper etching method, nanopatterns could be transferred into the bottom substrate.

(3) AFM was used to characterize micro- to nanostructures of protein on six surfaces with different chemical properties. The following conclusions have been obtained:

- Dense but non-uniform protein patterns with a single layer were immobilized on gold film through the formation of Au-S covalent bonds.
- Sparsely distributed, individual protein molecules were adsorbed on MHA SAMs surface due to repulsive electrostatic interactions.
- Branched protein patterns were formed on ODT SAMs with aggregates at knots via hydrophobic interactions.
- In the mixed SAMs of MHA and ODT with large concentration differences, the adsorption properties of the mixture SAMs were close to that of the dominant component. In the mixed SAMs of MHA and ODT with little

Conclusion and Recommendation for Future Work

concentration difference, the combination properties of the mixture SAMs were significantly changed. The amount of protein adsorbed on mixed SAMs was greater than that on the SAMs with single component due to coordination.

- The amount of protein adsorbed on six different surfaces decreased according to the following order: gold film > the mixture 1:10 SAMs > the mixture 1:1 SAMs > ODT SAMs > MHA SAMs (the mixture 10:1 SAMs).

6.2 The Limitations of AFM Nanopatterning

AFM-based nanotechnologies have demonstrated wide versatility, high precision, and high resolution in the fabrication of nanostructures compared to other technologies. However, there still exist the following limitations:

- Most of these methods are still at experimental stage. This is also the main limitation of the present research project. Fundamental studies have been done; however, studies for applications are weak due to the limited time.
- AFM-based nanotechnologies with a single tip have low efficiency, because nanostructures are fabricated in serial processes. This limitation could be overcome by developing tip arrays to realize patterning in a parallel process. Pioneering work has been conducted by Mirkin group and the IBM group. The tip has been developed from a conventional single tip to a passive tip array, where arrays containing 8, 25, and 1024 tips were microfabricated by Mirkin Group [318] and the IBM research group [95,96], respectively. In the passive tip array, all of the tips do the same motion and thus draw parallel

Conclusion and Recommendation for Future Work

patterns. Recently, an active tip array with 10 thermal bimorph active tips was fabricated [319]. The motion of the tips can be actuated individually independent of the adjacent tips. Therefore, the tips can be controlled to finish individual tasks. With the further development of highly parallel AFM probe arrays, the rapid fabrication and characterization of nanostructures may be realized.

- The ultimate resolution of these nanotechnologies is still ambiguous. The imaging resolution, especially lateral resolution, could be improved by making probes with a much smaller curvature radius. For example, the lateral resolution may approach 0.5 -1 nm if carbon nanotube probes are used. However, it is unclear whether such sharper probes could result in smaller structures.

- Characterization of some chemical and physical properties of the materials in these nanopatterns that have been produced is challenging. Compared with materials at a macroscopic scale, it is difficult to determine the properties of materials in nanostructures, thus preventing evaluations of the reproducibility and stability of the patterned nanostructures over time and in various environments. Sometimes the combination of other advanced instruments (such as scanning electron microscope, fluorescence microscope, X-ray Photoelectron Spectroscopy, and so forth) with AFM is required.

- Another limitation is the combination of AFM-based nanotechnologies with other techniques. A nanodevice is generally an integrated system that contains several functional parts. It is impossible to construct all of these

functional parts with only AFM-based nanotechnologies. For example, the electrodes in electronic nanodevices are commonly fabricated via photolithography.

6.3 Recommendation for Future Work

6.3.1 Dip-pen Nanolithography

Dip-pen nanolithography is a nanotechnique, which would be used to produce nanodevices for various applications. In Dip-pen nanolithography, the fundamental works have been studied. The future works should focus on applications. New ink-substrate systems for various applications can be designed by utilizing the obtained experience and knowledge about DPN. For example, a ferroelectric polymer, P(VDF-TrFE) have been deposited to gold substrate, and the DPN-generated micro- to nanopatterns of P(VDF-TrFE) have ferroelectric properties. The future work should utilize DPN to fabricate ferroelectric nanostructures for electrical, optical, biomedical, robotic, and sensing nanodevices. To fabricate a nanodevice is more difficult and troublesome than to fabricate the nanostructure, other functional parts may be fabricated using other techniques, such as photolithography, sputtering, CVD, etc. The alignment of all the functional parts is very important in order to obtain good quality. In addition to ferroelectric polymer, some other materials (conducting polymer, biomolecules) are alternate choices for fabricating functional nanodevices.

6.3.2 Anodic Nanooxidation

With the combination of etching and other proper techniques, anodic nanooxidation of semiconductors and metals can be used to prepare electric nanodevices of metals or semiconductors, such as field-effect transistor, quantum point, single electron memory, etc.

6.3.3 Force Nanolithography

By selecting a polymer with proper properties, force nanolithography can be used to prepare data storage nanodevices with high data storage density. Force nanolithography on unsintered PZT film can be used to study the piezoelectric properties at a nanometer scale.

References

1. S. A. Brooks, N. Dontha, C. B. Davis, J. K. Stuart, G. O'Neil and W. G. Kuhr, *Anal. Chem.* **72**, 3253 (2000).
2. J. A. M. Sondag-Huethorst, H. R. J. van Helleputte and L. G. J. Fokkink, *Appl. Phys. Lett.* **64**, 285 (1994).
3. A. A. Bergman, J. Buijs, J. Herbig, D. T. Mathes, J. J. Demarest, C. D. Wilson, C. T. Reimann, R. A. Baragiola, R. Hull and S. O. Oscarsson, *Langmuir* **14**, 6785 (1998).
4. W. M. Lackowski, P. Ghosh and R. M. Crooks, *J. Am. Chem. Soc.* **121**, 1419 (1999).
5. P. Ghosh, M. L. Amirpour, W. M. Lackowski, M. V. Pishko and R. M. Crooks, *Angew. Chem. Int. Ed.* **38**, 1592 (1999).
6. G. Binnig and H. Rohrer, *Helvetica Physica Acta* **55**, 726 (1982).
7. A. L. Weisenhorn, J. E. MacDougall, S. A. C. Gould, S. D. Cox and W. S. Wise, *Science* **247**, 1330 (1990).
8. G. Binnig, C. F. Quate and C. Gerber, *Phys. Rev. Lett.* **56**, 930 (1986).
9. G. Binnig, H. Fuchs and E. Stoll, *Surf. Sci.* **169**, L295 (1986).
10. G. Binnig, C. Gerber, E. Stoll, T. R. Albrecht and C. F. Quate, *Surf. Sci.* **189**, 1 (1987).
11. H. Iwasaki, T. Yoshinobu and K. Sudoh, *Nanotechnology* **14**, R55 (2003).
12. Q. Tang, S. Q. Shi and L. M. Zhou, *J. Nanosci. Nanotech.* **4**, 948 (2004).
13. Q. Tang, S. Q. Shi and L. M. Zhou, *Polymeric Nanostructures and Their Applications*. American Scientific Publisher (in press).

14. H. W. Lee, S. H. Kim, Y. K. Kwaka and C. S. Han, *Rev. Sci. Instrum.* **76**, 046108 (2005).
15. S. I. Lee, S. W. Howell, A. Raman, R. Reifenberger, C. V. Nguyen and M. Meyyappan, *Ultramicroscopy* **103**, 95 (2005).
16. J. Hu, X. D. Xiao, D. F. Ogletree and M. Salmeron, *Surf. Sci.* **327**, 358 (1995).
17. T. Thundat, X. Y. Zheng, G. Y. Chen, S. L. Sharp, R. J. Warmach and L. J. Schowalter, *Appl. Phys. Lett.* **63**, 2150 (1993).
18. D. Devecchio and B. Bhushan, *Rev. Sci. Instru.* **68**, 4498 (1997).
19. T. W. Kelley, E. L. Granstrom and C. D. Frisbie, *Adv. Mater.* **11**, 261 (1999).
20. J. Hu, X. D. Xiao, D. F. Ogletree and M. Salmeron, *Science* **268**, 267 (1995).
21. M. Munz, B. Cappella, H. Sturm, M. Geuss and E. Schulz, *Materials Contrasts and Nanolithography Techniques in Scanning Force Microscopy (SFM) and Their Application to Polymers and Polymer Composites*, *Adv. Polym. Sci.* **164**, 87 (2003).
22. K. H. Han, D. Spemann, R. Hohne, A. Setzer, P. Esquinazi and T. Butz, *Carbon* **41**, 785 (2003).
23. J. Frommer, *Scanning Tunneling Microscopy and Atomic Force Microscopy in Organic-Chemistry*, *Angew. Chem. Int. Ed.* **31**, 1298 (1992).
24. R. J. Hamers, *Scanned Probe Microscopies in Chemistry*, *J. Phys. Chem. B* **100**, 13103 (1996).

25. F. Saurenbach and B. D. Terris, *Imaging of Ferroelectric Domain-wall by Force Microscopy*, Appl. Phys. Lett. **56**, 1703 (1990).
26. R. Luthi, H. Haefke, K. P. Meyer, E. Meyer, L. Howald and H. J. Guntherodt, *Surface and Domain-Structures of Ferroelectric-Crystals Studied with Scanning Force Microscopy*, J. Appl. Phys. **74**, 7461 (1993).
27. R. Luthi, H. Haefke, P. Grutter, H. J. Guntherodt, L. Szczesniak and K. P. Meyer, *Surface and Domain-Structures of Ferroelectric GASH Crystals Studied by Scanning Force Microscopy*, Surf. Sci. **285**, L498 (1993).
28. S. V. Kalinin and D. A. Bonnel, *Local Potential and Polarization Screening on Ferroelectric Surfaces*, Phys. Rev. B. **63**, 125411 (2001).
29. M. Radmacher, R. W. Tilmann and H. E. Gaub, *Imaging Viscoelasticity by Force Modulation With the Atomic Force Microscope*, Biophys. J. **64**, 735 (1993).
30. S. H. Cohen, M. T. Bray and M. L. Lightbody, *Atomic Force Microscopy/Scanning Tunneling Microscopy*, Plenum Press• New York and London, 411 (1993).
31. M. E. Browning-Kelley, K. Wadu-Mesthrige, V. Hari and G. Y. Liu, *Langmuir* **13**, 343 (1997).
32. P. C. Braga and D. Ricci, *Atomic Force Microscopy: Biomedical Methods and Applications*, Humana Press, Totowa, New Jersey (2004).
33. O. Marti, H. O. Ribi, B. Drake, T. R. Albrecht, C. F. Quate and P. K. Hansma, *Atomic Force Microscopy of an Organic Monolayer*, Science **239**, 50 (1988).

34. E. Meyer, L. Howald, R. M. Overney, H. Heinzelmann, J. Frommer, H. J. Guntherodt, T. Wagner, H. Schier and S. Roth, *Molecular-Resolution Images of Langmuir-Blodgett-Films Using Atomic Force Microscopy*, *Nature* **349**, 398 (1991).
35. B. Drake, C. B. Prater, A. L. Weisenhorn, S. A. C. Gould, T. R. Albrecht, C. F. Quate, D. S. Cannell, H. G. Hansma and P. K. Hansma, *Imaging Crystals, Polymers, and Processes in Water with the Atomic Force Microscope*, *Science* **243**, 1586 (1989).
36. M. D. Kirk, T. Albrecht and C. F. Quate, *Low-Temperature Atomic Force Microscopy*, *Rev. Sci. Instrum.* **59**, 833 (1988).
37. E. L. Florin, V. T. Moy and H. E. Gaub, *Science* **264**, 415 (1994).
38. V. T. Moy, E. L. Florin and H. E. Gaub, *Science* **266**, 257 (1994).
39. G. U. Lee, D. A. Kidwell and R. J. Colton, *Langmuir* **10**, 354 (1994).
40. G. U. Lee, L. A. Chrisey and R. J. Colton, *Science* **266**, 771 (1994).
41. J. K. Stuart and V. Hlady, *Langmuir* **11**, 1368 (1995).
42. P. Hinterdorfer, W. Baumgartner, H. J. Gruber, K. Schilcher and H. Schindler, *Proc. Natl. Acad. Sci. USA* **93**, 3477 (1996).
43. S. Allen, X. Y. Chen, J. Davies, M. C. Davies, A. C. Dawkes, J. C. Edwards, C. J. Roberts, J. Sefton, S. J. B. Tendler and P. M. Williams, *Biochemistry* **36**, 7457 (1997).
44. U. Dammer, O. Popescu, P. Wagner, D. Anselmettid, H. J. Guntherodt and G. N. Misevic, *Science* **267**, 1173 (1995).
45. H. J. Butt, *J. Colloid Interface Sci.* **180**, 251 (1996).
46. Y. Arntz, J. D. Seelig, H. P. Lang, J. Zhang, P. Hunziker, J. P. Ramseyer, E. Meyer, M. Hegner and C. Gerber, *Nanotechnology* **14**, 86 (2003).

47. H. P. Lang, M. Hegner, E. Meyer and C. Gerber, *Nanotechnology* **13**, R29 (2002).
48. J. Fritz, M. K. Baller, H. P. Lang, H. Rothuizen, P. Vettiger, E. Meyer, H. J. Guntherodt, C. Gerber and J. K. Gimzewski, *Science* **288**, 316 (2000).
49. R. McKendry, J. Zhang, Y. Arntz, T. Strunz, M. Hegner, H. P. Lang, M. K. Baller, U. Certa, E. Meyer, H. J. Guntherodt and C. Gerber, *Proc. Natl. Acad. Sci. USA* **99**, 9783 (2002).
50. Y. Kim and C. M. Lieber, *Science* **257**, 375 (1992).
51. P. E. Sheehan and C. M. Lieber, *Science* **272**, 1158 (1996).
52. T. Junno, S. Anand, K. Deppert, L. Montelius and L. Samuelson, *Appl. Phys. Lett.* **66**, 3295 (1995).
53. C. Baur, B. C. Gazen, B. Koel, T. R. Ramachandran, A. A. G. Requicha and L. Zini, *J. Vac. Sci. Technol. B* **15**, 1577 (1997).
54. T. R. Ramachandran, C. Baur, A. Bugacov, A. Madhukar, B. E. Koel, A. Requicha and C. Gazen, *Nanotechnology* **9**, 237 (1998).
55. S. L. Brandow, W. J. Dressick, C. S. Dulcey, T. S. Koloski, L. M. Shirey, J. Schmidt and J. M. Calvert, *J. Vac. Sci. Technol. B* **15**, 1818 (1997).
56. T. Junno, K. Deppert, L. Montelius and L. Samuelson, *Appl. Phys. Lett.* **66**, 3627 (1995).
57. D. Q. Yang and E. Sacher, *Appl. Sur. Sci.* **210**, 158 (2003).
58. D. M. Schaefer and R. Reifenberger, *Appl. Phys. Lett.* **66**, 1012 (1995).
59. E. W. Wong, P. E. Sheehan and C. M. Lieber, *Science* **277**, 1971 (1997).
60. M. R. Falvo, G. J. Clary, R. M. Taylor, V. Chi, F. P. Brooks, S. Washburn and R. Superfine, *Nature* **389**, 582 (1997).

61. H. W. C. Postma, A. Sellmeijer and C. Dekker, *Adv. Mater.* **12**, 1299 (2000).
62. C. Thelander and L. Samuelson, *Nanotechnology* **13**, 108 (2002).
63. H. G. Hansma, J. Vesenka, C. Siegerist, G. Kelderman, H. Morrett, R. L. Sinsheimer, V. Elings, C. Bustamante and P. K. Hansma, *Science* **256**, 1180 (1992).
64. E. Henderson, *Nucleic Acids Res.* **20**, 445 (1992).
65. J. Hu, Y. Zhang, H. B. Gao, M.Q. Li and U. Hartmann, *Nano Letters* **2**, 55 (2002).
66. J. H. Lu, H. K. Li, H. J. An, G. H. Wang, Y. Wang, M. Q. Li, Y. Zhang and J. Hu, *J. Am. Chem. Soc.* **126**, 11136 (2004).
67. J. H. Lu, *Colloids and Surfaces B* **39**, 177 (2004).
68. S. Thalhammer, R. W. Stark, S. Muller, J. Wienberg and W. M. Heckl, *J. Struct. Biol.* **119**, 232 (1997).
69. R. W. Stark, S. Thalhammer, J. Wienberg and W. M. Heckl, *Appl. Phys. A* **66**, S579 (1998).
70. X. M. Xu and A. Ikai, *Biochem. Biophys. Res. Commun.* **248**, 744 (1998).
71. D. Fotiadis, D. J. Muller, G. Tsiotis, L. Hasler, P. Tittmann, T. Mini, P. Jenö, H. Gross and A. Engel, *J. Mol. Biol.* **283**, 83 (1998).
72. J. H. Hoh, G. E. Sosinsky, J. P. Revel and P. K. Hansma, *Biophys. J.* **65**, 149 (1993).
73. F. A. Schabert, C. Henn and A. Engel, *Science* **268**, 92 (1995).
74. D. J. Muller, G. Buldt and A. Engel, *J. Mol. Biol.* **249**, 239 (1995).
75. D. J. Muller, F. A. Schabert, G. Buldt and A. Engel, *Biophys. J.* **68**, 1681 (1995).

76. D. F. Fotiadis, S. Scheuring, S. A. Muller, A. Engel and D. J. Muller, *Micron* **33**, 385 (2002).
77. G. S. Blackman, C. M. Mate and M. R. Philpott. *Vacuum* **41**, 1283 (1990).
78. H. G. Hansma, S. A. C. Gould, P. K. Hansma, H. E. Gaub, M. L. Longo and J. A. N. Zasadzinski, *Langmuir* **7**, 1051(1991).
79. J. Garnaes, T. Bjornholm and J. A. N. Zasadzinski, *J. Vac. Sci. Technol. B* **12**, 1839 (1994).
80. T. Sumomogi, T. Endo, K. Kuwahara, R. Kaneko and T. Miyamoto, *J. Vac. Sci. Technol. B* **12**, 1876 (1994).
81. Y. Kim, J. L. Huang and C. M. Lieber, *Appl. Phys. Lett.* **59**, 3404 (1991).
82. E. Delawski and B. A. Parkinson, *J. Am. Chem. Soc.* **114**, 1661 (1992).
83. T. A. Jung, A. Moser, H. J. Hug, D. Brodbeck, R. Hofer, H. R. Hidber and U. D. Schwarz, *Ultramicroscopy* **42~44**, 1446 (1992).
84. T. Sumomogi, T. Endo, K. Kuwahara and R. Kaneko, *J. Vac. Sci. Technol. B* **13**, 1257 (1995).
85. R. Kaneko and E. Hamada, *Wear* **162~164**, 370 (1993).
86. S. Sundararajan and B. Bhushan, *Wear* **225~229**, 678 (1999).
87. T. Miyamoto, S. Miyake and R. Kaneko, *Wear* **162~164**, 733 (1993).
88. L. F. Chi, M. Anders, H. Fuchs, R. R. Johnston and H. Ringsdorf, *Science* **259**, 213 (1993).
89. H. J. Mamin and D. Rugar, *Appl. Phys. Lett.* **61**, 1003 (1992).
90. H. J. Mamin, B. D. Terris, L. S. Fan, S. Hoen, R. C. Barrett and D. Rugar, *IBM. J. Res. Develop.* **39**, 681 (1995).

91. H. J. Mamin, L. S. Fan, S. Hoen and D. Rugar, *Sensors and Actuators* **48**, 215 (1995).
92. B. W. Chui, T. D. Stowe, T. W. Kenny, H. J. Mamin, B. D. Terris and D. Rugar, *Appl. Phys. Lett.* **69**, 2767 (1996).
93. R. P. Ried, H. J. Mamin, B. D. Terris, L. S. Fan and D. Rugar, *J. Microelectromech. Syst.* **6**, 294 (1997).
94. B. W. Chui, T. D. Stowe, Y. S. Ju, K. E. Goodson, T. W. Kenny, H. J. Mamin, B. D. Terris, R. P. Ried and D. Rugar, *J. Microelectromech. Syst.* **7**, 69 (1998).
95. G. Binnig, M. Despont, U. Drechsler, W. Haberle, M. Lutwyche, P. Vettiger, H. J. Mamin, B. W. Chui and T. W. Kenny, *Appl. Phys. Lett.* **74**, 1329 (1999).
96. M. Lutwyche, C. Andreoli, G. Binnig, J. Brugger, U. Drechsler, W. Haberle, H. Rohrer, H. Rothuizen, P. Vettiger, G. Yaralioglu and C. Quate, *Sensors and Actuators* **73**, 89 (1999).
97. M. Despont, J. Brugger, U. Drechsler, U. Durig, W. Haberle, M. Lutwyche, H. Rothuizen, R. Stutz, R. Widmer, H. Rohrer, G. Binnig and P. Vettiger, *12th IEEE International Micro Electro Mechanical System Conference (MEMS99)*, Orlando, FL (1999), p. 564.
98. P. Vettiger, M. Despont and U. Drechsler, *IBM. J. Res. Develop.* **44**, 323 (2000).
99. L. L. Sohn and R. L. Willett, *Appl. Phys. Lett.* **67**, 1552 (1995).
100. U. Kunze and B. Klehn, *Adv. Mater.* **11**, 1473 (1999).
101. A. Notargiacomo, V. Foglietti, E. Cianci, G. Capellini, M. Adami, P. Faraci, F. Evangelisti and C. Nicolini, *Nanotechnology* **10**, 458 (1999).

102. S. Hu, A. Hamidi, S. Altmeyer, T. Koster, B. Spangenberg and H. Kurz, *J. Vac. Sci. Technol. B* **16**, 2822 (1998).
103. R. Klehn, S. Skaberna and U. Kunze, *Superlattices and Microstructures* **25**, 473 (1999).
104. B. Klehn and U. Kunze, *J. Appl. Phys.* **85**, 3897 (1999).
105. R. Magno and B. R. Bennett, *Appl. Phys. Lett.* **70**, 1855 (1997).
106. A. Avramescu, K. Uesugi and I. Suemune, *Jpn. J. Appl. Phys.* **36**, 4057 (1997).
107. L. A. Porter, Jr, A. E. Ribbe, J. M. Buriak. *Nano Lett.* **3**, 1043 (2003).
108. M. Wendel, S. Kuhn, H. Lorenz, J. P. Kotthaus and M. Holland, *Appl. Phys. Lett.* **65**, 1775 (1994).
109. S. Skaberna, M. Versen, B. Klehn, U. Kunze, D. Reuter and A. D. Wieck, *Ultramicroscopy* **82**, 153 (2000).
110. B. Irmer, R. H. Blick, F. Simmel, W. Godel, H. Lorenz and J. P. Kotthaus, *Appl. Phys. Lett.* **73**, 2051 (1998).
111. M. Versen, B. Klehn, U. Kunze, D. Reuter and A. D. Wieck, *Ultramicroscopy* **82**, 59 (2000).
112. V. Bouchiat and D. Esteve, *Appl. Phys. Lett.* **69**, 3098 (1996).
113. S. F. Lyuksyutov, R. A. Vaia, P. B. Paramonov, S. Juhl, L. Waterhouse, R. M. RAlch, G. Sigalov and E. Sancaktar, *Nature Materials* **2**, 468 (2003).
114. S. F. Lyuksyutov, P. B. Paramonov, S. Juhl and R. A. Vaia, *Appl. Phys. Lett.* **83**, 4405 (2003).
115. S. F. Lyuksyutov, P. B. Paramonov, R. A. Sharipov and G. Sigalov, *Phys. Rev. B* **70**, 174110 (2004).

116. P. Guthner and K. Dransfeld, *Appl. Phys. Lett.* **61**, 1137 (1992).
117. O. Kolosov, A. Gruverman, J. Hatano, K. Takahashi and H. Tokumoto, *Phys. Rev. Lett.* **74**, 4309 (1995).
118. C. H. Ahn, T. Tybell, L. Antognazza, K. Char, R. H. Hammond, M. R. Beasley, O. Fischer and J. M. Triscone, *Science* **276**, 1100 (1997).
119. T. Hidaka, T. Maruyama, M. Saitoh, N. Mikoshiba, M. Shimizu, T. Shiosaki, L. A. Wills, R. Hiskes, S. A. Dicarolis and J. Amano, *Appl. Phys. Lett.* **68**, 2358 (1996).
120. T. Tybell, C. H. Ahn and J. M. Triscone, *Appl. Phys. Lett.* **72**, 1454 (1998).
121. T. Tybell, C. H. Ahn and J. M. Triscone, *Appl. Phys. Lett.* **75**, 856 (1999).
122. X. Q. Chen, H. Yamada, T. Horiuchi, K. Matsushige, S. Watanabe, M. Kawai and P. S. Weiss, *J. Vac. Sci. Technol. B* **17**, 1930 (1999).
123. C. Durkan, M. E. Welland, D. P. Chu and P. Migliorato, *Phys. Rev. B* **60**, 16198 (1999).
124. C. Durkan, D. P. Chu, P. Migliorato and M. E. Welland, *Appl. Phys. Lett.* **76**, 366 (2000).
125. P. Paruch, T. Tybell and J. M. Triscone, *Appl. Phys. Lett.* **79**, 530 (2001).
126. S. V. Kalinin and D. A. Bonnel, *Appl. Phys. Lett.* **78**, 1116 (2001).
127. S. Xu and Y. G. Liu, *Langmuir* **13**, 127 (1997).
128. S. Xu, S. Miller, P. E. Laibinis and G. Y. Liu, *Langmuir* **15**, 7244 (1999).
129. J. F. Liu, J. R. Von Ehr, C. Baur, R. Stallcup, J. Randall and K. Bray,

- Appl. Phys. Lett. **84**, 1359 (2004).
130. N. A. Amro, S. Xu and G. Y. Liu, Langmuir **16**, 3006 (2000).
131. B. L. Jackson and J. T. Groves, J. Am. Chem. Soc. **126**, 13878(2004).
132. P. V. Schwartz, Langmuir **17**, 5971 (2001).
133. P. T. Hurley, A. E. Ribbe and J. M. Buriak, J. Am. Chem. Soc. **125**, 11334 (2003).
134. S. Xu, P. E. Laibinis and G. Y. Liu, J. Am. Chem. Soc. **120**, 9356 (1998).
135. J. C. Garno, Y. Yang, N. A. Amro, S. Cruchon-Dupeyrat, S. W. Chen and G. Y. Liu, Nano Letters **3**, 389 (2003).
136. J. F. Liu, S. Cruchon-Dupeyrat, J. C. Garno, J. Frommer and G. Y. Liu, Nano Letters **2**, 937 (2002).
137. X. Z. Wang, D. J. Zhou, T. Rayment and C. Abell, Chem. Commun. **4**, 474 (2003).
138. M. Z. Liu., N. A. Amro, C. S. Chow and G. Y. Liu, Nano Letters **2**, 863 (2002).
139. M. Z. Liu and G. Y. Liu, Langmuir **21**, 1972 (2005).
140. D.J. Zhou, K. Sinniah, C. Abell and T. Rayment, Langmuir **18**, 8278 (2002).
141. D. J. Zhou, K. Sinniah, C. Abell and T. Rayment, Angew. Chem. Int. Ed. **42**, 4934 (2003).
142. K. Wadu-Mesthrige, S. Xu, N. A. Amro and G. Y. Liu, Langmuir **15**, 8580 (1999).
143. K. Wadu-Mesthrige, N. A. Amro, J. C. Garno, S. Xu and G. Y. Liu, Biophys. J. **80**, 1891 (2001).

144. G. Y. Liu and N. A. Amro, Proc. Natl. Acad. Sci. USA **99**, 5165 (2002).
145. J. R. Kenseth, J. A. Harnisch, V.W. Jones and M. D. Porter, Langmuir **17**, 4105 (2001).
146. M. A. Case, G. L. Mclendon, Y. Hu, T. K. Vanderlick and G. Scoles, Nano Letters **3**, 425 (2003).
147. C. L. Cheung, J. A. Camarero, B. W. Woods, T. W. Lin, J. E. Johnson and J. J. De Yoreo, J. Am. Chem. Soc. **125**, 6848 (2003).
148. C. H. Jang, B. D. Stevens, P. R. Carlier, M. A. Calter and W. A. Ducker, J. Am. Chem. Soc. **124**, 12114 (2002).
149. T. L. Brower, J. C. Garno, A. Ulman, G. Y. Liu, C. Yan, A. Golzhauser and M. Grunze, Langmuir **18**, 6207 (2002).
150. S. Xu, N. A. Amro and G. Y. Liu, Appl. Surf. Sci. **175-176**, 649 (2001).
151. W. T. Muller, D. L. Klein, T. Lee, J. Clarke, P. L. Mceuen and P. G. Schultz, Science **268**, 272 (1995).
152. L. K. Bladell, S. Banerjee and S. S. Wong, Langmuir **18**, 5055 (2002).
153. S. Takeda, C. Nakamura, C. Miyamoto, N. Nakamura, M. Kageshima, H. Tokumoto and J. Miyake, Nano Letters **3**, 1471 (2003).
154. R. Maoz, S. R. Cohen and J. Sagiv, Adv. Mater. **11**, 55 (1999).
155. R. Maoz, E. Frydman, S. R. Cohen and J. Sagiv, Adv. Mater. **12**, 424 (2000).
156. J. H. Gu, C. M. Yam, S. Li and C. Z. Cai, J. Am. Chem. Soc. **126**, 8098 (2004).
157. R. Garcia, M. Calleja and H. Rohrer, J. Appl. Phys. **86**, 1898 (1999).
158. P. Avouris, T. Hertel, R. Martel, Appl. Phys. Lett. **71**, 285 (1997).
159. J. A. Dagata, T. Inoue and J. Itoh, J. Appl. Phys. **84**, 6891 (1998).

160. P. Auouris, R. Martel and T. Hertel, *Appl. Phys. A.* **66**, S659 (1998).
161. T. G. Ruskell, J. L. Pyle, R. K. Workman, X. Yao and D. Sarid, *Electro. Lett.* **32**, 1411 (1996).
162. F. Perez-Murano, C. Martin, N. Barniol, H. Kuramochi, H. Yokoyama and J. A. Dagata, *Appl. Phys. Lett.* **82**, 3086 (2003).
163. M. Calleja, J. Anguita, R. Garcia, K. Birkelund, F. Perez-Murano and J. A. Dagata, *Nanotechnology* **10**, 34 (1999).
164. K. Morimoto, F. Perez-Murano and J. A. Dagata, *Appl. Surf. Sci.* **158**, 205 (2000).
165. T. Teuschler, K. Mahr, S. Miyazaki, M. Hundhausen and L. Ley, *Appl. Phys. Lett.* **67**, 3144 (1995).
166. D. Stievenard, P. A. Fontaine and E. Dubois, *Appl. Phys. Lett.* **70**, 3272 (1997).
167. A. Majumdar, P. I. Oden, J. P. Carrejo, L. A. Nagahara, J. J. Graham and J. Alexander, *Appl. Phys. Lett.* **61**, 2293 (1992).
168. H. C. Day and D. R. Allee, *Appl. Phys. Lett.* **62**, 2691 (1993).
169. F. S. S. Chien, C. L. Wu, Y. C. Chou, T. T. Chen, S. Gwo and W. F. Hsieh, *Appl. Phys. Lett.* **75**, 2429 (1999).
170. D. W. Wang, L.M. Tsau and K. L. Wang, *Appl. Phys. Lett.* **65**, 1415 (1994).
171. R. Garcia, M. Calleja and P. M. Francesc, *Appl. Phys. Lett.* **72**, 2295 (1998).
172. M. Calleja and R. Garcia, *Appl. Phys. Lett.* **76**, 3427 (2000).
173. M. Tello and R. Garcia, *Appl. Phys. Lett.* **79**, 424 (2001).
174. F. Perez-Murano, G. Abadal and N. Barniol, *J. Appl. Phys.* **78**, 6797

- (1995).
175. D. P. Wang, V. A. Bykov, S. V. Lemesenko and J. Chin, *Electr. Microsc. Soc.* **20**, 620 (2001).
176. F. S. S. Chien, J. W. Chang and S. W. Lin, *Appl. Phys. Lett.* **76**, 360 (2000).
177. F. S. S. Chien, Y. C. Chou and T. T. Chen, *J. Appl. Phys.* **89**, 2465 (2001).
178. J. Kim, K. I. B. Song and S. Q. Lee, *Journal of Microscopy* **209**, 236 (2003).
179. S. A. Harfenist, M. M. Yazdanpanah and R. W. Cohn, *J. Vac. Sci. Technol. B* **21**, 1176 (2003).
180. S. Gwo, C. L. Yeh, P. F. Chen, Y. C. Chou, T. T. Chen, T. S. Chao, S. F. Hu and T. Y. Huang, *Appl. Phys. Lett.* **74**, 1090 (1999).
181. E. S. Snow and P. M. Campbell, *Appl. Phys. Lett.* **64**, 1932 (1994).
182. L. M. Tsau, D. W. Wang and K. L. Wang, *Appl. Phys. Lett.* **64**, 2133 (1994).
183. M. Yasutake, Y. Ejiri and T. Hattori, *Jpn. J. Appl. Phys.* **32**, L1021 (1993).
184. F. S. S. Chien, W. F. Hsieh, S. Gwo, A. E. Vladar and J. A. Dagata, *J. Appl. Phys.* **91**, 10044 (2002).
185. S. Hosaka, H. Koyanagi, A. Kikukawa. *Jpn. J. Appl. Phys.* **32**, L464 (1993).
186. J. Zheng, Z. Zhu and H. Chen, *Langmuir* **16**, 4409 (2000).
187. E. S. Snow and P. M. Campbell, *Science* **270**, 1639 (1995).
188. S. C. Minne, H. T. Soh and Ph. Flueckiger, *Appl. Phys. Lett.* **66**, 703

- (1995).
189. P. M. Campbell, E. S. Snow and P. J. McMarr, Appl. Phys. Lett. **66**, 1388 (1995).
190. R. Held, T. Heinzl and P. Studerus, Appl. Phys. Lett. **71**, 2689 (1997).
191. K. Matsumoto, Y. Gotoh and T. Maeda, Appl. Phys. Lett. **76**, 239 (2000).
192. G. Abadal, Z. J. Davis and A. Boisen, Probe Microscopy **2**, 121 (2001).
193. E. B. Cooper, S. R. Manalis and H. Fang, Appl. Phys. Lett. **75**, 3566 (1999).
194. R. D. Piner, J. Zhu, F. Xu, S. H. Hong and C. A. Mirkin, Science **283**, 661 (1999).
195. R. G. Nuzzo and D. L. Allara, J. Am. Chem. Soc. **105**, 4481 (1983).
196. G. Agarwal, L. A. Sowards, R. R. Naik and M. O. Stone, J. Am. Chem. Soc. **125**, 580 (2003).
197. Prasanna Chandrasekhar, *Conducting Polymers, fundamentals and applications*, Boston: Kluwer Academic (1999).
198. A. Noy, A. E. Miller, J. E. Klare, B. L. Weeks, B. W. Woods and J. J. DeYoreo, Nano letters **2**, 109 (2002).
199. M. Yu, D. Nyamjav and A. Ivanisevic, J. Mater. Chem. **15**, 649 (2005).
200. B. Kim, G. Pyrgiotakis and W. M. Sigmund, J. Nanosci. Nanotech. **4**, 221 (2004).
201. J. H. Lim and C. A. Mirkin, Adv. Mater. **14**, 1474 (2002).
202. B. W. Maynor, S. F. Filocamo, M. W. Grinstaff and J. Liu, J. Am. Chem. Soc. **124**, 522 (2002).
203. P. Xu and D. L. Kaplan, Adv. Mater. **16**, 628 (2004).

204. M. Su, M. Aslam, L. Fu, N. Q. Wu and V. P. Dravid, *Appl. Phys. Lett.* **84**, 4200 (2004).
205. S. Y. Jang, M. Marquez and G. A. Sotzing, *J. Am. Chem. Soc.* **126**, 9476 (2004).
206. R. McKendry, W. T. S. Huck, B. Weeks, M. Fiorini, C. Abell and T. Rayment, *Nano Letters* **2**, 713 (2002).
207. G. H. Degenhart, B. Dordi, H. Schonherr and G. J. Vancso, *Langmuir* **20**, 6216 (2004).
208. X. G. Liu, S. W. Guo and C. A. Mirkin, *Angew. Chem. Int. Ed.* **42**, 4785 (2003).
209. Y. Cho and A. Ivanisevic, *J. Phys. Chem. B* **108**, 15223 (2004).
210. Y. Cho and A. Ivanisevic, *J. Phys. Chem. B* **109**, 6225 (2005).
211. L. M. Demers, D. S. Ginger, S. J. Par, Z. Li, S. W. Chung and C. A. Mirkin, *Science* **296**, 1836 (2002).
212. L. Wei, X. Hong, W. Guo, Y. B. Bai and T. J. Li, *Chemical Journal of Chinese University* **23**, 1368 (2002).
213. D. L. Wilson, R. Martin, S. Hong, M. Cronin-Golomb, C. A. Mirkin and D. L. Kiplan, *Proc. Natl. Acad. Sci. USA* **98**, 13660 (2001).
214. K. B. Lee, J. H. Lim and C. A. Mirkin, *J. Am. Chem. Soc.* **125**, 5588 (2003).
215. J. Hyurk, D. S. Ginger, K. B. Lee, J. Heo, J. M. Nam and C. A. Mirkin, *Angew. Chem. Int. Ed.* **42**, 2309 (2003).
216. J. M. Nam, S. W. Han, K. B. Lee, X. G. Liu, M. A. Ratner and C. A. Mirkin, *Angew. Chem. Int. Ed.* **43**, 1246 (2004).
217. Y. Li, B. W. Maynor and J. Liu, *J. Am. Chem. Soc.* **123**, 2105 (2001).

218. G. Agarwal, R. R. Naik and M. O. Stone, *J. Am. Chem. Soc.* **125**, 7408 (2003).
219. H. Jung, C. K. Dalal, S. Kuntz, R. Shah and C. P. Collier, *Nano Letters* **4**, 2171 (2004).
220. F. N. Yan, L. H. Chen, Q. L. Tang and R. Wang, *Bioconjugate. Chem.* **15**, 1030 (2004).
221. J. C. Smith, K. B. Lee, Q. Wang, M. G. Finn, J. E. Johnson, M. Mrksich and C. A. Mirkin, *Nano Letters* **3**, 883 (2003).
222. D. Nyamjav and A. Invanisevis, *Adv. Mater.* **15**, 1805 (2003).
223. D. Nyamjav and A. Invanisevis, *Biomaterials* **26**, 2749 (2005).
224. J. Hyun, W. K. Lee, N. Nath, A. Chilkoti and S. Zauscher, *J. Am. Chem. Soc.* **126**, 7330 (2004).
225. H. Zhang, Z. Li and C. A. Mirkin, *Adv. Mater.* **14**, 1472 (2002).
226. K. B. Lee, E. Y. Kim, C. A. Mirkin and S. M. Wolinsky, *Nano Letters* **4**, 1869 (2004).
227. K. B. Lee, S. J. Park, C. A. Mirkin, J. C. Smith and M. Mrksich, *Science* **295**, 1702 (2002).
228. J. Hyun, S. J. Ahn, W. K. Lee, A. Chilkoti and S. Zauscher, *Nano Letters* **2**, 1203 (2002).
229. L. M. Demers, S. J. Park, T. A. Taton, Z. Li and C. A. Mirkin, *Angew. Chem. Int. Ed.* **40**, 3071 (2001).
230. D. E. Meyer and A. Chilkoti, *Nat. Biotechnol.* **17**, 112 (1999).
231. J. D. Gerding, D. M. Willard and A. V. Orden, *J. Am. Chem. Soc.* **127**, 1106 (2005).
232. H. Zhang, R. Elghanian, N. A. Amro, S. Disawal and R. Eby, *Nano*

- Letters **4**, 1649 (2004).
233. X. G. Liu, L. Fu, S. Hong, V. P. Dravid and C. A. Mirkin, *Adv. Mat.* **14**, 231 (2002).
234. L. Fu, X. Liu, Y. Zhang, V. P. Dravid and C. A. Mirkin, *Nano Letters* **3**, 757 (2003).
235. G. Gundiah, N. S. John, P. J. Thomas, G. U. Kulkarni, C. N. R. RAO and S. Heun, *Appl. Phys. Lett.* **84**, 5341 (2004).
236. M. B. Ali, T. Ondarcuhu, M. Burst and C. Joachim, *Langmuir* **18**, 872 (2002).
237. M. Su, X. G. Liu, S. Y. Li, V. P. Dravid and C. A. Mirkin, *J. Am. Chem. Soc.* **124**, 1560 (2002).
238. B. W. Maynor, Y. Li and J. Liu, *Langmuir* **17**, 2575 (2001).
239. L. A. Porter, Jr. H. C. Choi, J. M. Schmeltzer, A. E. Ribbe, Lindsay C. Elliott and J. M. Buriak, *Nano Letters* **2**, 1369 (2002).
240. D. A. Weinberger, S. G. Hong, C. A. Mirkin and B. W. Wessels and T. B. Higgins, *Adv. Mate.* **12**, 1600 (2000).
241. H. Zhang, S. W. Chung and C. A. Mirkin, *Nano Letters* **3**, 43 (2003).
242. T. Stifter, O. Marti and B. Bhushan, *Phys. Rev. B* **62**, 13667 (2000).
243. J. Jang, G. C. Schatz and M. A. Ratner, *J. Chem. Phys.* **116**, 3875 (2002).
244. J. Jang, G. C. Schatz and M. A. Ratner, *Phys. Rev. Lett.* **90**, 156104 (2003).
245. B. L. Weeks, A. Noy and A. E. Miller, *Phys. Rev. Lett.* **24**, 255505 (2002).
246. P. E. Sheehan and L. J. Whitman, *Phys. Rev. Lett.* **88**, 156104 (2002).

247. P. V. Schwartz, *Langmuir* **18**, 4041(2002).
248. S. Rozhok, R. Piner and C. A. Mirkin, *J. Phys. Chem. B* **107**, 751 (2003).
249. J. Jang, S. Hong, G. C. Schatz and M. A. Ratner, *J. Chem. Phys.* **115**, 2721 (2001).
250. K. A. Peterlinz and R. Georgiadis, *Langmuir* **12**, 4731 (1996).
251. P. Amanda, J. Jang, G. C. Schatz, M. A. Ratner and S. Hong, *Phys. Rev. Lett.* **90**, 115505 (2003).
252. R. Schellin, G. Hess and W. Kuehnel, *IEEE Transactions on Electrical Insulation* **27**, 867 (1992).
253. P. Lum, *IEEE Transactions on Ultrasonics, Ferroelectrics, and Frequency Control* **43**, 536 (1996).
254. M. Toda, *IEEE Transactions on Ultrasonics, Ferroelectrics, and Frequency Control* **49**, 299 (2002).
255. D. K. Schwartz, *Annu. Rev. Phys. Chem.* **52**, 107 (2001).
256. E. D. Pylant and G. E. Poirier, *Science* **272**, 1145 (1996).
257. G. E. Poirier, W. P. Fitts and J. M. White, *Langmuir* **17**, 1176 (2001).
258. A. V. Bune, S. Ducharme, V. M. Fridkin, L. M. Blinov, S. P. Palto, N. Petukhova and S. Yudin, *Appl. Phys. Lett.* **67**, 3975 (1995).
259. S. P. Palto, L. M. Blinov, E. Dubovik, V.M. Fridkin, N. Petukhova, A.V. Sorokin, K. erkhovskaya, S. G. Yudin and A. Zlatkin, *Europhys. Lett.* **34**, 465 (1996).
260. L. M. Blinov, V. M. Fridkin, S. P. Palto, A. V. Sorokin, S. G. Yudin, *Thin Solid Films* **284-285**, 474 (1996).
261. A. V. Bune, V. M. Fridkin, S. Ducharme, L. M. Blinov, S. P. Palto, A. V.

- Sorokin, S. G. Yudin and A. Zlatkin, *Nature* **391**, 874 (1998).
262. X. Q. Chen, H. Yamada, Y. Terai, T. Horiuchi, K. Matsushige and P. S. Weiss, *Thin Solid Films* **353**, 259 (1999).
263. S. Rozhok, P. Sun, R. Piner, M. Lieberman and C. A. Mirkin, *J. Phys. Chem. B* **108**, 7814 (2004).
264. J. E. Sader, J. W. M. Chon and P. Mulvaney, *Rev. Sci. Instrum.* **70**, 3967 (1999).
265. D. S. Ginger, H. Zhang, and C. A. Mirkin, *Angew. Chem. Int. Ed.* **43**, 30 (2004).
266. J. Haaheim, R. Eby, M. Nelson, J. Fragala, B. Rosner, H. Zhang and G. Athas, *Ultramicroscopy* **103**, 117 (2005).
267. C. B. Ross, L. Sun, and R. M. Crooks, *Langmuir* **9**, 632 (1993).
268. T. Hsu, and J. M. Cowley, *Ultramicroscopy* **11**, 239 (1983).
269. V. M. Hallmark, S. Chiang, J. F. Rabolt, J. D. Swalen and R. J. Wilson, *Phys. Rev. Lett.* **59**, 2879 (1987).
270. N. Kasupke and M. Henzler, *Surf. Sci.* **92**, 407 (1980).
271. L. Daikhin and M. Urbakh, *Phys. Rev. E* **49**, 1424 (1994).
272. K. A. Peterlinz and R. Georgiadis, *Langmuir* **12**, 4731 (1996).
273. H. Ohigashik and K. Koga, *Jpn. J. Appl. Phys.* **21**, L455 (1982).
274. A. Ivanisevic and C. A. Mirkin, *J. Am. Chem. Soc.* **123**, 7887 (2001).
275. H. Jung, R. Kulkarni and C. P. Collier, *J. Am. Chem. Soc.* **125**, 12096 (2003).
276. S. E. Kooi, L. A. Baker, P. E. Sheehan and L. J. Whiteman, *Adv. Mater.* **16**, 1013 (2004).
277. Z. Q. Wei, C. Wang and C. L. Bai, *Surf. Sci.* **467**, 185 (2000).

278. P. A. Thiel and T. E. Madey, Surf. Sci. Rep. **7**, 221 (1987).
279. S. Lee and R. W. Staehle, Corrosion **52**, 843 (1996).
280. H. Zhang and C. A. Mirkin, Chem. Mater. **16**, 1480 (2004).
281. P. E. Sheehan, L. J. Whitman, W. P. King and B. A. Nelson, Appl. Phys. Lett. **85**, 1589 (2004).
282. E. J. Peterson, B. L. Weeks, J. J. De Yoreo and P. V Schwartz, J. Phys. Chem. B **108**, 15206 (2004).
283. S. S. Blawas and W. M. Reichert, Biomaterials **19**, 595 (1998).
284. M. Mrksich and G. M. Whitesides, Trends Biotechnol. **13**, 228 (1995).
285. D. V. Nicolau, T. Taguchi, H. Taniguchi and S. Yoshikawa, Langmuir **14**, 1927 (1998).
286. A. Bernard, E. Delamarche, H. Schmid and B. Michel, Langmuir **14**, 2225 (1998).
287. E. Delamarche, A. Bernard, H. Schmid and B. Michel, Science **276**, 779 (1997).
288. N. Patel, G. H. W. Sanders, K. M. Shakesheff and S. M. Cannizzaro, Langmuir **15**, 7252 (1999).
289. P. M. St. John, R. Davis, N. Cady and J. Czajka, Analytical chemistry **70**, 1108 (1998).
290. J. Y. Fang and C. M. Knobler, Langmuir **12**, 1368 (1996).
291. J. Y. Fang, C. M. Knobler, M. Gingery and F. A. Eiserling, J. Phys. Chem. B **101**, 8692 (1997).
292. C. D. Bain and G. M. Whitesides, Science **240**, 62 (1988).
293. C. D. Bain and G. M. Whitesides, J. Am. Chem. Soc. **110**, 3665 (1988).

294. C. D. Bain and G. M. Whitesides, *J. Am. Chem. Soc.* **110**, 6560 (1988).
295. C. D. Bain, J. Evall and G. M. Whitesides, *J. Am. Chem. Soc.* **111**, 7155 (1989).
296. C. D. Bain and G. M. Whitesides, *J. Am. Chem. Soc.* **111**, 7164 (1989).
297. C. Pale-Grosdemange, E. S. Simon and K. L. Prime, *J. Am. Chem. Soc.* **113**, 12 (1991).
298. K. L. Prime and G. M. Whitesides, *Science* **252**, 1164 (1991).
299. C. Roberts, C. S. Chen, M. Mrksich, V. Martichonok, D. E. Ingber and G. M. Whitesides, *J. Am. Chem. Soc.* **120**, 6548 (1998).
300. N. Patel, M. C. Davies, M. Hartshorne, R. J. Heaton and C. J. Robers, *Langmuir* **13**, 6485 (1997).
301. A. Guiomar, J. T. Guthrie and S. D. Evans, *Langmuir* **15**, 1198 (1999).
302. T. G. Grasel, J. A. Pierce and S. L. Cooper, *J. Biomed. Mater. Res.* **21**, 815 (1987).
303. L. Li, S. Chen and S. Jiang, *Langmuir* **19**, 2974 (2003).
304. N. B. Sheller, S. Petrash and M. D. Foster, *Langmuir* **14**, 4535 (1998).
305. O. Mori and T. Imae, *Colloids and Surfaces B* **9**, 31 (1997).
306. P. Ying, Y. Yu, G. Jin and Z. Tao, *Colloids and Surfaces B* **32**, 1 (2003).
307. X. Wang, L. Yu, C. Li, F. Zhang, Z. Zheng and X. Liu, *Colloids and Surfaces B* **30**, 11 (2003).
308. M. M. Browne, G. V. Lubarsky, M. R. Davidson and R. H. Bradley, *Surface Science* **553**, 155 (2004).
309. J. Kim, R. Yamasaki, J. Park, H. Jung, H. Lee and T. Kawai, *Journal*

- of Bioscience and Bioengineering **97**, 138 (2004).
310. T. Peters, JR, *Advances in Protein Chemistry: Serum Albumin* (Academic Press: NewYork) **37**, 161 (1985).
311. T. Nonogaki, S. Xu, S. Kugimiya, S. Sato, I. Miyata and M. Yonese, *Langmuir* **16**, 4272 (2000).
312. C. Chaiyasut and T. Tsuda, *Chromatography* **22**, 91 (2001).
313. X. Chen, N. Patel, M. C. Davies, C. J. Roberts, S. J. B. Tendler, P. M. Williams, J. Davies, A. C. Dawkes and J. C. Edwards, *Appl. Phys. A* **66**, S631 (1998).
314. Ch. C. Dupont-Gillain, C. M. J. Fauroux, D. C. J. Gardner and G. J. Leggett, *J. Biomed. Mater. Res. A* **67A**, 548 (2003).
315. J. Y. Yoon, H. Y. Park, J. H. Kim and W. S. Kim, *Journal of Colloid and Interface Science* **177**, 613 (1996).
316. S. E. Creager and J. Clarke, *Langmuir* **10**, 3675 (1994).
317. C. C. Dupont-Gillain, B. Nysten and P. G. Rouxhet, *Polym. Int.* **48**, 271 (1999).
318. S. H. Hang and C. A. Mirkin, *Science* **288**, 1808 (2000).
319. X. F. Wang, D. A. Bullen, J. Zou, C. Liu and C. A. Mirkin, *Journal of Vacuum Science and Technology B* **22**, 2563 (2004)